Production and PAC studies of ^{83}Rb/^{83m}Kr solid state calibration sources for the KATRIN experiment

Dissertation
zur
Erlangung des Doktorgrades (Dr. rer. nat.)
der
Mathematisch-Naturwissenschaftlichen Fakultät
der
Rheinischen Friedrich-Wilhelms-Universität Bonn

vorgelegt von
Marius Lennart Arenz
aus
Siegburg

Bonn, 2017

Angefertigt mit Genehmigung
der
Mathematisch-Naturwissenschaftlichen Fakultät
der
Rheinischen Friedrich-Wilhelms-Universität Bonn

1. Gutachter: Priv. Doz. Dr. Reiner Vianden
2. Gutachter: Prof. Dr. Karl Maier

Tag der Promotion: 29.09.2017
Erscheinungsjahr: 2017

And the heart of the matter is hardly to perceive

Sieges Even - Paramount
Text: Markus Steffen

Contents

1. Introduction

Modern large-scale experiments are designed to answer key questions in physics. Trying to extract information about the very nature of the universe, these experiments have grown over time. International collaborations work on set-ups with increasing complexity and costs. Nonetheless, the key question is rarely the only one asked and answered during the commissioning of such an experiment. Usually, a wealth of related scientific and technical problems from various more or less related scientific fields arise and need to be solved to achieve the final goal.

In such a way this work is related to one of the present large-scale experiments: The KArlsruhe TRItium Neutrino (KATRIN) experiment. It aims to determine the neutrino mass to an unprecedented precision of $0.2\,\mathrm{eV}\,c^{-2}$. This is an improvement of one order of magnitude compared to the current upper limit of 2.1 keV. In the last century our understanding of the neutrino has evolved dramatically: From being a mere remedy to save the laws of energy and momentum conservation the neutrino has evolved to a particle being an integral part of the Standard Model. Initially the neutrino was considered a purely hypothetical particle, thereafter it was assumed to be massless for decades. In 2015 the Nobel prize was awarded for the discovery of neutrino oscillations, their presence showing that neutrinos *have* mass. Still, some of its properties are unknown to this day, one of them being its mass. The knowledge of the neutrino mass is the key to improve cosmological models and to extend the Standard Model.

The KATRIN experiment studies the tritium β-decay kinematics to deduce the neutrino mass. The emitted electrons' kinetic energy close to the β-spectrum's endpoint is analysed using a high-precision Magnetic Adiabatic Collimation combined with an Electrostatic (MAC-E) filter spectrometer. During these measurements, the spectrometer's retarding voltage is monitored using a nuclear standard: a well-known Conversion Electron (CE) line emitted by $^{83\mathrm{m}}$Kr. Because of their favourable properties the experiment uses substrates ion implanted with ^{83}Rb, a generator of the desired $^{83\mathrm{m}}$Kr with considerably longer half life.

The first part of this work focusses on the production of these ion implanted samples at the BONn Isotope Separator (BONIS) facility. The necessary changes to the ion source to obtain sufficient ion implantation efficacies are described. Two retarding lenses are integrated into the mass separator set-up to allow for a wide range of implantation energies and beam spot sizes.

Samples implanted with ^{83}Rb/^{83m}Kr can not only be used for calibration purposes at the KATRIN experiment. The decay of ^{83}Rb and ^{83m}Kr to ^{83}Kr populate γ-γ and e-γ radiation cascades, a fundamental prerequisite for the application of the Perturbed Angular Correlation (PAC) method. This well-established technique of nuclear solid state physics measures the hyperfine interaction between the probe nucleus' Nuclear Quadrupole Moment (NQM) and an Electric Field Gradient (EFG) at the probes' lattice site. Due to the short range of the interaction, PAC measurements allow to extract information from the direct vicinity of the implanted probes.

The second part of this thesis focusses on the design and the construction of a PAC measurement apparatus for the probe nuclei ^{83}Rb(^{83}Kr) and ^{83m}Kr(^{83}Kr). Only one (unpublished) work reports on the use of ^{83}Rb(^{83}Kr) as probe nucleus up to now. The present work will show the feasibility of PAC measurements using these new probe nuclei. The set-up's mechanical and electronic design is discussed. In particular, the application of Avalanche Photo Diodes (APDs) as detectors for low energy γ quanta and CEs in PAC measurements is explored. These detectors are used in conjunction with a custom build voltage sensitive preamplifier for a time resolution in the ns range.

Finally, the substrates used for the KATRIN experiment are studied using the PAC method, giving insight into the incorporation lattice sites of ^{83m}Kr and its generator nuclide ^{83}Rb.

2. The KATRIN experiment

The KArlsruhe TRItium Neutrino (KATRIN) experiment is the upcoming next-generation experiment to determine the neutrino mass to an unprecedented precision. If no neutrino mass signal will be observed in the five years of measurement, the upper limit will be $m_{\bar{\nu}_e} = 0.2\,\mathrm{eV}\,c^{-2}$ with a confidence level of 90 %. If a positive signal is measured, the discovery potential is 5σ for $m_{\bar{\nu}_e} = 0.35\,\mathrm{eV}\,c^{-2}$ [KATRIN04].

This chapter gives a brief introduction into the history of neutrinos and the ongoing search for the neutrino mass (section 2.1). In sections 2.2 and 2.3 the KATRIN experiment, its main components and their working principles are sketched briefly. This work contributes to the monitoring of the high voltage system, hence, the monitoring concept is described in more detail in section 2.4.

2.1. The search for the neutrino (mass)

The neutrino's story[1] began with the β-decay's discovery and the identification of the β-radiation being electrons. In analogy to the discrete energy of emitted α and γ radiation, the β-particles were expected to be emitted with a well-defined energy as well. In contrast to this anticipation, the energy spectrum proved to be continuous. It is a characteristic of a two-body decay, however, that the energies of the decay products are kinematically determined by the masses of the outgoing particles. Thus, the β-decay seemed to violate the law of conservation of energy and momentum. In 1930 Pauli postulated a solution that would save these conservation laws: He proposed a third particle (later on called neutrino by Fermi) being emitted carrying away the unobserved energy deficiency [Pauli30].

The first experimental evidence of the (electron) antineutrino[2] was found in 1956 by Reines and Cowan. In a large tank of water sandwiched between layers of liquid scintillator they observed the inverse beta decay

$$\bar{\nu}_e + p \rightarrow n + e^+ \tag{2.1}$$

using the positron's annihilation radiation [ReiCow56].

For a long time neutrinos were assumed to be massless and all measurements up to now confirm this hypothesis within their precision. However, there *is* proof for neutrinos having

[1] Of course this section can not give a full list of all neutrino experiments. Here only some milestones are mentioned.

[2] At this time ν_μ and ν_τ were not known.

a finite mass: the neutrino oscillations. When in 1968 Davis and Harmer [DavHar68] measured the solar neutrino flux exploiting the reaction

$$\nu_e + {}^{37}\mathrm{Cl} \rightarrow {}^{37}\mathrm{Ar} + e^- \tag{2.2}$$

the results differed significantly from the theoretical values calculated by Bahcall and Bahcall [BahBah68]. The existence of neutrino oscillations was suggested by Gribov and Pontecorvo [GriPon69] in the following year. In 2002, the SNO (Sudbury Neutrino Observatory) collaboration published results proving the existence of neutrino oscillations [SNO02]. The use of heavy water made this experiment sensitive to all three neutrino flavours in the solar flux, showing that electron neutrinos actually transform into μ and τ neutrinos. The experiment confirmed the previous results and the total observed flux matched the prediction from the solar model. The exploited charged current reaction

$$\nu_e + d \rightarrow p + p + e^- \tag{2.3}$$

is sensitive to electron neutrinos only, whereas the neutral current and elastic scattering reactions

$$\nu_{e,\mu,\tau} + d \rightarrow n + p + \nu_{e,\mu,\tau} \tag{2.4}$$

$$\nu_{e,\mu,\tau} + e^- \rightarrow \nu_{e,\mu,\tau} + e^- \tag{2.5}$$

are sensitive to all three neutrino flavours. The existence of neutrino flavour oscillations implies the neutrino having a non-zero mass. Unfortunately, neutrino oscillation experiments are not sensitive to neutrino masses but only to differences of the neutrino masses squared.

The search for the neutrino mass is not just an academic task. Due to the neutrinos being the second-most abundant particles in the universe, their contribution to the total energy might be considerable. Furthermore, the knowledge of the neutrino mass will help to expand the Standard Model that included the neutrino as massless for a long time.

The current upper limit for the mass of the electron neutrino is set by two experiments based on a direct kinematic approach carried out in Mainz and Troitsk. They are 2.3 eV c^{-2} and 2.1 eV c^{-2}, respectively [KATRIN04]. Both experiments make use of the tritium β-decay as well.

2.2. The KATRIN approach

The KATRIN experiment uses a model-independent, kinematic approach to determine the neutrino mass or its upper limit. During the beta decay of tritium

$$T \rightarrow {}^{3}\mathrm{He} + e^- + \bar{\nu}_e \tag{2.6}$$

an electron and an anti-neutrino are emitted. The decay's energy is distributed between the ^{3}He nucleus' and the electron's kinetic energy as well as the neutrino's rest mass and kinetic

energy. This leads to a continuous energy spectrum of the emitted electron, see figure 2.1 for a sketch of the tritium β-spectrum. At the spectrum's endpoint of 18.6 keV, the electrons gain the maximum kinetic energy, leaving just enough energy for the neutrino to be created. Hence, by studying the endpoint region of the tritium β-spectrum, the neutrino mass can be deduced.

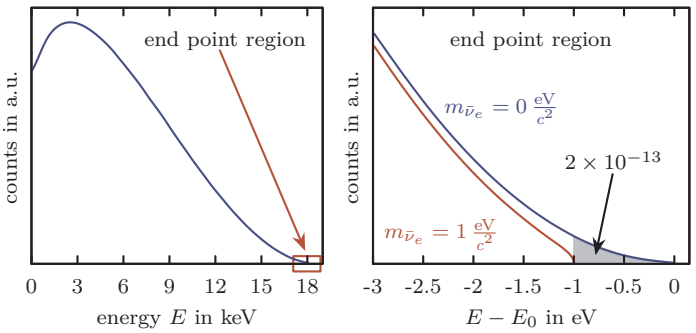

Figure 2.1.: The tritium β-spectrum (left) and a magnification of the endpoint region (right) with $E_0 = 18.6\,\mathrm{keV}$. The blue line shows the spectrum's shape for $m_{\bar{\nu}_e} = 0\,\mathrm{eV}\,c^{-2}$, the red line for $m_{\bar{\nu}_e} = 1\,\mathrm{eV}\,c^{-2}$. The area shaded in grey contains only 2×10^{-13} of the electrons emitted in the Windowless Gaseous Tritium Source (WGTS).

To carry out such an experiment with the described sensitivity, a wealth of minor and major experimental challenges have to be overcome. Three of which are sketched in the following: Only electrons emitted with an energy close to the endpoint energy carry information on the neutrino mass. In practice only 2×10^{-13} of all tritium decays are of interest for the KATRIN experiment. To obtain a reasonable count rate at the detector, a high luminosity tritium source is needed. Furthermore, the tritium can not be contained in a closed volume, any window material would cause energy losses and would, thus, make the experiment impossible. The WGTS described in section 2.3.2 solves this problem.
The emitted electrons need to be analysed by a high resolution spectrometer with good angular acceptance and background reduction. Spectrometers of the Magnetic Adiabatic Collimation combined with an Electrostatic (MAC-E) filter type combine these benefits. The working principle is sketched briefly in section 2.2.1. At the KATRIN experiment, three MAC-E filters are used. Two of them are operating in the main beamline to analyse the incoming tritium β-decay electrons: the pre-spectrometer and the main spectrometer (see sections 2.3.5 and 2.3.6, respectively).
A third major task is to control the retarding potential of up to 35 kV of the main spectrometer to a precision of better than 3 ppm. The retarding voltage is reduced to less than 10 V by a high precision voltage divider. The resulting voltage can be measured by a state-of-the-art high precision voltmeter. As a cross check, a nuclear standard is used. The K-Conversion Electron (CE) of the 32 keV transition (abbreviated K-32) in $^{83\mathrm{m}}$Kr with its energy of 17.8 keV being close to the tritium endpoint is monitored using the same high voltage supply and the third MAC-E filter, the Monitor Spectrometer (MoS). The monitoring process is described in section 2.4 in more detail.

2.2.1. MAC-E filters

To determine the neutrino mass from the endpoint of the tritium β-spectrum a spectrometer with both a high energy resolution and a high luminosity is necessary. The Magnetic Adiabatic Collimation combined with an Electrostatic (MAC-E) filter technique [BeaPor80] used for both preceding neutrino mass experiments at Mainz and Troitsk [WeiDeg99; LobAse99] fulfils both requirements and will be applied at the KATRIN experiment.

A MAC-E filter consists of an evacuated spectrometer tank and two superconducting magnets at both ends of the tank, a sketch of its working principle can be found in figure 2.2. The magnetic field created by the solenoids is axially symmetric and inhomogeneous. Depending on the size of the tank and the field B_{max} inside the solenoids, the magnetic field in the spectrometer's centre B_{min} can differ by several orders of magnitude from B_{max}. Additionally, an electric field symmetric to the spectrometer's central plane is applied (the most negative voltage is applied on the central electrode). Its field lines are perpendicular to this plane and are nearly parallel to the magnetic field lines in this plane.
An electron emitted in the source will travel towards the spectrometer along a magnetic field line. Depending on the initial angle between its emission direction and the magnetic field, it will move in a more or less pronounced spiral around the field line. During this cyclotron motion, its total momentum[3] is split in a component parallel $p_{\parallel}$ and perpendicular $p_{\perp}$ to the field lines. Using the electron's perpendicular momentum component (or the corresponding kinetic energy), its orbital magnetic momentum μ can be expressed as

$$\mu = \frac{1}{2} qrv = \frac{p_{\perp}^2}{2m_e B} = \frac{E_{\perp}}{B} \tag{2.7}$$

with the magnetic field B, the electron's mass m_e, its charge q, its velocity v and the electron cyclotron resonance radius r. As the electron encounters the magnetic field gradient, a force

$$\vec{F} = \nabla(\vec{\mu} \cdot \vec{B}) \tag{2.8}$$

accelerates the electrons towards weaker magnetic fields. Energy conservation requires the perpendicular velocity component to decrease at the same time. Simultaneously, electrons have to move against the electric field $\mathscr{E}$, limiting the acceleration. In this case, the magnetic field change per cyclotron revolution is small and the transformation can be considered adiabatic. As a consequence, μ is a constant of motion. Therefore, considering equation (2.7), a decrease of B along the electrons trajectory by some orders of magnitude, leads to a decrease in orders of magnitude of $p_{\perp}$. Hence, in the spectrometer's central plane where the magnetic field is minimal, the so-called analysing plane, the electrons travel nearly parallel to the electric and magnetic field lines. In the analysing plane the effect of the magnetic field is minimised while the electron's kinetic energy is analysed whether it is sufficient to overcome the antiparallel electric field.
Electrons with sufficient kinetic energy are reaccelerated after passing the analysing plane and

[3] Because electrons emitted by tritium are far from being relativistic, none of the calculations here are relativistic.

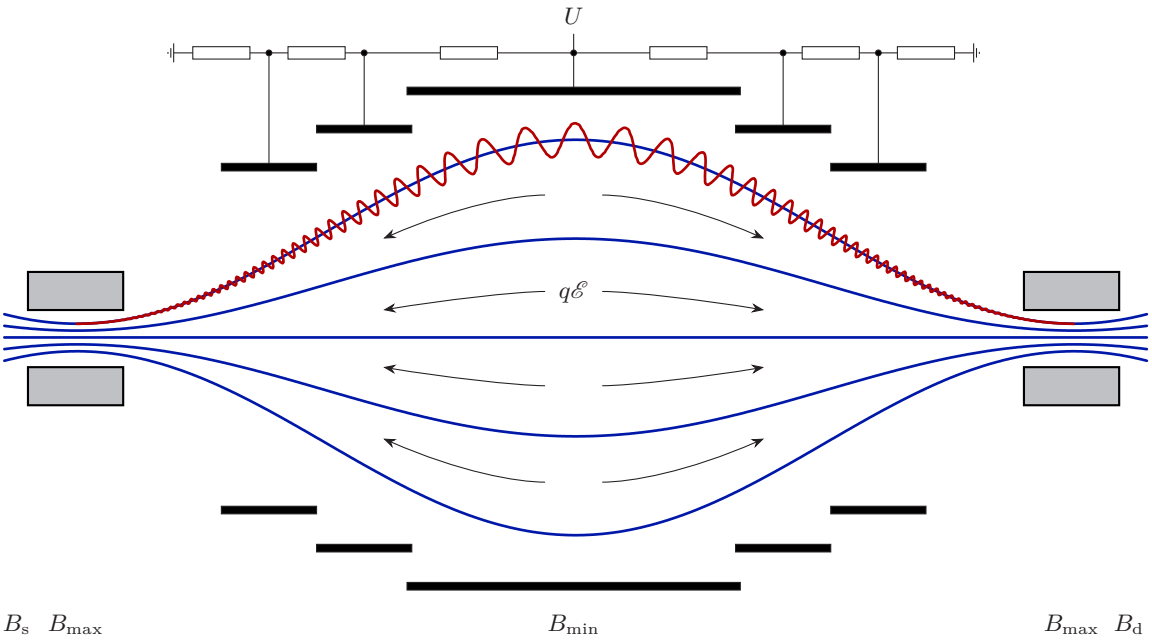

Figure 2.2.: The working principle of a MAC-E filter. The two super-conducting solenoids shown in grey create the magnetic field lines shown in blue. The magnetic field is maximal in the solenoids, it is minimal in the centre of the spectrometer. The magnetic field lines define the path around which the cyclotron motion, sketched in red for one field line, takes place. An electric retarding potential is applied via the cylindrical electrodes depicted in black. The force $q\mathscr{E}$ acts on electrons entering the electric field. B_d is the magnetic field after the solenoid, focussing the electrons on the detector, B_s is the magnetic field in the source.

undergo the inverse transformation. They are focussed towards the second superconducting solenoid. Because the MAC-E filter is a high-energy pass, the resulting spectra are integral spectra.

A MAC-E filter's energy resolving power follows directly from equation (2.7):

$$\frac{E}{\Delta E} = \frac{B_{max}}{B_{min}} \tag{2.9}$$

2.3. An overview of the KATRIN experiment

The KATRIN experiment is being set-up on the Campus North of the (KIT) Karlsruhe Institute for Technology with some components already being commissioned and operational. Its approximately 70 m long beamline consists of seven sections discussed in sections 2.3.1 to 2.3.7 and shown in figure 2.3. The following descriptions are based on the KATRIN

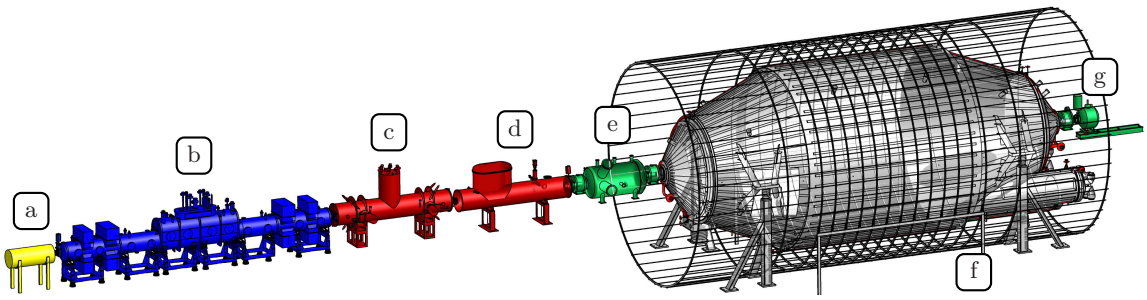

Figure 2.3.: A drawing of the roughly 70 m long KATRIN beamline including all major components (similar to [KATRIN04]). a = rear section, b = Windowless Gaseous Tritium Source (WGTS), c = Differential Pumping Section (DPS), d = Cryogenic Pumping Section (CPS), e = pre-spectrometer, f = main-spectrometer, g = Focal Plane Detector (FPD). The Monitor Spectrometer (MoS) is not shown.

design report [KATRIN04], for a more detailed description of the components, the reader is referred to this document.

2.3.1. The Rear section

The rear section closes the WGTS on the experiment's rear end (see figure 2.3 for the position in the beamline). Its main task is to create a defined electrical potential at the end of the beamline for the plasma created by decays and ionisations in the WGTS. The gold plated rear wall represents this termination. Additionally, by detecting bremsstrahlung of electrons hitting the rear wall, the tritium activity in the WGTS can be monitored continuously. Furthermore an electron gun will be placed behind the rear wall. It can provide an electron beam for a wide range of tasks like testing of the transmission function of the whole beam tube.

2.3.2. The Windowless Gaseous Tritium Source (WGTS)

The electrons from the tritium β-decay have to be guided to the spectrometer and detector without energy loss to achieve the required energy resolution. This constraint is overcome by using the Windowless Gaseous Tritium Source (WGTS). Tritium is injected in the centre of this 10 m long tubular cryostat. The WGTS is terminated by the rear section and is connected to the Differential Pumping Section (DPS) downstream without any windows that could cause electron energy loss. The inserted molecules diffuse to the end of the WGTS where TurboMolecular Pump (TMP) remove most of the them from the tube. The recovered gas is recycled by a recovery system, tritium molecules moving further downstream will be removed from the beam tube by either the DPS or the Cryogenic Pumping Section (CPS). During the experiment's operation, a tritium injection rate of $1.7 \times 10^{11}\,\mathrm{Bq\,s^{-1}}$ is targeted. A huge fraction of all electrons emitted in downstream direction are guided towards the

DPS and the spectrometers by seven superconducting solenoids. The WGTS is kept at 27 K in two-phase neon bath with an uncertainty of only 30 mK.

2.3.3. The Differential Pumping Section (DPS)

The tritium leaving the WGTS towards the detector section needs to be removed from the beamline before it can reach the spectrometers without blocking the electrons. In the Differential Pumping Section (DPS) the beamline is split into five segments, each of them tilted by 20° with respect to the previous segment. While the electrons are guided through the beam tube by the magnetic field generated by five superconducting solenoids, four TMP reduce the tritium flow by five orders of magnitude.

2.3.4. The Cryogenic Pumping Section (CPS)

The tritium flow reduction achieved by the DPS is not sufficient for the KATRIN experiment. The traces of tritium leaving the DPS would generate an intolerable background contribution, if they would arrive at the spectrometers. The Cryogenic Pumping Section (CPS) is the subsequent countermeasure and is mounted directly after the DPS, see figure 2.3. The CPS consists of two subsections, each comprising three straight elements tilted by 20° with respect to each other. Six superconducting solenoids guide the electrons from the WGTS through the CPS while a straight way for tritium molecules is blocked. The walls of the CPS are cooled to liquid He temperature and a layer of Ar gas is condensed on the surface adsorbing tritium molecules. In this way, an additional tritium flow reduction by seven orders of magnitude is realised.
The Forward Beam Monitor (FBM) can be inserted into the beamline at one of the pump ports of the CPS. The FBM is used to monitor the β-electron flux. It consists of two preamplifier boards, each equipped with a Positive Intrinsic Negative (PIN) diode mounted on a cantilever. The diodes can be moved through the whole beam tube to scan the electron flux just before the pre-spectrometer.

2.3.5. The pre-spectrometer

As described in section 2.2, only the electrons with an energy close to the endpoint energy of 18.6 keV carry information on the neutrino mass. To avoid ionisation of residual gas by the superfluous electrons in the main spectrometer volume, electrons below a threshold energy of 18.3 keV are rejected by the pre-spectrometer. This corresponds to an electron flux reduction by a factor of 10^6. The pre-spectrometer is a MAC-E filter as described in section 2.2.1. In contrast to the main spectrometer, for the pre-spectrometer high voltage stability and the energy resolution are not critical.

2.3.6. The main spectrometer

The main spectrometer is the KATRIN experiment's main analysing tool. This MAC-E filter's huge dimensions (10 m diameter, 23.3 m length) allow for a 9 m wide flux tube in the analysing plane with magnetic fields in the order of 0.3 mT. With $B_{\max} = 6\,\mathrm{T}$ and an electron energy of 18.6 keV, equation (2.9) yields an energy resolution of $\Delta E \approx 0.93\,\mathrm{eV}$.
The vessel is kept on elevated potential and works as a guard electrode for the two-layered wire electrodes covering its inner wall. The wires are kept on a slightly more negative potential. Hence, secondary electrons generated by interactions with cosmic muons are reflected back on the vessel wall by the wire electrodes.
The whole vessel is kept at ultra-high vacuum conditions with a pressure in the 10^{-11} mbar range. Six TMP and 3 km of Non-Evaporable-Getter (NEG) strips are utilised. The NEG strips are mounted behind baffles cooled to liquid nitrogen temperature to capture Rn emanating from the getter strips [KATRIN16].
The main spectrometer is surrounded by air coils and a low field correction system to exclude influences from earth's magnetic field and stray fields from superconducting magnets.

2.3.7. The Focal Plane Detector (FPD)

Electrons passing the main spectrometer are guided to the PIN diode-type Focal Plane Detector (FPD). Its active area with 90 mm diameter is divided into 148 pixels of equal area. The central four pixels form a circle, being surrounded by twelve concentric rings, each subdivided into twelve segments. The detector system is surrounded by γ-shielding and a plastic scintillator veto system to tag incoming cosmic muons.

2.4. High voltage monitoring

The retarding voltage applied to the main spectrometer needs to be controlled to a precision of better than 3 ppm to meet the design specifications. To ensure this level of accuracy, the retarding potential is monitored by three redundant methods. The first method is the conduction of regular direct calibration runs of the main spectrometer with CEs of well-known energies emitted by a condensed $^{83\mathrm{m}}$Kr source.
The second method is the direct measurement of the high voltage applied to the main spectrometer. Suitable commercial high-precision voltmeters operate at voltages up to 10 V. Hence, the retarding voltage has to be reduced to this voltage range. Because no off-the-shelf voltage dividers are available, two high-precision voltage dividers with a long-term stability of 1 ppm were developed [ThüMar09], making a direct voltage measurement feasible.
The third method makes use of a nuclear standard. The same high voltage applied to the main spectrometer is applied to another MAC-E filter, the MoS. In the MoS the well-known K-CE line of the 32.2 keV transition in $^{83\mathrm{m}}$Kr is observed. Its energy of 17.8 keV is close to the tritium endpoint energy of 18.6 keV, the difference can be compensated by biasing the CE source.

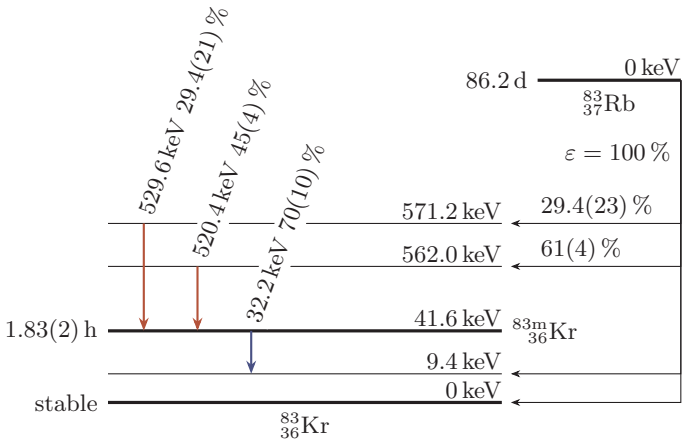

Figure 2.4.: A simplified decay scheme of ^{83}Rb/^{83m}Kr based on data by McCutchan [McCutc15]. The ^{83m}Kr level is populated by nearly 75 % of all ^{83}Rb decays. A more detailed sketch can be found in figure 4.3.

2.4.1. Solid state calibration sources

The solid state ^{83m}Kr sources needed for the high voltage monitoring have to fulfil a number of requirements.

The short half life of ^{83m}Kr of just 1.83 h [McCutc15] poses a problem. It is possible to condense a sub-monolayer of ^{83m}Kr on a Highly Oriented Pyrolytic Graphite (HOPG) substrate and renew this layer regularly. This principle is used to calibrate the main spectrometer and yields good results. However, these kind of sources are huge, sophisticated and expensive apparatuses [Ostric09].
To circumvent the ^{83m}Kr half life restrictions, ^{83}Rb can be used as generator for ^{83m}Kr. ^{83}Rb has a half life of 86.2 d and populates the ^{83m}Kr level with nearly 75 % of its decays [McCutc15]. A simplified decay scheme of ^{83}Rb can be found in figure 2.4. The long ^{83}Rb half life is beneficial for the long-term application of the CE sources but poses a serious problem if the spectrometer is contaminated with it. Hence, the ^{83}Rb has to be retained in the source. After the ^{83}Rb and before the ^{83m}Kr decay, during its half life of 1.83 h, diffusion or desorption processes may happen. ^{83m}Kr atoms not remaining in the CE source are lost for the calibration process. Hence, ^{83m}Kr has to be retained in these sources as well. Two kinds of sources have been experimentally explored: vacuum evaporated and ion implanted samples.

Experiments with vacuum evaporated ^{83}Rb sources show some disadvantages. In the production process, ^{83}Rb solution is evaporated on a backing in vacuum conditions and at elevated temperatures. Aside from the obvious vulnerability of the ^{83}Rb layer at a touch, the ^{83m}Kr retention proved to be below 20 % and to vary from source to source. Furthermore, the ^{83}Rb is exposed to the surrounding conditions, even in vacuum an interaction of residual gas with the ^{83}Rb atoms can not be avoided. An investigation of these sources' properties and further literature references can be found in the work of Zbořil [Zbořil11].

The problems present in the vacuum evaporated sources can be solved by ion implanting ^{83}Rb into a substrate material. The first sources of this type for the KATRIN experiment

were produced and analysed by Zbořil [Zbořil11]. The ^{83}Rb deposition depth can be controlled by the implantation energy. Neither the ^{83}Rb nor the ^{83m}Kr atoms are exposed to the surrounding conditions. These sources are still vulnerable against scratching but no ^{83}Rb is released when the implanted surface is touched. In ion implanted sources, the ^{83m}Kr retention still varies but is usually at least as high as 80 % [Slezák15a]. Current ion implanted calibration sources are HOPG chips implanted with energies between 4 keV and 30 keV at the BONn Isotope Separator (BONIS) facility in Bonn. The development of these sources presented in this work and the work of Slezák [Slezák15a] is the result of a close cooperation. The in-depth analysis of the calibration sources' performance was carried out by the mentioned author, while the implantations and improvements of implantation parameters are described in this work.

3. The PAC method

This chapter gives a short introduction to the theory of the Perturbed Angular Correlation (PAC) method. After a less formal overview, the underlying theoretical background of the unperturbed γ-γ angular correlations is sketched briefly and extended to e-γ angular correlations. Subsequently, the theory of the PAC is sketched briefly. These discussions essentially follow the treatise by Frauenfelder et al. [FraSte68]. Detailed and exhaustive discussions on these topics can be found in the literature [BieRos53; FraSte68; Butz89; SchWei92]. For an in-depth discussion on e-γ correlations and the related difficulties, again the reader is referred to the literature [RosBie52; FraSte68; BieRos53].
Sometimes the term angular correlation refers to directional correlation comprising polarisation correlation. In this work, however, no polarisation is measured. Hence, the term angular correlation is used synonym to directional correlation, the following theoretical discussion is restricted to this case as well.

3.1. A less formal overview

In this section some of the theory presented in later sections as well as some prerequisites are discussed without an extensive mathematical formalism. Firstly, the angular correlation of free nuclei and emission pattern for oriented nuclei are reviewed. Secondly, the PAC in the presence of Electric Field Gradients (EFGs) and some properties of the latter are sketched, following the treatise of Schatz et al. [SchWei92].

3.1.1. Free nuclei and angular correlation

A nucleus in an initially exited state $|I_\mathrm{i} m_\mathrm{i}\rangle$ can de-excite into a final state $|I_\mathrm{f} m_\mathrm{f}\rangle$ with the nuclear spins $I_\mathrm{i}, I_\mathrm{f}$ and the associated magnetic quantum numbers $m_\mathrm{i}, m_\mathrm{f}$ by emitting a radiation quantum R with defined angular momentum $|\ell_1 m_1\rangle$. The following selection rules [Jackso99] apply

$$|I_\mathrm{i} - I_\mathrm{f}| \leq \ell_1 \leq I_\mathrm{i} + I_\mathrm{f} \qquad\qquad m_1 = m_\mathrm{i} - m_\mathrm{f} \tag{3.1}$$

From the solutions of Maxwell's equations expressed in multipole fields, one can calculate the angular distribution of the emitted radiation with respect to the nuclear spin's orientation. Every transition allowed by equation (3.1) has a well defined emission characteristic, describable by the normalised vector spherical harmonics $\vec{X}_{\ell m}$ [Jackso99]. The

angular distribution of the emission for pure dipole and quadrupole radiation is shown in figure 3.1.

Adding an intermediate level $|Im\rangle$ to the system allows two successive transitions with the emission of R_1 and R_2, a so-called R_1-R_2 cascade. Such a system is sketched in figure 3.2. For each emission cascade, the emission direction $\vec{k_1}$ of R_1 is correlated to $\vec{k_2}$ of R_2 due to angular momentum conservation. Despite this correlation, the observed emission pattern of R_2 is still isotropic due to the random orientation of the nuclear spins I_i of the initial state. However, it is possible to select nuclei with spins pointing in a distinguished direction and measure the angular correlation if two radiations R_1 and R_2 are emitted successively in a radiation cascade. Assuming R_1 is always detected in direction $\vec{k_1}$, an ensemble of nuclei with non-isotropic spin orientation is selected. The following emission of R_2 will show an angular correlation with respect to $\vec{k_1}$. Some demonstrative examples of radiation cascades can be found in Schatz et al. and Frauenfelder et al. [SchWei92; FraSte68].

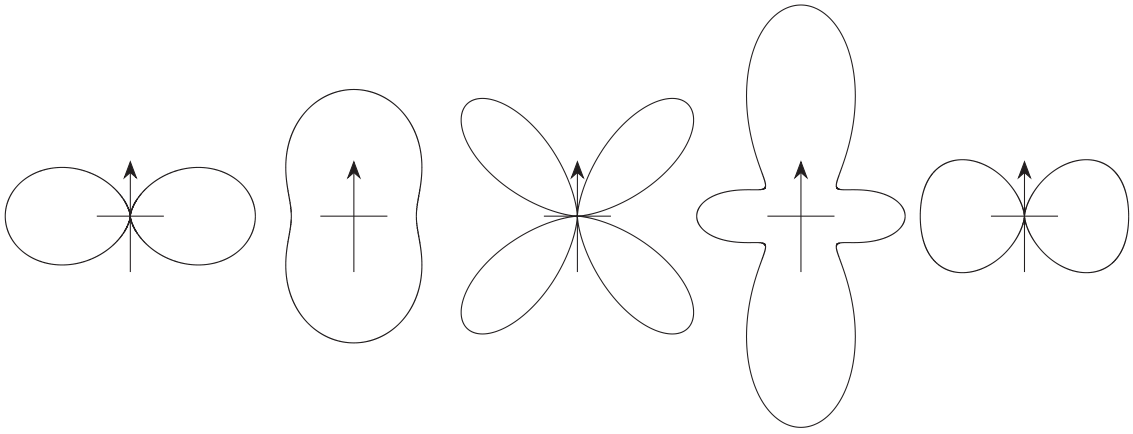

Figure 3.1.: A Sketch of the radiation patterns for pure dipoles and quadrupoles given by the vector spherical harmonics $|\vec{X}_{\ell m}|^2$ with respect to the nuclear spin's orientation I_i indicated by the arrow [SchWei92; Jackso99]. The angular quantum numbers for each angular distribution as well as their (not normalised) formal representation are given below the patterns.

3.1.2. Probe nuclei in matter and Electric Field Gradients (EFGs)

Inserted into a substrate, the nucleus may be subject to a magnetic flux density and will be surrounded by charges creating an electric potential at its site. In the former case, the magnetic flux density and the nuclear magnetic dipole moment, in the latter case the EFG and the nucleus' charge distribution interact. Both hyperfine interactions will lift the m-degeneracy of the cascade's intermediate nuclear level and lead to a perturbation of the

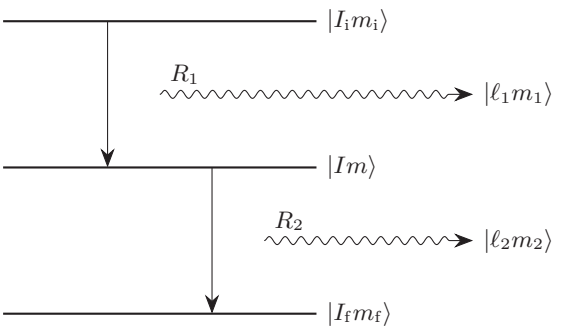

Figure 3.2.: A three level system with the nomenclature used in the present work. A nucleus initially in state $|I_\mathrm{i} m_\mathrm{i}\rangle$ emits R_1 with the quantum numbers $|\ell_1 m_1\rangle$ during the decay to its intermediate level $|Im\rangle$. Successively, by emitting R_2 characterised by $|\ell_2 m_2\rangle$ it reaches its final state $|I_\mathrm{f} m_\mathrm{f}\rangle$.

angular correlation. In this work the magnetic interaction between the nucleus' magnetic moment and magnetic fields are of no interest and thus are not considered any further.

In a substrate, the nucleus with charge distribution $\varrho(\vec{r})$ is surrounded by charges creating a potential $\Phi(\vec{r})$ at the its site. Expanding the potential in a Taylor series at $\vec{r} = 0$ separates the nucleus' energy in this potential into a monopole, a dipole and a quadrupole part:

$$E = \underbrace{\Phi_0 \cdot \int \varrho(\vec{r}) \mathrm{d}^3 r}_{E^{(0)}\text{: monopole}} + \underbrace{\sum_{\alpha=1}^{3} \left(\frac{\partial \Phi}{\partial x_\alpha}\right)_0 \cdot \int \varrho(\vec{r}) x_\alpha \mathrm{d}^3 r}_{E^{(1)}\text{: dipole}} + \underbrace{\frac{1}{2} \sum_{\alpha,\beta} \left(\frac{\partial^2 \Phi}{\partial x_\alpha x_\beta}\right)_0 \cdot \int \varrho(\vec{r}) x_\alpha x_\beta \mathrm{d}^3 r}_{E^{(2)}\text{: quadrupole}} + \ldots \tag{3.2}$$

The monopole term $E^{(0)}$ represents the Coulomb energy for a point-like charge and is the same for all isotopes of one element. It does contribute to the potential energy of the lattice but it is of no relevance for angular correlation measurements. $E^{(1)}$ describes the interaction between the electric dipole moment created by the nucleus' charge distribution and the electric field. Quantum mechanically, the expectation value of the nuclear dipole moment vanishes and thus $E^{(1)} = 0$. The symmetric 3×3 matrix

$$\left(\frac{\partial^2 \Phi}{\partial x_\alpha x_\beta}\right)_0 = \Phi_{\alpha\beta} \tag{3.3}$$

can be diagonalised using a principal axis transformation. Exploiting that $\Phi_{\alpha\alpha}$ can be written as a traceless part $V_{\alpha\alpha}$ and a part containing the trace, one can write

$$E^{(2)} = E_\mathrm{Q} = \frac{e}{6} \sum_\alpha V_{\alpha\alpha} Q_{\alpha\alpha} \tag{3.4}$$

with the tensor of the Nuclear Quadrupole Moment (NQM)

$$Q_{\alpha\alpha} = \frac{1}{e} \int \varrho(\vec{r}) \left(3x_\alpha^2 - r^2\right) \mathrm{d}^3 r \tag{3.5}$$

$V_{\alpha\alpha}$ is the tensor of the EFG. It is traceless and can thus be described by two independent parameters. After choosing a principal axis reference frame in which $|V_{zz}| \geq |V_{yy}| \geq |V_{xx}|$

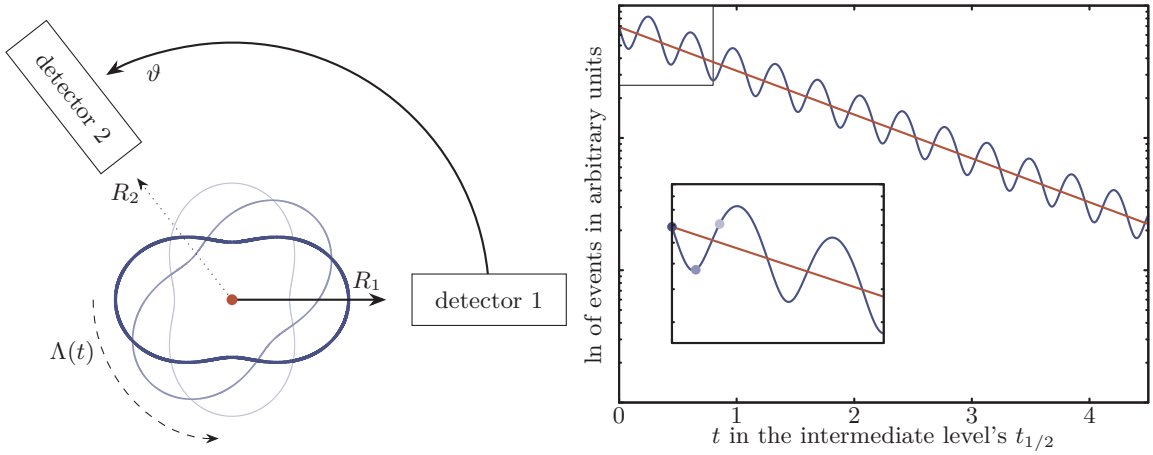

Figure 3.3.: The PAC in the semi-classical picture.
Left side: Two detectors are set up spanning a fixed angle ϑ, both pointing towards the red dot representing the sample. Radiation R_1 is detected with detector 1 selecting a set of nuclei with aligned nuclear spins I_i and thus nuclei with the same emission pattern for R_2 being detected with detector 2. This emission pattern not yet changed by the EFG is shown in dark blue. In the classical picture, the interaction between NQM and EFG causes the emission pattern to precess, indicated by the dashed arrow, the time evolution operator and the lighter blue emission patterns.
Right side: The exponential decay of the intermediate state without interaction between NQM and EFG is shown in red. With interaction, the event rate of detector 2 is modulated by the precession of the emission pattern, shown in blue. The blue and light blue dots in the zoom box correspond to the event rate for the emission pattern orientation on the left hand side of the figure in the same colour.

one can choose V_{zz} and

$$\eta = \frac{V_{xx} - V_{yy}}{V_{zz}} \tag{3.6}$$

the asymmetry parameter to parametrise the EFG. Hence, $0 \leq \eta \leq 1$. In the special case of an axially symmetric EFG, η vanishes. For $V_{xx} = V_{yy} = V_{zz}$ which is the case for cubic symmetry, both η and V_{zz} have obviously to be zero due to the vanishing trace.

As already discussed above, the interaction between EFG and NQM will lift the m-degeneracy of the cascade's intermediate level I. Only levels with the same absolute value of m remain degenerate. Secondly, it will cause time dependent transitions between the different, now non-degenerate m-states of I, represented by the time evolution operator $\Lambda(t)$. In a semi-classical picture, the EFG exerts a torque on the nuclear quadrupole moment causing a precession of the emission characteristic. Thus the angular correlation of the second radiation R_2 is changed with respect to a fixed emission direction $\vec{k_1}$ of R_1 and consequently becomes time dependent. This situation is shown on the left side of figure 3.3 for a simplified emission pattern.

Obviously, an anisotropic angular distribution of the emitted radiation is a fundamental prerequisite to perform angular correlation measurements. The detection of R_1 in one fixed direction selects a set of nuclei with aligned nuclear spins I_i, thus overcoming the problem of the nuclei's spins being randomly orientated in space.
The result of such a measurement is an exponential decay of the intermediate state as long as there is no EFG present. With EFG this exponential curve is periodically modulated by the precessing emission pattern as shown in figure 3.3 on the right side. The frequencies contributing to this modulations contain information on the EFG the probe nucleus is subjected to and thus about its environment in the sample. Due to the r^{-3} dependency of the EFG [KauVia79] the studied volume in the sample is restricted to the immediate vicinity of the probe nuclei.

As a matter of course, the need for successive emission of a R_1-R_2 cascade, constitutes some restrictions on the nuclei which can be used for PAC measurements. A detailed discussion on the required properties of PAC probe nuclei and ^{83}Rb(^{83}Kr) as well as $^{83\mathrm{m}}$Kr(^{83}Kr) in particular can be found in section 4.4.
In general, PAC measurements can be performed with many kinds of radiation including cascades with an arbitrary mixture of α- and β-particles; γ-quanta and Conversion Electrons (CEs). In this work only γ-γ and e-γ cascades are measured, and only the relevant theory is summarised.

3.2. γ-γ angular correlations of free nuclei

In order to construct the directional correlation function $W(\vec{k_1}, \vec{k_2})$, in this section a nucleus decaying through a nuclear radiation cascade as shown in figure 3.2 is considered. In this discussion I_i, I and I_f denote the nuclear spin of the initial, the intermediate and the final state, respectively. m_i, m and m_f are the associated magnetic quantum numbers.

Through the emission of radiation R_1 in direction $\vec{k_1}$ the nucleus makes a transition from the initial state, designated $|I_\mathrm{i} m_\mathrm{i}\rangle$, to the intermediate state $|Im\rangle$. Successively, radiation R_2 is emitted in direction $\vec{k_2}$ through which the nucleus reaches its ground state $|I_\mathrm{f} m_\mathrm{f}\rangle$. Symbolically one can write

$$|I_\mathrm{i} m_\mathrm{i}\rangle \overset{R_1(\vec{k_1})}{\longrightarrow} |Im\rangle \overset{R_2(\vec{k_2})}{\longrightarrow} |I_\mathrm{f} m_\mathrm{f}\rangle \tag{3.7}$$

The physical meaning of the function $W(\vec{k_1}, \vec{k_2})\mathrm{d}\Omega_1\mathrm{d}\Omega_2$ is defined as the probability for nucleus to decay via a R_1-R_2 cascade as mentioned above, emitting R_j in direction $\vec{k_j}$ and in the solid angle $\mathrm{d}\Omega_j$ for $j = 1, 2$.

It is assumed throughout this chapter that the nuclei can be considered free. This means either no extranuclear perturbations are present, their time average vanishes or the intermediate state I is short-lived and no interactions between the external fields and the nucleus may occur.

Restricting the theoretical considerations to directional correlation experiments with a random population of the initial state I_i, the angular correlation function can be expressed as

$$W(\vec{k_1},\vec{k_2}) = \sum_{m_\mathrm{f}} P_\mathrm{f}(m_\mathrm{f}) = \sum_{m_\mathrm{f}} \langle m_\mathrm{f}| \, \varrho_\mathrm{f}(\vec{k_1},\vec{k_2}) \, |m_\mathrm{f}\rangle$$
$$= \sum_{m\check{m}} \langle m| \, \varrho(\vec{k_1}) \, |\check{m}\rangle \, \langle \check{m}| \, \varrho(\vec{k_2}) \, |m\rangle \, . \tag{3.8}$$

The density matrix $\varrho_\mathrm{f}(\vec{k_1},\vec{k_2})$ fully describes the probability $P_\mathrm{f}(m_\mathrm{f})$ to find a nucleus in the final state m_f after the decay cascade from an arbitrary state m_i. Obviously, the angular correlation function has to depend on the sum over the occupation probability of all magnetic quantum numbers of the final state, given a known preceding decay described by ϱ_f. The density matrix ϱ_f can be broken up into two parts, each solely describing the first or the second transition.

$$\langle m| \, \varrho(\vec{k_1}) \, |\check{m}\rangle = S_1 \sum_{m_\mathrm{i}} \langle m| \, \mathscr{H}_1 \, |m_\mathrm{i}\rangle \, \langle \check{m}| \, \mathscr{H}_1 \, |m_\mathrm{i}\rangle^\star \tag{3.9}$$

$$\langle \check{m}| \, \varrho(\vec{k_2}) \, |m\rangle = S_2 \sum_{m_\mathrm{f}} \langle m_\mathrm{f}| \, \mathscr{H}_2 \, |m\rangle \, \langle m_\mathrm{f}| \, \mathscr{H}_2 \, |\check{m}\rangle^\star \tag{3.10}$$

For $j = 1, 2$ the coefficients S_j indicate a sum over unmeasured radiation properties. $\mathscr{H}_j$ is the interaction operator for the emission of radiation R_j. The subsequent abbreviation was used:

$$\langle m| \, \mathscr{H}_1 \, |m_\mathrm{i}\rangle \equiv \langle I, m, \vec{k_1}| \, \mathscr{H}_1 \, |I_\mathrm{i} m_\mathrm{i}\rangle \quad \text{and} \quad \langle m_\mathrm{f}| \, \mathscr{H}_2 \, |m\rangle \equiv \langle I_\mathrm{f}, m_\mathrm{f}, \vec{k_2}| \, \mathscr{H}_2 \, |I m\rangle \tag{3.11}$$

The directional correlation function is now independent of any rotation about the emission directions $\vec{k_1}$ or $\vec{k_2}$ and just depends on the angle spanned by both emission directions. This situation is illustrated in figure 3.4. Besides, the nucleus being in the coordinate system's origin, its choice is arbitrary. As a consequence and through some extensive calculations, the directional correlation function can be parametrised by the Legendre polynomials $P_k(\cos\vartheta)$:

$$W_{\gamma\text{-}\gamma}(\vec{k_1},\vec{k_2}) = W_{\gamma\text{-}\gamma}(\vartheta) = \sum_{k \text{ even}}^{k_\mathrm{max}} A_k(\ell_1 \check{\ell}_1 I_\mathrm{i} I) A_k(\ell_2 \check{\ell}_2 I_\mathrm{f} I) P_k(\cos\vartheta) = \sum_{k \text{ even}}^{k_\mathrm{max}} A_{kk} P_k(\cos\vartheta) \tag{3.12}$$

The coefficients A_{kk} are normalised

$$A_{00} = 1 \tag{3.13}$$

The summation index k is even as long as only directions and linear polarisation are measured [BieRos53]. The following selection rules apply [FraSte68]:

$$0 \leqq k \leqq \mathrm{Min}(2I, \ell_1 + \check{\ell}_1, \ell_2 + \check{\ell}_2) = k_\mathrm{max} \qquad \text{for mixed multipole radiation} \tag{3.14}$$

$$0 \leqq k \leqq \mathrm{Min}(2I, \ell_1, \ell_2) = k_\mathrm{max} \qquad \text{for pure multipole radiation} \tag{3.15}$$

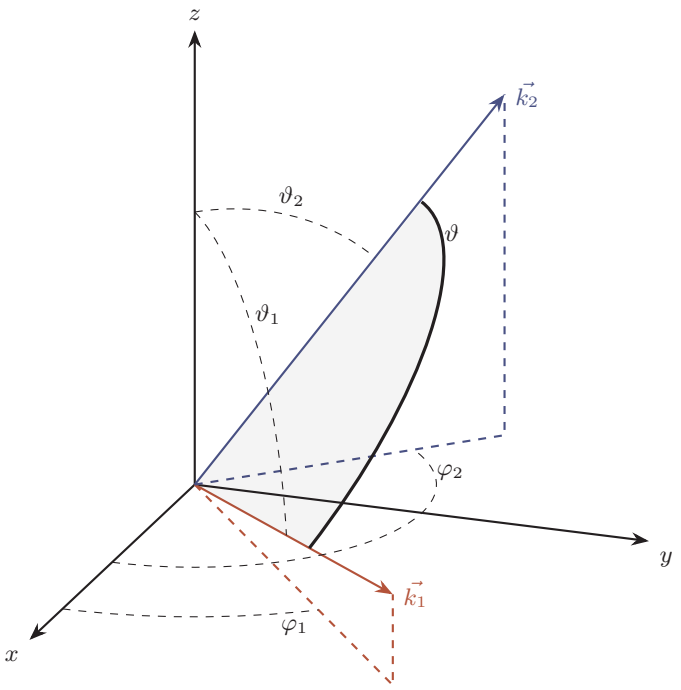

Figure 3.4.: Generalised coordinates for PAC measurements similar to sketches in Schatz et al. and Frauenfelder et al. [SchWei92; FraSte68]. Radiation R_1 is detected in direction $\vec{k}_1$ under angles φ_1 and ϑ_1, R_2 in direction $\vec{k}_2$ under angles φ_2 and ϑ_2. $\vec{k}_1$ and $\vec{k}_2$ span the angle ϑ. The coordinate system is arbitrary, the emitting nucleus is situated in the origin.

Here ℓ_j denotes the multipolarity of a pure transition and $\check{\ell}_j$ the multipolarity of a potential admixture with $\ell_j < \check{\ell}_j$ and $j = 1, 2$.
The coefficients A_k can be expressed as

$$A_k(\ell_1\check{\ell}_1 I_\mathrm{i} I) = \frac{F_k(\ell_1\ell_1 I_\mathrm{i} I) + 2\delta_1(\gamma)F_k(\ell_1\check{\ell}_1 I_\mathrm{i} I) + \delta_1^2(\gamma)F_k(\check{\ell}_1\check{\ell}_1 I_\mathrm{i} I)}{1+\delta_1^2(\gamma)}. \tag{3.16}$$

An expression for $A_k(\ell_2\check{\ell}_2 I_\mathrm{f} I)$ can be found analogously. The F-coefficients F_k can be calculated directly from the formulae given by e.g. Frauenfelder et al. [FraSte68] or taken from literature where they are tabulated [FerRos68; BieRos53; FraSte68] for all relevant values of ℓ_j, $\check{\ell}_j$, I_i, I_f and I.
$\delta_j(\gamma)$ is the amplitude mixing ratio of the multipolarities ℓ_j and $\check{\ell}_j$, either M1 + E2 or rarely E1 + M2, for the emission of γ_j. Higher order admixtures are of little experimental relevance since they are suppressed by the angular and parity selection rules [FraSte68] and can thus be safely neglected. Values for $\delta_j(\gamma)$ for $^{83\mathrm{m}}$Kr and other nuclei with $A = 83$ can be found in the respective issue of the Nuclear Data Sheets [McCutc15].

3.3. Perturbed γ-γ angular correlations

As already sketched in section 3.1.2, an extranuclear EFG will lift the intermediate state's m-degeneracy. Additionally, an interaction between EFG and the NQM will cause transitions between the now non-degenerate m-states. Hence, R_2 is emitted from an intermediate level with altered m-population. The perturbation depends mainly on the interaction time, i.e.

the half life t_h of the intermediate level and on the magnitude of the interacting quantities, i.e. on the magnitude of the EFG and the NQM.

The change in population of the intermediate level's m-states can be described by the unitary time evolution operator

$$\Lambda(t) = e^{-\frac{i}{\hbar}\cdot\mathscr{H}t} \tag{3.17}$$

which acts on the final states $|m_\mathrm{a}\rangle$ of the first decay and changes them to $|m_\mathrm{b}\rangle$, the initial states of the second decay. Here, $\mathscr{H}$ is the Hamiltonian characterising the interaction between EFG and the nucleus. The angular correlation function now becomes time dependent and can be written:

$$W(\vec{k_1},\vec{k_2},t) = \sum_{\substack{m_\mathrm{a},\check{m}_\mathrm{a}\\ m_\mathrm{b},\check{m}_\mathrm{b}}} \langle m_\mathrm{a}|\,\varrho(\vec{k_1})\,|\check{m}_\mathrm{a}\rangle\,\langle\check{m}_\mathrm{b}|\,\varrho(\vec{k_2})\,|m_\mathrm{b}\rangle\,\langle m_\mathrm{b}|\,\Lambda(t)\,|m_\mathrm{a}\rangle\,\langle\check{m}_\mathrm{b}|\,\Lambda(t)\,|\check{m}_\mathrm{a}\rangle^\star \tag{3.18}$$

For directional correlation experiments, the time dependent representation of the angular correlation function for a nucleus subject to extranuclear fields can be written as:

$$\begin{aligned} W(\vec{k_1},\vec{k_2},t) = \sum_{\substack{k_1,k_2\\ N_1,N_2}} & A_{k_1}(\ell_1\check{\ell}_1 I_\mathrm{i} I) A_{k_2}(\ell_2\check{\ell}_2 I_\mathrm{f} I) G^{N_1N_2}_{k_1k_2}(t)\,[(2k_1+1)(2k_2+1)]^{-\frac{1}{2}} \\ & \times {Y^{N_1}_{k_1}}^\star(\vartheta_1,\varphi_1) Y^{N_2}_{k_2}(\vartheta_2,\varphi_2) \end{aligned} \tag{3.19}$$

with the perturbation factor

$$\begin{aligned} G^{N_1N_2}_{k_1k_2}(t) = \sum_{m_\mathrm{a},m_\mathrm{b}} & (-1)^{2I+m_\mathrm{a}+m_\mathrm{b}}\,[(2k_1+1)(2k_2+1)]^{\frac{1}{2}} \begin{pmatrix} I & I & k_1 \\ \check{m}_\mathrm{a} & -m_\mathrm{a} & N_1 \end{pmatrix} \\ & \times \begin{pmatrix} I & I & k_2 \\ \check{m}_\mathrm{b} & -m_\mathrm{b} & N_2 \end{pmatrix} \langle m_\mathrm{b}|\,\Lambda(t)\,|m_\mathrm{a}\rangle\,\langle\check{m}_\mathrm{b}|\,\Lambda(t)\,|\check{m}_\mathrm{a}\rangle^\star, \end{aligned} \tag{3.20}$$

fully describing the external perturbation using the spherical harmonics $Y^{N_j}_{k_j}(\vartheta_j,\varphi_j)$ and the Wigner 3-j symbols. The definitions of the directions and angles are the same as in section 3.2 and are shown in figure 3.4.

3.3.1. Static electric quadrupole interaction

If the probe nuclei are subject to axially symmetric static EFGs only, like in this work, the perturbation factor can be simplified. In this case, the time evolution operator $\Lambda(t)$ and the interaction Hamiltonian $\mathscr{H}$ can be diagonalised and $N_1 = N_2 = N$ [Butz89; FraSte68]. Now the perturbation factor reads

$$\begin{aligned} G^{NN}_{k_1k_2}(t) = \sum_{m} & [(2k_1+1)(2k_2+1)]^{\frac{1}{2}} \begin{pmatrix} I & I & k_1 \\ \check{m} & -m & N \end{pmatrix} \begin{pmatrix} I & I & k_2 \\ \check{m} & -m & N \end{pmatrix} \\ & \times \exp\left(-i/\hbar\,(E_m - E_{\check{m}})\,t\right) \end{aligned} \tag{3.21}$$

By calculating the energy eigenvalues E_m and $E_{\check{m}}$, the perturbation function can be simplified even further. As sketched in section 3.1, one can choose a principal axes system in a way that the EFG's tensor V becomes diagonal. If one chooses the largest component to be aligned with the z axis, it is $|V_{zz}| \geq |V_{yy}| \geq |V_{xx}|$. The asymmetry parameter

$$\eta = \frac{V_{xx} - V_{yy}}{V_{zz}} \quad \text{with} \quad \sum_{\alpha} V_{\alpha\alpha} = 0 \tag{3.22}$$

describes the deviation from the axially symmetric EFG with $0 \leq \eta \leq 1$. Together with V_{zz} it characterises V in this case. For axial symmetry with respect to the z axis, the asymmetry parameter vanishes and the EFG is fully characterised by V_{zz}. The evaluation of the quadrupole interaction energy eigenvalues in the axial case yields

$$E_m = \frac{eQV_{zz}}{4I(2I-1)}(3m^2 - I(I+1)) \tag{3.23}$$

with the intermediate level's spin I and and the quadrupole moment Q. Introducing the quadrupole frequency

$$\omega_Q = \frac{eQV_{zz}}{4I(2I-1)\hbar} \tag{3.24}$$

the energy difference between two m-states can be written as

$$|E_m - E_{\check{m}}| = 3\hbar|m^2 - \check{m}^2|\omega_Q \tag{3.25}$$

Due to the squared magnetic quantum numbers, levels with the same absolute value of m remain degenerate, while the other levels are split non-equidistantly. Obviously, the splitting depends on the nuclear spin. For $I = 7/2^+$ this is shown in figure 3.5. For half-integer intermediate level spins, like for both cascades ^{83m}Kr(^{83}Kr) and ^{83}Rb(^{83}Kr) with $I = 7/2^+$ used in this work, the smallest non-vanishing energy difference is

$$\omega_0 = 6\omega_Q \quad \text{with} \quad n = \frac{1}{2}|m^2 - \check{m}^2| \tag{3.26}$$

For purely electric interactions, only the real part of $G^{NN}_{k_1,k_2}$ is needed [AldAlb53]. Now, the perturbation factor can be expressed as

$$G^{NN}_{k_1k_2}(t) = \sum_n S^{k_1k_2}_{nN} \cos(n\omega_0 t) \tag{3.27}$$

with the coefficients

$$S^{k_1k_2}_{nN} = \sum_{m,\check{m}} \begin{pmatrix} I & I & k_1 \\ \check{m} & -m & N \end{pmatrix} \begin{pmatrix} I & I & k_2 \\ \check{m} & -m & N \end{pmatrix} [(2k_1+1)(2k_2+1)]^{\frac{1}{2}} \tag{3.28}$$

Here, the summation is just to be carried out if the condition for n from equation (3.26) is fulfilled.
Obviously, from equation (3.27), the perturbation can be expressed as a superposition

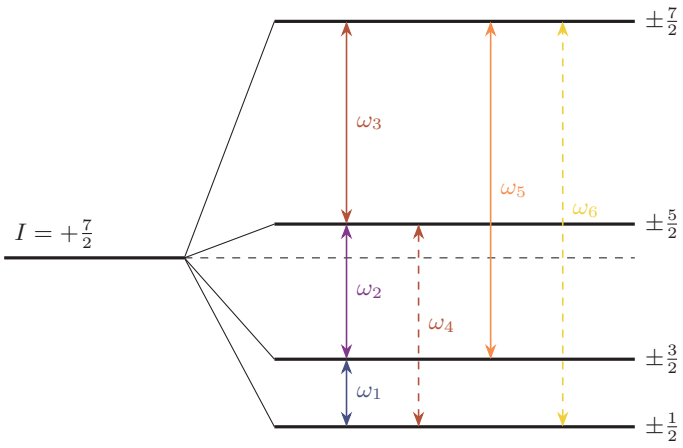

Figure 3.5.: The hyperfine splitting of a spin $7/2^+$ level for axially symmetric EFGs. This resembles the situation for ^{83m}Kr(^{83}Kr) and ^{83}Rb(^{83}Kr) with a spin $7/2^+$ intermediate level. All possible transitions are shown, the energy splitting is to scale. ω_6 and ω_4 do not contribute because all $S_{6N}^{k_1k_2}$ and $S_{4N}^{k_1k_2}$ vanish.

of cosine functions, each one weighted by a factor $S_{nN}^{k_1k_2}$. These factors neither depend on the orientation of the detectors nor of the sample. However, the quantum number N occurring in the Wigner 3-j symbols connects them to the spherical harmonics depending on the angles ϑ_j and φ_j in the spherical harmonics' reference frame, see equation (3.19) and figure 3.4. The axial EFG's orientation in the laboratory frame is defined by the azimuthal angle Φ and the polar angle Θ spanned by the EFG and the axis of the start detector, see figure 3.6. The coordinate transformation from the laboratory coordinate system introduces a Φ and Θ dependency in all angles ϑ_j and φ_j in the spherical harmonics' reference frame. Unlike in the case of the unperturbed angular correlation, generally, in equation (3.19) factors $A_{k_1}A_{k_2}$ with $k_1 \neq k_2$ can occur. However, these interference terms only occur for $k_{\max} \geqq 4$ [FraSte68] and are thus not relevant in this work. With $k_1 = k_2 = k$ the perturbation factor can be written in its final form

$$G_{kk}^{NN} = \sum_n S_{nN}^{kk} \cos(n\omega_0 t) \tag{3.29}$$

with the weighting factors

$$S_{nN}^{kk} = \sum_{m,\check{m}} \begin{pmatrix} I & I & k \\ \check{m} & -m & N \end{pmatrix}^2 (2k+1) \tag{3.30}$$

These weighting factors can easily be calculated from equation (3.30) and are tabulated by Alder et al. [AldAlb53]. In contrast to the semi-classical example in figure 3.3, more than just one frequency contributes to the measured signal. The emission pattern rotates with the fundamental rotation frequency ω_0 and its harmonics given by $n\omega_0 \equiv \omega_n$. All possible transitions for a nucleus with $I = 7/2^+$ are shown in figure 3.5. The possible frequencies ω_n in this case relate to $\omega_0 \equiv \omega_1$ in the following way:

$$\begin{array}{ccccccccccc} \omega_1 & : & \omega_2 & : & \omega_3 & : & (\omega_4) & : & \omega_5 & : & (\omega_6) \\ 1 & : & 2 & : & 3 & : & (3) & : & 5 & : & (6) \end{array} \tag{3.31}$$

Frequencies in parenthesis do not contribute because the corresponding weighting factor $S_{nN}^{k_1k_2}$ vanishes. Additionally, the contribution of different frequencies depends on the angle

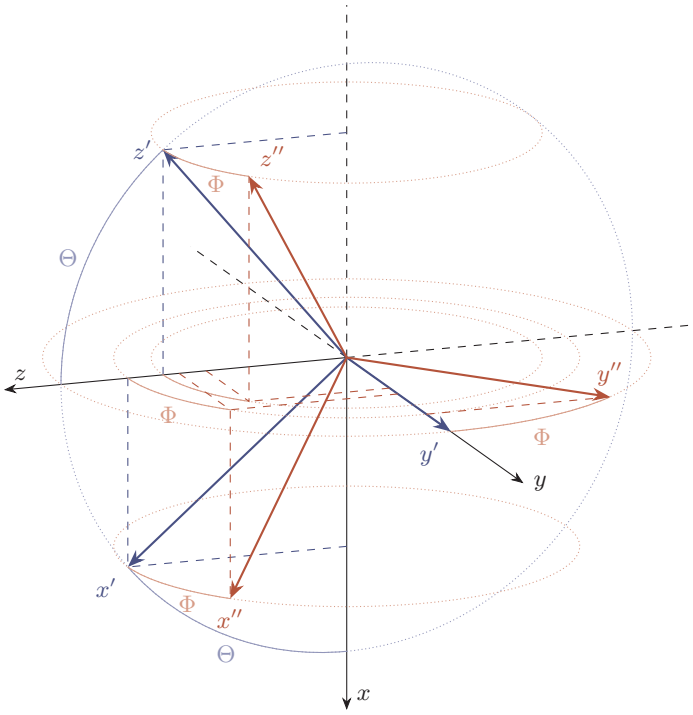

Figure 3.6.: The laboratory coordinate system and the axial EFG's orientation. The start detector is on the z axis, the EFG's largest component V_{zz} points in direction z'' defined by the rotations by Θ around the y axis and Φ around the x axis. The first and second rotation and the resulting coordinate systems are shown in blue and red, respectively. Projections on laboratory system's planes are shown dashed.

between EFG and the detectors for monocrystalline samples, an effect not explainable in the semi-classical picture.

All measurements in this work are carried out in a geometry with $\Theta = 90°$ and $\Phi = 45°$. A simulation of measured signal for an $I = 7/2^+$ intermediate level in this measurement geometry is shown in figure 3.7.

3.3.1.1. Polycrystalline samples

In the special case of a polycrystalline sample with random orientation of the EFGs, one has to average over all EFG orientations, i.e. over all ϑ_j and φ_j. The perturbation function in this case reads

$$G_{kk}(t) = \sum_n s_{kn} \cos(n\omega_0 t) \tag{3.32}$$

with the coefficients

$$s_{kn} = \sum_{m,\check{m}} \begin{pmatrix} I & I & k \\ \check{m} & -m & -\check{m}+m \end{pmatrix}^2 \tag{3.33}$$

not depending on the quantum number N any more. The definition of n from equation (3.26) and $k_1 = k_2 = k$ are still valid. The perturbation function, thus, no longer depends on the orientation of the sample but on the angle ϑ spanned by $\vec{k_1}$ and $\vec{k_2}$ only. For a nucleus with an intermediate level with spin $I = 7/2^+$ implanted in a polycrystalline substrate, a simulated measurement signal is shown in figure 3.7.

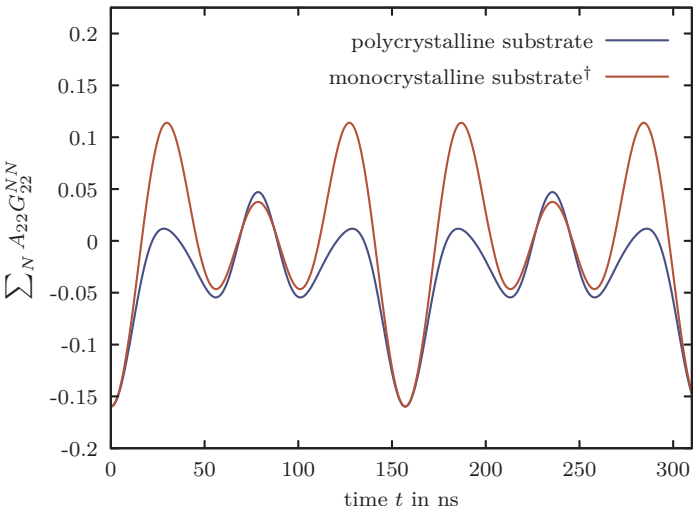

Figure 3.7.: $\sum_N A_{22}G_{22}^{NN}$ examples simulated for the $I = 7/2^+$ intermediate level of ^{83m}Kr in mono and polycrystalline substrates. Here, ω_1 is 40 MHz for both cases. †: The monocrystalline substrate is assumed to be measured with $\Theta = 0°$ and $\Phi = 45°$.

3.3.2. The perturbation function of nuclear ensembles

The formulae derived for polycrystalline and monocrystalline samples in equations (3.27) and (3.32), respectively, describe the behaviour of nuclei subject to identical perturbations. However, probe nuclei can be incorporated on different unique lattice sites i causing differing EFGs for each of these sites. In this case, the experimental perturbation function is a superposition of i parts

$$G_{kk}^{NN}(t) = \sum_i f_i G_{kk,i}^{NN}(t) \tag{3.34}$$

The weight of each contribution depends on the fraction f_i of nuclei on these unique lattice sites. The sum over all f_i is unity.

In a real crystal probe nuclei will be subject to slightly different EFGs even if they are all incorporated on the same unique lattice site. This is caused by e.g. statistical distribution of vacancies in the probe nucleus' vicinities. As a consequence, small differences $\Delta\omega_0$ from the average interaction frequency ω_0 occur. For moderate frequency spreads $\Delta\omega_0$, the distributions of these frequencies can be approximated by either a Gaussian or a Lorentzian distribution. With this the perturbation function can be expressed as [RogVas75]

$$G_{kk}^{NN}(t) = \sum_n S_{nN}^{kk} \exp\left(-(\omega_n t\delta)^p \cdot p^{-1}\right) \cdot \cos\left(n\omega_0 t\right) \tag{3.35}$$

with the damping parameter $\delta = \Delta\omega_0/\omega_0$ being a measure for the width of the frequency spread around ω_0. It is often quoted in %. For $p = 1$ the distribution is Lorentzian, while it is Gaussian for $p = 2$. This model breaks down for small frequencies and strong damping values if the frequency distribution reaches negative frequencies in frequency space. The results of the measurements presented in section 10.3 show strong damping in most cases. To avoid problems due to the limitations of this model, in this work the narrower Gaussian distribution with $p = 2$ is used. Simulations of signals with different damping parameters δ for a nucleus with an intermediate level with $I = 7/2^+$ implanted in a polycrystalline substrate are shown in figure 3.8.

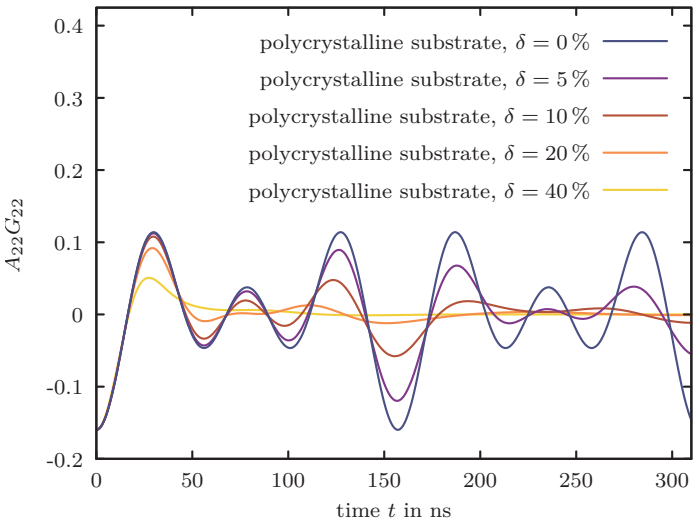

Figure 3.8.: Examples for the effect of damping due to a frequency distribution around ω_0. The $A_{22}G_{22}$ (normalised to $W(\vec{k_1}, \vec{k_2}, 0) = A_{22}$) value for the $I = 7/2^+$ intermediate level of ^{83}Kr implanted in a polycrystalline substrate is simulated with $\omega_0 = 40\,\mathrm{MHz}$ for different values of δ.

3.4. Internal conversion angular correlations

In the situation of internal conversion angular correlations, the formal description is somewhat more difficult due to the correlation's additional dependency on the nuclear charge, the parity changes, and the energies of the converted transitions. A general treatment of the theory needs to treat relativistic electrons due to the latter dependency. A thorough discussion of angular correlation measurements involving at least one CE can be found in works by Biedenharn et al. and Rose et al. [BieRos53; RosBie52]. In this work, the full formalism will not be reviewed. Instead, simplifications relevant for measurements with the nucleus $^{83\mathrm{m}}$Kr will be applied greatly simplifying the mathematical description of the problem.

3.4.1. The particle parameter b_k

If one of the transitions during a decay cascade leads to the emission of a CE, the angular correlation is changed depending on the probe nucleus' charge, the energy of the CE, the parity of the transition and the shell from which the electron was ejected. This change is expressed by the particle parameter b_k. Assuming an e-γ cascade with multipole admixtures allowed in the unconverted transition and detectors with cylindrical symmetry, the directional correlation function reads

$$W_{\text{e-}\gamma}(\vartheta) = \sum_{k\text{ even}}^{k_{\max}} b_k(\ell_1\check{\ell}_1; e) A_k(\ell_1\check{\ell}_1 I_\mathrm{i} I; e) A_k(\ell_2\check{\ell}_2 I_\mathrm{f} I) P_k(\cos\vartheta) \tag{3.36}$$

with the particle parameter

$$b_k(\ell_1\check{\ell}_1; e) = \frac{c_{k0}(\ell_1\check{\ell}_1; e)}{c_{k0}(\ell_1\check{\ell}_1; \gamma)} \tag{3.37}$$

defined by the ratio of the Racah radiation parameters $c_{k0}(\ell_1\check{\ell}_1;x)$ for directional correlation measurements (without polarisation measurements) [FraSte68]. x denotes the particle parameter's associated type of radiation, in this case e for CEs and γ. The same nomenclature is used for the particle parameter itself and for the relevant coefficient A_k. The definition of the more general $c_{\kappa\tau}$ can be found in the literature [FraSte68; BieRos53]. The K-CEs used in this work are emitted with an energy of 17.8 keV and a multipolarity of $l_1 = 3$. The particle parameters b_2 for K-shell conversion are calculated for $0.3 < E_e/(mc^2) < 5$ for different nuclear charges by Rose et al. [RosBie52] and can be found in figure 3.9 for $\ell_1 = 3$. The normalization of the particle parameter is

$$b_0 = 1 \tag{3.38}$$

If the first transition is the converted one and does not contain multipole admixtures, then $\ell_1 \equiv \check{\ell}_1$ and $A_k(\ell_1\check{\ell}_1 I_i I;e) \equiv A_k(\ell_1\check{\ell}_1 I_i I)$ [FraSte68]. Furthermore, if CEs travelling at non-relativistic speeds, i.e. $E_e/mc^2 \ll 1$, are assumed, the application of an extrapolation towards the non-relativistic limit is justified. For pure electronic transitions, the particle parameter can now be calculated by

$$b_2(\ell_1\check{\ell}_1;e) = \frac{\ell_1(\ell_1+1)}{\ell_1(\ell_1+1)-3} \tag{3.39}$$

An additional condition to use this formula is $\alpha Z \ll 1$ [BieRos53; RosBie52]. Z is the nuclear charge and α is assumed to be the fine-structure constant, although it is not explicitly stated by the authors. The energy dependence of b_2 and the non-relativistic limit for electric octupole radiation is shown in figure 3.9. Particle parameters for $k > 2$ can be obtained by the recurrence formula

$$b_k(\ell_1\ell_1;e) = 1 + \frac{k(k+1)[\ell_1(\ell_1+1)-3]}{3[2\ell_1(\ell_1+1)-k(k+1)]}(b_2(\ell_1\ell_1;e)-1) \tag{3.40}$$

The particle parameter obtained from these formulae becomes independent of the nuclear charge and the electron's energy.
Using this, the directional correlation function from equation (3.36) can be simplified and differs from equation (3.12) by just one multiplicative factor, $b_k(\ell_1\ell_1;e)$ and the first factor A_k does not contain any multipole admixtures any more:

$$W_{\text{e-}\gamma}(\vartheta) = \sum_{k\ \text{even}}^{k_{\max}} b_k(\ell_1\ell_1;e)A_{kk}P_k(\cos\vartheta) \tag{3.41}$$

with the definition of A_{kk} from equation (3.12) and the Legendre polynomials P_k.

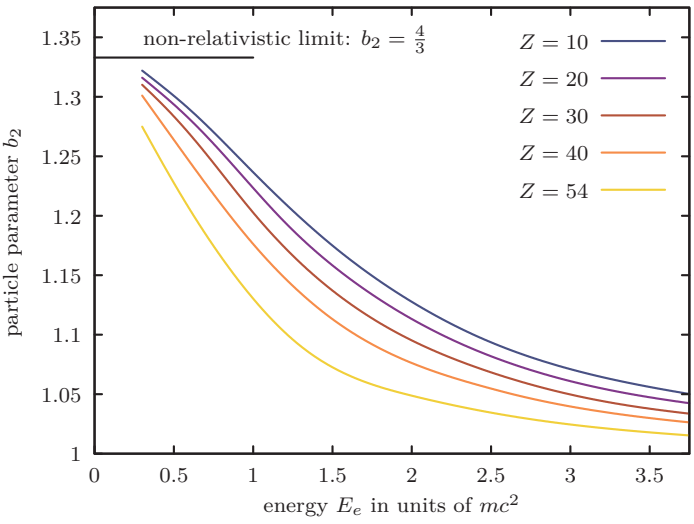

Figure 3.9.: The energy dependence of the particle parameter b_2 for nuclei with selected nuclear charges and electric octupole radiation, adopted from Rose et al. [RosBie52]. In the non-relativistic limit b_2 becomes independent of the nuclear charge, all curves shown converge for $E_e \to 0$.

4. Experimental details

The formalism presented in the previous chapters is valid for idealised set-ups with point-like detectors and samples only. In this chapter the theory of corrections for a real PAC set-ups, like intrasource scattering (section 4.1) and geometrical corrections (section 4.2) is discussed. The coincidence and the background count rate depending on the solid angle covered by the detectors and the activity of the sample is calculated in section 4.3. Furthermore, in section 4.4 the nucleus ^{83}Rb and its daughters ^{83m}Kr and ^{83}Kr are presented, an overview over the production of ^{83}Rb is given in section 4.6. The γ-γ and e-γ cascades emitted by ^{83}Rb(^{83}Kr) and ^{83m}Kr(^{83}Kr) used for PAC measurements are introduced in section 4.4, the corresponding anisotropies are calculated in section 4.5.
The experimental set-up developed in this work is presented in the dedicated chapter 9.

4.1. Intrasource scattering

While intrasource scattering is in general no major issue for measuring γ-γ directional correlations, it becomes important when dealing with e-γ cascades, especially for thick samples or low energy electrons. It has been shown by Frankel [Franke51] based on works by Goudsmit et al. [GouSau40a; GouSau40b] that this change can be expressed by a constant factor s_k, which will be called scattering parameter in this work. The directional correlation function then reads:

$$W_{\text{e-}\gamma}(\vartheta) = \sum_{k \text{ even}}^{k_{\max}} s_k(Z, M, E_e, \delta) b_k A_{kk} P_k(\cos\vartheta) \tag{4.1}$$

Here b_k is the particle parameter defined in section 3.4, A_{kk} are defined like in equation (3.12) and P_k are the Legendre polynomials.
The factor s_k depends on the sample material's atomic number Z, its molar mass M in $\mathrm{mg\,mol^{-1}}$, the area density δ of the layer the electrons have to penetrate in $\mathrm{mg\,cm^{-2}}$ and on the CE's energy $\chi = E_e/mc^2$. In figure 4.1 a nomogram showing s_k for some Z and a wide range of E_e and δ is depicted. The scattering parameter can be expressed as

$$s_k = \frac{1 - e^{-n_k \cdot \delta}}{n_k \cdot \delta} \tag{4.2}$$

with

$$n_k = c \cdot \frac{Z^2(1+\chi)^2}{M(2\chi+\chi^2)^2} k(k+1) \left(\ln\left(\frac{150\sqrt{2\chi+\chi^2}}{\sqrt[3]{Z}} \right) - \sum_{\xi=2}^{k} \frac{1}{\xi} \right) \tag{4.3}$$

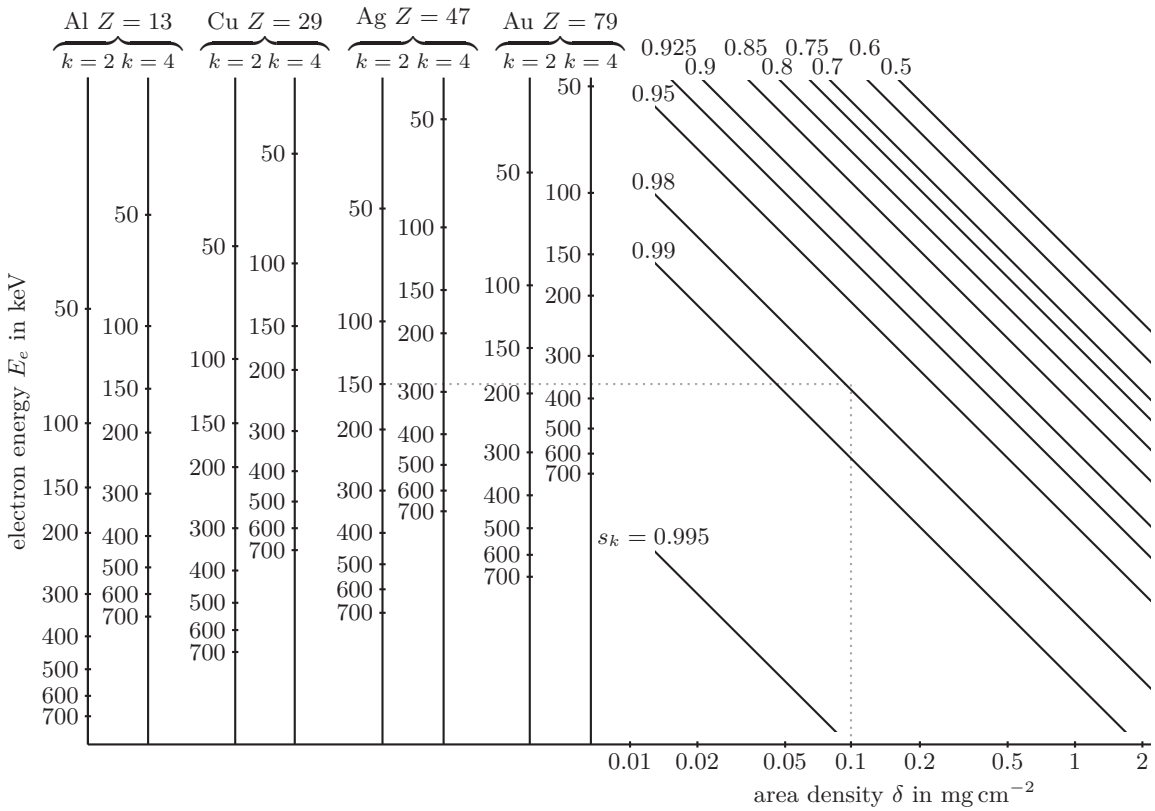

Figure 4.1.: An excerpt from a nomogram adopted from Gimmi et al. [GimHee56] showing s_k for the elements Al, Cu, Ag and Au for CE energies ranging from 50 keV to 700 keV and a sample thickness from 0.01 mg cm^{-2} to 2 mg cm^{-2}. The dashed line shows the scattering parameter $s_2 \approx 0.98$ for 150 keV electrons penetrating a silver sample with an area density of 0.1 mg cm^{-2} as example.

and $c = 0.302 \times 10^{-3}$ mol cm^{-2} [GimHee56]. Although not stated by the authors, a normalization of

$$s_0 = 1 \tag{4.4}$$

is assumed. The derivation of this formula is based on some assumptions made by Goudsmit et al. [GouSau40a] and is thus restricted to certain cases: It is valid only for thin scatterers, assumes equal path lengths for all electron trajectories, disregards backscattering and all scattering processes are assumed to be elastic. However, it was verified by experiments [GolFra56] that s_k is valid even for rather thick scatterers.

4.2. Geometrical corrections

Besides, the corrections for radiation-specific changes of the angular correlation function, some geometrical corrections have to be taken into account. Up to now detectors as well as

the sample were assumed to be point-like. In the following subsections deviations from this idealised case are discussed.

4.2.1. Corrections for finite detector size

The larger the detectors used for angular correlation measurements are, the higher the obtained coincidence count rate will be. All considerations up to now are based on the assumption of the detectors and the sample being point-like. However, using detectors with finite size changes the measured angular correlation function. Calculating the expected change for a known detector geometry allows to correct the angular correlation function accordingly, thus making measurements with finite size detectors possible without approximations. Such calculations can be found in the literature [Rose53; BarLam71; FeiFra55], a summary is compiled by Frauenfelder et al. [FraSte68]. A sketch of the geometrical situation relevant for this work is shown in figure 4.2. The change of the angular correlation caused by the experimental set-up, the spatial extension of the detectors, can be expressed by a change of the coefficients A_{kk}:

$$A_{kk} = A_{kk}^{\mathrm{exp}} / q_k \tag{4.5}$$

where A_{kk}^{exp} are the A_{kk} determined by the experiment. In general, for cylindrical detectors the multiplicative correction q_k can be expressed as a product of two factors

$$q_k(r_j, d_j, \varepsilon_j, E_j, \alpha_j) = q_{k,1}(r_1, d_1, \varepsilon_1, E_1, \alpha_1) \cdot q_{k,2}(r_2, d_2, \varepsilon_2, E_2, \alpha_2) \tag{4.6}$$

for both detectors enumerated with $j = 1, 2$ of the form

$$q_{k,j} = \frac{\int_0^{\pi/2} \varepsilon_j(E_j, \alpha_j) P_k(\cos\alpha_j) \sin\alpha_j \, \mathrm{d}\alpha_j}{\int_0^{\pi/2} \varepsilon_j(E_j, \alpha_j) \sin\alpha_j \, \mathrm{d}\alpha_j} \tag{4.7}$$

with the normalization

$$q_{0,j} = 1 \tag{4.8}$$

Here ε_j is the efficacy of detector j when it is hit by a radiation of energy E_j with an incident angle α_j; P_k are the Legendre polynomials. For low γ energies (e.g. smaller than 100 keV for Ge(Li) detectors [BarLam71]) where photo effect is the dominant process of energy deposition, the efficacy can be written as

$$\varepsilon_j(E_j, \alpha_j) = 1 - e^{-\mu_{\mathrm{t}}(E_j) D(\alpha_j)} \tag{4.9}$$

with the total mass absorption coefficient $\mu_{\mathrm{t}}(E_j)$ and the active thickness $D(\alpha_j)$ of the detector.
The factors $q_{k,j}$ have to be calculated numerically knowing the efficacy of the detectors for all incident angles. If one assumes the efficacy to be angle independent, then $\varepsilon_j(E_j, \alpha_j) \equiv \varepsilon_j(E_j)$. In this case, which is realistic for the detection of low energy electrons

with solid state detectors, the corrections can be simplified and calculated analytically [FraSte68]:

$$q_{2,j} = \frac{1}{2}\cos\beta \cdot (1 + \cos\beta) \tag{4.10}$$

$$q_{4,j} = \frac{1}{8}\cos\beta \cdot (1 + \cos\beta)\,(7\cos^2\beta - 3) \tag{4.11}$$

for $k \leq 4$ with $\beta = \tan^{-1}(r_j/d_j)$, r_j the detector radius and d_j the distance between detector and sample. The geometrical situation (including a sample of finite size; its influence is discussed in section 4.2.2) is shown in figure 4.2. The angular correlation function for e-γ correlations now reads

$$W_{\text{e-}\gamma}(\vartheta) = \sum_{k\ \text{even}}^{k_{\max}\leq 4} q_k(E_j, \varepsilon_j, r_j, d_j) s_k b_k A_{kk} P_k(\cos\vartheta) \tag{4.12}$$

with $j = 1, 2$, the scattering parameter and the particle parameter as in introduced in section 4.1 and section 3.4.1, respectively, the definition of A_{kk} from equation (3.12) and the Legendre polynomials P_k.
The angular correlation function for γ-γ cascades is now

$$W_{\gamma\text{-}\gamma}(\vartheta) = \sum_{k\ \text{even}}^{k_{\max}\leq 4} q_k(E_j, \varepsilon_j, r_j, d_j) A_{kk} P_k(\cos\vartheta) \tag{4.13}$$

4.2.2. Corrections for finite sample size

Assuming a point-like source yields good results if the source radius is small compared to the distance between sample and detectors. For electron sources, however, the activity is often distributed in a thin layer and in a larger area to avoid intrasource scattering (see section 4.1). In this case the aforementioned condition is not met, the experimental angular correlation function will thus be changed. In general, it is complicated to calculate the influence of a source of arbitrary shape, in the literature the calculations are restricted to some relevant cases. The corrections for various source geometries have been addressed by e.g. Walter et al. and Feingold et al. [WalHub50; FeiFra55] for cylindrical sources, Gimmi et al. [GimHee56] for square sources which can be applied to circular sources as well and Verheul et al. [VerBlo65] for square and circular sources.
The discussion in this work is restricted to circular sources because the ion implanted samples used are typically of this shape. The situation with circular detectors and sample relevant for this work is shown in figure 4.2. The distance d_j between the detectors and the sample is given by the distance between the centre of the sample O and the centres of the detectors C_j for $j = 1, 2$. The normal vectors on the detectors $\vec{n}_j$ point towards the centre of the sample O and span the angles ϑ_j with the normal vector $\vec{n}_\text{s}$ of the sample. The point R on the sample emits two radiations hitting the detectors in P_j, respectively. The vector between the detector's centre and the point hit by radiation is decomposed into an x and

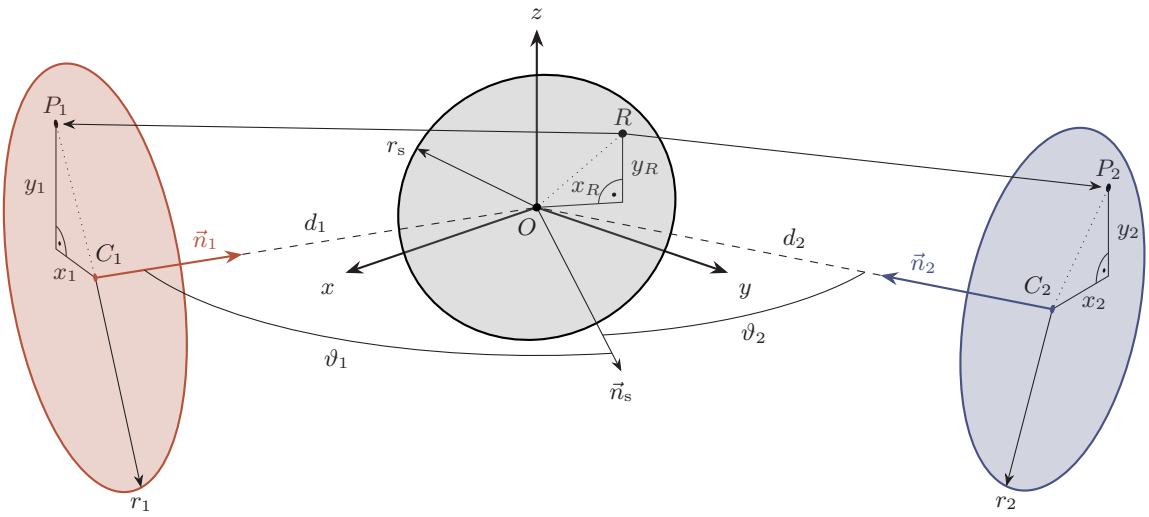

Figure 4.2.: The geometrical situation for the derivation of the corrections for finite sample and detector size [VerBlo65]. The circular sample with normal $\vec{n}_\mathrm{s}$ is placed with its centre in the origin O. An uniform distribution of the radioactive probe nuclei over the sample is assumed, $\eta(x_R, y_R) = \text{const}$. Both detectors D_j are circular, have diameters r_j and are assumed to have an incident angle independent efficacy ε. Their normal vectors $\vec{n}_j$ point from the centres C_j towards the origin O and span the angle ϑ_j with the sample's normal. The distance between detector j and sample is given by d_j.
A nucleus on point R emits two radiations hitting the detectors in P_j. x_j and y_j are coefficients in the decompositions of the vector $\overrightarrow{C_j P_j} = x_j \cdot \vec{e}_{x,j} + y_j \cdot \vec{e}_{y,j}$ in a two dimensional Cartesian coordinate system in the detector plane. The same considerations hold true for the sample, in this case P_j is replaced by R and C_j by O.

y component $\overrightarrow{C_jP_j} = x_j \cdot \vec{e}_{x,j} + y_j \cdot \vec{e}_{y,j}$ in a Cartesian coordinate system in the detector plane. Also $\overrightarrow{OR} = x_R \cdot \vec{e}_{x,R} + y_R \cdot \vec{e}_{y,R}$.
In order to calculate the corrections to the angular correlation function, Verheul et al. [VerBlo65] have solved the necessary integrals up to the third order of the parameters x_R/d_j, x_j/d_j and y_j/d_j with $j = 1, 2$. Besides the assumption of a circular source with uniform distribution of activity $\eta(x_R, y_R)$, circular detectors of constant, i.e. angle independent efficacy ε, $k_{\max} = 4$ was assumed. The resulting corrections are

$$\begin{aligned}
a_0 =& 1 - \frac{1}{4}(A_{22} + A_{44})\left(\frac{r_s^2}{d_1^2} + \frac{r_s^2}{d_2^2}\right) + \left(A_{22} + \frac{15}{8}A_{44}\right)\left(\frac{r_s \sin\vartheta_1}{d_1} - \frac{r_s \sin\vartheta_2}{d_2}\right)^2 \\
&+ \left(\frac{3}{8}A_{22} + \frac{5}{4}A_{44}\right)\left(\frac{r_s \sin\vartheta_2}{d_1} - \frac{r_s \sin\vartheta_1}{d_2}\right)^2 + \left(\frac{1}{2}A_{22} + \frac{1}{2}A_{44}\right)\frac{r_s^2}{d_1 d_2}\sin\vartheta_1 \sin\vartheta_2 \\
&+ \left(3A_{22} + \frac{5}{4}A_{44}\right)\left(\frac{r_s \sin\vartheta_1}{d_1} - \frac{r_s \sin\vartheta_2}{d_2}\right)\left(\frac{r_s \sin\vartheta_2}{d_1} - \frac{r_s \sin\vartheta_1}{d_2}\right)\cos 2\vartheta \\
&+ \left(\frac{3}{2}A_{22} - \frac{5}{6}A_{44}\right)\frac{r_s^2}{d_1 d_2}\cos 2\vartheta
\end{aligned} \tag{4.14}$$

$$\begin{aligned}
a_2 =& 1 - \left(\frac{1}{2} + \frac{5}{4}\frac{A_{44}}{A_{22}}\right)\left(\frac{r_s^2}{d_1^2} + \frac{r_s^2}{d_2^2}\right) + \left(2 + 15/2\frac{A_{44}}{A_{22}}\right)\left(\frac{r_s \sin\vartheta_1}{d_1} - \frac{r_s \sin\vartheta_2}{d_2}\right)^2 \\
&+ \frac{35}{8}\frac{A_{44}}{A_{22}}\left(\frac{r_s \sin\vartheta_2}{d_1} - \frac{r_s \sin\vartheta_1}{d_2}\right)^2 + \left(1 + 5/2\frac{A_{44}}{A_{22}}\right)\frac{r_s^2}{d_1 d_2}\sin\vartheta_1 \sin\vartheta_2 \\
&+ \frac{35}{2}\frac{A_{44}}{A_{22}}\left(\frac{r_s \sin\vartheta_1}{d_1} - \frac{r_s \sin\vartheta_2}{d_2}\right)\left(\frac{r_s \sin\vartheta_2}{d_1} - \frac{r_s \sin\vartheta_1}{d_2}\right)\cos 2\vartheta \\
&+ \frac{35}{6}\frac{A_{44}}{A_{22}}\frac{r_s^2}{d_1 d_2}\cos 2\vartheta
\end{aligned} \tag{4.15}$$

$$a_4 = 1 - \left(\frac{r_s^2}{d_1^2} + \frac{r_s^2}{d_2^2}\right) + 5\left(\frac{r_s \sin\vartheta_1}{d_1} - \frac{r_s \sin\vartheta_2}{d_2}\right)^2 + 2\frac{r_s^2}{d_1 d_2}\sin\vartheta_1 \sin\vartheta_2 \tag{4.16}$$

The expressions a_k are all independent of the detector radii r_j. This means that corrections for finite detector size can be applied separately. In general, the latter are more important for the calculation of the angular correlation function [VerBlo65]. In contrast to the other corrections and changes to the angular correlation function, the correction for finite sample size mixes components of $k = 4$ and $k = 2$.
After applying the corrections for finite sample size, the angular correlation function for e-γ cascades is

$$W_{\text{e-}\gamma}(\vartheta) = \sum_{k \text{ even}}^{k_{\max} \leq 4} a_k(A_{22}, A_{44}, r_s, d_j, \vartheta_j) q_k s_k b_k A_{kk} P_k(\cos\vartheta) \tag{4.17}$$

with q_k, s_k and b_k as defined in section 4.2.1, section 4.1 and section 3.4.1, respectively. The definition of A_{kk} from equation (3.12) was used, P_k are the Legendre polynomials. For γ-γ cascades the angular correlation function reads

$$W_{\gamma\text{-}\gamma}(\vartheta) = \sum_{k \text{ even}}^{k_{\max} \leq 4} a_k(A_{22}, A_{44}, r_s, d_j, \vartheta_j) q_k A_{kk} P_k(\cos\vartheta) \tag{4.18}$$

4.3. Accidental and true coincidences

The signal in a PAC measurement is the time between the detection of two radiations R_1 and R_2 emitted in a radiation cascade by one nucleus. In practice, however, the detected radiations might not originate from the same but from two nuclei and still be detected in the time window relevant for the measurement. These events contribute to a constant background in the PAC spectrum. Also, other radiation detected in the same energy window, e.g. due to an overlap with a neighbouring γ line, contributes to this background. Other sources of background can be neglected for the measurements with ^{83}Rb(^{83}Kr) and ^{83m}Kr(^{83}Kr).
The number of detected events of the desired radiation is determined by the source's activity A, the solid angles Ω_j covered by the two detectors, their detection efficacies ε_j and by the emission probabilities p_j of R_j, $j = 1, 2$. It can be written [SchWei92]

$$N_j = A\, \varepsilon_j\, \Omega_j\, p_j \tag{4.19}$$

The true coincidence count rate is determined by the rate of start events N_1 being detected in the start detector multiplied by the probability to detect the second quantum

$$N_{\text{true}} = A\, \varepsilon_1\, \Omega_1\, p_1\, \varepsilon_2\, \Omega_2\, p_2 \tag{4.20}$$

For accidental coincidences, the second quantum is not emitted successively. Hence, this rate is calculated by multiplying the count rates N_1 and N_2.

$$N_{\text{acc}} = N_1\, N_2\, \tau = A^2\, \varepsilon_1\, \Omega_1\, p_1\, \varepsilon_2\, \Omega_2\, p_2\, \tau \tag{4.21}$$

with τ being the time interval after the detection of R_1 in which R_2 is expected. The true coincidences increase linearly with the activity, while the accidental coincidences increase with the square of the activity. From equations (4.20) and (4.21) the ratio of true and accidental coincidences can be calculated [SchWei92]:

$$\frac{N_{\text{true}}}{N_{\text{acc}}} = \frac{1}{A\tau} \tag{4.22}$$

For a given ratio $N_{\text{true}}/N_{\text{acc}}$ and τ this limits the sample's activity.

4.4. ^{83m}Kr/^{83}Kr and ^{83}Rb/^{83}Kr as probe nuclei

The most important requirement for a PAC probe nucleus is the presence of three nuclear energy levels and a radiation cascade involving these levels during the de-excitation of the nucleus. In the transition from the initial to the intermediate level the radiation R_1 is emitted and successively radiation R_2 when the nucleus de-excites from the intermediate to the final level.
The nucleus ^{83}Rb decays via two alternative cascades, ^{83}Rb(^{83}Kr) and by populating the isomeric ^{83m}Kr state ^{83m}Kr(^{83}Kr). A decay scheme of ^{83}Rb/^{83m}Kr is shown in figure 4.3.

The first cascade (shown in red in the decay scheme) uses the 552.6 keV γ quantum (in the following referred to as 553 keV γ quantum) emitted during the nucleus' transition from the 562 keV level to the 9.4 keV level as start quantum. 16 % of all ^{83}Rb decays populate this cascade. The 9.4 keV γ quantum emitted when the nucleus de-excites from this level to the ground state is used as stop signal. Although the only possible transition leads to the ground state, the γ yield of this transition is just 5.8 % due to the conversion coefficient of $\alpha(9.4\,\text{keV}) = 16.3(3)$ [McCutc15]. It is difficult to use these emitted CEs as stop signals. The particle parameter that influences the anisotropy (see section 3.4.1) depends on the shell off which the electron is ejected. Using electrons from different shells as stop in the same measurement would lead to mixed anisotropy contributions making the calculation of the anisotropy difficult. Hence, the energy resolution of the set-up had to be sufficient to separate the emitted CEs of the L,M and N shell with energies in the range of 7.5 keV to 7.7 keV, 9.1 keV to 9.2 keV and 9.4 keV, respectively [VénKaš09]. This is not possible with the chosen detector and preamplifier system.

The second cascade (shown in blue in figure 4.3) uses the K-CE of the 32.2 keV transition from the 41.6 keV to the 9.4 keV level. The conversion coefficient of this transition is $\alpha(32.2\,\text{keV}) = 1950$ (no uncertainty given) [McCutc15] leading to a total γ intensity of just 0.036 %. However, the 17.8 keV K-CE is well suited for PAC measurements and is emitted with a probability of 17.6 % [VénKaš09]. If deduced from the values given in the Nuclear Data Sheets of $A = 83$ [McCutc15], the result 16(5) % is in good agreement with the result before. It is well distinguishable from the neighbouring L-CEs with energies ranging from 30.2 keV to 30.5 keV [VénKaš09] and the Kβ_1 X-ray line with 14.1 keV [ThoLin09]. Its energy is high enough to be detected with an off-the-shelf windowless Si solid state detector. The 9.4 keV γ quantum emitted when the nucleus de-excites from the isomeric level into the stable ground state is used as stop signal. Due to the fact that both cascades populate the same intermediate level, they use the same stop signal as well. Hence, the above discussion of this transition holds true for the second cascade as well.

The interaction between the NQM and the EFG takes place after the first transition, before the final level is reached. Thus, the half life and the quadrupole moment of this niveau play an important role for the measurements.
The half life is required to be in the range between 10 ns and some µs [SchWei92]. The lower limit is due to time resolution limitations of the experimental set-up, for too high half lives accidental coincidences dominate the measurement.
For the probe nuclei ^{83m}Kr(^{83}Kr) and ^{83}Rb(^{83}Kr) and both cascades, the half life of the intermediate state is 155.1(12) ns [McCutc15]. Being far away from both limits, this is an ideal value for PAC measurements.
The quadrupole moment of the intermediate level should not be smaller than 1 mb. Its interaction with an electric field gradient determines the interaction frequency, a too small one makes the data evaluation difficult and unreliable.
The ratio $Q_\text{i}/Q_\text{f} = 1.958(2)$ of the quadrupole moments of the intermediate level and the final state have been measured in various ^{83}Kr compounds by Mößbauer spectroscopy [HolSch77]. Knowing the ground state's quadrupole moment $Q_\text{f} = 251(5)$ mb [Kuiper61] the intermediate state's value of $Q_\text{i} = 491(10)$ mb can be deduced. This value disagrees

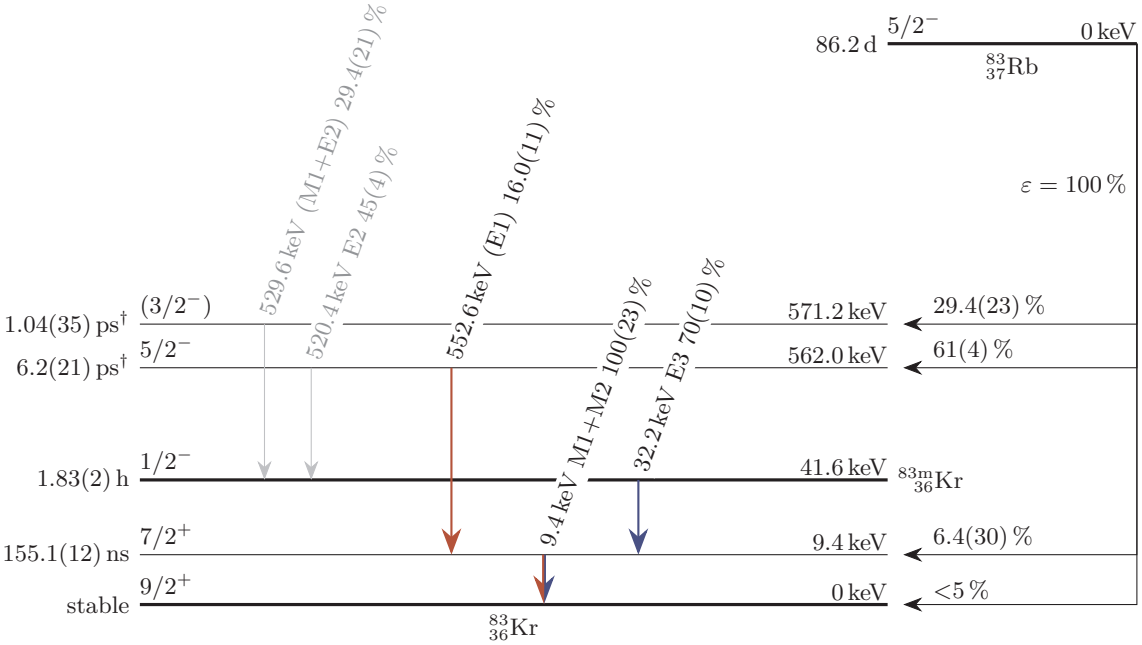

Figure 4.3.: The decay scheme of ^{83}Rb, adopted from [McCutc15] and simplified. Transitions with an intensity of below 1 % are omitted. The given transition energies and probabilities are rounded to the first decimal place. The latter are the sums of γ and CE transition probabilities. Uncertainties are given if they are still relevant after rounding.
Both cascades that are suited to carry out PAC measurements decay via the 9.4 keV level and are highlighted in blue and red, respectively. The 552.6 keV γ quantum serves as start signal for the γ-γ cascade (red), for the e-γ cascade (blue) the 17.8 keV K-CE of the 32.2 keV transition is used because of the high conversion coefficient of $\alpha(32.2\,\text{keV}) = 1950$ (no uncertainty given). The emission probability of such an electron is 16(5) %, see section 4.4. In both cases the 9.4 keV γ quantum is used as stop signal. It is emitted with a probability of 5.9 % due to the conversion coefficient of $\alpha(9.4\,\text{keV}) = 16.3(3)$ [McCutc15].
All transition probabilities are calculated from the tables for ^{83}Rb decaying via EC decay given in [McCutc15]. For values marked with † the excited ^{83}Kr nucleus was produced by ^{84}Kr(pol d, ^{3}He) ^{83}Kr, not by electron capture decay of ^{83}Rb.

slightly with the value 507(3) mb obtained by computational methods [KelPyy01]. However, both values are well suitable for PAC measurements. In this work the experimental value of Q_i will be used.

As described in section 3.1.2, in a semi-classical picture, the interaction of the nucleus' quadrupole moment and and external EFG causes a precession of the emission probability pattern of the second radiation R_2 with respect to the fixed emission direction of R_1. This precession can only generate a signal if this pattern is anisotropic. Hence, the anisotropy directly translates into the measurement signal amplitude and thus should be as big as possible.
The 553 keV-9.4 keV γ-e cascade of ^{83}Rb(^{83}Kr) has been used for PAC measurements before by Haas [Haas77]. Still, the cascade's anisotropy can not be found in literature and is therefore calculated in section 4.5.

4.5. Calculation of the anisotropy for ^{83m}Kr/^{83}Kr and ^{83}Rb/^{83}Kr

In this section the anisotropies and the corresponding anisotropy parameters of both cascades, the 553 keV-9.4 keV γ-γ and the 17.8 keV-9.4 keV e-γ are calculated. Changes of the anisotropy due to geometrical considerations like finite sample and detector size as well as intrasource scattering are not considered here but in section 9.5.

The start quantum of the γ-γ cascade, the 553 keV γ line is a pure electric dipole transition from the spin $5/2^-$ 562 keV level to the intermediate spin $7/2^+$ 9.4 keV level. The e-γ cascade is started by the transmission from the spin $1/2^-$ 41.6 keV isomeric level of ^{83m}Kr. The K-CE of this pure octupole transition is used as start signal and like in the case of the γ-γ cascade, the 9.4 keV level is populated. During the subsequent decay from there to the stable $9/2^+$ ground state, the 9.4 keV γ, a magnetic dipole, electric quadrupole mixture with amplitude mixing ratio $\delta = 12.9(3) \times 10^{-3}$ [McCutc15], is emitted. All these values can be found summarised in the ^{83}Rb decay scheme in figure 4.3. Using equation (3.16), the amplitude mixing ratio, and the F-parameters from Biedenharn et al. [BieRos53], one now can calculate the corresponding coefficients $A_k(\ell_{1/2}\check{\ell}_{1/2}I_{i/f}I)$ for all relevant transitions. They can be combined to the anisotropy coefficients A_{kk}, see equation (3.12).

The particle parameter is calculated using the non-relativistic approximation in equation (3.39) with $\ell = 3$ for a pure octupole transition for $k = 2$. The result $b_2 = \frac{4}{3}$ is in good agreement with $b_2 = 1.3$ from Biedenharn et al. [BieRos53] calculated for $Z = 40$

k	$A_{kk}^{\gamma\text{-}\gamma}$	$A_{kk}^{\text{e-}\gamma}$	b_k	$A^{\gamma\text{-}\gamma}$	$A^{\text{e-}\gamma}$
2	0.056	-0.1407	4/3		
4	0	5×10^{-6}	5		
				0.087	-0.257

Table 4.1.: The anisotropy A, the anisotropy coefficients A_{kk} and the particle parameters b_k for $k = 2, 4$ and both used cascades.

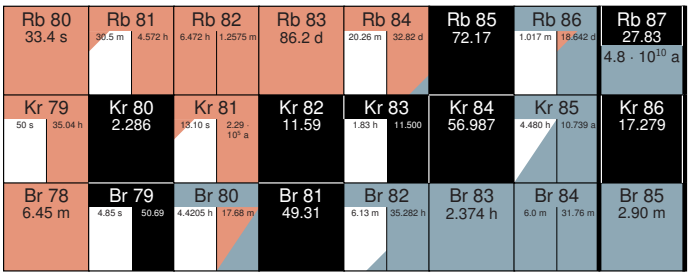

Figure 4.4.: Data on the isotopes relevant during the production of ^{83}Rb taken from the Live Chart of Nuclides [IAEA17], arranged like in the Karlsruhe Nuclide Chart [MagPfe06]. Uncertainties are not shown.

and $E_e/(mc^2) = 0.3$ and with the the values shown in figure 3.9 adopted from Rose et al. [RosBie52]. For $k = 4$ the recursion relation in equation (3.40) is used, the resulting parameter is $b_4 = 5$.

The four detectors used in this work subtend a 90° angle with their neighbouring detectors (see figure 9.2). Using these angles and the anisotropy parameters and the particle parameters the anisotropy

$$A = \frac{W(180°) - W(90°)}{W(90°)} \tag{4.23}$$

[FraSte68] is calculated. The anisotropy coefficients, the particle parameters and the anisotropies are compiled in table 4.1.

4.6. Production of ^{83}Rb

The ^{83}Rb implanted in solids at the BONn Isotope Separator (BONIS) facility (see chapter 7 for a detailed description) is produced either at the isochronous cyclotron of the Helmholtz-Institut für Strahlen- und Kernphysik (HISKP) in Bonn, Germany or the U-120M cyclotron of the Nuclear Physics Institute (NPI) in Řež, Czech Republic. However, at each facility, a different nuclear reaction is exploited in the production process. Both well-established processes are summarised in this work, more detailed descriptions can be found in works by Rasulbaev et al. [RasMai08; Rasulb10] for the production in Bonn and in works by Vénos et al. [VénŠpa05; VénSle14] for the production in Řež.

Next to ^{83}Rb other Rb isotopes are produced at both facilities. They don't play a role for the production of ^{83}Rb ion implanted samples. Either they decay rapidly due to a short half life, or their implantation is suppressed by the mass separating process at the BONIS facility, see section 7.6.4.

4.6.1. ^{83}Rb production in Bonn

At the isochronous cyclotron in Bonn, a liquid Br target is irradiated by 54 MeV doubly ionised He ions. Of the two isotopes ^{79}Br and ^{81}Br with natural abundance of 50.69 % and

49.31 % [IAEA17], respectively (see figure 4.4), the latter can be used to produce ^{83}Rb. The reaction

$$^{81}\mathrm{Br}(\alpha, 2\mathrm{n})^{83}\mathrm{Rb} \tag{4.24}$$

with a maximum cross section of $\sigma = 1300\,\mathrm{mb}$ at an α particle energy of 26 MeV [SopDup12] is exploited.

The 54 MeV α particle beam provided by the isochronous cyclotron penetrates a 100 µm Al foil that separates the accelerator vacuum from the cooling water cycle and 100 µm of de-mineralised cooling water before hitting the target ampoule. This ampoule with outer diameter of 6 mm and a wall thickness of 200 µm contains the liquid Br target. After penetrating the quartz wall, the particles enter the Br with an energy of 45.5 MeV and travel roughly 1 mm before they are stopped in the target [RasMai08]. Average beam currents of up to 0.8 µA are used during the irradiations yielding ^{83}Rb activities of up to 0.5 MBq µA^{-1} h^{-1} [Rasulb10]. After a week, the short lived isotopes produced alongside ^{83}Rb have decayed. The only remaining radioactive isotope apart from ^{83}Rb is ^{84}Rb with a half life of 32.8 d [AbrBos09]. To isolate the Rb isotopes, the ampoule is cracked open, letting the excess Br evaporate in an air flow. The fumes are led through a sodium-thiosulfate solution, binding the aggressive Br [Rasulb10].

The remaining ^{83}Rb, presumably present as RbBr compound, is solved in de-mineralised water. Small amounts of the solution are deposited on the bottom of the positive surface ionisation ion source's W furnace (see section 7.3). It is evaporated using an infrared lamp before the next drop is deposited. This process is repeated until the whole solution is used up. Before the implantation, 0.5 mg of the stable carrier $^{\mathrm{nat.}}$Rb in form of RbCl is added.

4.6.2. ^{83}Rb production in Řež

At the U-120M cyclotron in Řež, a 13 bar Kr gas target is irradiated with 26 MeV protons [Lebeda17]. Nuclear reactions on the stable isotopes ^{82}Kr, ^{83}Kr and ^{84}Kr with natural abundances of 11.59 %, 11.50 % and 56.99 % [IAEA17], respectively (see figure 4.4), contribute to the production of ^{83}Rb. The excitation function of the

$$^{\mathrm{nat.}}\mathrm{Kr}(\mathrm{p}, x\mathrm{n})^{83}\mathrm{Rb} \tag{4.25}$$

reaction reaches its maximum for 380 mb [KovTár91]. The 15 µA proton beam provided on an external beamline of the U-120M cyclotron enters the pressurised target with 25.4 MeV [Lebeda17] through a Ti window. The beam energy is reduced to approximately 16.4 MeV in the Kr gas. The ^{83}Rb yield in this energy range is optimal (4.4 MBq µA^{-1} h^{-1} [Lebeda17]) while the co-production of ^{84}Rb is minimised [VénŠpa05]. After one week all co-produced short lived activities have decayed. In contrast to the ^{83}Rb production by α-irradiation of Br, next to ^{84}Rb a significant amount of ^{86}Rb with a half life of 18.6 d [NegSin15] is produced. The activity ratio ^{83}Rb:^{84}Rb:^{86}Rb at the end of the irradiation is roughly 100:31:8 [VénSle14].
The Rb activity is deposited on the target chamber walls during the irradiation and is

washed out with de-ionised water. In this solution, Rb is present as a single charged cation Rb^+ and its counter-anion is most probably OH^- [Lebeda16]. The solution is deposited on the bottom of the positive surface ionisation ion source's furnace (see section 7.3) drop-wise and is evaporated using an infrared lamp. Prior to the implantation, 0.5 mg of the stable carrier RbCl is added in the furnace bottom. Practically all ^{83}Rb is then present in the form of RbCl [Lebeda16].

5. Data analysis

Before the experimental perturbation function can be obtained, the original data from the experiment has to be processed. The necessary steps are described in sections 5.1 and 5.2. Thereafter, the perturbation function can be fitted to the data as described in section 5.3.

5.1. Data preparation

The coincidence count rate measured in a PAC experiment is a superposition of various components. For two detectors i, j spanning an angle ϑ and a time t between the detection of radiation R_1 and R_2 it can be written [SchWei92]

$$N_{i,j}(\vartheta, t) = A\, e^{-\ln(2)t/t_\mathrm{h}} W(\vartheta, t) + B_{i,j} \tag{5.1}$$

with the sample activity A, the intermediate state's half life t_h and the time dependent angular correlation function $W(\vartheta, t)$. B_{ij} is the background created by accidental coincidences. The function of interest, the perturbation function contained in $W(\vartheta, t)$, is superimposed by the background and the exponential decay of the intermediate state.

During the decay of ^{83}Rb to ^{83}Kr two simultaneous radiations are emitted for both cascades in use. These events are detected simultaneously in a pair of detectors and thus lead to events at $t = 0$ and thus a defined time zero channel in every time spectrum. A more detailed description of these simultaneous events can be found in section 10.2.3. A misaligned time zero channel may cause significant time independent spurious contributions in the first ns of the time spectra [AreHoh80]. To continue with the data evaluation, firstly, the time zero channel needs to be found for every recorded spectrum. Time zero channel offsets between spectra can be caused by e.g. electronic components with differing internal delays. One can easily correct for these differences by shifting the spectra if the time zero channel is known Secondly, the background caused by accidental coincidences needs to be eliminated. The background may vary from spectrum to spectrum due to e.g. differing intrinsic amplifications or detection probabilities, hence this step has to be carried out for each recorded spectrum. This can be accomplished by fitting an exponential function plus a constant to each spectrum and subtracting the constant part from the measured data. For this step the program *Showfit* [Ruske01] is used.

5.2. The $R(t)$-value

After the correction of the time zero channel and the subtraction of the background, the so-called $R(t)$-value can be calculated. For a measurement using three detectors and resulting in two spectra, one 90° and one 180° spectrum the $R(t)$-value reads [AreHoh80]

$$R(t) = 2\frac{N_{1,3}(180°, t) - N_{1,2}(90°, t)}{N_{1,3}(180°, t) + 2N_{1,2}(90°, t)} \tag{5.2}$$

In comparison to set-ups with four detectors, measurements with three fixed detectors comprise some drawbacks. While this configuration does well in measuring the precessional part of the angular correlation function, its time independent part may be subject to errors because the single detection efficacies do not cancel out in the $R(t)$-value. This can lead to spurious time independent contributions [AreHoh80]. Furthermore, in the three detector configuration a misalignment of the sample may not fully cancel out but lead to a y offset of the resulting time spectrum. For samples that absorb a significant fraction of the emitted radiation, the same problem occurs. For the calculation of the $R(t)$-value, the program *Showfit* [Ruske01] is used.

5.3. Fitting the data

For fitting theoretical perturbation functions to the measured time spectra, the program Nightmare [Nédéle07] is used. Its least square fit algorithm is based on NNFit written by Barradas [Barrad92]. It is capable of handling a wide range of intermediate level spins, custom time calibrations, magnetic as well as electric interactions, mono and polycrystalline substrates and multiple fractions of different probe environments. The angles Θ and Φ between start detector and V_{zz}, the direction of the strongest EFG component, (see section 3.3.1 and figure 3.6) can be varied freely. The weighting factors s_{kn} or S_{kn} are calculated including the angular dependence given by the spherical harmonics. Also, non-axial field gradients and Lorentzian as well as Gaussian damping according to equation (3.35) can be included in the fit.

The full anisotropy is not observed in the measurement. It is limited by experimental limitations like the non-zero solid angle covered by the detectors. The effects relevant to this work are discussed in sections 4.1 and 4.2. The effective anisotropy is calculated from the emission's anisotropy and all altering factors. Firstly, the anisotropy of the e-γ cascade is multiplied by the particle parameter. The anisotropies of both cascades as well as the particle parameters are evaluated in section 4.5. The effective anisotropy is obtained by multiplying the result by correction factors for intrasource scattering, finite detector size and finite sample size. For the experimental apparatus set up in this work, these factors are determined in section 9.5. Any further deviations between observed and calculated anisotropy can be attributed to a fraction of probe atoms on undefined and non-unique lattice sites. In Nightmare, a multiplicative constant can be used to fit the theoretical perturbation function to the measured time spectrum.

For both, the e-γ and the γ-γ cascades used in this work, the 9.4 keV γ quanta are used as stop signal. One detector for this radiation is placed towards the not implanted side of the sample (see figure 9.2 for a schematic of the set-up). Especially for samples with a high density and atomic number, a significant fraction of the radiation might get absorbed in the sample on its way to the detector (see chapter 6 for absorption of the used sample materials). This will lead to a y offset of the resulting time spectrum. Also, if the sample is not positioned exactly in the point where the surface normals of the detectors cross, such an offset will appear. In Nightmare, an additive constant is used to compensate for this.

The interaction frequency $\omega_0 \equiv \omega_1$ from equation (3.26) is returned in Mrad s^{-1} by Nightmare. From this, the quadrupole frequency ω_Q from equation (3.24) can be calculated. However, the ω_Q depends on the intermediate level's spin I. The quadrupole coupling constant ν_Q is independent of the spin. It is defined as [SchWei92]

$$\nu_Q = \frac{eQV_{zz}}{h} \tag{5.3}$$

and is often used in the literature. For $I = 7/2^+$, the interaction frequency ω_0 is connected to the quadrupole coupling constand by

$$\nu_Q = \frac{7}{\pi}\omega_0 \tag{5.4}$$

6. The samples and their properties

All samples for Perturbed Angular Correlation (PAC) measurements and the calibration samples for the KArlsruhe TRItium Neutrino (KATRIN) experiment are produced by ion implantation of ^{83}Rb at the BONn Isotope Separator (BONIS) facility. The mass separator facility and the implantation process is described in chapter 7 later in this work. The determination of the implanted ion's beam spot size, which is an important tool for the characterisation of the mass separator performance and the samples, is already treated in section 6.1. Furthermore, in this chapter, thermal annealing, as a method to reduce the crystallographic damage caused during the implantation, is discussed (section 6.3). The program used to simulate the ions' penetration depth and implantation damage is introduced in section 6.2. The daughter nucleus ^{83m}Kr of the implanted ^{83}Rb is a noble gas and may not be retained in the sample after the decay. The so-called ^{83m}Kr retention is covered in section 6.4, the sample materials and their properties are discussed in section 6.5. In section 6.6 the phenomenon that the energy of the Conversion Electrons (CEs) emitted by ion implanted sources changes over time and some consequences for the implantation process are discussed. Finally, the measurement of the sample activity is discussed in section 6.7.

6.1. Beam spot size measurements

The beam spot size characterises the lateral distribution of a radionuclide in a sample implanted at the mass separator. For PAC measurements small beam spots are advantageous (see section 4.2.2) while for the KATRIN experiment larger beam spots can have a positive effect on a sample's performance, see section 6.6. Hence, the beam spot size is measured before samples are mounted in the Monitor Spectrometer (MoS). Additionally, beam spot size measurements are an indispensable tool during the test and for the characterisation of ion lenses (see section 7.5) at the BONIS facility.

A reliable way to examine the beam spot size is a radiographic image using a Timepix detector [LloBal07]. It is a $(14.08 \times 14.08)\,\mathrm{mm}^2$ sized Si chip detector with 256×256 independent pixels with individual readout. An example of such a radiography can be found in figure 6.1.
At the BONIS facility, no Timepix detector is available. Hence, all Timepix measurements have been carried out by Slezák, Sentkerestiová and Vénos [Slezák15a; Slezák15b; Slezák16b; Sentke16a; Sentke16b; SenVén16]. A description of the measurement process and all possible difficulties can be found in the work of Slezák [Slezák15a].

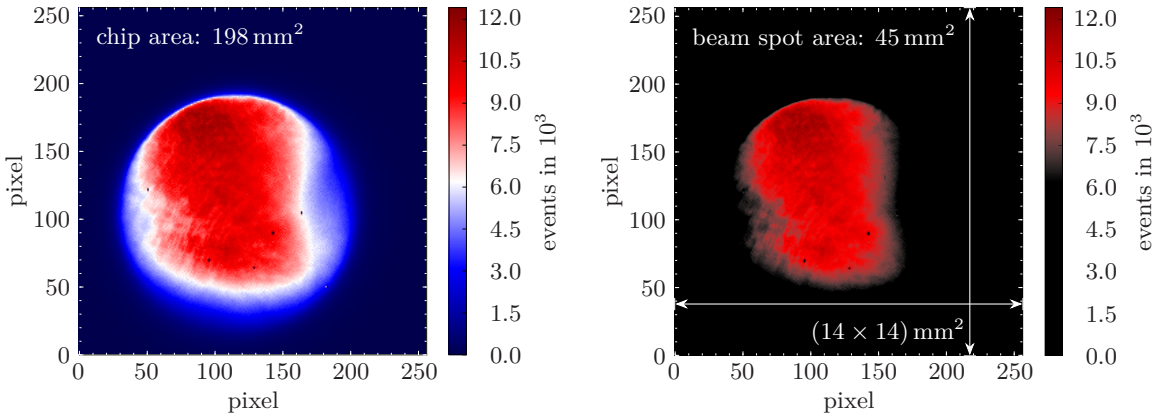

Figure 6.1.: An example for the determination of the beam spot size. On the left side, the original Timepix measurement is shown. On the right side, all non-red pixels are coloured black. After counting the non-black pixels, the beam spot area can be calculated. The Timepix measurement is taken from Sentkerestiová [Sentke16b].

In the radiographic images, the white region represents the area where the event rate is half of the rate at the maximum. Areas with higher count rates are coded red, the rest in blue. The area limited by the centre of the white area is called beam spot size, this definition is analogue to the one used by Slezák [Slezák15a]. Unlike in the mentioned work, where the area is determined with the help of a Monte-Carlo simulation from the original measured data, in this work, a simpler method based on the Timepix beam spot figures is used. The red pixels defining the beam spot are counted, from the total pixels in the measurement and the chip size, the beam spot size is calculated. This way, no uncertainty is obtained. The results of this method match the results from Slezák [Slezák15a] within 2 %. The details of this method are discussed in appendix B.1.

6.2. SRIM and implantation depth profiles

The program Stopping and Range of Ions in Matter (SRIM) [ZieZie10] (version 2013.00) is used to simulate the penetration depth of ions that impinge on the surface of a sample during an ion implantation. SRIM uses the TRansport of Ions in Matter (TRIM) Monte Carlo code by Biersack et al. [BieHag80]. It is developed to determine the ion range, the damage as well as the angular and energy distribution of backscattered and transmitted ions. To reduce computing time, some simplifying assumptions are made.
The trajectory of a particle starts with a given energy and incident direction and ends as soon as the particle leaves the sample or its energy drops below a threshold. The target is considered amorphous, hence, lattice effects like channeling can not appear in the simulation. While travelling through the sample, the projectile continuously looses energy by interactions with electrons. This energy loss is considered independent of the energy losses due to scattering on sample nuclei. Nuclear reactions and relativistic effects are not included in TRIM.

By simulating 2×10^5 ions for each sample, an implantation depth profile is obtained for a given implantation energy, projectile nucleus and target material. Such simulations are carried out for all sample materials with different implantation energies and are plotted in the respective sections 6.5.1 to 6.5.4. For all samples a 3 nm thick residual gas layer is assumed. For the sake of simplicity, in the simulation it is represented by a layer of pure C with a density of $2.25\,\mathrm{g\,cm^{-3}}$. The simulated ^{83}Rb activity ending up in this layer is compared to the measured activity in the work by Slezák [Slezák15a] resulting in a good agreement of both values.

6.3. Thermal annealing

During the process of ion implantation, the impinging ions cause crystallographic damage, mostly displacements and vacancies, in the targeted sample. In this work, the ions' energy is bigger by two to three orders of magnitude than the displacement energy of an atom in a lattice. During a collision process, the primary projectile may transfer a considerable amount of energy to a lattice atom, ejecting it from its lattice site. Depending on the kinetic energy of this atom, it may become a secondary projectile and create lattice damage or further tertiary projectiles itself until it looses all its energy. If no vacancy is available for recombination with a projectile, it becomes an interstitial. Depending on the projectile's and lattice constituents' atomic masses, the amount and distribution of damage to the lattice may vary, even for a fixed implantation energy.

The crystallographic damage in the sample is partially recovered by recombination of vacancies and interstitials by thermal and vacancy induced diffusion during the implantation. However, after an ion implantation the defect concentration will typically be much higher than in thermodynamic equilibrium. By increasing the sample temperature, the thermal diffusion can be accelerated. Most of the implantation damage can be recovered if the sample is annealed at a sufficiently high temperature. This temperature depends on the sample material and can often be found in literature.

During this annealing, the mobility of the implanted atoms will increase as well. On the one hand, this may support the incorporation of the implanted nucleus in the lattice if it is energetically favourable. If not, implanted atoms may be able to leave the substrate. For two substrates, the ^{83}Rb loss during thermal annealing is measured during an annealing programme. With a High Purity Ge (HPGe) detector, the sample's activity is determined using the 520 keV to 553 keV γ lines. For the annealing, the sample is placed in a glass tube, which is evacuated subsequently. The glass tube is inserted into a pre-heated tube furnace and is kept there for 15 min. Now, the activity is remeasured. These steps are repeated with increasing annealing temperatures up to 1370 K. The activity loss is normalised to the initial activity, plots of these measurement are shown in sections 6.5.1 and 6.5.2, where the respective substrates are discussed. A more detailed description of these measurements can be found in [Kürten13].

6.4. ^{83m}Kr retention

From the ^{83}Rb activity measurements during the thermal annealing programme it is obvious that the ^{83}Rb alkali metal atoms do not leave the sample materials Pt and graphite, even at elevated temperatures of up to 900 K, see figures 6.3 and 6.6. After the implantation of ^{83}Rb, the radionuclide decays to the noble gas ^{83m}Kr. If such an atom leaves the sample before it decays, it is lost for measurements relying on the emission of the 17.8 keV CE by ^{83m}Kr. The high voltage calibration in the MoS and the Forward Beam Monitor (FBM) calibration for the KATRIN experiment as well as the PAC measurements using the nuclei ^{83m}Kr(^{83}Kr) use the 17.8 keV CE. The ^{83m}Kr retention is a relative number between zero and one describing a sample's capability to retain ^{83m}Kr. To measure the retention, the sample is mounted in a small enclosure. The 32.2 keV γ line emitted by ^{83m}Kr is measured, once with the enclosure sealed gas-tight and once open. Gaseous ^{83m}Kr leaving the chamber will not contribute to the total events. Thus, by comparing the total events of both measurements, the retention is obtained. The measurement method is described in detail by Slezák [Slezák15a]. All retention measurements stated in this work are carried out by Slezák, Sentkerestiová and Vénos [Slezák15a; Slezák15b; Sentke16a; Sentke16b; SenVén16].

6.5. Sample materials

The samples produced by ion implantation at the BONIS facility serve different purposes. Firstly, ion implanted solid state CE sources are needed as nuclear standard, to monitor the high voltage system of the KATRIN experiment. These samples are typically implanted with an activity of 2.5 MBq to 3.5 MBq. Secondly, such samples are used for a high rate calibration of the FBM of the KATRIN experiment. ^{83}Rb activities in the order of 10 MBq are desired for these sources. In section 2.3, both applications and their role in the KATRIN experiment are sketched. Lastly, ion implanted samples are measured using the PAC method. For these measurements ^{83}Rb activities from 300 kBq to 500 kBq are sufficient. The substrates implanted in this work for either of the three purposes are discussed in this section.

6.5.1. Platinum

Pt is used as substrate for ion implanted sources for the KATRIN experiment because it was expected to provide a well defined environment for ^{83}Rb [Zbořil11]. Its mechanical toughness, the chemical inertness and the stability in high vacuum conditions [Slezák15a] are advantageous as well. The $> 99.99\,\%$ pure and 25 µm thick Pt samples are obtained from Goodfellow [Goodfe17] (article number PT000240) and are 12 mm in diameter. Prior to the implantation, these samples are cleaned two times in an ultrasonic bath in acetone and methanol [Vénos13]. These sources are investigated in great detail by Slezák and Zbořil [Slezák15a; Zbořil11]. Some of the properties of Pt samples are summarised in table 6.1

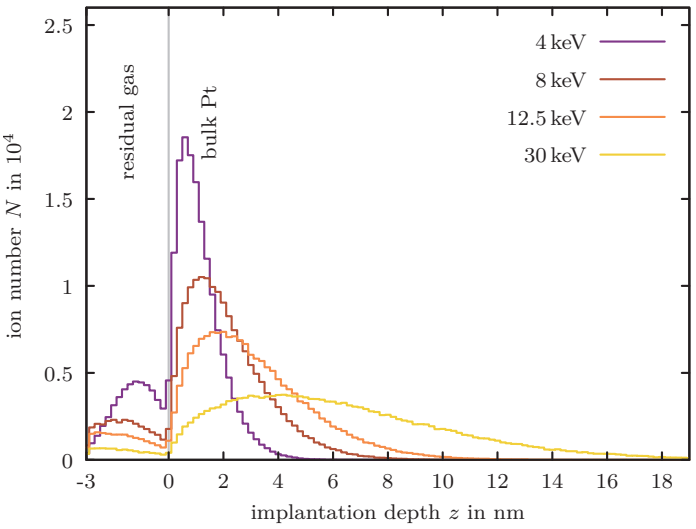

Figure 6.2.: SRIM simulations of ^{83}Rb ion implantations at different energies in Pt. A fraction of the ^{83}Rb is scattered back into the residual gas layer.

Pt sample properties		
lattice structure	fcc, polycrystalline	
density	$21.45\,\mathrm{g\,cm^{-3}}$	
^{83m}Kr retention	$> 78.6(17)\,\%$	
used for	MoS	PAC
purity	$> 99.99\,\%$	$99.95\,\%$
thickness	$25\,\mu\mathrm{m}$	$1\,\mu\mathrm{m}$
sample surface	$\varnothing 12\,\mathrm{mm}$	$(12 \times 12)\,\mathrm{mm}^2$
9.4 keV γ transmission	$\approx 0\,\%$	$\approx 75\,\%$

Table 6.1.: Some properties of the Pt samples. The table is compiled based on data from [KopHer07], [Slezák15a],[Goodfe17] and [HenGul93]

The high density and atomic number of Pt causes a shallow implantation depth profile, even at an implantation energy of 30 keV, see figure 6.2. At the same time some ^{83}Rb is scattered back into the residual gas layer and a lot of crystallographic damage in form of dislocations and vacancies is created. Duesing et al. [DueSch69] suggest that annealing temperatures around 700 K are sufficient to recover most of the implantation damage. The results of the annealing programme show no ^{83}Rb loss up to these temperatures, see figure 6.3. Retention measurements by Slezák show a ^{83m}Kr retention better than 78.6(17) % [Slezák15a].

The samples used for the KATRIN experiment are not suited for PAC experiments. Due to the high density and atomic number, the 25 µm sample nearly fully absorbs the 9.4 keV γ stop line that has to be detected on the sample side that is not implanted with ^{83}Rb. For PAC measurements, a 1 µm thin Pt foil without polyethylene backing is used. The intra-source absorption is reduced to $\approx 25\,\%$ this way. The foil with 99.95 % purity is obtained from Goodfellow (article number PT000200).
The CEs are affected by the high density and atomic number as well. Despite the shallow implantation depth profile obtained with implantation energies of 4 keV or 8 keV, corrections to the anisotropy due to intra source scattering are necessary, see section 9.5.3.

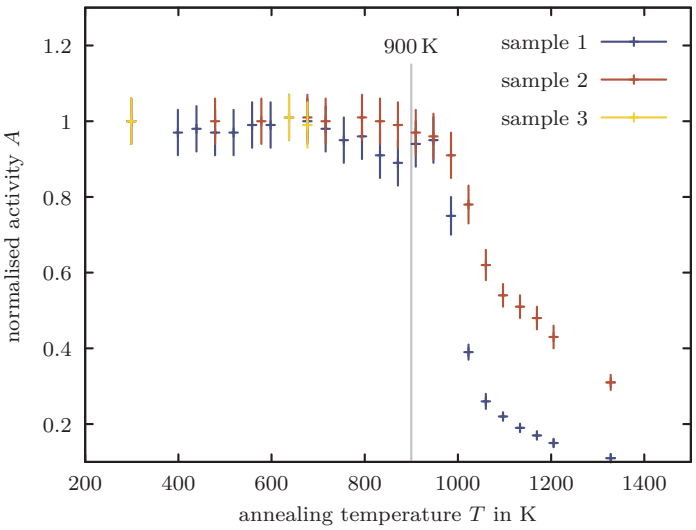

Figure 6.3.: The results of the annealing programme with 15 min annealing steps of ^{83}Rb implanted Pt. At 1000 K significant amounts of ^{83}Rb starts to leave the sample. Annealing at 900 K is possible without ^{83}Rb losses.

6.5.2. Highly Oriented Pyrolytic Graphite (HOPG)

Highly Oriented Pyrolytic Graphite (HOPG) is a synthetic form of graphite produced by pyrolysis with a purity of better than 99.99 % [SPISup15] obtained from SPI Supplies. It consists of honeycomb-shaped graphene layers in an ABAB stacking called α-graphite. For the samples used as solid state calibration source in the MoS at the KATRIN experiment, the highest available quality (grade SPI-1) with a mosaic spread of 0.4(1)° and a lateral grain size of typically $\lesssim 3$ mm [SPISup17] is used. The c-axis is perpendicular to the sample surface, the chips can be considered to be pseudo monocrystalline. The $(10 \times 10)\,\mathrm{mm}^2$ HOPG chips are cleaved parallel to the face before the implantation, resulting in two samples of 0.5 mm thickness. If the resulting surface shows protruding flakes of material, adhesive tape is pressed to the surface. When the tape is removed, it takes these flakes with it. This process is repeated until a satisfactory flat sample surface is achieved. Some properties of the HOPG samples are summarised in table 6.2.

For PAC measurements, the cheaper grade SPI-2 chips are used. They are treated in the same way as described above.

HOPG sample properties	
lattice structure	α-graphite, pseudo monocryst.
density	$2.27\,\mathrm{g\,cm^{-3}}$
$^{83\mathrm{m}}$Kr retention	$> 89.5(21)$ %
used for	MoS & PAC
purity	> 99.99 %
thickness	≈ 0.5 mm
sample surface	$(10 \times 10)\,\mathrm{mm}^2$
9.4 keV γ transmiss.	≈ 74 %

Table 6.2.: Some properties of the HOPG samples. The table is compiled based on data from [SPISup15], [SPISup17], [Slezák15a] and [HenGul93]

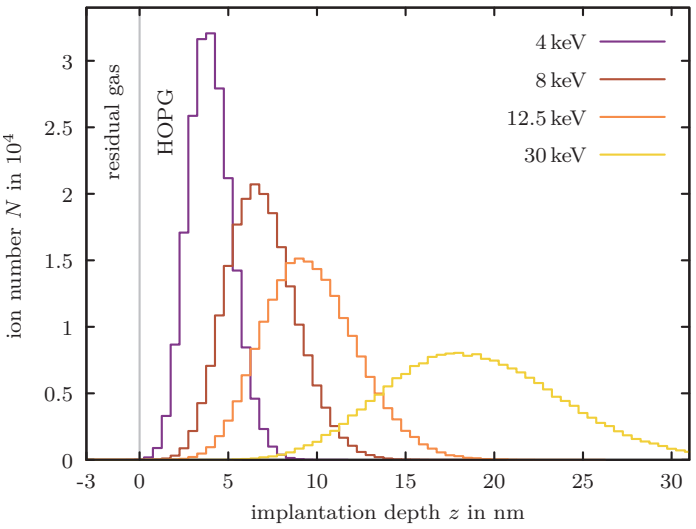

Figure 6.4.: SRIM simulations of ^{83}Rb ion implantations at different energies in HOPG. For shallow implantation depth profiles, low implantation energies are required.

The low density and atomic number causes a deep implantation of ^{83}Rb with no ions being backscattered. Consequently, low implantation energies are necessary to achieve shallow implantation depth profiles. SRIM simulations for different implantation energies are shown in figure 6.4. HOPG is soft and vulnerable to scratching and has to be handled with exceptional care after the ion implantation to prevent release of ^{83}Rb. Measurements by Slezák indicate a ^{83m}Kr retention better than 89.5(21) % [Slezák15a].

6.5.2.1. Rb and Kr lattice sites in HOPG

From literature it is known that Rb intercalates in C single crystals and HOPG chips [KamDre80; DreDre81]. Depending on the intercalant concentration, the temperature and the sample production process, intercalant layers of different stage n are formed. Here the stage number n indicates the C layers between two intercalant layers. In the work by Kambe et al. [KamDre80] Rb occupies an interstitial lattice site between two of HOPG's graphene layers changing the ABAB graphene layer stacking to e.g. AαA, again depending on sample preparation and temperature. Here, A denotes a graphene layer and α an intercalate layer. For more information on intercalation processes and Rb intercalation in HOPG, the reader is referred to the works by Kambe et al. and Dresselhaus et al. [KamDre80; DreDre81].
In contrast to the samples prepared by the two-zone vapour transport method in the mentioned works, the HOPG samples in this work are ion implanted. During this process, Rb is deposited in the host lattice which is damaged during the implantation. It is possible that local stacking changes to incorporate the intercalate occur.

A Rb or Kr interstitial will not recombine with a single vacancy in a HOPG graphene layer and become a substitutional. Such a vacancy is surrounded by three nearest neighbours, restricting the atomic radius of a potential substitutional to half the bond length $d/2 = 70.75\,\text{pm}$ [Binder99; SPISup15] in a hard-sphere model, see figure 6.5. However, the atomic

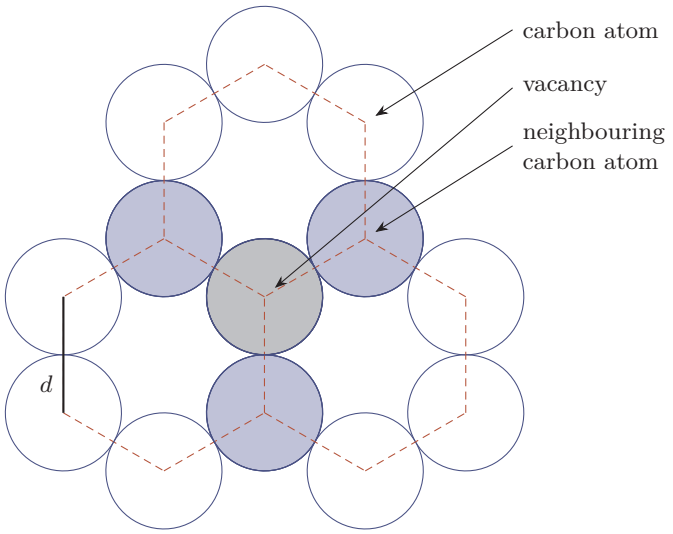

Figure 6.5.: The geometry of a vacancy in one of HOPG's graphene layers. The vacancy shown in grey is surrounded by three carbon nearest neighbours shown in blue. In a hard sphere model, only interstitials with a maximal atomic radius equal or smaller than half the bond length $d/2 = 70.75\,\text{pm}$ [Binder99; SPISup15] can recombine with this single vacancy.

radii of Rb, Kr and Rb^+ are 285 pm, 85 pm and 78 pm, respectively. Recombinations with vacancy clusters are not excluded by this argument.

6.5.2.2. HOPG annealing behaviour and Kr and Rb mobility

Platonov et al. [PlaTro75] state that annealing processes in HOPG are activated in three main temperature ranges: From 473 K to 873 K small defect complexes of interstitials recover. This is in agreement with Kambe et al. [KamDre80] who report a change in intercalate ordering at annealing temperatures of 747 K. No loss of Rb is reported by the authors. This is supported by the annealing programme carried out in this work. Starting from 900 K ^{83}Rb losses are visible. The results are shown in figure 6.6. The annealing programme was measured with high purity polycrystalline graphite rather than HOPG.
In the temperature range 1073 K to 1773 K vacancy diffusion occurs, while in the range of 1473 K to 2273 K large loops of interstitials and vacancies recover. It follows that in contrast to vacancies, ^{83}Rb is mobile at the annealing temperatures used for this sample.
From the Kr retention measurements, a Kr mobility even at room temperature can be concluded. If no diffusion processes would occur, the Kr retention would be 100 %. Most probably these movements occur in the planes between the weakly bound graphene layers parallel to the sample surface. The majority of ^{83}Rb atoms are implanted less than 5 nm below the surface. If the movement in c-direction was likely, the Kr retention would be much lower.

Kr losses during the annealing are of no concern because ^{83}Rb permanently generates ^{83m}Kr.

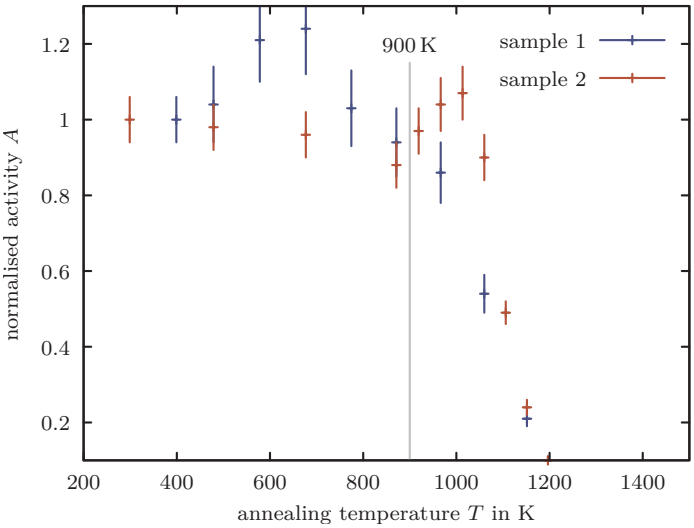

Figure 6.6.: The results of the annealing programme with 15 min annealing steps of ^{83}Rb implanted polycrystalline graphite. At 1050 K ^{83}Rb starts to diffuse out of the sample. An annealing at 900 K is possible without ^{83}Rb losses. All retention measurements were carried out before the data were evaluated, thus the reason for the two outliers at 600 K and 700 K could not be reconstructed afterwards.

6.5.3. Beryllium

Be samples are solely used for PAC measurements. From ion beam channeling measurements of ion implanted metal substrates, the alkali metal Cs as well as the noble gas Xe are known to occupy an octahedral interstitial lattice site [ViaKau80] in the hexagonal close-packed (hcp) host lattice [KopHer07] Be. As an alkali metal with an atomic radius of 256 pm (compared to 284 pm of Cs) [FraKar76] a similar behaviour can be expected for Rb. For the noble gas Kr with an atomic radius of 85 pm a behaviour comparable to Xe (atomic radius 100 pm) [FraKar76] can be expected as well. An Electric Field Gradient (EFG) is expected at this lattice site, Be is thus used for the first PAC measurements shown in section 10.3.

Be sample properties	
lattice structure	hcp, polycrystalline
density	1.87 g cm^{-3}
^{83m}Kr retention	not measured
used for	PAC
purity	99 %
thickness	100 µm
sample surface	(14 × 14) mm^2
9.4 keV γ transmission	≈ 99 %

Table 6.3.: Some properties of the Be sample. The table is compiled based on data from [KopHer07] and [HenGul93]

The atomic number of 4 in conjunction with the low density of 1.85 g cm^{-3} cause a low absorption of the 9.4 keV stop γ quantum. For the 100 µm thick, polycrystalline foil of 99 % purity a transmission of 99 % is calculated. For an implantation energy of 4 keV an implantation depth of 5 nm is achieved, see figure 6.7. Intra-source scattering does not play a major role for Be, see section 9.5.3. Some properties of Be are compiled in table 6.3.

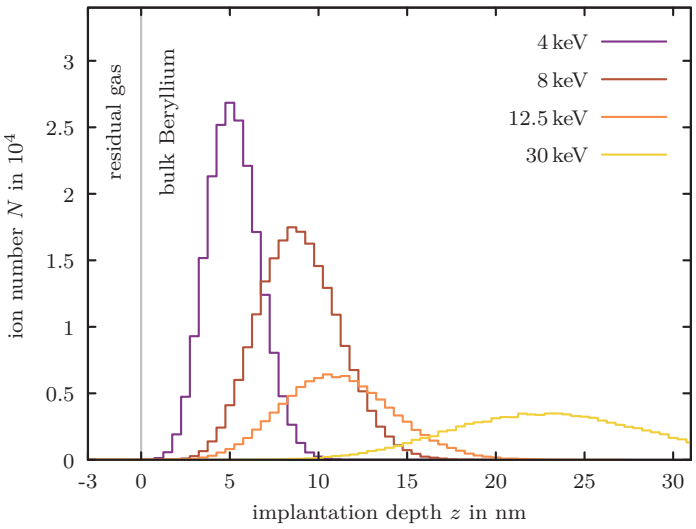

Figure 6.7.: SRIM simulations of ^{83}Rb ion implantations at different energies in Be. The implantation depth profiles are the widest of all samples used in this work. No backscattering occurs.

6.5.4. Zinc oxide (ZnO)

ZnO is only used as solid state electron source for calibration purposes at the KATRIN experiment. It is a semi-conductor that crystallises in wurtzite structure. Being an oxide itself, oxidation does not pose a problem for this substrate. The *c*-plane oriented samples' surface is $(5 \times 5)\,\mathrm{mm}^2$ with a thickness of 0.5 mm. They are obtained from Crystec GmbH, Berlin. The low atomic number in comparison to Rb, causes a wider implantation depth profile than in Pt. The annealing programme reveals that an annealing at 900 K is possible without loss of ^{83}Rb [Kürten13]. At this temperature, most of the lattice damage from ion implantation is recovered [Keßler08]. The work with this substrate is discontinued after two samples due strong energy drifts of the K-CE line (see section 6.6 for an explanation of the drift).

6.5.5. Aluminium

Al samples are ion implanted for solid state electron sources used at the KATRIN experiment to calibrate the FBM. For these samples, a well defined environment of the implanted ^{83}Rb as well as the purity of the substrate does not play a role. However, to avoid X-ray fluorescence in the range of interest, as little alloying elements as possible with fluorescence emission close to the relevant 17.8 keV CE line should be present. The substrate material is the wrought alloy AlMgSi1 (DIN EN 573-3: EN AW-6082) with main alloying elements Mg and Si [ThyKru13b]. The X-ray fluorescence energies of up to 1.8 keV of these elements are below the detection threshold of 4 keV [Elling16] of the FBM. The substrate may contain some other alloying elements listed in table 6.4 along with the respective Kβ_1 X-ray fluorescence energies. If the admixture of these elements poses a problem, the current alloy can be replaced by AlMgSi (DIN EN 573-3: EN AW-6060) which contains less alloying elements but is more difficult to machine [ThyKru13a].

Table 6.4.: Alloying elements of the alloy AlMgSi1 and the possible alternative AlMgSi [ThyKru13b; ThyKru13a] and their $K\beta_1$ X-ray fluorescence energies [ThoLin09].

Alloy. elem.	fraction in AlMgSi1/%	fraction in AlMgSi/%	$K\beta_1$/keV
Mg	0.60 to 1.20	0.35 to 0.60	1.3
Si	0.70 to 1.30	0.30 to 0.60	1.8
Ti	0.00 to 0.10	0.00 to 0.10	4.9
Mn	0.40 to 1.00	0.00 to 0.10	6.5
Fe	0.00 to 0.50	0.10 to 0.30	7.0
Cu	0.00 to 0.10	0.00 to 0.10	8.9
Zn	0.00 to 0.10	0.00 to 0.15	9.6

Without proper cleaning, Al is covered by an amorphous, typically 10 nm thick Al_2O_3 layer. This oxide layer recovers quickly after its removal. Only seconds at ambient air and room temperature are sufficient to create 1 nm of Al_2O_3 on the surface, after a day 3 nm to 5 nm are recovered [ReiZwe55]. An implantation in this layer is unfavourable due to a ^{83m}Kr retention that can be as low as 30 % [Sentke16b], while the retention of pure Al is 95 % [Slezák15c]. Both values are measured with ion implanted and untreated Al samples. The sample with low retention is implanted with 4 keV, depositing the ^{83}Rb nearly entirely in the oxide layer. The implantation of the high retention sample is carried out with 30 keV. Nearly all of the ^{83}Rb can pass the Al_2O_3 this way. The Al_2O_3 layer can be removed by pickling in sodium hydroxide (NaOH) [ReiZwe55], the following reaction takes place [Binder99]

$$2Al + 2NaOH + 6H_2O \longrightarrow 2Na[Al(OH)_4] + 3H_2 \uparrow \tag{6.1}$$

To obtain an oxide-free surface, the polished sample is moved in NaOH for 2 min. The sodium aluminate created during this reaction is soluble in water and ethanol. Hence, the sample is moved in water for five minutes and is wiped twice without being removed from the liquid. The same procedure is repeated with ethanol. All liquids used are purged with dry nitrogen gas for 15 min prior to the cleaning and the whole process is carried out in dry Ar atmosphere. The sample is brought to the mass separator in a Ar filled vessel and is mounted in the Ar flooded collector chamber.

For the FBM calibration source, a beam spot as small as possible is desired. Hence, the BONIS retarding lens is used to implant this sample, limiting the implantation energy to the range from 4 keV to 12.5 keV. Because scattering and energy losses of the emitted electrons does not play a role for this count rate stability calibration, the highest possible implantation energy of 12.5 keV is used to reduce problems with the Al_2O_3 layer. A SRIM simulation of an ion implantation at 12.5 keV of an untreated and a chemically cleaned Al sample is shown in figure 6.8. For the simulation of the cleaned substrate, it is assumed that 3 nm of Al_2O_3 recover after the cleaning process and during mounting the sample in the collector chamber. Despite this overestimate, most of the ^{83}Rb is implanted in Al.

The Al sample is a small, 8 mm high block with a 11 mm diameter disc-shaped target area on top. A thread on the bottom side is used to mount the sample on a metal rod allowing for a quick and precise positioning in the BONIS lens. The target is clamped in an Al case and a protective Al sheet with an 8 mm opening is mounted on top. Left and right

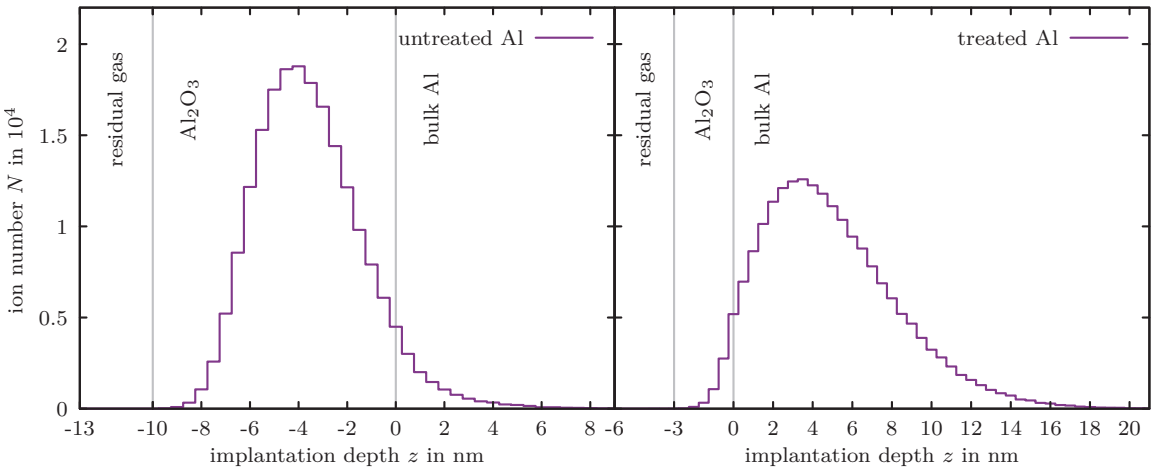

Figure 6.8.: Implantation depth profiles for 12.5 keV implantation energy of cleaned and untreated Al. An Al_2O_3 layer of 3 nm is assumed to have recovered after the cleaning procedure.

body part are kept together by two M3 stainless steel screws, four M2 stainless steel screws fix the protective sheet on the body. The footprint of the mounted case is $(24 \times 20)\,\mathrm{mm}^2$ with a total height of 11 mm. The lid covering the aperture opens sideways to allow for an operation even with the detector mounted closely in front of the source. No parts protrude to facilitate a small distance between calibration source and FBM detector while minimising the risk of touching and damaging its bare Si PIN diode. The sample and its housing are shown in figure 6.9.

6.6. Stability measurements and ^{83}Rb peak concentration

The samples ion implanted at the BONIS facility are used to monitor the retarding voltage applied to the main spectrometer. The 17.8 keV K-CE emitted by $^{83\mathrm{m}}$Kr (abbreviated K-32), a daughter nucleus of the implanted generator nuclide ^{83}Rb, is used as a nuclear standard as described in section 2.4. The KATRIN specifications require the Gaussian variations of the high voltage to be smaller than 60 mV during a KATRIN measurement run of two months [KATRIN04]. This corresponds to a stability of 3.2 ppm at 18.6 keV. It was observed for nearly all ion implanted sources that the energy of the emitted CEs change linearly over time in the range of one ppm per month. Hence, usually a limit of 1.6 ppm per month is stated for this so-called energy drift. An example of the drift of two Pt samples can be found in figure 6.10. The phenomenon of the energy drift is studied by Slezák [Slezák15a] in great detail for different substrates and implantation energies. The reader is referred to this work for more detailed characterisation and more data on this effect. The origin of this drift is not understood yet.

A similar drift behaviour is found for Pt as well as for HOPG samples. However, Slezák [Slezák15a; Slezák16a] observed an increase of the energy drift for samples with smaller beam

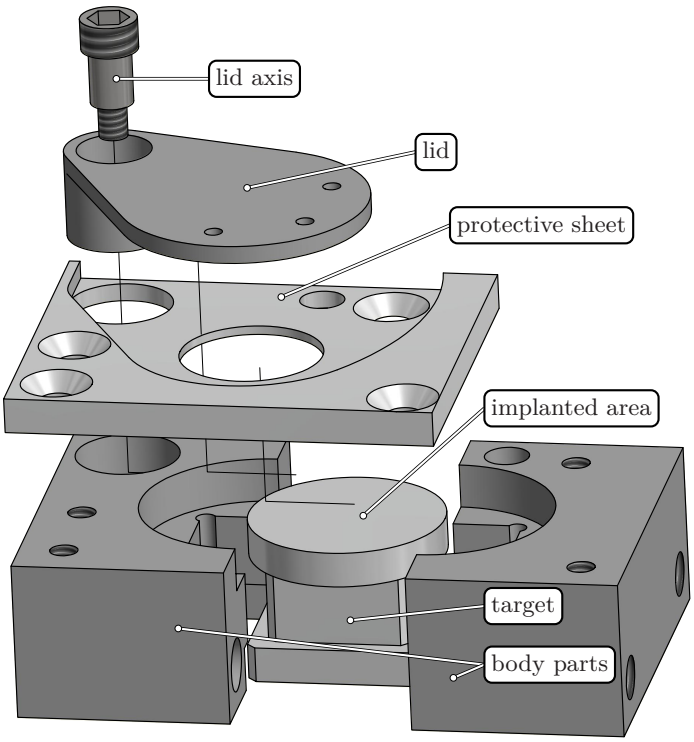

Figure 6.9.: The FBM solid state calibration source and its housing.The two M3 screws keeping left and right body parts together and the four M2 screws fixing the protective sheet on the body are not shown. All screws are stainless steel. Constructed with Autodesk Inventor 2015 for educational purposes.

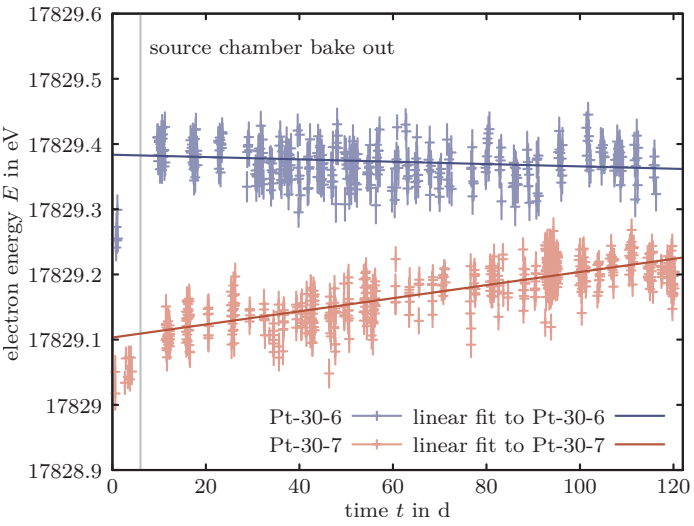

Figure 6.10.: An example for the energy drift shown for two ion implanted samples [Slezák15a]. The samples are labelled with the following code: substrate-implantation energy-serial number. Points before the grey line marking the source chamber's bake out are not included in the fit. Comparable measurements are carried out for all samples and substrate types [Slezák15a].

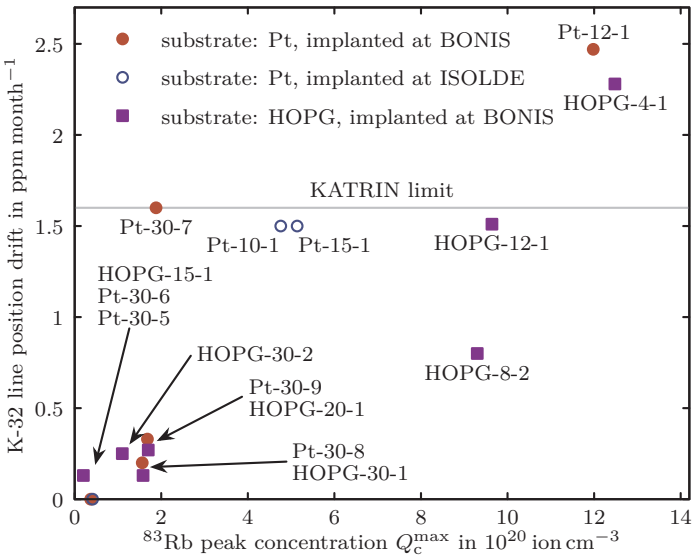

Figure 6.11.: The drift of the K-32 CE line for various samples implanted at the BONIS and the Isotope mass Separator On-Line DEvice (ISOLDE) facility with different ^{83}Rb peak concentrations Q_c^{max}. For higher ^{83}Rb peak concentration the energy drift increases. The samples' name convention is: substrate-implantation energy-serial number. The data points of the samples Pt-30-5 and Pt-30-6 overlap. The data are taken from Slezák [Slezák16a].

spots and lower implantation energies. For these samples, the ^{83}Rb/^{83m}Kr concentration in the ion implanted region is higher. To quantify this, the ^{83}Rb peak concentration is introduced:

$$Q_c^{max} = \varrho_l^{max} Q_s^{max} \tag{6.2}$$

It is an estimate for maximal ion concentration in ions cm^{-3} in the implanted source with the peak surface dose Q_s^{max} and the maximal relative longitudinal ^{83}Rb implanted dose ϱ_l^{max}. The latter is obtained using SRIM (see section 6.2) and is defined as

$$\varrho_l^{max} = \frac{m^{max}}{m_{tot} \Delta d} \tag{6.3}$$

with the maximum of the longitudinal ^{83}Rb distribution m^{max}, the total number of simulated ions m^{tot} and the bin width Δd. The maximal surface dose is defined equivalently:

$$Q_s^{max} = \varrho_s^{max} N = \frac{n^{max}}{n_{tot} \Delta S} N \tag{6.4}$$

with the area of one Timepix detector pixel ΔS, the total of all measured events n_{tot} in a Timepix measurement, the maximal event number of all pixels n^{max} and the number of implanted atoms N. These definitions and a more detailed treatise can be found in the work by Slezák [Slezák15a]. Plotting the peak concentration of the samples ion implanted for the KATRIN experiment reveals a correlation between the peak concentration and the energy drift, see figure 6.11.

6.6.1. Consequences for the ion implantation

The CEs emitted by ^{83m}Kr have to penetrate a thin layer of substrate before their energy is analysed. The fraction of electrons passing this layer with (nearly) no energy loss, the

so-called no-loss-electrons, are used for the monitoring process, all other electrons are rejected by the Magnetic Adiabatic Collimation combined with an Electrostatic (MAC-E) filter, see section 2.4. The closer to the surface the implanted ^{83}Rb and its daughter ^{83m}Kr are incorporated, the more no-loss-electrons will leave the sample resulting in two advantages: Firstly, more electrons per activity are available for the monitoring process. As a consequence, either weaker sources can be produced to reduce the irradiation of personnel or more electrons can be measured in the same time interval. Secondly, less electrons generating background are present. This can be achieved by keeping the implantation energy low, so that the implantation depth profile is shallow and closer to the surface, see e.g. figure 6.4. However, at the same time the shallow implantation depth profile causes an increase in the ^{83}Rb concentration in the implanted volume. For these sources an increased energy drift is observed. A good example is the sample HOPG-4-1 implanted with a low implantation energy of just 4 keV and exhibiting a drift of over 2 ppm per month, see figure 6.11.
From equation (6.4) it is obvious that the advantages of a high no-loss-electron to loss-electron ratio for samples implanted with a low implantation energy can be kept if the beam spot size increases. In this way, the ^{83}Rb concentration is kept low due to the lateral spread of the implanted activity while the ^{83}Rb is deposited close to the surface at the same time. To achieve this, the ISOLDE retarding lens is installed in the BONIS set-up, see section 7.4.2.

6.7. Activity determination

All energy spectra in the present work are measured with a standard cylindrical HPGe detector. This detector is calibrated using calibrated ^{152}Eu, ^{137}Cs and ^{133}Ba sources. After recording spectra of all three sources and subtracting the background, the event number in each γ line is determined. Using the branching ratios for all three radio isotopes from the literature [NuDat16], the detection efficacy for each line and a certain distance between sample and detector can be calculated. A function of the form

$$\psi(a, b, c, d, E) = a \cdot b^E + c \cdot E + d \tag{6.5}$$

is fitted to the data points determined before to obtain a continuous relation between the energy of the incident γ radiation and the detector's efficacy. For more details on the fit and for a discussion of the error propagation, see appendix A. In figure 6.12 the energy dependent efficacy for a distance of $d = 350$ mm between detector and sample is shown.

The number of events in one γ line can not be determined using a Gaussian fit to the line, mainly because of a skew in the line shape towards the low energy side, mostly caused by incomplete charge carrier collection [PhiMar76]. Extensive discussions on the line shapes in spectra recorded with HPGe detectors as well as on analytical functions to fit these data (automatically) can be found in literature, [PhiMar76; VarTri69; HelLee80]. Here, when only ^{83}Rb and ^{84}Rb spectra are analysed, a simpler but still sufficient approach is used.

A Gaussian function with linear background is fitted to the line's right flank to estimate the mean and the standard deviation μ and σ. Now, all events in all channels within the interval $[\mu - 4\sigma, \mu + 4\sigma]$ are added up. Afterwards the background modelled by a constant and a linear function is subtracted, see figure 6.13 for a visualisation. For a more detailed discussion of the evaluation of γ lines, see appendix B.2.

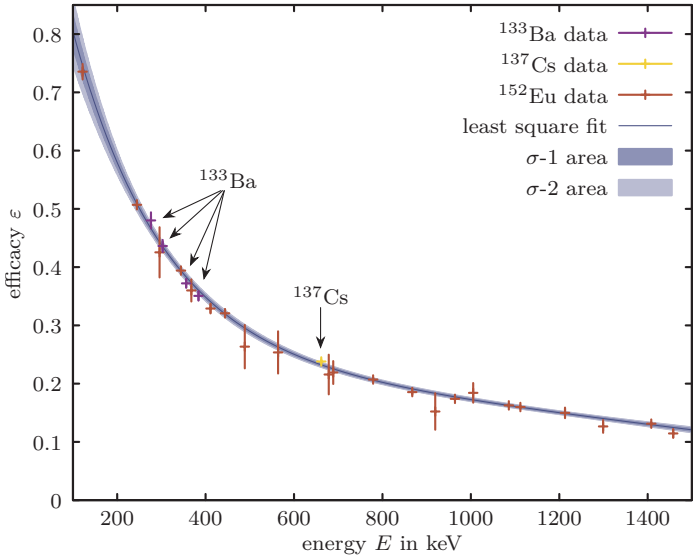

Figure 6.12.: The efficacy measurements of the HPGe detector of all three calibration samples with a least square fit of equation (6.5) and σ-1 and σ-2 uncertainty regions. The χ^2/dof of the fit is 0.95.

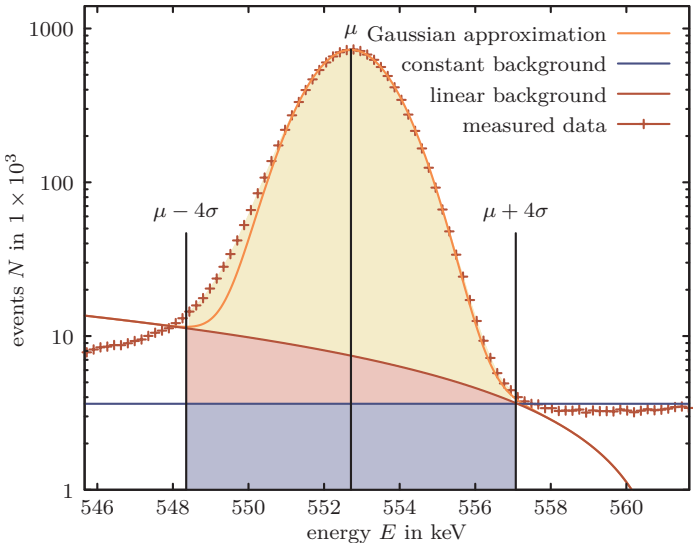

Figure 6.13.: An illustration of the activity determination from a spectrum recorded with a HPGe detector. The Gaussian fit is used to obtain an estimate of μ and σ only. The background contributions are shaded in blue and red while the remaining events after background subtraction in this line are shaded in yellow.

7. The BONIS facility

The ion implantation of all samples used in this work is carried out at the BONn Isotope Separator (BONIS). This multi-purpose, high-resolution isotope separator is capable of separating a wide range of isotopes until beyond the transuranic elements [SevBel09; Eversh16]. Ion beams of different isotopes can be produced using ion sources of positive and negative surface ionisation, Nielsen, Sidenius, and sputter type [Freita79].
Depending on the requirements of the experiment, ion implanted samples with energies ranging from 4 keV to 12.5 keV and from 30 keV to 160 keV are possible within routine operation. The lower limits can be reduced to 100 eV [FreHei76] and 15 keV, increasing the beam spot size and reducing the implantation efficacy.

In this chapter, an overlook of the BONIS facility, its components (section 7.1) and the ^{83}Rb implantation process (section 7.2) is given. The used positive surface ionisation ion source and the changes applied to it in this work are described in section 7.3. The ion beam retarding lenses included in the BONIS set-up are discussed and characterised in section 7.4. The Resulting beam spot sizes with and without retarding lenses are compared (section 7.5) and the admixture of undesirably implanted ions as well as the mass resolution are estimated (section 7.6). Finally the evolution of the implantation efficacy over the last years is discussed in section 7.7.

7.1. The mass separator layout

This section gives a brief overview of the the mass separator's set-up, its main components and their role during an implantation. Those parts altered, enhanced, or improved during the course of the present work are discussed in more detail. Furthermore, both performance and limits of the mass separator with respect to the tasks in work are discussed. For an overview of the mass separator and the operating place of each part listed below, see figure 7.1. The description of components starts with the ion source and follows the beam from right to left. Commonly used parameters during ^{83}Rb implantations are listed in table 7.1.

positive surface ionisation ion source: Origin of the ion beam is the ion source. For the implantation of ^{83}Rb, a positive surface ionisation source with a W ioniser is used. Prior to the implantation, the stable carrier $^{nat.}$Rb in form of RbCl together with the radioactive ^{83}Rb are deposited in the ioniser. During the operation of the mass separator, the evaporation and ionisation of the projectile material takes place inside this ioniser. The ion source is operated at a positive potential determining the

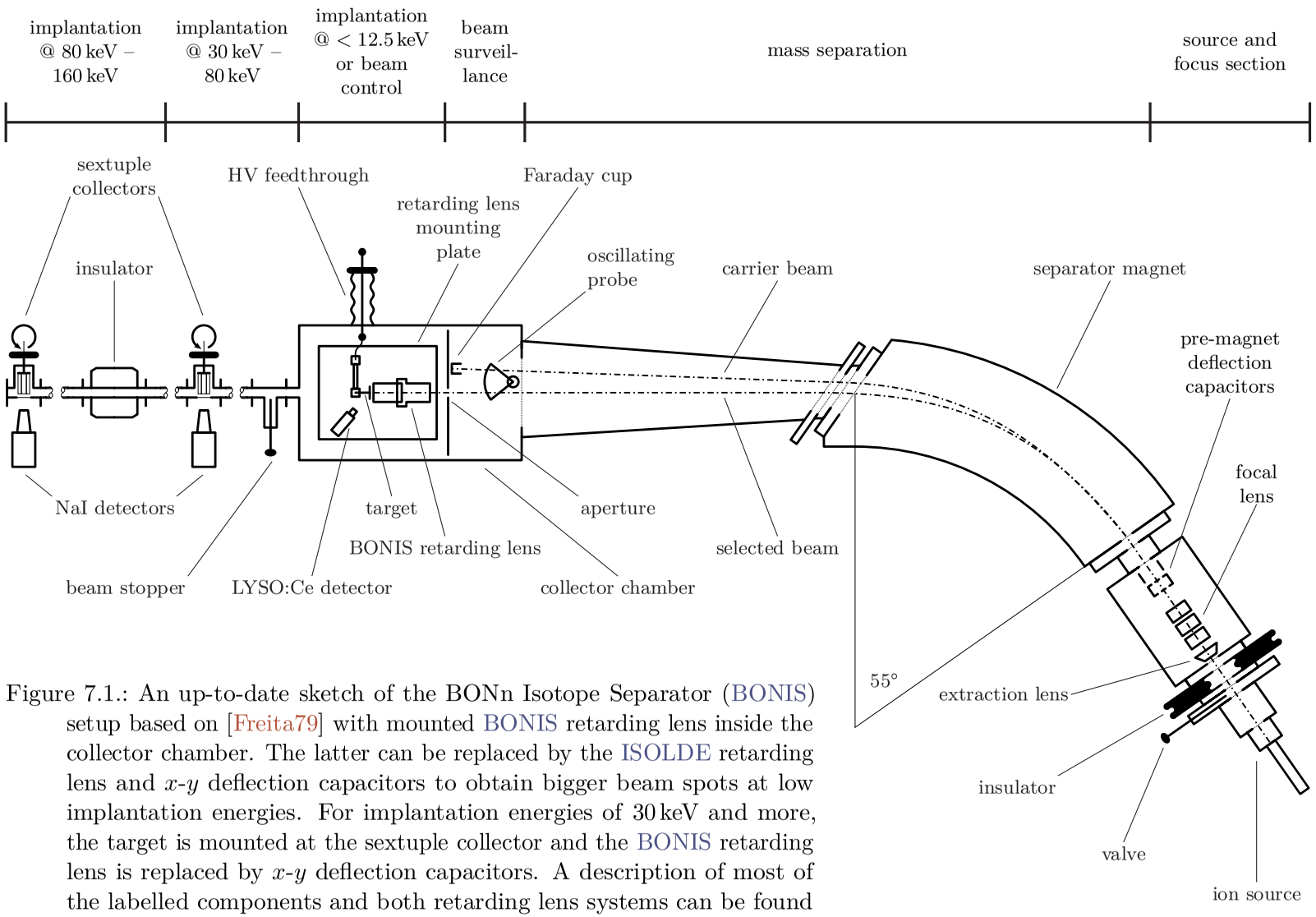

Figure 7.1.: An up-to-date sketch of the BONn Isotope Separator (BONIS) setup based on [Freita79] with mounted BONIS retarding lens inside the collector chamber. The latter can be replaced by the ISOLDE retarding lens and x-y deflection capacitors to obtain bigger beam spots at low implantation energies. For implantation energies of 30 keV and more, the target is mounted at the sextuple collector and the BONIS retarding lens is replaced by x-y deflection capacitors. A description of most of the labelled components and both retarding lens systems can be found in section 7.1, 7.4.1 and 7.4.2, respectively.

Table 7.1.: Standard mass separator parameters during ^{83}Rb implantations. The used values depend on the implantation energy and are subject to changes during the implantation.

positive surface ionisation ion source potential	15 kV to 40 kV
extraction lens potential (with respect to ion source)	−3 kV to −6 kV
focal lens potential	10 kV to 20 kV
separation magnet field strength	0.11 T to 0.18 T
Faraday cup ^{85}Rb current	∼ 0.15 µA

implantation energy. The potential of the ion source with respect to ground will be referenced as pre-acceleration voltage if a retarding lens is used. In section 7.3 the positive surface ionisation source is discussed in more detail.

extraction lens: Together with the ioniser cap's spherical indentation (see section 7.3.1 for a more detailed description of the ioniser), the extraction lens forms the electric field used to extract the positively charged ions leaving the ion source. The applied voltage is subject to change when the focal lens systems voltage is changed as both systems' voltages have to be matched to maintain a maximal ion extraction efficacy and a small beam diameter.

focal lens: In order to ensure an optimal separation process in the mass separator magnet, the beam extracted via the extraction lens has to be focussed towards the magnet. The focal lens reduces the divergence of the beam leaving the extraction lens. The applied voltage may be varied to assure a good match to the extraction lens' voltage and may be changed again during the implantation in order to maintain the desired beam properties.

pre-magnet deflection capacitors: The ion beam focussed by the focal lens can be aligned with the entry slit of the mass separator magnet using the pre-magnet deflection capacitors.

separation magnet: The mass separation is realised by magnetic separation in a field created by a water cooled magnet manufactured by Nuclesa. The particle trajectory's radius is 1.5 m and the bending angle 55°. The magnet can be operated at magnetic fields of up to 0.45 T [FreHei70].

collector chamber: The collector chamber houses the oscillating probe, an aperture and a Faraday cup, which are part of the beam control set-up. Furthermore, x-y deflection capacitors or either of two available retarding lenses can be mounted inside. If a retarding lens is used, the target and a detector for real-time activity measurement are mounted in the collector chamber. During implantations the pressure in the collector chamber is usually in the range of 5×10^{-7} mbar.

oscillating probe: During an implantation the beam profiles of the mass separated beams are monitored using the oscillating probe. Fine tuning of the extraction and the focal voltage are carried out and monitored using the visual feedback of the beam's cross section provided by the oscillating probe.

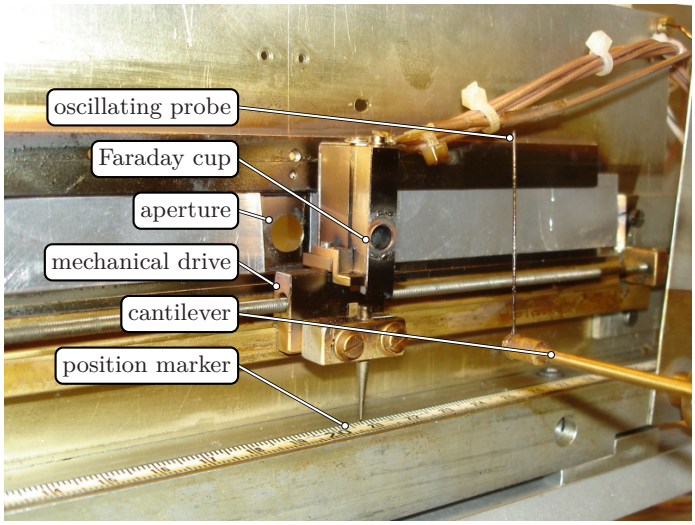

Figure 7.2.: The oscillating probe, the Faraday cup and the aperture inside the collector chamber of the BONIS facility.

This probe consists of a beam-parallel cantilever with a perpendicularly mounted carbon pin at its end. This pin intersects the plane in which the beams of different masses enter the collector chamber (see figure 7.2). The oscillation at its eigen frequency of approximately 30 Hz parallel to the beam plane is triggered by an attuned electric oscillator. Consequently, the carbon pin crosses the ion beams with different masses close to the to be implanted beam. The current created by the ions hitting the pin is converted to a voltage signal and is plotted versus the position giving a one dimensional real-time image of the beam's cross-section, see figure 7.18.

Faraday cup: During an implantation the beam of a stable isotope neighbouring the implanted radio isotope aims at the Faraday cup. The Faraday cup suppresses the loss of secondary electrons produced by ion impact and measures the incident current. This current is a measure for the ion source's ion yield. The Faraday cup can be moved perpendicularly to the beam using a mechanical drive, see figure 7.2

aperture: The separated ion beam passes an aperture restricting the beam diameter to a predefined value. A reduction of the beam contamination at the expense of implantation efficacy is achieved. Depending on the diameter the aperture may block both, a part of the desired beam and contributions from neighbouring beams overlapping with the desired ion beam.

deflection capacitors: The deflection capacitors are mounted behind the aperture and are used without retarding lens and in conjunction with the Isotope mass Separator On-Line DEvice (ISOLDE) retarding lens. By applying a constant voltage to the x-y deflection capacitors, the ion beam can be aimed at a target mounted on the sextuple collector or in the ISOLDE retarding lens. By superimposing a triangular alternating voltage in horizontal (period of 3.6 ms) and vertical direction (period of 15 ms), the beam can be swept over the sample,

increasing the beam spot size if necessary. The amplitude can be varied in in both directions and is usually referenced in scale divisions. Per scale division 1.7 V are applied to one plate while −1.7 V is applied to the opposite plate.

retarding lens set-ups: Within the usual parameters the mass separator is operated at ion source potentials of down to 30 kV, in extreme cases 15 kV. If a further reduction of the implantation energy is necessary, either the BONIS or the ISOLDE retarding lens system is used. Both are tested with ^{83}Rb for implantation energies down to 4 kV. The BONIS retarding lens system is tuned towards small beam spots and replaces the deflection capacitors in the collector chamber while the ISOLDE retarding lens is mounted behind these capacitors. Both systems include a real time activity measurement set-up. Further details on both retarding lenses and the detector system can be found in sections 7.4.1 to 7.4.3.

beam stopper: In cases of problems, e.g. a sudden drop in mass resolution due to a electric discharge in the ion source, the beam stopper can be used to prevent the beam from hitting the sample mounted at one of the sextuple collectors.

sextuple collectors: When the mass separator is operated without either of the retarding lens systems, up to five targets can be mounted on either of two sextuple collectors. Both can be rotated, either one of the targets or a KBr screen used to monitor the beam spot size, is hit by the ion beam. The first collector is on ground potential, the second one on an negative potential of up to −80 kV making implantations with energies of up to 160 keV possible. On both collectors all five samples can be implanted successively without breaking the vacuum.

NaI scintillation detectors: These detectors are used to monitor the implanted activity during the course of the implantation. Apart from the total implanted activity the implanted activity per time can be measured. The former information is needed to stop the implantation as soon as a sufficient amount of activity is implanted, the latter is important to keep track of the ion source's ion yield.

7.2. The ^{83}Rb implantation process

Before some of the mass separator's parts are discussed in more detail in sections 7.3 and 7.4, the implantation process from the production of the ^{83}Rb activity to the delivery of the implanted sample is reviewed quickly.

After the production of the ^{83}Rb activity at the Helmholtz-Institut für Strahlen- und Kernphysik (HISKP) in Bonn or at the Nuclear Physics Institute (NPI) in Řež (see section 4.6), it is deposited in the so-called furnace, see section 7.3. Before the implantation, approximately 0.5 mg of $^{\text{nat.}}$Rb in form of RbCl is inserted into the furnace as a carrier. This W tube is mounted in the ion source which is inserted in the source region of the mass separator, see figure 7.1.
Depending on the requirements of the experiment, one of the retarding lenses described in

section 7.4 allowing for implantation energies ranging from 4 keV to 12.5 keV with different beam spot sizes can be mounted in the collector chamber. If one of these lenses is used, a single sample is mounted on it.
For implantations with energies above 30 keV and up to 160 keV one of the sextuple collectors is used. Up to five samples can be mounted on the sextuple collectors.
Prior to the implantation the detector measuring the implanted activity on the used implantation site is recalibrated using a ^{83}Rb sample of known activity. The radioactive background changes after every implantation due to residual activity remaining in the set-up. It is remeasured before the implantations begin and after each sample's implantation is finished.

At the beginning of the implantation run the ion source is heated up slowly. The heating current of the front cathode (see figure 7.3) is increased in 10 A steps and then kept at each value for 10 min until a current of 40 A is reached. In contrast to the other steps, the 20 A current is kept for a longer time. Usually, the pressure in the ion source increases drastically when residual gas is desorbing from the cathode and other components of the source. This bake-out phase lasts 30 min.

After heating up, the cathode current is increased to 45 A and the electron impact voltage is turned on. It accelerates the electrons emitted by the cathode by glow discharge towards the furnace, increasing the ion source's temperature drastically by electron impact. The ion source is ready for the implantation.

During the implantation, the ion source's temperature is monitored using the thermocouples mounted in the ion source itself. The beam width, its position and the current of the stable carrier are surveilled using the Faraday cup and the oscillating probe, both situated in the collector chamber. The implanted activity and the activity increase per time can be measured using the detectors mounted on every implantation site.

When the implantation is finished, the implanted sample is removed from the target holder and its activity is measured using a High Purity Ge (HPGe) detector.

If the sample is used in the Monitor Spectrometer (MoS) of the KArlsruhe TRItium Neutrino (KATRIN) experiment, the sample is dispatched to the NPI in Řež, where ^{83m}Kr retention and radiographic measurements are carried out (see section 6.4 and section 7.5, respectively). Subsequently, the sample is delivered to the Karlsruhe Institute of Technology (KIT) campus where it is mounted in the MoS for measurement.

7.3. The positive surface ionisation source

The ion source used for ion implantations of ^{83}Rb is of the positive surface ionisation type. This type is specially suited for elements with a low first ionisation potential of $\leq$ 7 V [JohBol73], like Rb. A detailed sketch of the ion source can be found in figure 7.3.

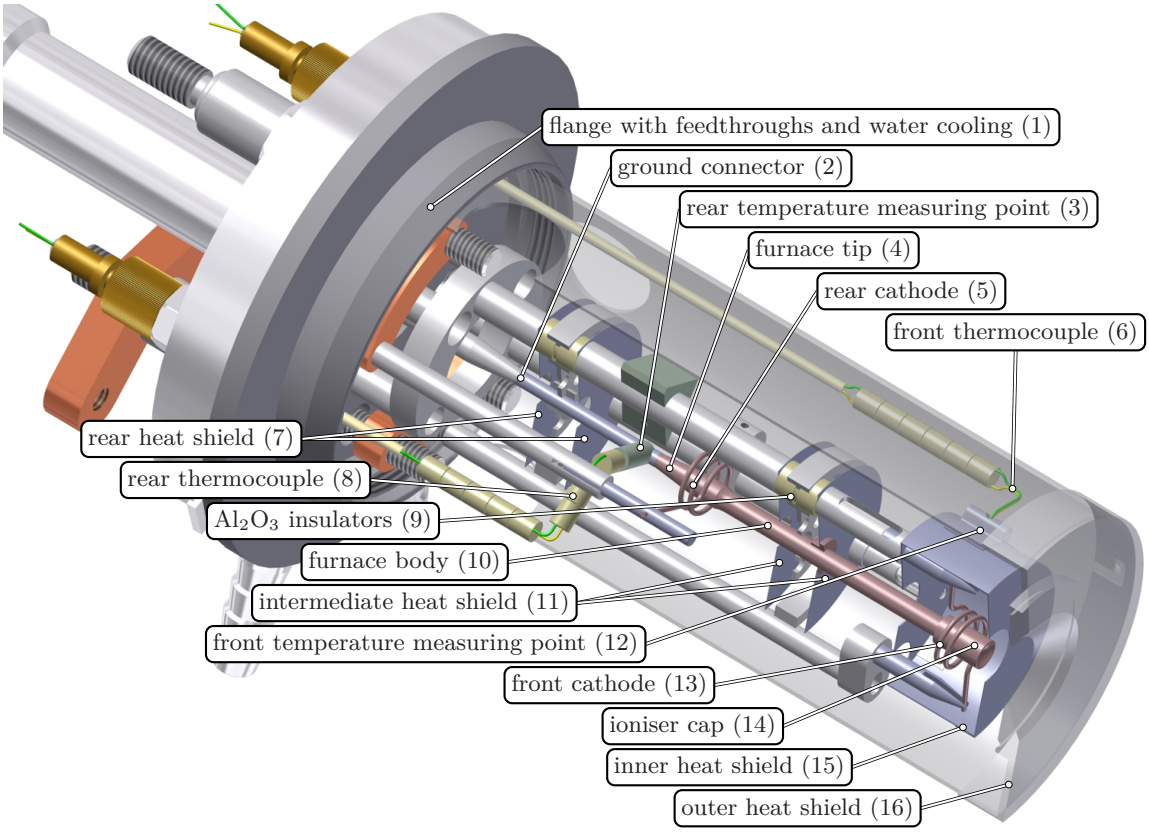

Figure 7.3.: A cross section of the positive surface ionisation source used to implant ^{83}Rb at the BONIS facility. The materials used are colour coded: W = red, Ta = blue, Al_2O_3 = yellow, boron nitride = green and stainless steel = grey. The thermocouples are shown in bright yellow and green. Image updated and based on works by Kotz [Kotz12]. Constructed using Autodesk Inventor 2015 for educational purposes.

Its core component is a hollow cylindrical anode which is used as ionisation surface, evaporation chamber and container for the ^{83}Rb to be ionised and the carrier $^{nat.}$Rb. It is closed with a dedicated W cap. These components are called furnace and ioniser cap, respectively, their geometry is described in section 7.3.1 in more detail. Older furnace versions are discussed in section 7.3.3.
The furnace is surrounded by two coil-shaped W electrodes (item 5 and 13), the front and rear cathode, emitting electrons by thermal emission. These are accelerated towards the furnace and heat the ioniser cap and furnace by electron impact.
The temperature of a Ta heat shield, the so-called inner heat shield surrounding the ioniser cap, can be measured with a Pt/PtRh thermocouple touching the heat shield from the outside, see figure 7.3, item 6. Although a direct measurement of the ioniser cap's temperature is not possible because of the high temperatures, the indirect temperature measurement still provides indispensable information on the operating temperature of the ion source. During ^{83}Rb implantations, temperatures in the range of 1100 K to 1400 K are usually measured. A second thermocouple of the same type is placed directly below the

furnace, shown in figure 7.3 as item 3. It is enclosed in an isolating boron nitride shell, directly contacting the ground connector in which the rear part of the furnace is inserted in (item 8). As long as the rear heating electrode is not used, temperatures in the range of 770 °C to 820 °C are common. If the rear part of the furnace is heated, temperatures measured by this thermocouple can reach 870 °C to 1070 °C. Aside from the inner heat shield, an intermediate Ta heat shield is installed between both cathodes to prevent heating of the rear furnace part by radiation emitted by the front furnace part.
The whole ion source is surrounded by an outer heat shield and is mounted on a water cooled flange.

After an implantation, the ion source is contaminated with ^{83}Rb. To avoid unnecessary irradiation of personnel, the ion source is stored for at least two half lifes (i.e. 172 d) before it is refurbished for the next implantation. This, however, restricts the implantation frequency to two implantations per year. This is sufficient for the KATRIN experiment but makes test implantations in between difficult.
Until September 2016, only one of these sources was available. Within the course of this work, a second ion source is build up. In this way, more frequent implantations are possible and the sources can be refurbished with less irradiation of personnel.
Furthermore, in case of a failure of the ion source during an implantation, the defective ion source can be replaced by a refurbished one. Repairing an ion source after a partial implantation is to be avoided at all costs, the source is highly contaminated and there is no time to let the activity die off.

7.3.1. The furnace design

The furnace is the ion source's core component. It is container for the projectile material, evaporation chamber and ioniser at the same time and is mounted in the ion source (figure 7.3, item 10). It is manufactured from a 99.95 % pure, polycrystalline W welding electrode. A sketch of all the furnace's components can be found in figure 7.4. To increase the mechanical stability, the outer tube diameter is increased at the rear end. A plug closing the tube and fitting into the ground connector (see figure 7.3, item 2) is pressed into the thicker end of the tube. The plug is then welded onto the tube. This welding can just be accomplished if the tube is manufactured from a welding electrode. Any attempts to weld tubes produced from other 99.95 % pure W failed so far.
The other side of the tube is closed with a tight-fitting cap with a 0.5 mm hole to release the beam of ionised Rb. The cap's shape is optimised to make possible a maximum extraction of ions via the extraction lens of the mass separator.

It is known from literature [DatTay56; Hillec68] that the ionisation efficacy of ^{83}Rb on W exceeds 90 % for temperatures around 1200 K. For higher temperatures it decreases as described by the Saha-Langmuir equation [Hillec68]. For ion sources with furnaces comparable to the one described in this chapter (e.g. [JohBol73]), however, the ionisation efficacy can be much higher than suggested by this equation and reach values close to 100 % [LatRai75]. These sources are typically operated at temperatures around 3000 K. The increased ion yield is caused by the fields and space charges created by the ions and

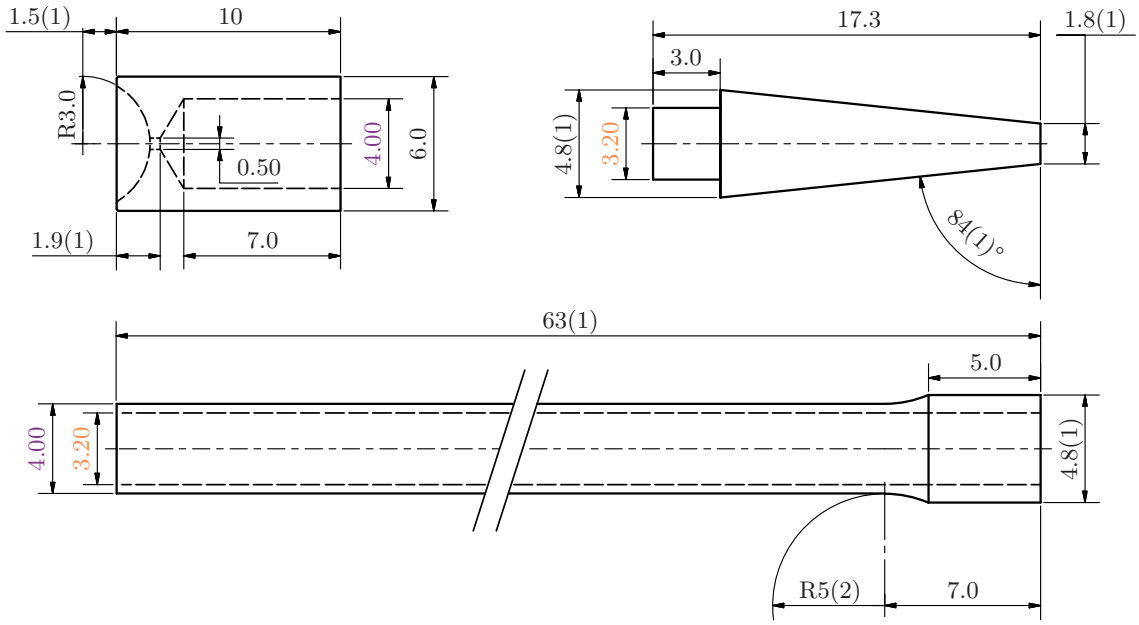

Figure 7.4.: A sketch of the furnace components. All of them are manufactured from 99.95 % pure, polycrystalline W. The tube is produced from a welding electrode. All dimensions are given in mm, tolerances are ±5 of the last digit if not stated otherwise. Parts with the coloured dimensioning have to be matched to fit tightly.

electrons emitted by thermal emission inside the furnace leading to a higher extraction probability for ionised atoms. This destroys the equilibrium conditions assumed for the derivation of the Saha-Langmuir equation [LatZub74].
At temperatures around 3000 K the ionisation efficacy becomes independent of the ioniser material, but instead depends on the extracted ion current which can be controlled with the opening diameter of the furnace and the ioniser temperature. Oxidation of the ionisation surface can be neglected [LatRai75].

The positive surface ionisation ion source of the BONIS facility is usually operated with a vapour pressure of 1 mbar in the furnace. For the compounds RbBr and RbCl, a pressure of 1 mmHg ≈ 1.3 mbar is reached at a temperature of 1054 K and 1065 K, respectively [Stull47]. It is thus desirable to maintain 3000 K at the ioniser cap while being able to control the lower part's temperature independently in the region of 1050 K.
Hence, the furnace is designed to allow for a maximal difference in temperatures between its bottom and the ioniser cap within the spacial constraints of the ion source. Firstly, the furnace is as long as the ion source's mechanical dimensions allow. In this way the thermal resistance and the surface for heat dissipation is increased. Secondly, the tube's wall thickness is reduced to 0.4 mm to increase the thermal resistance even further. To realise these thin walls, the tube has to be manufactured via CNC Electrical Discharge Machining (EDM).

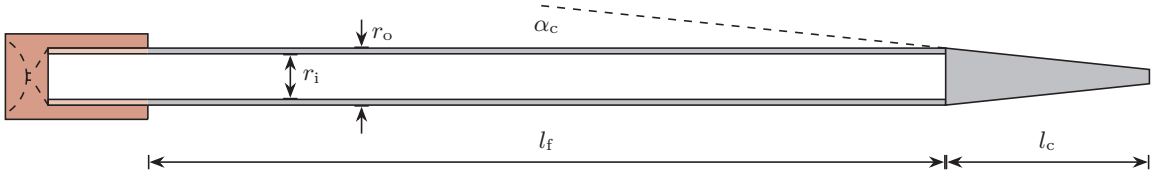

Figure 7.5.: The furnace geometry as assumed for the simulation of the temperature distribution to scale. The red parts are not included, here a constant temperature T_1 is assumed. All parameters given in this sketch can be varied freely in the program.

7.3.2. Simulation of the temperature distribution of the furnace

During an implantation using the positive surface ionisation source, it is not possible to measure the temperature of the ioniser cap or any other point of the furnace. The thermocouples placed in the ion source are not in direct contact with the furnace or the ioniser cap, see figure 7.3, and there is no window to use pyrometry during the implantation. To gain a better understanding of the temperature distribution on the furnace during operation, a program to simulate the heat transfer through the furnace is written. In the present work this program is reviewed, a thorough description including the source code can be found in [Schäbe12].

To facilitate the simulation, the geometry of the furnace is slightly simplified. The ionising cap is assumed to have a constant temperature T_1, keeping the end of the tube not covered by the cap at this temperature. Hence, the cap does not play a role in the simulation and is thus not included. The furnace itself is assumed to be a tube of length l_f with constant outer and inner radius r_o and r_i. At the lower end, a solid truncated cone with length l_c and a chamfer angle of α_c is appended. A sketch of the furnace geometry assumed for the simulation is shown in figure 7.5.

In the simulation, the tube and the cone are treated separately but in an analogue manner. The following discussion, illustrated in figure 7.6, is thus limited to the furnace's tubular part. The tube (and the resulting parts) are bisected n times, creating 2^n tube segments. A temperature is assigned to each of the two cross sectional surfaces of the ith ($i \in [1, 2^n]$) element: T_i is assigned to the surface closer to the heated end, to the other T_{i+1}. Apart from T_1, which is fixed at a predefined value, the choice of these start values is arbitrary. Using these temperatures, starting from $i = 1$, all T_i are calculated using the heat flux equation

$$\underbrace{\varepsilon\sigma A_s(T_i - T_b)^4}_{\Phi_{rad}^{out}} = \underbrace{\lambda(T_i)\frac{A_c}{l_f/2^n}(T_{i-1} - T_i)}_{\Phi_{con}^{in}} - \underbrace{\lambda(T_i)\frac{A_c}{l_f/2^n}(T_i - T_{i+1})}_{\Phi_{con}^{out}} \tag{7.1}$$

with the contributions Φ_{con} from thermal conductivity and Φ_{rad} from radiation obeying the Stefan-Boltzmann law. The cross sectional and skin areas are denoted A_c and A_s, respectively, $\lambda(T)$ is the temperature dependent thermal conductivity, σ the Stefan-Boltzmann constant, ε the emissivity and T_b the background temperature.

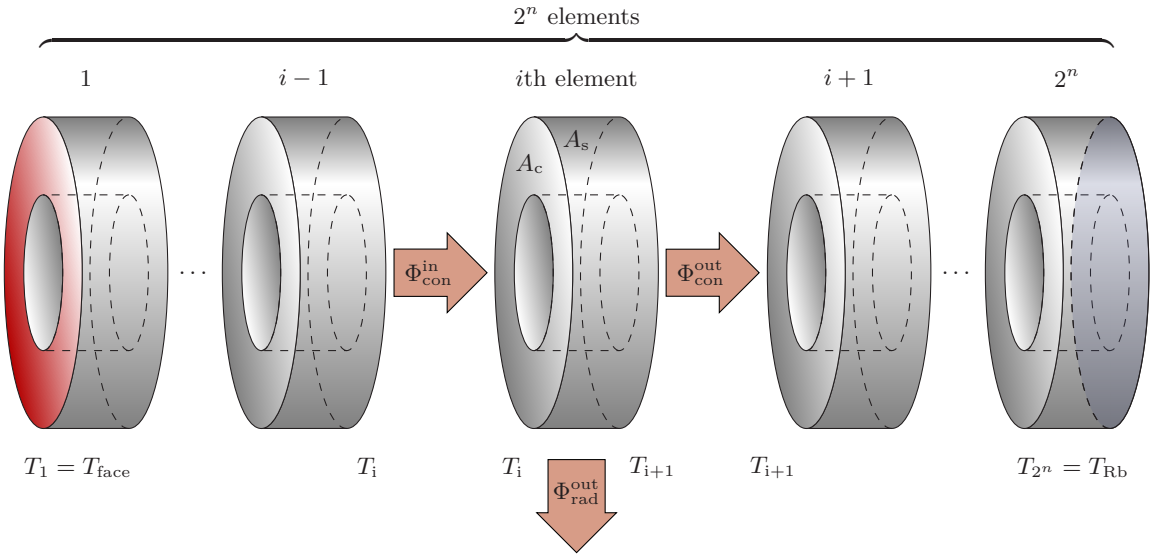

Figure 7.6.: A sketch of the working principle of the program simulating the temperature distribution on the ion source's W furnace. Bisecting the furnace (and the resulting elements) n times yields 2^n slices. The temperature on the left face of the ith element is T_i, T_{i+1} is the temperature of the right face. Fixing T_1 (marked in red), heat transport due to conduction in the elements with cross sectional area A_c is considered. Radiation losses from the outer skin surface A_s are included in the simulation for all elements as well. Heat transport by radiation inside the bore and heat conduction into the ground electrode touching the lower part of the furnace, however are not considered. The temperature T_{2^n} on the right face of the last element (marked in blue) can be identified with the temperature where the ^{83}Rb activity is deposited. The truncated cone is appended after the 2^nth slice and adds further 2^n elements which are evaluated using the same principle.

The truncated cone is divided in 2^n segments and is appended after the 2^nth tube element resulting in a total of $2 \cdot 2^n$ elements for the whole furnace.

The total emissivity of W depends on many factors including temperature, composition, state of the surface, fabrication technique and previous thermal treatment. During the production process the furnaces are exposed to an unknown liquid dielectric during the EDM. When welding the tip onto the W tube, the material is heated to an unspecified temperature. The surface is not monitored and its quality may hence change from furnace to furnace.
The emissivity values obtained in the literature are measured using cleaned or electropolished samples with well-defined properties and can thus only be considered to be approximations for the W used for the production of the furnaces. Because direct emissivity measurements are not possible in this work, literature values taken from Verret et al. [VerRam78] are used to approximate the emissivity.

Except for the geometrical simplifications equation (7.1) is based on and the estimation of

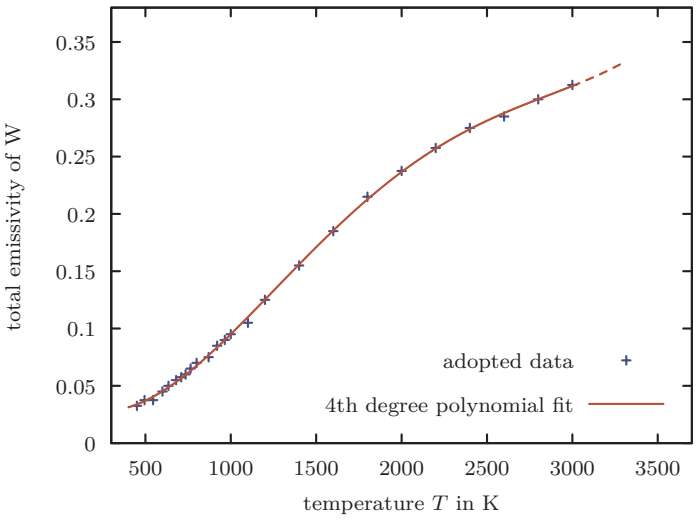

Figure 7.7.: The total emissivity of W as a function of temperature. The data are adopted from Verret et al. [VerRam78], no uncertainties are given. The polynomial interpolation is needed for the simulation of the temperature distribution on the furnace, see section 7.3.2. The extrapolation for $T > 3000\,\mathrm{K}$ might not be accurate.

the emissivity, some further assumptions are made:

- For the simulation the furnace is assumed to be situated in an ideal vacuum without contact to any other objects. In practice, the furnace is contacted by the ground connector (see figure 7.3, item 2). This connector is in contact with the ground electrode outside the ion source at ambient pressure and room temperature. The resulting additional thermal flux is not considered in the simulation and makes the simulation overestimate the temperature of all furnace segments.

- The inner surface of the furnace is assumed to be in a radiation equilibrium. Energy transport by radiation in the cylinder is neglected.

- Although a background temperature is included in the simulation, it is assumed to be the same for all furnace segments. In practice, the heat shields create three regions of different background temperatures.

- From equation (7.1) it is obvious that T_i is calculated using T_{i-1} and T_{i+1}. Consequently, determining T_i changes the preconditions used to calculate T_{i-1}. Hence, this algorithm has to be repeated for all T_i until the changes from iteration step to iteration step are negligible.

- The heat dissipation due to radiation for the ith element in equation (7.1) depends only on the temperature T_i and ignores the possible temperature gradient on the element. This approach can only generate correct results if the elements are sufficiently small. In practice $n = 8$ is sufficient to exclude an influence of this approximation.

For the simulation, all radii, lengths and angles are given by the mechanical dimension of the furnace. The ioniser cap's temperature is estimated to be as high as 3300 K. During tests with different ioniser caps, a Ta cap with melting point 3269 K [MalLan39] was partially molten.

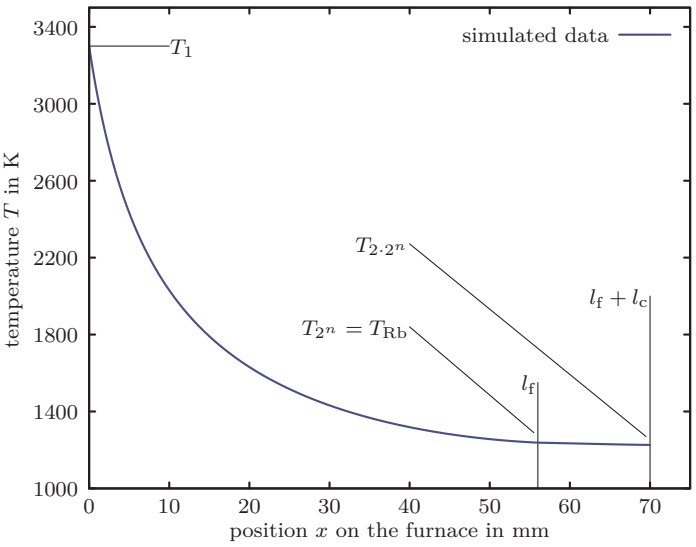

Figure 7.8.: The results of the simulation of the temperature distribution on the furnace. In this simulation the temperature at the ^{83}Rb deposition site is 1238 K. All parameters assumed for this simulations are summarised in table 7.2.

In the original version of the simulation [Schäbe12] the emissivity was assumed to be constant for the whole furnace. However, the simulation is updated by Schäbe [Schäbe16] to include a temperature dependent emissivity based on data by Verret et al. [VerRam78]. The given data are interpolated using a 4th degree polynomial, see figure 7.7. For the temperature range from 3000 K to the assumed ioniser cap temperature of 3300 K, no data are available. In this range, the same polynomial is used to extrapolate the emissivity values, shown as dashed line in figure 7.7. No physical model is supporting the extrapolation, the emissivity values used may thus be inaccurate.

The background temperature is chosen to be 800 K, based on the temperature readings of the lower thermocouple (see figure 7.3, item 8) during ^{83}Rb implantations. This thermocouple indicates temperatures between 773 K and 823 K for the ground electrode directly below and in contact with the furnace. Of course, this choice will underestimate the background temperature inside the inner heat shield and before the intermediate heat shield (items 15 and 11 in figure 7.3, respectively). However, the effect of the background temperature is small unless it is close to the furnace temperature which is only the case for the rear part of the furnace. In this region, the background temperature influences the slope of the temperature curve and thus the temperature of the ^{83}Rb deposition site.

The chosen parameters as well as the resulting temperature at the end of the cone and at the Rb site are summarised in table 7.2, the temperature distribution is shown in figure 7.8. The simulation gives a temperature of 1238 K at the Rb deposition site. This is roughly 180 K more than desired. However, this result can only be considered as an indicator for the general temperature range for the temperatures at the lower part of the furnace, especially because the contact with the ground electrode is neglected.
From the simulation it is concluded that the furnace is operating in an acceptable temperature range for ^{83}Rb implantations. This is supported by the increase in implantation efficacy achieved, see section 7.7.

parameter	abbrev.	value
furnace length	l_f	56 mm
cone length	l_c	14 mm
outer radius	r_o	2 mm
inner radius	r_i	1.6 mm
chamfer angle	α_c	6°
bisections	n	10
start temperature	T_1	3300 K
background temperature	T_b	800 K
Rb temperature	T_Rb	1238 K
cone end temperature	$T_{2\cdot 2^n}$	1226 K

Table 7.2.: The geometrical and temperature parameters used for the simulation of the temperature distribution of the furnace (top) as well as its results (bottom). T_Rb is the temperature at the Rb deposition site and is relevant for the vapour pressure. The temperature distribution is shown in figure 7.8.

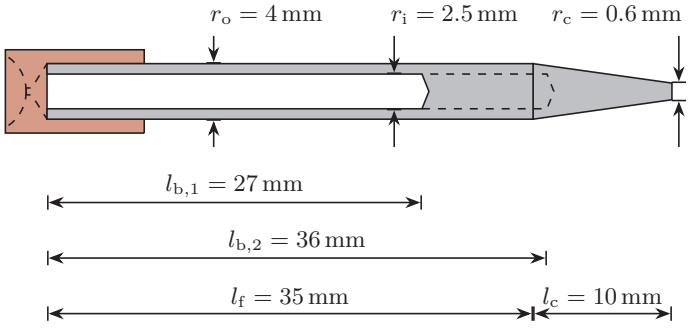

Figure 7.9.: The furnace designs used prior to and in the beginning of this work. They had 0.75 mm wall thickness and a bore depths of 27 mm and 36 mm, respectively.

7.3.3. Earlier furnace versions

The furnace discussed in this work up to now is the latest version currently in use. However, over the course of this work, the furnace design was subject to some changes.
The original furnace was manufactured from one piece in the workshop of the HISKP. The part was produced by lathing and drilling with a total length of 45 mm, an outer diameter of 4 mm and an inner diameter of the bore of 2.5 mm with a depth of 27 mm. The following furnace versions keep the outer dimension and the bore diameter but gradually increase the bore depth to 36 mm. From the beginning of this work, this furnace design was used until end of the year 2011. A sketch of this furnace design can be found in figure 7.9.

The simulation described in section 7.3.2 is used to study the temperature distribution on the furnaces manufactured according to the old design. The simulation results are shown in figure 7.10. Obviously, the thermal decoupling of the ioniser cap and the Rb deposition site is not sufficient to operate the former at temperatures above 3000 K while keeping temperatures at the latter close to 1050 K where the vapour pressure of RbCl is in the range of 1.3 mbar.
Operating the cap at temperatures around 1400 K keeps the temperature at the Rb deposit close to values achieved using the new furnace design. However, the advantages for the ion yield gained from a high operation temperature are lost.

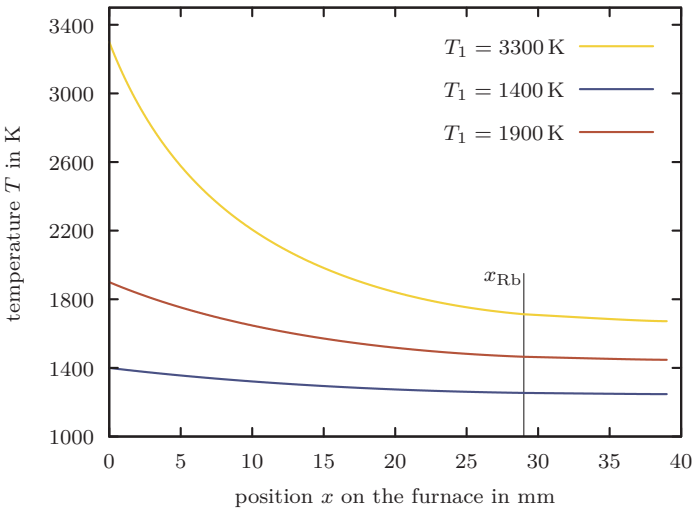

Figure 7.10.: Simulations of the temperature distribution on an old furnace with 36 mm bore depth and 0.75 mm wall thickness (figure 7.9) with 800 K background temperature. Compared to the present design, cap temperatures of 3300 K lead to 1800 K at the Rb deposition site; to achieve comparable temperatures there, the cap temperature has to be kept at 1400 K.

Also, the strong coupling between both temperature zones makes fine tuning of the temperatures during the implantation difficult.

To reduce the temperature coupling and increase the implantation efficacy, a bigger bore diameter while retaining the outer diameter as well as an increase in bore depth is necessary. Due to the hardness and brittleness of W, these design changes can not be realised with lathing and drilling in the workshop of the HISKP any more. Even with specialised drills and new tools for each furnace production, either the drill breaks or the workpiece cracks. The method of EDM allows for a significant increase in the bore diameter because the workpiece is not subject to mechanical strain during the manufacturing process. The bore diameter is increased to 3.2 mm, reducing the wall thickness to just 0.4 mm. However, the 63 mm deep blind hole planned for this furnace poses a problem for the production. A small misalignment of the eroding wire will cause a hole close to the tip of the furnace. Two of these furnaces are produced by an external company in 2011 and are used from the end of the year 2011 to autumn 2012.

Since autumn 2012 the version described in section 7.3.1 is in use. Its main advantage in comparison to the previously described design is the reduced price. The tube costs just one sixth of the furnace fully manufactured by EDM. The manufacturing of the tip, which has to be inserted into the tube, the assembly and the welding is done in the workshop of the HISKP.

7.4. Retarding lenses

In regular operation mode, the implantation energy at the BONIS facility is defined by the voltage applied to the ion source while the target and the rest of the mass separator set-up is on ground potential. However, the ion source can be operated at voltages ranging from 30 kV to 80 kV only. In extreme situations this range can be be extended to 15 kV at the

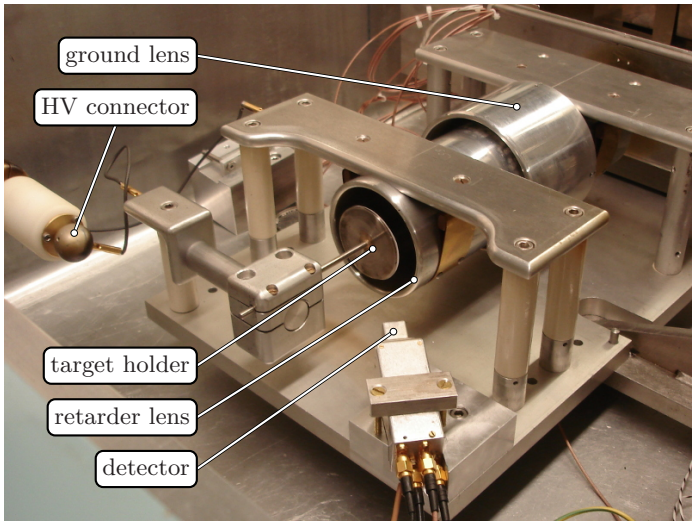

Figure 7.11.: The BONIS retarding lens mounted in the collector chamber with all important parts highlighted.

expense of ion yield. If implantation energies below 30 keV are desired, usually it is the best choice to use one of the two retarding lenses described in this section.

7.4.1. The BONIS retarding lens

The BONIS retarding lens is described by Freitag et al. [FreHei76] and is routinely used for implantations with energies in the range of 4 keV to 12.5 keV. It is possible, however, to implant at much lower energies of down to 100 eV [FreHei76].

The retarding lens system is inserted in the collector chamber, just behind the oscillating probe and the aperture, replacing the deflection capacitors, see figure 7.1. Without deflection capacitors there is no way to influence the beam spot position on the target and no means to increase the beam spot diameter by sweeping the beam.

The lens system consists of a cylindrical ground electrode, followed by the also cylindrical retarding electrode, see figure 7.11. The ground electrode creates well-defined field lines before the ions enter the retarding lens. The latter is on the same potential as the ion source, thus retarding the ion beam to virtually 0 keV. The target is mounted on a target holder with conducting scotch tape and is inserted into the retarding lens. A voltage of up to 12.5 kV relative to the retarding potential is applied to the target holder. The limit is created by the voltage supply and the insulators, in principle higher voltages are possible. This additional potential defines the implantation energy, it re-accelerates the decelerated ions according to the applied voltage.
The detector described in section 7.4.3 has been added to the ion source's mounting plate, see figure 7.11. Hence, the activity implanted using the BONIS retarding lens can be measured in real-time.

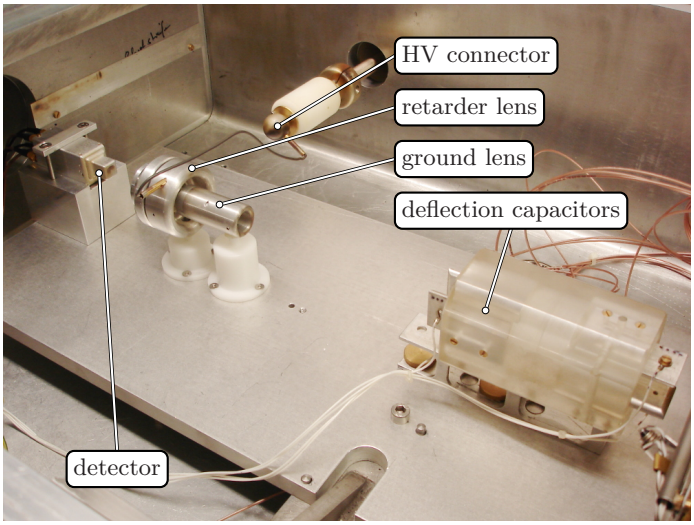

Figure 7.12.: The ISOLDE retarding lens mounted in the collector chamber with all important parts highlighted. The ground connector cable attached to the ground lens is missing on this picture.

7.4.2. The ISOLDE retarding lens

Unlike for Perturbed Angular Correlation (PAC) measurements, where small beam spots are advantageous, large beam spot areas can increase the implanted source's performance for the use in the MoS, see section 6.6. The ISOLDE retarding lens allows to control the beam spot size and reduce the implantation energy at the expense of implantation efficacy.

The Isotope mass Separator On-Line DEvice (ISOLDE) retarding lens was used for ion implantations at the ISOLDE facility, CERN by Zbořil [Zbořil11] and Slezák [Slezák15a]. It was operated at 15 keV implantation energy. Recently, this retarding lens has been brought to Bonn and is integrated into the BONIS set-up, see figure 7.12.

Similar to the BONIS lens, the beam enters a cylindrical ground electrode creating a defined potential around the beam and in front of the target. However, unlike the BONIS lens, the beam is not decelerated and then re-accelerated again. The ion source's voltage minus a defined acceleration voltage is applied directly to the retarding lens accommodating the target holder including the target at the same potential.

The small mechanical dimensions of the ISOLDE retarding lens set-up make an integration into the collector chamber of the BONIS facility feasible. To include the lens system alongside the x-y deflection capacitors, a new mounting plate with insulating posts for the retarding lens and mounting spots for the x-y deflection capacitors is manufactured. Thus, in contrast to the BONIS retarding lens, the x-y deflection capacitors are still available to influence the beam spot position and influence the beam spot size.
Due to the small mechanical dimensions, the ISOLDE lens is more prone to electrical discharges. Especially, because the lens consists of more parts between which residual gas may cause local pressure peaks increasing the risk even more. The lens has to be operated in pressures below 1×10^{-5} mbar to keep the discharge probability low.
For the implantation of one sample, this does not pose a problem. However, as soon as two

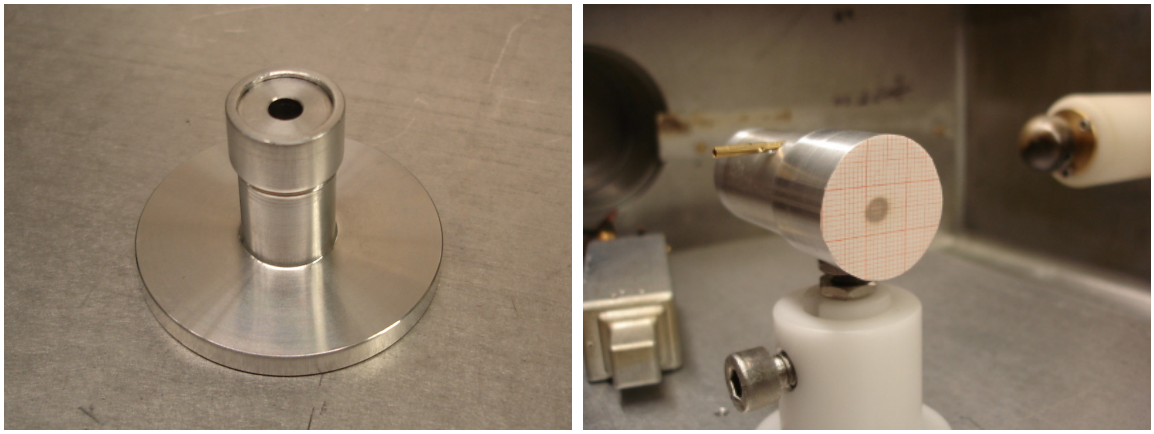

Figure 7.13.: Left side: The target holder manufactured for the use with the ISOLDE lens and the detector described in section 7.4.3. The hollow cylinder reduces absorption, the wide base facilitates mounting the samples. During the implantation, the target holder is inserted into the retarding lens from behind, the target pointing towards the ground lens.
Right side: The beam spot on the paper target mounted on the ground lens visualises the entry point of the beam in the lens. The small deviation from the centre can be compensated using the deflection capacitors.

or more samples are to be implanted, the collector chamber has to be opened to exchange the samples. During this time and the time until the pressure drops to 1×10^{-5} mbar again, the ion source is not cooled down to avoid additional thermal strain and the ions leaving the source during this time are wasted.

To provide real-time and in-situ activity measurements, the detector described in section 7.4.3 is mounted on a post behind the ISOLDE retarding lens on the beam axis. The 520 keV, 529 keV and 553 keV γ radiation used to measure the implanted activity during ^{83}Rb implantations needs to pass through the sample and the sample holder. To reduce absorption, the original target holder is replaced by a tube-shaped Al holder with a 0.5 mm thin mounting surface, see figure 7.13 on the left side.

To verify the correct alignment of the lens system, test beams of stable isotopes and paper targets are used. To save the positive surface ionisation source optimised for Rb implantations for the following ^{83}Rb implantation, a beam of stable and singly ionised Er ions is produced using another source of the positive surface ionisation type.
The ions should enter the lens system on the axis of the cylindrical ground electrode. To visualise the entry point, the ground electrode is covered with an Al cap with an attached paper target. In the tests, the beam hits the ground electrode slightly off-centre, see figure 7.13 on the right side. This deviation can, however, be compensated using the deflection capacitors.

Once the alignment of the ground lens is completed, the cap covering the ground lens is removed. Now the beam spot position on the target holder inserted into the retarding

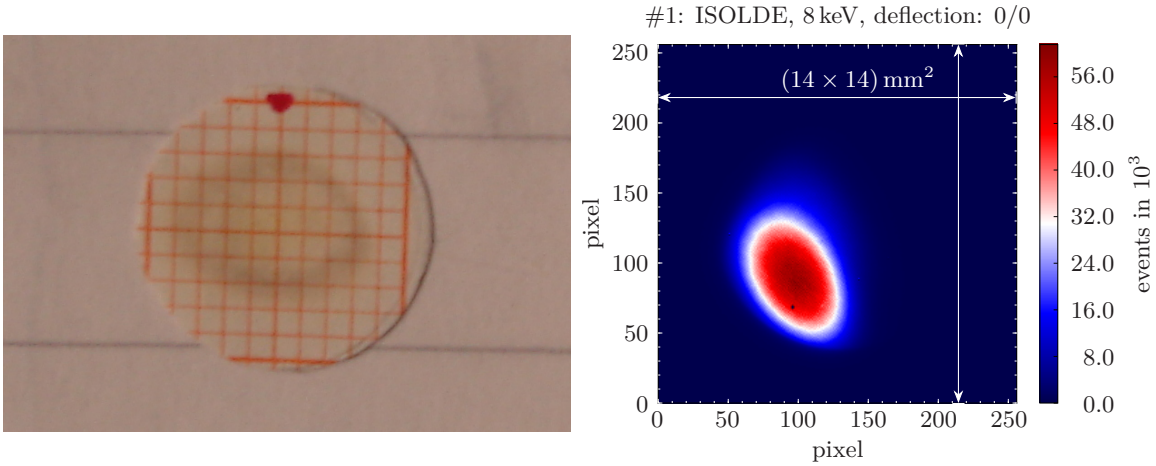

Figure 7.14.: Beam spots produced during the test irradiations using the ISOLDE retarding lens. On the left side a paper target implanted with stable Er at 8 keV without alternating voltage applied to the deflection capacitors is shown. On the right side, a beam spot measurement of a ^{83}Rb implantation with the same parameters is depicted. The radiographic image is obtained as described in section 6.1. Both images are magnified but true to scale. Obviously, the right beam spot is smaller and does not exhibit the ring-like structure visible on the paper target. The right picture is taken from Slezák [Slezák15b].

lens from behind is checked. The target holder is shown in figure 7.13 on the left side, the position of the retarding lens in figure 7.12. For the first experiments, paper targets are used again. They are mounted on the target holder like a regular target. A beam spot produced with 8 keV implantation energy and without applying an alternating field to the deflection capacitors is shown in figure 7.14 on the left side. The beam hits the target with a slight deviation from the centre and shows an elliptical shape caused by edge focussing. Deviations of 1 mm to 2 mm of beam centre and target centre are usually encountered in samples implanted at the BONIS facility. The test implantations are continued with ^{83}Rb. These samples are examined using radiography as described in section 6.1. A paper target implanted with stable Er at 8 keV and the radiographic image of an Al target implanted with ^{83}Rb at 8 keV are shown for direct comparison in figure 7.14.

Despite the correct alignment of the lens, the probability for the beam spot not being centred or activity being implanted into the lens is much higher for the ISOLDE lens than on the sextuple collector and with the BONIS retarding lens. The beam spot position on the former can be monitored using a KBr screen, the focussing properties of the latter render it nearly impossible not to hit the target.
The ISOLDE lens, however, neither shows these focussing properties, nor is there a way to check the beam spot position optically during an implantation. Prior to any implantation using this retarding lens, it is thus necessary to verify the correct beam spot position using an implantation of stable ^{85}Rb into a paper target. This implantation has to be carried out using the same ion source and furnace used for the following implantation of ^{83}Rb.

An exchange of either the furnace or the ion source is not possible because it creates a misalignment which has to be compensated by this calibration. During the mounting of the paper target, the implantation and the recovering of the vacuum afterwards, taking roughly half an hour, the ^{83}Rb emitted by the ion source is wasted. The use of the ISOLDE lens, thus decreases the implantation efficacy.

7.4.3. Real-time and in-situ activity measurement

Neither the ISOLDE, nor the BONIS retarding lens were equipped with instrumentation to determine the implanted activity in real-time before. In both cases, when producing samples for the KATRIN experiment or for PAC measurements it is crucial to stop the implantation, once the desired activity is implanted. In this work, a detector to work with both lens systems is build up for in-situ and real-time activity measurements.

Both retarding lenses are mounted in the collector chamber. Placing a detector on the outside is not advantageous due to the 20 mm thick Al walls. Furthermore, there is no possibility to place a detector close to the target position outside the collector chamber due to spatial constraints. It is thus necessary to mount a detector in the collector chamber. This, however, imposes some restrictions on the detector itself:

size: The confined space in the collector chamber requires the detector to be as small as possible, especially when using the bigger BONIS retarding lens. Additionally, to avoid electric discharges, a safety distance between detector and retarding lens is necessary.

electric field shielding: The detector has to be well shielded against the influence of electric fields. Both, constant fields created by the retarding lens as well as alternating fields produced by the deflection capacitors are present in the collector chamber.

vacuum compatibility: Regular operation under vacuum conditions is necessary without negative effect on the vacuum due to outgassing.

For the activity measurement in the collector chamber, radiation in the energy range of X-rays of the implanted ions can not be used. The recombinations of the implanted ions as well as of the impact-ionised atoms of the target cause a continuous flux of X-rays not related to the implanted activity. Thus, direct detection of radiation with an APD is no option since the quantum efficacy rapidly drops with increasing γ energy, see figure 8.3. For ^{83}Rb implantations, only the remaining 520 keV, 530 keV and 553 keV γ lines can be used. In this energy range a scintillation crystal can be used and read out by either an APD or a small PhotoMultiplier (PM). In these measurements, only the energy spectrum is recorded. Hence, it is not necessary to use the fast voltage sensitive preamplifier module developed in this work.

A $(20 \times 10 \times 10)\,\mathrm{mm}^3$ LYSO:Ce crystal is chosen as scintillator for this detector system. It features a three times higher light yield than BGO (Bismuth Germanium Oxide) and due to its high effective nuclear charge and density a stopping power almost twice as high as BaF

Figure 7.15.: The components used to build up the real-time and in-situ detector used in the collector chamber of the BONIS facility. From left to right: Hamamatsu's S8664-1010 APD with polished surface, the charge sensitive preamplifier SP883a [Honisc15] and the LYSO:Ce crystal wrapped in PTFE tape and inserted in its Al case. All components are roughly to scale.

(Barium Fluoride) [ValVia10]. Finally, in contrast to NaI (Sodium Iodide), this scintillation crystal type is not hygroscopic and thus easy to handle.
The LYSO:Ce crystal is coupled to and read out by an S8664-1010 APD with an active area of $(10 \times 10)\,\mathrm{mm}^2$ and polished surface. Its photo sensitivity is sufficiently high in the emitting range of LYSO:Ce, see figure 8.7. This APD type is discussed in detail in section 8.2.
A charge sensitive preamplifier (version number SP883a) developed at the university of Basel and utilised in the work of Honisch [Honisc15] is used to read out the APD. This amplifier is tailored to be used in conjunction with APDs of the type S8664-1010 or similar devices. The present version is tuned to be operated without further downstream electronics, save a spectroscopy amplifier. An in-depth discussion of this amplifier, its properties and its circuit diagram can be found in the work by Honisch [Honisc15]. The APD, the preamplifier chip and the LYSO:Ce crystal are shown in figure 7.15.

The scintillation crystal is optically coupled to the APD using silicone oil and wrapped in in white PTFE tape to reduce light losses on the faces not in contact with the detector. Scintillation crystal, APD and preamplifier are mounted in a tightly fitting Al case, providing sufficient shielding from the electric fields in the collector chamber. The case's corners are rounded to reduce the probability of electric discharges. The venting channels of 1 mm diameter connect the cavity of the case and the collector chamber via at least one 90° bend to allow for quick evacuation without weakening the shielding. SubMiniature version A (SMA) jacks on the rear provide reliable, well-shielded and sturdy connection to supply voltage, high voltage and to the spectroscopy amplifier. The fully mounted detection system is depicted in figure 7.16 on the left side.

The preamplifier's signal is further amplified by a standard spectroscopy amplifier and displayed on a Multi Channel Analyzer (MCA), see figure 7.16 on the right side. For ^{83}Rb implantations, the detector is calibrated using a ^{83}Rb sample whose activity is determined using a HPGe detector as described in section 6.7. The calibration is thus only valid for ^{83}Rb activity.

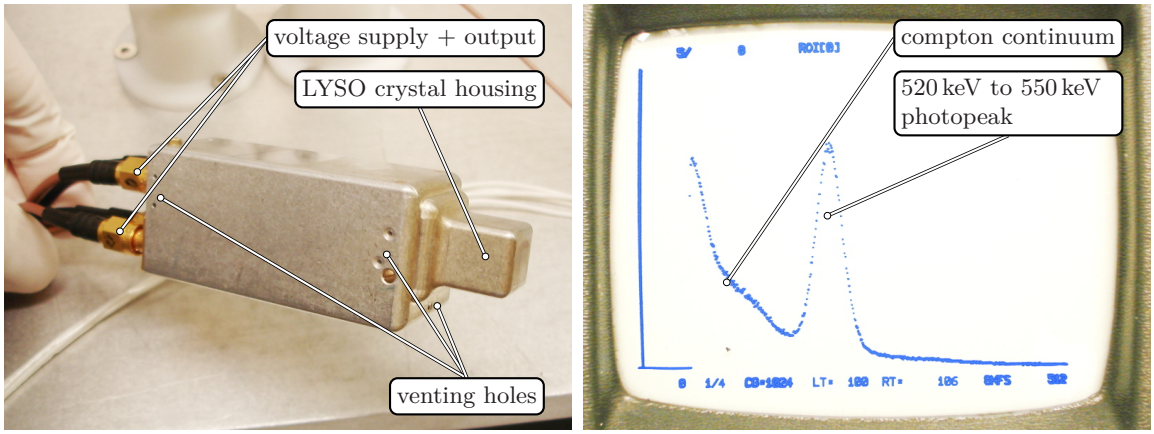

Figure 7.16.: Left side: The fully assembled detector system mounted in the collector chamber when using either of the retarding lenses. The detector is shown mounted in the collector chamber in figures 7.11 and 7.12.
Right side: A ^{83}Rb calibration spectrum recorded with a 512 channel MCA at the BONIS facility. The colors have been edited for better readability. The 520 keV, the 530 keV and 553 keV lines can not be resolved, but are clearly separated from the Compton continuum.

7.5. Beam spot size comparison

Paper targets are well suited to check the alignment of the lenses but they are no reliable means to determine the beam spot size. The spots produced by implantation of stable isotopes in paper targets are bigger than those produced with radioactive isotopes implanted in regular targets. When implanting stable isotopes, the current is usually much higher than for implantations of radioactive isotopes. Consequently the number of positively charged ions deposited in the target, as well as the number of created secondary electrons leaving the target per time unit, is much higher as well. Compared to the regular targets, paper is a non-conductor. A region of space charge may be formed, widening the beam due to Coulomb repulsion when the ions approach the target, especially for low implantation energies. The ring-shaped structure observed with more or less pronunciation in all beam spots from implantations in paper with stable isotopes, see figure 7.14 for an example, supports this hypothesis. It is never seen in one of the beam spots using conducting targets and a ^{83}Rb beam.

A reliable way to determine the beam spot size is a radiography using a Timepix detector as described in section 6.1. In the following, typical beam spot sizes for all three implantation sites are discussed and some example beam spots are shown.

The sextuple collector: In the case when no retarding lens is used and the target is mounted on the sextuple collector, the beam spot size can be changed using the deflection capacitors. The smallest possible beam spot at 30 keV implantation energy is usually of

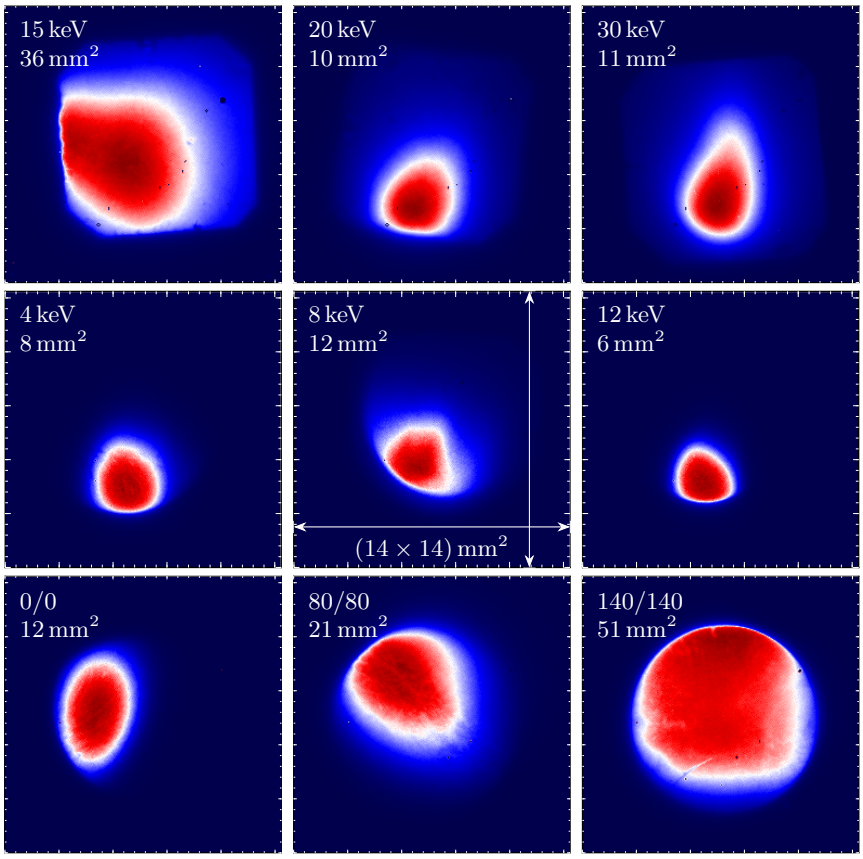

Figure 7.17.: A direct comparison of beam spots, each row implanted in one implantation run at all three commonly used implantation sites with either varying implantation energies or deflection values. For the relation between deflection voltage and scale divisions, see section 7.1.
Top row: Beam spots implanted with different implantation energies on the sextuple collector. Implantation energies of 15 keV and 20 keV are non-standard parameters. The deposition rate in the case of the 15 keV implantation was very low, the beam is very wide. This indicates suboptimal operation of the focal lens system. The implantation with 20 keV was feasible without an increase in beam spot size.
Middle row: Beam spots obtained using the BONIS retarding lens. The beam spot size is nearly independent of the implantation energy. Deflection capacitors are not available to change the beam spot shape. The halo around the 8 keV beam spot is caused by a widened beam due to a nearly depleted ion source.
Bottom row: Implantation results obtained with the ISOLDE retarding lens. Here the implantation energy is fixed, the deflection values are varied. The beam spot size can be controlled without impairing the ion source operation. Activity losses occur if ^{83}Rb is implanted in the lenses.
The colour scale is not shown in these pictures, the relative scale (dark blue: no events, white: half maximum, dark red: maximum) is the same for all pictures. The orientation of the sample is not necessarily the same during implantation and Timepix measurement. The sample is roughly centred on the Timepix chip. The top six pictures are taken from Slezák [Slezák15a; Slezák15b], the others are measured by Sentkerestiová and Vénos [SenVén16].

elliptical shape with an area of approximately 10 mm^2 to 12 mm^2. Example beam spots for different implantation energies, including non-standard implantations energies like 15 keV and 20 keV are shown in the top row in figure 7.17.

The BONIS retarding lens: The BONIS retarding lens is optimised towards an optimal focus of the ion beam and, thus, towards a small beam spot. This is achieved by a precise alignment in the beam, the homogeneous electric fields created by the large lenses and the re-acceleration of the ions towards the target. Typical beam spots produced using the BONIS retarding lens are shown in figure 7.17 in the middle row. Beam spots implanted with this ion lens usually have areas of 8 mm^2 to 6 mm^2 for implantation energies from 4 keV to 12.5 keV.

The ISOLDE retarding lens: With its smaller dimensions, the ISOLDE retarding lens does not provide a focussing comparable to the BONIS lens and produces slightly bigger beam spots without deflection,which are approximately 12 mm^2 in area. It is thus not suited for implantations of PAC sources and other occasions where small beam spots are desired. For set-ups like the MoS of the KATRIN experiment requiring a larger beam spot, however, this property is no disadvantage. The deflection capacitors, which can be mounted alongside the ISOLDE lens, can be used to produce even larger beam spots covering nearly the whole sample of 12 mm in diameter in ^{83}Rb. Beam spot areas of 20 mm^2 to 50 mm^2 are possible with the correct choice of the deflection voltage. Three beam spots, without and with two different deflection capacitor voltages can be found in figure 7.17, all beam spots recorded during the tests of this lens are shown in figures B.3 and B.4.

7.6. Mass resolution and undesirably implanted ions

During implantations at the BONIS facility there are three main reasons for undesirably implanted ions: pre-acceleration voltage breakdowns, beam contamination and beam instabilities. While pre-acceleration voltage breakdowns mostly occur during implantations with high implantation energies or retarding lenses, beam instabilities are commonly encountered during most implantations. The extend of beam contamination, i.e. the admixture of neighbouring isotopes depends on the parameters of the implantation itself.

7.6.1. Pre-acceleration voltage breakdowns

The origin of pre-acceleration voltage breakdowns are electric discharges between ion source and ground potential. These may occur either in the ion source itself or in the retarding lens which is on source potential as well. In general, they occur rarely during ^{83}Rb implantations on the sextuple collector due to the low pre-acceleration voltage of 30 keV. If a retarding lens is employed, the probability of discharges increases, especially for the ISOLDE lens.

This lens consists of more parts possibly trapping gas and the parts on different potential are closer to each other.

If such a pre-acceleration breakdown occurs the ion source potential quickly and continuously drops until it reaches zero and then rises again until it reaches the pre-set value again. During this process ions with kinetic energies between the set value and close to zero can leave the source and will thus be mass-separated by the magnet at a fixed field value. With the prerequisite of equal kinetic energy for the incident particles no longer met, ions with a constant $(U_{\text{source}} \cdot m)/q$ ratio will pass the separation magnet, rather than ions with a constant m/q ratio. Here U_{source} is the ion source potential, m and q the ion's mass and charge, respectively. In case of a beam breakdown all beams consisting of heavier ions leaving the ion source will be swept over the sample for the duration of the voltage drop. The contribution of ions implanted this way is especially relevant if the carrier material used during the implantation has a higher mass than the ion to be implanted. However, this contribution is difficult to estimate because it depends on the unknown ion current in all heavier ion beams and the duration of the breakdown and the voltage recovery which are even more difficult to assess.

7.6.2. Beam instabilities

Beam instabilities is a collective term for variations in beam diameter and beam position. Some of them are common phenomena during implantations requiring readjustment of the mass separator's parameters by the operator. These instabilities can be monitored using the oscillating probe and the current measured with the Faraday cup.
Commonly, beam instabilities are caused by drifts in all voltages and currents applied to e.g. separator magnet, extraction lens, and focal lens system over the course of the implantation. These effects can easily be countered by fine-tuning the respective voltages and currents.
During an implantation of ^{83}Rb the ion source is heated to temperatures around 3000 K. This gives rise to thermal deformation of components mounted close to the furnace, especially if they are not protected by the heat shields. For a sketch of the ion source and its components see figure 7.3. These mechanical effects can cause misalignment of the ion source's components close to the furnace. As these changes occur on time scales of many hours, the operator can adapt the respective parameters of the ion source and the mass separator.
In the case of implantations on consecutive days using the same ion source, each cooling and heating cycle between 3000 K and 270 K puts a lot of strain on the ion source. This may result in strong variations in the ion source's behaviour and increases the probability for failure.

Additionally, the electrons emitted by the heating coils impinging on the furnace remove material by sputtering. The sputtered W atoms condense in the ion source and on the insulators. Together with the aforementioned thermal deformations, the reduced dielectric strength can lead to electric discharges in the electron impact heating system. This causes an immediate change in beam width and position, followed by a decrease in ionisation efficacy. These discharges in the electron impact heating system tend to happen more often

with an ion source being used for many days without refurbishing. They are the most severe beam instabilities, because the operator does not have a chance to avert them or counter their effect by an appropriate change in parameters. The only possible measure is to close the beam stopper as quickly as possible to reduce the amount of undesirably implanted ions. A frequent occurrence of electric discharges in the electron impact heating signalises the need for refurbishing and an imminent failure of the ion source.

It is not possible to calculate or predict the contribution of beam instabilities to the undesirably implanted ions and it may vary from implantation to implantation. However, in measurements of the average beam contamination based on the ^{84}Rb implanted (see section 7.6.3), these effects are included as a systematic error.

7.6.3. Beam contamination of ^{83}Rb beams

The mass resolution of the mass separator depends on the mass of the isotope to be implanted and the pre-acceleration voltage. A high isotope mass and a low pre-acceleration voltage both result in a decrease of mass resolution, the overlap of the beam to be implanted and beams of neighbouring isotopes, e.g. carrier, becomes more pronounced. While for an implantation of ^{254}Es at 160 keV even admixtures of ^{252}Cf are present [SevBel09], for ^{181}Hf at 80 keV only directly neighbouring isotopes were found implanted [Freita77].

For implantations of ^{83}Rb, there are four relevant isotopes possibly contributing to a beam contamination: the two naturally abundant isotopes ^{85}Rb and ^{87}Rb, the carrier material during the implantation and the two radioactive isotopes ^{84}Rb and ^{86}Rb (see figure 4.4) with half lifes of 33.1 d [HuhLiu00] and 18.6 d [MiyGot81], respectively, which are produced alongside ^{83}Rb, see section 4.6. After the irradiation process, the target is left for one week for the short lived isotopes to die off. All lighter Rb isotopes have a half life of less than 6.5 h, decay into Kr isotopes [IAEA17] and evaporate during this time.
Consequently the most relevant radioactive beam contamination is an admixture of ^{84}Rb because it is heavier by one mass number. Averaged over one implantation run, the ^{84}Rb deposition on the sample can be determined directly due to its radioactive nature if it did not decay between the production and the implantation process. The radioactive ^{86}Rb is not relevant as beam contamination due to its short half life, its small cross-section during the production and its high mass in comparison to ^{83}Rb.
In comparison to ^{84}Rb, the probability for a ^{85}Rb ion being implanted is much smaller, but the huge amount of the stable carrier atoms in the source in comparison to the ^{83}Rb atoms makes it relevant for beam contamination. Usually 0.5 mg of $^{\text{nat.}}$Rb containing 72.17 % of ^{85}Rb [IAEA17] are deposited in the furnace. ^{87}Rb does not play a role for beam contamination, the mass separation is effective enough to prevent any implantation of this isotope.

7.6.3.1. Estimation of the ^{85}Rb admixture

Due to its radioactive nature, the admixture of ^{84}Rb can be measured directly. This is not possible for stable ^{85}Rb. However, there is a way to roughly estimate the admixture of ^{85}Rb. Because the following considerations are estimates, no uncertainties are stated. Let $\bar{S}_{84}(E, A = 83)$ be the admixture of ^{84}Rb with a ^{83}Rb beam during an implantation with energy E:

$$\frac{A_\mathrm{f}^{84}}{A_\mathrm{f}^{83}} = \bar{S}_{84}(E, A = 83) \cdot \frac{A^{84}}{A^{83}} \tag{7.2}$$

with $A_\mathrm{f}^{83/84}$ the ^{84}Rb and ^{83}Rb activities deposited in the furnace prior to the implantation and the activities $A^{83/84}$ implanted in the sample. Obviously, for $\bar{S}_{84} \to 0$ the mass separation is ideal, where for $\bar{S}_{84} = 1$ there is no mass separation at all. If the average admixture $\bar{S}_{84}(E, A = 83)$ of ^{84}Rb in a beam is known, the admixture of ^{85}Rb $\bar{S}_{85}(E, A = 83)$ defined analogously to $\bar{S}_{84}$ can be estimated assuming the following:

beam spacing: The beams are equidistant with $\mu = 0, d, 2d$ for ^{83}Rb, ^{84}Rb, and ^{85}Rb, respectively.
This is true for isotopes close to each other, like in this case.

Rb release: The release rate from the ion source for ^{83}Rb ions equals the one for ^{84}Rb and ^{85}Rb.
This assumption is well justified by experimental experience. When no increase in deposited ^{83}Rb activity can be measured any more, the ^{85}Rb current measured on the Faraday cup decreases drastically as well. This is caused by a drop in vacuum pressure of all Rb isotopes.

beam spot shape: The beam spot is circular and its radius is $a \cdot \sigma$.
From the radiographic images of the samples used to estimate the admixture, see figure 7.19, deviations from a circular shape are obvious.

beam spot position: The beam spot is centred on the circular sample.
The beam spot position can only be assessed by radiography if the sample position on the Timepix detector is known, which is in general not the case. An exception are all three samples implanted on the sextuple collector, see figure 7.19 where the whole sample surface is covered with traces of ^{83}Rb. Obviously, deviations from the central positions can occur, even on the sextuple collector, where the beam spot can be monitored using a KBr screen. For implantations with the BONIS retarding lens, deviations from the centre are likely to be smaller due to the focussing property of this lens.
Additionally, the samples themselves are not circular but squared with 10 mm edge length. The corners are capped to reduce the diagonal to 12 mm.

beam profile: All three beam profiles can be described using a normal distribution with the same standard deviation σ.
The beam profile is usually not normally distributed around its centre, a Gaussian often underestimates the peak height and deviates from the measured profile at the

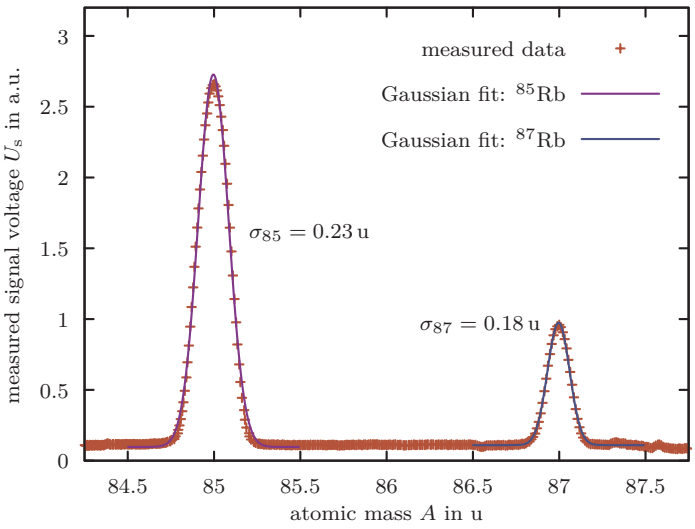

Figure 7.18.: The beam profile measured with the oscillating probe during a ^{83}Rb implantation run with 30 keV at the BONIS facility. The lines of the naturally abundant elements are nearly normally distributed, deviations can be seen at the peak and on the leading and trailing edges. The lines of the radioactive ^{83}Rb and ^{84}Rb are not visible, the beam currents are too low.

edge of the peak. A beam profile measured using the oscillating probe is shown in figure 7.18. Still, for an estimation of the beam contamination a normal distribution is an easy-to-handle approximation fitting the beam profile well enough.
The standard deviation of the lines consisting of the naturally abundant isotopes ^{85}Rb and ^{87}Rb differ by 20 % to 30 %. This beam widening can be explained by ions interacting with each other during the drift between separator magnet and target.

Finally, the average admixture of ^{85}Rb in the ^{83}Rb beam can be expressed as:

$$\bar{S}_{85} = \frac{1}{2} + \frac{1}{2}\mathrm{erf}\left(-\mathrm{erf}\left(\frac{A_\mathrm{s}}{A_\mathrm{s}+A_\mathrm{b}}\right) + 2\mathrm{erf}^{-1}\left(2\bar{S}_{84}-1\right)\right) \tag{7.3}$$

The derivation of this formula can be found in appendix B.4.

7.6.3.2. Determination of $\bar{S}_{84}(E, A = 83)$

Given a sufficient amount of ^{84}Rb in the furnace before the implantation, traces of this isotope may be implanted in the sample and may thus be detected during the activity measurement of the sample. Usually, before an implantation the amount of ^{84}Rb in the furnace is small due to two reasons: Firstly, between the production of the activity and the implantation itself, usually one month passes. Due to the half life of just 33.1(1) d of ^{84}Rb [HuhLiu00], before the implantation, at least half of the ^{84}Rb has already decayed. Secondly, due to the production process (see section 4.6 for details), the amount of ^{84}Rb is lower by a factor 3, compared to ^{83}Rb. The ^{83}Rb and ^{84}Rb activities after the production as well as the production time are known. Hence, the respective activities at the time of the ion implantation can be calculated.

Let a sample be implanted in two different implantation runs at t_1 and t_2 using activity from different furnaces with known ^{84}Rb/^{83}Rb activity ratio $r_i = A^{84}_{\mathrm{f},i}/A^{83}_{\mathrm{f},i}$. Here f denotes the activity in the furnace, $i = 1, 2$ is the number of the implantation. Let the activity of

both radio isotopes implanted after the second implantation be known. It can be expressed as

$$A^{83/84}(t_2) = A_1^{83/84} \exp\left(\frac{-\ln(2)}{t_\mathrm{h}^{83/84}} \cdot (t_1 - t_2)\right) + A_2^{83/84} \tag{7.4}$$

with the activity $A_i^{83/84}$ implanted during the ith implantation and the half lifes $t_\mathrm{h}^{83/84}$. The ^{84}Rb activity implanted during each of the implantations can be expressed using the average admixture $\bar{S}_{84}(E, A = 83)$ and the implanted ^{83}Rb activity

$$A_i^{84} = r_i A_i^{83} \bar{S}_{84} \tag{7.5}$$

If the fraction F of the total ^{83}Rb activity implanted during the second run is known, all activities $A_i^{83/84}$ can be written in terms of $A^{83}(t_2)$. This can be measured after both implantations. Obviously

$$A_2^{83} = A^{83}(t_2)F \qquad \text{and} \qquad A_2^{84} = r_2 A_2^{83} \bar{S}_{84} \tag{7.6}$$

Solving equation (7.4) for $A = 83$ for A_1^{83} and plugging in yields

$$A_1^{83} = A^{83}(t_2)(1 - F) \exp\left(\frac{\ln(2)}{t_\mathrm{h}^{83}}(t_1 - t_2)\right) \qquad \text{and} \qquad A_1^{84} = r_1 A_1^{83} \bar{S}_{84} \tag{7.7}$$

Plugging equations (7.6) and (7.7) into equation (7.4) for $A = 84$ and solving for $\bar{S}_{84}$ yields

$$\bar{S}_{84} = P(t_2) \left[(1 - F) \exp\left(\ln(2)(t_1 - t_2)\left(\frac{1}{t_\mathrm{h}^{83}} - \frac{1}{t_\mathrm{h}^{84}}\right)\right) r_1 + r_2 F\right]^{-1} \tag{7.8}$$

with $P(t)$ the ^{84}Rb/^{83}Rb ratio in the sample at time t. For one implantation run, this means for $F = 0$ and $t_1 = t_2$, this equation simplifies to

$$\bar{S}_{84} = \frac{P(t_1)}{r_1} \tag{7.9}$$

7.6.3.3. Evaluation of ^{84}Rb and ^{85}Rb admixtures

Usually, the furnaces used for implantations do not contain more than 10 % to 15 % activity of ^{84}Rb compared to ^{83}Rb. Ideally the production of the activity starts roughly two months before the implantations take place to allow for sufficient decay time for short-lived isotopes (see section 4.6), the deposition in the furnace and the transport of the activity from Řež to Bonn. After the mass separation, there are only some hundred Bq of ^{84}Rb implanted in the sample. An analysis of these traces is usually not done.
For one implantation in this work, however, the furnace is loaded with 24 % ^{84}Rb leading to a more pronounced ^{84}Rb contamination of the samples. Furthermore, implantations with four different implantation energies and on two different implantation sites are carried out in this implantation run. Here, the beam contamination can be studied depending on the implantation energy and comparing different implantation sites. For this implantation, a

furnace number	1st	2nd
activity production date	18/03/15	18/06/15
produced ^{83}Rb activity	80.5 MBq	90 MBq
produced ^{84}Rb activity	27 MBq	28 MBq
implantation date	29/06/15	07/07/15
^{83}Rb before implantation	35 MBq	77 MBq
^{84}Rb before implantation	3 MBq	19 MBq

Table 7.3.: Data for the furnaces used to estimate the ^{84}Rb and ^{85}Rb admixtures provided by Lebeda [Lebeda15].

second furnace is used after the first one depleted. However, it is possible to disentangling both implantations with the calculations presented in section 7.6.3.2.

For four samples, three of them implanted with 15 keV, 20 keV and 30 keV on the sextuple collector and one sample implanted with 8 keV using the BONIS retarding lens using activity from two different furnaces, the admixture of ^{85}Rb is estimated. The first furnace used contains less than 10 % ^{84}Rb activity in comparison to ^{83}Rb, while the second one contains 24 %. The ^{83}Rb and ^{84}Rb activities after the production are given by Lebeda [Lebeda15] and are summarised in table 7.3 along with some other informations about the loaded activity.
For two of the samples, both furnaces are used. From measurements using the integrated LYSO:Ce detector, it is known how much of the ^{83}Rb is implanted using each furnace. Using this, the known activity ratios of both discussed Rb isotopes as well as the known implantation dates, the average ^{84}Rb admixture $\bar{S}_{84}$ can be calculated using equation (7.8). Knowing the implanted ^{83}Rb activity in the paper backing behind the sample, and $\bar{S}_{84}$, equation (7.3) can be used to estimate the admixture of ^{85}Rb.

All results presented here are integral results over a whole implantation lasting up to 8 h. Also, it is assumed that no beam breakdowns occur, which is not documented. The ^{84}Rb implanted during beam breakdowns is incorrectly attributed to an increased beam width in this consideration.

In the following, the four samples' areas as well as their ^{84}Rb admixtures are discussed and compared. The radiographies of all samples are shown in figure 7.19. The results of the ^{84}Rb and ^{85}Rb admixture calculations, the beam spot sizes and all implanted activities are summarised in table 7.5.

30 keV sample: The samples implanted with an energy of 30 keV are considered as reference because this implantation energy is the lowest in standard operation conditions. The beam spot's major axis is 5.5 mm, the minor axis 3.5 mm with a total area of 12 mm^2. On the radiography in figure 7.19 the beam spot exhibits a tail to the top to the picture which is most probably because the furnace had been exchanged during the implantation. This can easily cause a slight misalignment resulting in a shift of the beam spot afterwards and thus a widened combined beam spot. The ^{84}Rb admixture as defined in equation (7.2) is $\bar{S}_{84}(30\,\text{keV}, A = 83) = 4.5 \times 10^{-3}$.

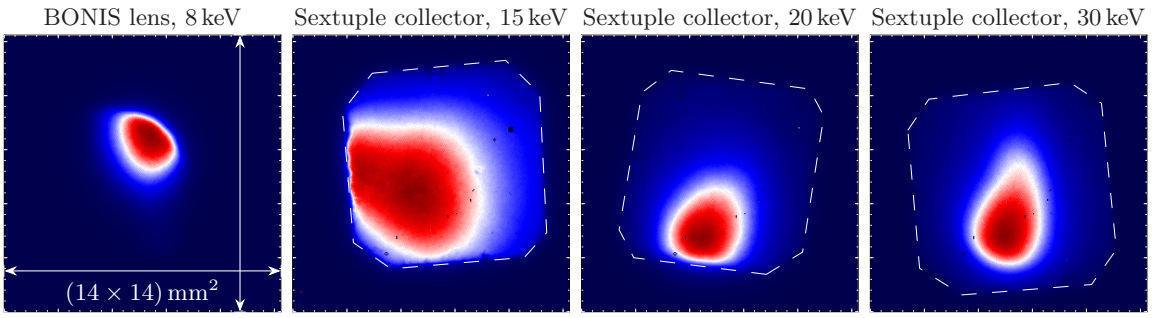

Figure 7.19.: The beam spots used to estimate the ^{84}Rb and ^{85}Rb admixture. None of them is circular as it has to be assumed for the calculation. The samples implanted on the sextuple collector have traces of ^{83}Rb spread over the whole surface, the edges of the substrate can be estimated. This is shown with a thin dashed line in the radiographies. The beam spot is not centred in either case. The position of the source on the Timepix chip is not documented, hence, the beam spot position for the remaining sample can not be assessed using this radiography.
The colour scale is not shown in these pictures, the relative scale (dark blue: no events, white: half maximum, dark red: maximum) is the same for all pictures. The pictures are taken from Slezák [Slezák15b].

20 keV sample: The beam spot on the sample implanted with an energy of 20 keV on the sextuple collector exhibits a major axis of 4.2 mm and a minor axis of 3.8 mm with an area of 10 mm^2 and is thus a bit smaller than the beam spot implanted with 30 keV. This is most probably because only one furnace was used. A radiography is shown in figure 7.19. The admixture $\bar{S}_{84}(20\,\mathrm{keV}, A = 83) = 1.1 \times 10^{-2}$ of ^{84}Rb is higher by more than a factor two. This may be caused by a different deviation of the beam spot from the centre of the sample causing the ^{84}Rb beam to be closer to the sample. (The implanted ^{84}Rb activity can not be compared directly, because the 30 keV sample was implanted using two furnaces with different ^{84}Rb content.) Heavier isotopes, like ^{84}Rb, pass the mass separator magnet deflecting the ions to the left (in direction of the ions' movement) with a less bend trajectory. Thus these isotopes exit the magnet on the right side of the lighter ^{83}Rb beam. If the ^{83}Rb beam hits the target on the left side of its centre, more of these heavier isotopes get implanted.
Because the deposition of ^{83}Rb is not impaired by the 20 keV implantation energy, these implantations can be considered feasible without major disadvantages compared to the 30 keV. This was the lower energy limit before.

15 keV sample: The sample implanted with 15 keV implantation energy shows significant differences in comparison to both other samples implanted on the sextuple collector. The beam spot is significantly larger with a major axis of 8.4 mm, a minor axis of 6.5 mm and an area of 36 mm^2. This is obvious from the radiography shown in figure 7.19. The amount of ^{83}Rb in the paper backing is comparable to the activity implanted in the sample itself. The admixture of ^{84}Rb $\bar{S}_{84}(15\,\mathrm{keV}, A = 83) = 3.3 \times 10^{-2}$ is a factor three larger

than for implantations with 20 keV. The activity deposition during this implantation was exceptionally slow, most probably due to losses in the separator magnet and on its entry slit.
Considering these results, it is concluded that implantations with 15 keV are feasible but yield unfavourable results and should be avoided if possible.

8 keV sample: The implantation with 8 keV is carried out using the BONIS retarding lens. The beam spot is smaller than all other beam spots with a major axis of 3.2 mm, a minor axis of 2.4 mm and an area of 5 mm^2, see figure 7.19. Nearly no activity is implanted in the paper backing. The admixture of ^{84}Rb $\bar{S}_{84}(8\,\text{keV}, A = 83) = 7.0 \times 10^{-4}$ is the smallest of all samples in this batch.
Implantations using the BONIS retarding lens are superior to implantations on the sextuple collector regarding all aspects. However, this retarding lens imposes restrictions on the implantation. Firstly, the implantation energy can only be adjusted to up to 12.5 keV. Secondly, the beam spot shape can not be altered due to the lack of deflection capacitors. If these restrictions do not pose a problem, an implantation using the BONIS lens should be preferred to the sextuple collector.

7.6.4. The mass resolution of ^{83}Rb beams

In this work, the mass resolution of the BONIS setup was not measured dedicatedly. However, from the beam profiles obtained from the oscillating probe or a Gaussian fit to these, see figure 7.18, a lower limit for the mass resolution can be estimated. The oscillating probe crosses all beams with a non-constant velocity on a circular trajectory with a carbon pin of finite thickness. Additionally, for both naturally abundant isotopes ^{85}Rb and ^{87}Rb, the current during the implantations is in the range of 0.15 µA and 0.5 µA, respectively. This might lead to a widening of the beam due to Coulomb repulsion of the ions on their way from the mass separator magnet to the oscillating probe.
The mass resolution calculated according to the peak width definition from Todd [Todd91], is given by the ratio of the Full Width at Half Maximum (FWHM) of the lines and the line position and is summarised in table 7.4.

$$R = \frac{m}{\Delta m_{\text{FWHM}}} \tag{7.10}$$

When estimating the ^{84}Rb admixture, the line width and the distance between two neighbouring isotope lines are calculated, see appendix B.4. These values can be combined with the fact that samples are 10 mm wide, hence, $a\sigma \approx 5$ mm, see section 7.6.3.1 for more details. The results of this estimate are listed in table 7.4. However, these values are estimated based on implantations lasting approximately 8 h each and all occurring beam instabilities and breakdowns are included in these numbers. They thus have to be considered a lower limit for long lasting implantations. This is emphasised by the big difference between the mass resolution for 30 keV determined by the different methods.

Table 7.4.: Mass resolution estimates for ^{83}Rb beams at the BONIS facility from oscillating probe measurements (see figure 7.18) and admixture measurements (see section 7.6.3) All values have to be considered lower limits, see section 7.6.4.

isotope	^{83}Rb	^{85}Rb	^{87}Rb
oscillating probe: data @ 30 keV	–	370	477
oscillating probe: fit @ 30 keV	–	409	577
^{84}Rb admixture @ 30 keV	132	–	–
^{84}Rb admixture @ 20 keV	119	–	–
^{84}Rb admixture @ 15 keV	92	–	–
^{84}Rb admixture @ 8 keV	204	–	–

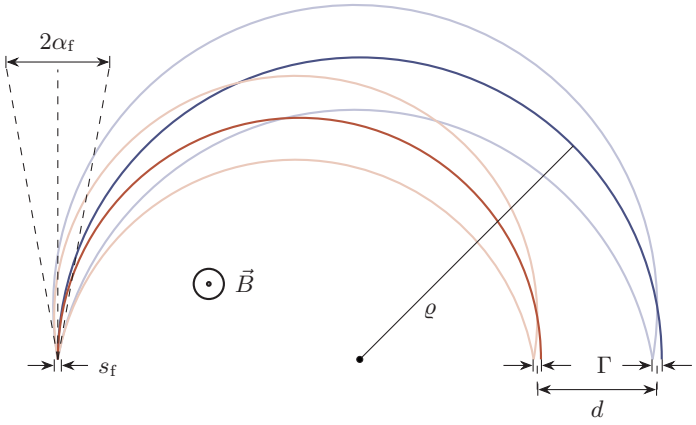

Figure 7.20.: Particle trajectories in a separator magnet. d is the distance between isotopes of neighbouring mass, Γ the width of a mono-isotopic beam, s_f the width of the ion source's opening and α_f the divergence angle of the beam leaving the ion source.

The mass resolution measured in a dedicated experiment using a 70 keV Ar^+ beam is roughly 1000 [FreHei70] using the same definition of the mass resolution as above.

For samples implanted on the same implantation site, the mass resolution decreases with lower implantation energies. This behaviour is typical for magnetic mass separation. During an implantation, the furnace's opening with diameter s_f is mapped to the target as beam spot with diameter ϱ. With the beam spot width Γ, the beam divergence angle α_f, the ion's mass m, the magnetic field B and the ion source's potential V, the separation quality d/Γ can be expressed as [Eversh16]

$$\frac{d}{\Gamma} = m^{-1} \cdot \left(\frac{s_\mathrm{f}}{\varrho} + \alpha_\mathrm{f}^2 + \frac{\Delta V}{V} + 2\frac{\Delta B}{B} \right)^{-1} = m^{-1} \cdot R \tag{7.11}$$

The particle trajectories of two mono-isotopic beams in a magnetic field are illustrated in figure 7.20. Ions emitted by an ion source on reduced potential have a reduced momentum requiring a smaller magnetic field for the mass separation. From equation (7.11) follows a reduced mass resolution R for a reduced source potential V and magnetic field B.

Implantation energy	8 keV	15 keV	20 keV	30 keV
Implantation site	BONIS lens	sext. collector	sext. collector	sext. collector
Activity from 1st furnace	0 %	75 %	0 %	51 %
1st implantation	09/07/15	29/06/15	07/07/15	30/06/15
2nd implantation	–	08/07/15	–	07/07/15
implanted ^{83}Rb activity	4.0 MBq	0.5 MBq	2.8 MBq	2.6 MBq
^{83}Rb activity in backing	37 kBq	0.4 MBq	1.1 MBq	0.9 MBq
implanted ^{84}Rb activity	0.4 kBq	1.7 kBq	4.6 kBq	1.0 kBq
Major beam spot axis	3.2 mm	8.4 mm	4.2 mm	5.5 mm
Minor beam spot axis	2.4 mm	6.5 mm	3.8 mm	3.5 mm
Beam spot size	5 mm^2	36 mm^2	10 mm^2	11 mm^2
$\bar{S}_{84}(E, A = 83)$	7.0×10^{-4}	3.3×10^{-2}	1.1×10^{-2}	4.5×10^{-3}
$\bar{S}_{85}(E, A = 83)$	1.2×10^{-19}	4.4×10^{-6}	6.4×10^{-9}	9.7×10^{-11}
^{84}Rb/^{83}Rb ion ratio	1.5×10^{-4}	7.0×10^{-3}	2.2×10^{-3}	9.5×10^{-4}
^{85}Rb/^{83}Rb ion ratio	2.0×10^{-16}	4.9×10^{-3}	1.1×10^{-5}	2.5×10^{-8}
^{83}Rb activity	3 MBq	3 MBq	3 MBq	3 MBq
^{84}Rb activity	0.4 kBq	20 kBq	6.7 kBq	2.9 kBq
^{85}Rb ions	6.5×10^{-3}	2.4×10^{11}	3.5×10^{8}	5.3×10^{6}

Table 7.5.: Top: Measured key data on the implantations of the samples which are used to estimate the ^{84}Rb and ^{85}Rb admixtures. All given activity values are dated to the last of both implantation dates.
Middle: A summary of the measured ^{84}Rb and the estimated ^{85}Rb admixtures for the samples shown in figure 7.19 including major and minor axes as well as the area of the beam spot.
Bottom: Ion ratios calculated assuming standard parameters for an ion implantation for the KATRIN experiment: The activity is assumed to be implanted 30 d after the production. At this time 100 MBq of ^{83}Rb and 21 MBq of ^{84}Rb remain in the furnace. 0.5 mg $^{\text{nat.}}$Rb in form of RbCl is assumed to be added as carrier, the natural abundance of ^{85}Rb is 72.17 % [IAEA17]. Furthermore, it is assumed that 3 MBq ^{83}Rb samples are implanted.

7.7. The implantation efficacy

The Bonn Isotope Separator is tuned towards maximum flexibility, the capability to separate ions until beyond the transuranic elements at the expense of implantation efficacy [Eversh16]. For most implantations an efficacy in the range of 1 % to 3 % is not uncommon [Freita77; FreHei70]. For implantations of ^{83}Rb for the KATRIN experiment, where up to three samples with activities of up to 3.5 MBq each are required, a higher efficacy is advantageous. In principle it is possible to load the furnace with activities in the GBq range at the NPI in Řež, but in order to prevent unnecessary irradiation of personnel this is to be avoided.

There are two main factors improving the implantation efficacy. Firstly, the ion source has been modified accordingly to accept a furnace of increased length and reduced wall thickness, as described in detail in section 7.3.1. This enables the operation of the ion source with less coupled ionisation and evaporation temperatures.
Secondly, the experience gathered by the operator during many test implantations is of great importance. Especially the correct temperature adjustment during the implantation is crucial to reach a high implantation efficacy.

The implantation efficacy is the ratio of the ^{83}Rb activity implanted in the targets and the ^{83}Rb activity in the furnace at the beginning of the implantation and is thus always an integral value for one or multiple implantation runs. It is *not* the ratio of activity passing the mass separator magnet and the activity in the furnace.
The result of this definition is that the determined efficacy values have to be considered lower limits in all cases. The following situations reduce the efficacy according to this definition, even though the activity was separated correctly and is implanted somewhere:

activity implanted in lenses: If a retarding lens is used for the implantation some of the activity might be implanted in the lens itself. This effect is most pronounced for the ISOLDE lens, when aiming for a big beam spot with high deflection values.

activity implanted in backings: For implantations on the sextuple collector and using the BONIS retarding lens, a paper backing is placed behind the sample to prevent an implantation in the target holder. Depending on the implantation energy, especially on the sextuple collector up to $\sim 45\,\%$ of the activity reaching the collector can be implanted in the paper backing for implantations with non-standard parameters. This value is considerably lower for operation within the standard parameters, see table 7.5.

sample changes: If one of the retarding lenses is used, a sample change requires to break the vacuum. After changing the sample, the vacuum has to recover, the whole process takes roughly 30 min. Especially for the ISOLDE lens a fair vacuum of at least 1×10^{-5} mbar is required, otherwise electric discharges will occur due to ionised residual gas in this small ion lens. During this time the ion source is not cooled down to avoid thermal strain, the separated activity is implanted into a vacuum shutter during this time.

calibrating the ISOLDE lens: There is no way to check the beam spot position during the implantation when the ISOLDE lens is used, see section 7.4.2. To ensure a correct adjustment of the deflection capacitors, it is necessary to implant ^{85}Rb into a paper target to verify the beam spot position. During this time ^{83}Rb is wasted. Of course the collector chamber has to be vented twice for this procedure. If necessary, this process has to be repeated.

heating up and cooling down: During the heating-up and the cool-down of the ion source, no implantation takes place. Albeit the temperatures are not ideal for evaporation and ionisation of Rb, ionised or unionised atoms might leave the furnace and are lost for the implantation process.

required activity reached: The samples prepared for the measurement in the MoS of the KATRIN experiment as well as the samples used for PAC measurements have upper activity limits. As soon as all samples are implanted with the requested activity, the implantation is stopped. Activity left in the furnace is left to decay.

activity safety margin: Prior to an implantation of samples to be measured at the MoS of the KATRIN experiment, the activity used for the implantation is loaded into the furnace at the NPI in Řež. There, usually twice the amount of the ^{83}Rb needed is loaded into the furnace as a safety margin. In case of problems during the implantation, the additional activity increases the chance for finishing the implantation using the same furnace after the problem is fixed.

ion source breakdown: Long implantation runs can last several days. During the night the ion source is shut down, the recurring heating and cooling cycles put a lot of strain on the ion source causing a breakdown at some point. Such a breakdown usually marks the end of an implantation. Activity left in the furnace is left to decay.

stable current on target: The sextuple collector is equipped with an ampère meter. The current generated by the ^{83}Rb activity is too low to be measured. Before the furnace is depleted, the width of the isotope beams may increase, giving rise to an overlap between these beams. This will cause a non-zero ^{85}Rb current on the sextuple collector, in this case the implantation is immediately aborted.

test implantations: During test implantations, the limits of the mass separator are explored (e.g. implantations with 15 keV implantation energy) or new hardware configurations (e.g. the ISOLDE retarding lens) are tested. During these implantations the efficacy may drop significantly.

undocumented tests: Not all tests are fully documented. The measurement of the activity in furnaces causes additional irradiation of personnel. Thus, for minor tests, furnaces used for implantations of samples for the MoS at the site of the KATRIN experiment are reused. The activity implanted should be be taken into account for the implantation efficacy for this particular furnace.

The implantation efficacies of all recorded implantations, the activity loaded in the furnace at the beginning of the implantation as well as the percental ^{83}Rb usage in the furnace are plotted versus time in figure 7.21. Additionally, the bore depth in the furnace, the wall thickness and the production procedure are displayed. The results presented in this graph are discussed in detail in section 7.7.1.

7.7.1. Discussion of the efficacy evolution

Before the design of the furnaces was revised as described in section 7.3.3 no implantation efficacy above $\sim 2\,\%$ is reported. At the beginning of this work, ^{86}Rb is used, when no ^{83}Rb is available. ^{86}Rb can be bought off-the-shelf and has a shorter half life of just 18.6 d [MiyGot81] and thus does not contaminate the ion source for a long time while showing the same behaviour during the implantation.

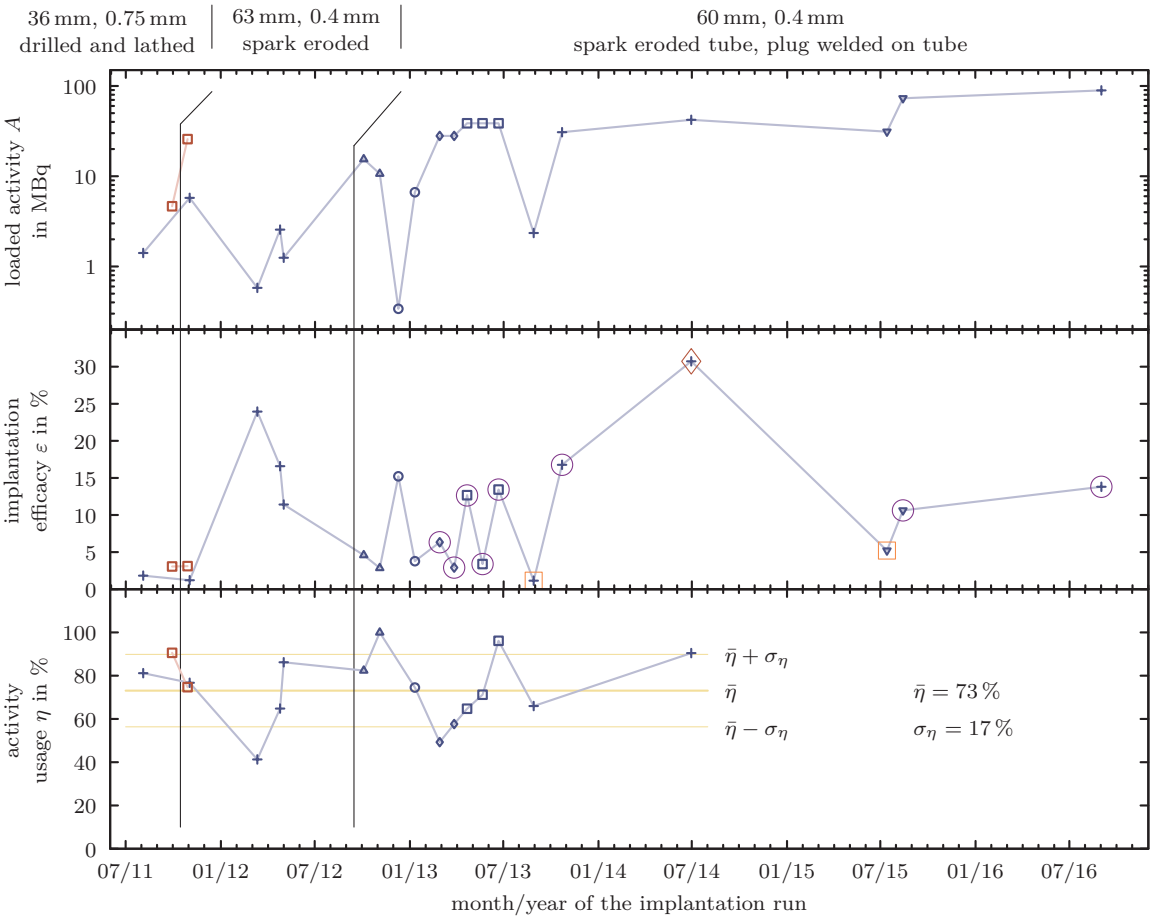

Figure 7.21.: The furnace depth, its wall thickness including the manufacturing process (above the graphs) (see sections 7.3.1 and 7.3.3), as well as loaded activity (top graph), implantation efficacy (middle graph) and furnace activity usage (bottom graph) over time. Consecutive implantations within a short time are marked with the same open symbols. The symbols after the first are shifted by one month to improve the readability. Red symbols mark implantations with ^{86}Rb, blue symbols with ^{83}Rb. The lines between the points are to guide the eye, uncertainties are too small to be displayed on this scale.
Points surrounded by a purple circle indicate the requested activity being implanted successfully, the implantation is stopped. Orange squares indicate experimental implantations, red diamonds indicate an ion source breakdown. All implantations prior to 2013 are considered experimental.

Using the first longer furnace version with thin walls, the first implantation efficacies above 10 % are achieved. However, these efficacies could not be reproduced in the next implantations with more ^{83}Rb loaded in the furnace. The next implantations, until the beginning of 2013, are used to find better parameters for the implantation of ^{83}Rb with the new furnace.

Starting with the implantations in March 2013, regular implantations of samples for the KATRIN experiment are carried out. These samples are measured in the MoS to characterise the samples produced in Bonn. These measurements are discussed in the work of Slezák [Slezák15a]. For these implantations one furnace per sample is delivered, as soon as the requested activity is reached the next furnace is used. This leads to limited efficacies during this time.
In the end of 2013 and in 2014, still one furnace per sample is delivered but the samples are implanted using only one furnace. This increase in efficacy can be explained by more experience of the mass separator operator, no further changes to the hardware were made. During these implantations, peak efficacy values of 17 % and 31 % are reached.
To reduce costs, starting from 2015, only one furnace is loaded with ^{83}Rb. As a safety margin, more ^{83}Rb than the previous implantations suggest to be necessary is deposited in the furnace. All these implantations are stopped after the requested activity is reached, the remaining activity is left to decay. Here, the mentioned safety margin reduces the possible efficacy.

7.8. Conclusions and outlook

As a result of this work, the BONIS facility is prepared to reliably produce ion implanted ^{83}Rb sources for the KATRIN experiment on a regular basis. This is due to the changes in the set-up and the experience gained by the separator staff during the years of development.

The positive surface ionisation source is modified to maintain ideal evaporation temperatures at the deposition site of the ^{83}Rb while being operated at ionisation temperatures of up to 3300 K. The implantation efficacy is increased by more than an order of magnitude, reaching values of up to 31 %.
To be able to implant samples four times a year without unnecessary irradiation of personnel, or be able to replace a defective ion source if needed, a second ion source is constructed.

Next to the retarding lens that was already present since 1976 [FreHei76], a new retarding lens is implemented in the collector chamber of the mass separator. In contrast to the previous retarding lens excelling at implanting small beam spots, this lens can be used together with the deflection capacitors. Using these, the activity can be spread out over the whole sample. This allows for the production of samples with large beam spots and implantation energies down to 4 keV keeping the ^{83}Rb peak concentration low. This has a positive effect on the samples used for the high voltage calibration at the KATRIN experiment.

A detector system mountable in the collector chamber is developed. It allows in-situ and real-time measurements of the implanted activity when either of the retarding lenses are used.

The capabilities of all discussed set-ups are thoroughly explored and characterised. It turns out implantations with energies of down to 20 keV are well possible on the sextuple collector. This reduces the gap between the maximal implantation energy of the retarding lenses of 12.5 keV and the minimal implantation energy possible using the sextuple collector.

Future experiments could be focussed on the ioniser and the furnace. The cap hole diameter can have an influence on the extracted current [LatRai75]. This in turn influences the fields in the furnace and has an effect on the ionisation efficacy in the furnace. A smaller cap hole might decrease the extracted current but increase the ionisation efficacy and with this the implantation efficacy.
With some additional modification of the ion source, a furnace 10 mm longer than the one shown in section 7.3.1 can be used. With a second ion source at hand, the modifications do not pose a problem for the routine operation of the mass separator. It is technically feasible to reduce the wall thickness of the used furnaces to 0.3 mm. Experiments have to verify if the effect justifies the higher price of the W tubes.
The furnaces used for implantations up to now are not cleaned beforehand. A pre-heating in an oxygen atmosphere could remove residual gas, carbon and oxygen layers [ZakPei10] prior to the implantation and, thus, could increase the ionisation efficacy.

8. Choice of the detectors

In order to carry out Perturbed Angular Correlation (PAC) measurements with ^{83}Rb(^{83}Kr) and ^{83m}Kr(^{83}Kr) as probe nuclei, suitable detectors have to be chosen. The decay scheme with all relevant transitions can be found in figure 4.3. To make use of both available cascades in one set-up, both start radiations, the 553 keV γ and the 17.8 keV Conversion Electron (CE), as well as the 9.4 keV stop signal have to be registered by detectors with appropriate properties.
To detect the 553 keV γ line a Caesium Fluoride (CsF) scintillation crystal with PhotoMultiplier (PM) readout is chosen, see section 8.1. For the 9.4 keV γ quanta and the 17.8 keV CEs, windowless Avalanche Photo Diodes (APDs) are used. The APDs considered for this work and their properties are discussed in section 8.2, while alternatives to APDs are listed and discussed in section 8.3.

8.1. Detection of the 553 keV γ quanta with a CsF detector

The Caesium Fluoride (CsF) scintillation detector is used to detect the 553 keV start quantum of the γ-γ cascade. The scintillation crystal is 2 ” in diameter and 2 ” thick. It is coupled to a PM, the slow signal is taken from the 9th dynode, the fast signal from the last. For γ quanta of 500 keV, the detection probability is 83 %. It is calculated for 500 keV from values given by Lavoie [Lavoie73] rather than for 553 keV because no data sheet and no more precise values are available.
The CsF scintillation detector is chosen for its fast signals. It offers signal rise times in the ns range making is especially suitable for fast timing purposes. Sample signals recorded with ^{83}Rb γ radiation between 520 keV and 553 keV are shown in figure 8.1. The limited energy resolution of roughly 20 % [MosAll83] does not pose a problem for the PAC measurements because the neighbouring γ lines only contribute to the background.

8.2. Detection of the 9.4 keV γ quanta and the 17.8 keV CEs with APDs

Avalanche Photo Diodes (APDs) are solid state semiconductor devices, which are capable of direct photon and particle detection. Their doping profile creates a high-electric field multiplication region when a suitable reverse bias voltage is applied. Charge carriers entering this region with typical electric fields of $\gtrsim 10\,\mathrm{V\,\mu m^{-1}}$ will be accelerated and multiplied by impact ionisation leading to an intrinsic gain in the range of 50 to 2000 [BarKis06]

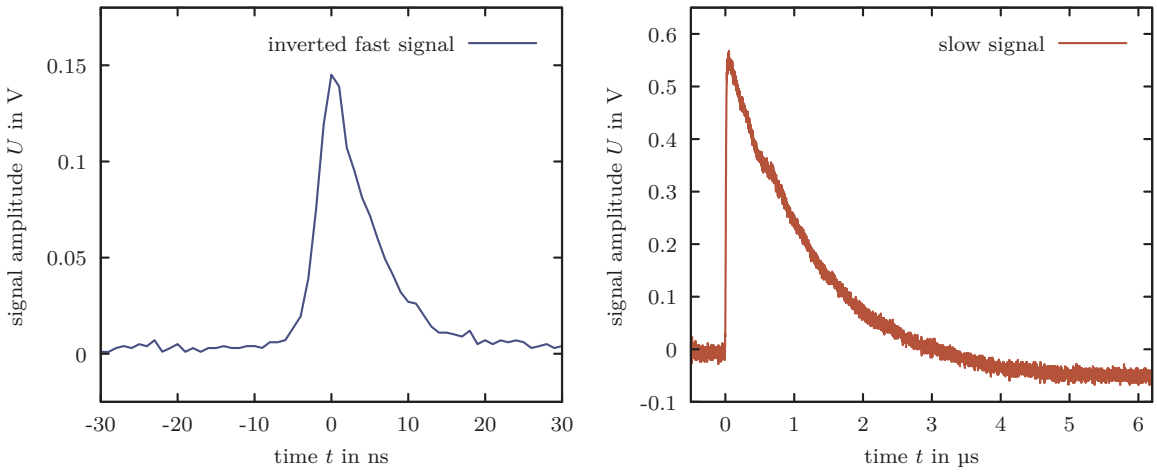

Figure 8.1.: Inverted fast and slow signal outputs taken from the PM mounted after the CsF scintillation crystal.

depending on the device and the applied bias voltage. Up to a certain bias voltage, APDs can be operated in linear mode where the signal amplitude is proportional to the energy deposited in the device.

Three different types of APDs are available commercially, which differ in the doping structure and the consequent properties: Bevelled edge, reach-through and reverse reach-through [KatSai05]. For this work, only the last two are of interest, a sketch of the doping profiles of these two APD types is shown in the top row of figure 8.2.

The depletion layer of reach-through APDs consists of a wide drift region with a low-electric field ($\sim 2\,\mathrm{V\,\mu m^{-1}}$) [KatSai05] at the front of the detector, followed by a narrow high-field multiplication region in the back of the device. All charge carriers that are created in this drift region that are usually in the range of $\sim 100\,\mu\mathrm{m}$ are subject to the full multiplication. A qualitative sketch of the electric field magnitude and the charge carrier multiplication as a function of the depth of radiation absorption is shown in figure 8.2 in the second and third row. A drawback of this configuration is that most of the dark current electrons are multiplied as well making reach-through APDs noisy [KatSai05].

The reverse reach-through APDs' depletion layer comprises a narrow high-field multiplication region at the front and a low-field drift region in the back of the device. This design is especially suited for the use with scintillator crystals, that usually emit light with 500 nm or less. This light is absorbed within the first 1 µm to 3 µm, the resulting charge carriers undergo full multiplication in the high-field region that is $\sim 5\,\mu\mathrm{m}$ from the surface of the device [KatSai05]. The electric field strength as well as the multiplication of charge carriers as function of creation depth is shown in figure 8.2 in row two and three. APDs of the reverse reach-through type are, on the one hand, less advantageous for direct detection of more penetrating radiation like γ or X-rays that deposit energy deeper than the high-field region, resulting in incomplete charge carrier multiplication. On the other

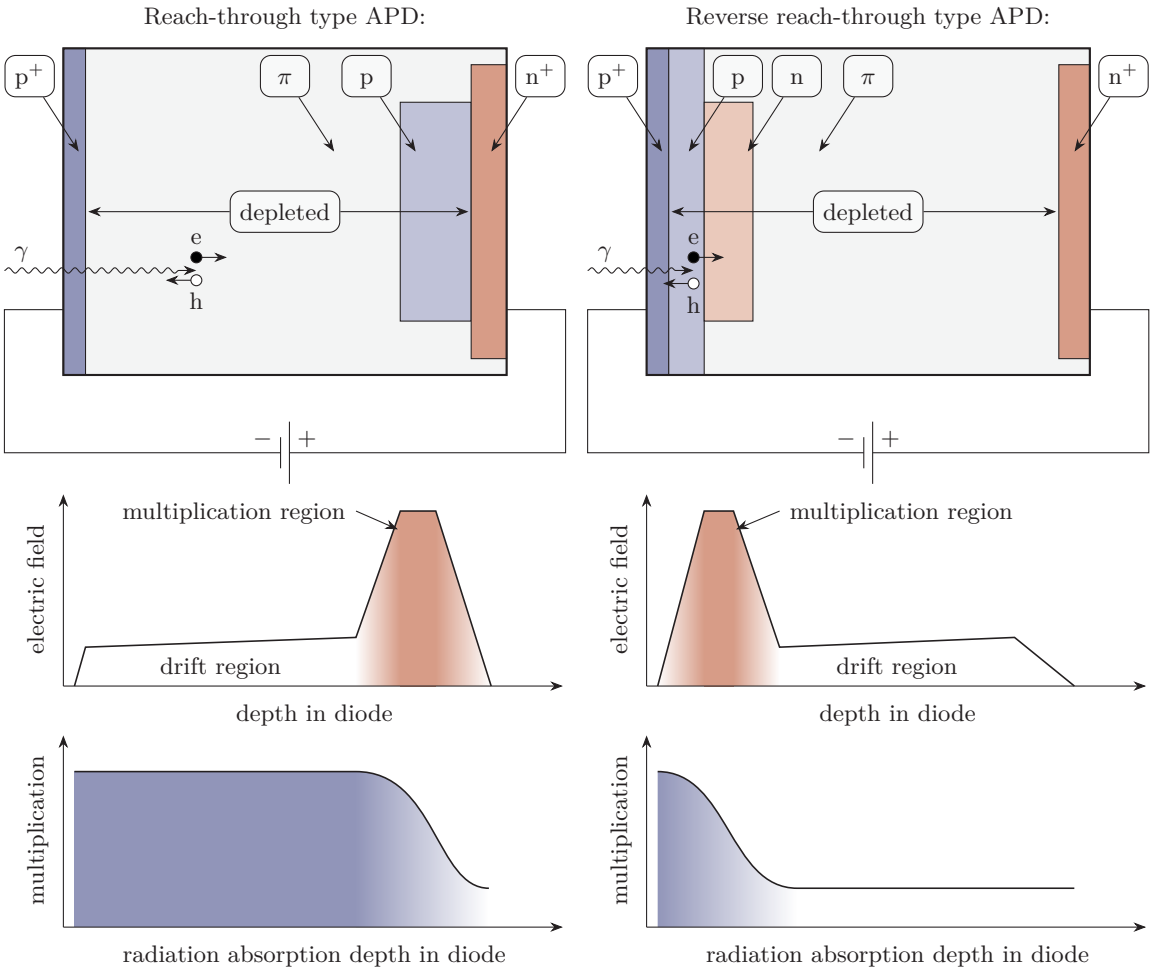

Figure 8.2.: A qualitative summary of the properties of reach-through (left) and reverse reach-through (right) APDs.
Top row: The common doping profile of the respective APD type similar to Baron et al. [BarKis06]. Radiation enters from the front of the device, pointing to the left side in this sketch. The heavily doped p^+ and n^+ regions form metal semiconductor contacts and give rise to the electric field causing the drift in the slightly p doped intrinsic π region. The n and p doped regions create the high electric fields that cause the charge carrier multiplication. In the sketch a reverse bias is applied, in both cases the anode is on the left side.
Centre row: A quantitative plot of the relative value of the electric field depending on the depth in the diode adopted from Baron et al. [BarKis06]. The drift region is shown in white, the multiplication region in red.
Bottom row: The charge carrier multiplication as a function of the depth of charge carrier creation, qualitatively, adopted from Kataoka et al. [KatSai05]. Charge carriers created in the dark blue region are subject to the complete charge carrier multiplication.

hand, only dark current holes undergo multiplication reducing the noise contribution [KatSai05].

8.2.1. Active area

In principle, for an ideal PAC measurement set-up with a point-like source, there is no constraint on the size of the detector's active area. Detectors with smaller active area have to be moved closer towards the sample to keep a desired solid detection angle constant. APDs are available off-the-shelf with an active area from $\sim 10^{-1}\,\mathrm{mm}^2$ to $10^2\,\mathrm{mm}^2$.

However, if one considers a finite size of the activity distribution, it is advantageous to use a detector with an active area that is considerably bigger than this distribution. Firstly, if source and detector are of a similar size, corrections that may involve inaccurate simplifications (e.g. uniform, circular deposition of radioactivity) have to be applied. These corrections diminish with the square of source radius over distance from source to detector. Secondly, with smaller detectors that have to be positioned more closely to each other and to the sample, all surrounding parts have to be smaller as well. A smaller sample, sample holder, preamplifier and preamplifier case are harder to design and manufacture. Furthermore, it makes aligning the sample and the detectors cumbersome. Thirdly, measuring the distances between detectors and samples gets more difficult and the relative uncertainties get bigger as the distances get smaller.

Due to these facts, large area detectors that make a bigger distance between sample and detector feasible are preferable. This, however, reduces the available detectors to a relatively short list. Available models at the time when the detectors were ordered were: Excelitas[1] C30703FH-200T, Excelitas C30703FH-120T, Hamamatsu S8664-1010 and devices from Advanced Photonix and Radiation Monitoring Devices. The detectors from the latter two companies were classified as not reliable by Baron et al. [Baron06] and were thus not considered for this experiment.

With increasing active area of these detectors, the terminal capacitance increases as well. This renders the detection system consisting of detector and preamplifier more prone to oscillations and instabilities. Furthermore, the signal amplitude for devices with higher capacitance is smaller [BarKis06]. These characteristics have to be taken into account when selecting the detector and designing the amplifier circuit.

8.2.2. Detection probability

A high detection probability is a key requirement for a detector to be used for PAC measurements with the probe nucleus ^{83m}Kr. In contrast to other methods involving radioactive

[1] Excelitas devices were sold under the brand names Perkin Elmer and EG&G before. Literature references appearing with those brand names are still valid for the Excelitas detector.

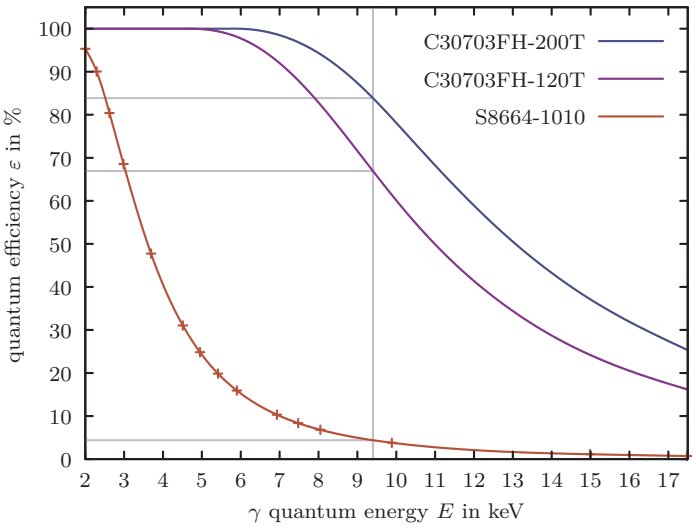

Figure 8.3.: The quantum efficacy versus incident γ quantum energy of the Excelitas C30703FH-200T, C30703FH-120T [Exceli14a] and Hamamatsu's S8664-1010 [Hamama16a] with 200 µm, 120 µm and 5 µm active layer thickness, respectively. The data for the Hamamatsu APD is calculated based on values from Henke et al. [HenGul93] and interpolated with a cubic spline. The efficacies for the 9.4 keV γ stop line the efficacies are 84 %, 67 % and 4.4 %, respectively.

sources, in PAC measurements, a small detection probability can not be compensated by a higher activity of the sample. Here the ratio of true to accidental coincidences drops like the reciprocal activity, see equation (4.22).

In order to detect electrons with energies around 17.8 keV the absence of a resin or glass window covering the detector chip is crucial. All electrons in the relevant energy range are absorbed in such a window. Excelitas' C30703FH-200T and C30703FH-120T are windowless devices by default, Hamamatsu's S8664-1010 can be ordered without resin cover. The bare detector chip is covered by a not depleted passivation layer. This silicon oxide or nitride film of approximately 1 µm for the Hamamatsu detector [Hamama16a] and 1.2 µm for the Excelitas chip [Exceli16] does not induce a relevant energy loss for electrons of 17.8 keV in comparison with the energy resolution of the detection system. The energy resolution is measured in section 9.3.3.
For detecting 9.4 keV γ radiation, detector windows absorb a fraction of the incident radiation depending on thickness and material.

The quantum efficacy of APDs depends on the thickness of the active layer, i.e. the layer in which charge carrier creation due to photoelectric or Compton effect leads to a signal that is subsequently amplified by the intrinsic gain of the APD. The detection probability of electromagnetic radiation up to an energy of 18 keV is plotted in figure 8.3 for both Excelitas reach-through type detectors of the C30703FH family and the Hamamatsu S8664-1010, a reverse reach-through device. Further favourable consequences of a thick active layer are an increased signal height and a reduced terminal capacitance of the detector [BarKis06]. However, the signal rise time increases as well due to the constant maximal drift speed of charge carriers in the semiconductor.

8.2.3. Signal shape

The output signal shape of APDs differs depending on their properties and the properties of the preamplifier they are read out with. The most important detector characteristics for the signal shape are terminal capacitance and active thickness. Unless stated otherwise, the detectors discussed here are operated with the preamplifier board described in section 9.2.

8.2.3.1. Signal rise time

Next to the detection probability, the signal rise time is crucial because it limits the time resolution of the PAC experiment. The signal rise time can be estimated using the bulk electron drift speed in the Si detector chip. The drift velocity depends on the temperature, the crystal orientation, the impurity density of the detector chip and on the electric field strength in the drift region. To obtain an upper limit, a high purity material with the $\langle 111 \rangle$ axis being aligned parallel to the drift direction is assumed. Although the detector chip might get warmer during a measurement, a temperature of 300 K is used to approximate the drift velocity.
Using values from Jacoboni et al. [JacCan77], one obtains an upper limit for the drift velocity of approximately $100\,\mu m\,ns^{-1}$. For the C30703FH-200T and C30703FH-120T with 200 µm and 120 µm active thickness, minimal signal rise times of 2 ns and 1.2 ns are obtained, respectively. For both detectors a signal rise time of 5 ns is specified in the datasheet [Exceli14a]. For Hamamatsu's S8664-1010 with 45 µm active thickness, a minimal signal rise time of 0.45 ns is calculated.

The signal rise time is measured for two detectors, Excelitas' C30703FH-200T and Hamamatsu's S8664-1010 in combination with the preamplifier used in the scope of this work and an Agilent Technologies MSO 9254A 2.5 GHz oscilloscope with $20\,GSa\,s^{-1}$. However, the amplifier itself may constitute limitations on the signal shape due to its noise characteristic and bandwidth restrictions, see section 9.2.
The automatic rise time determination of the oscilloscope was used to measure the rise times and automatically create a histogram for many events. The time from 10 % to 90 % of the signal amplitude is measured. For both detector types, the histograms show a tail either to slower rise times (for the Hamamatsu S8664-1010) or to faster rise times (for the Excelitas C30703FH-200T).

The rise time histogram of Hamamatsu's S8664-1010 can be found in figure 8.4 on the right side. The estimation for the typical rise time of the S8664-1010 detector combined with the Sequentially Arranged High-gain AmplifieR (SAHAR) module (see section 9.2 for a detailed discussion) is 1.35 ns, disregarding the tail towards slower rise times. The main contributions for this tail are signals distorted by signal-noise interference. There are two ways how this kind of interference artificially increases the determined rise time and cause the tail towards slower rise times. In the first case, the signal starts on a positive noise bump. The oscilloscope interprets the start of the underlying noise bump as start of the signal, thus increasing the rise time by the time span between start of the noise

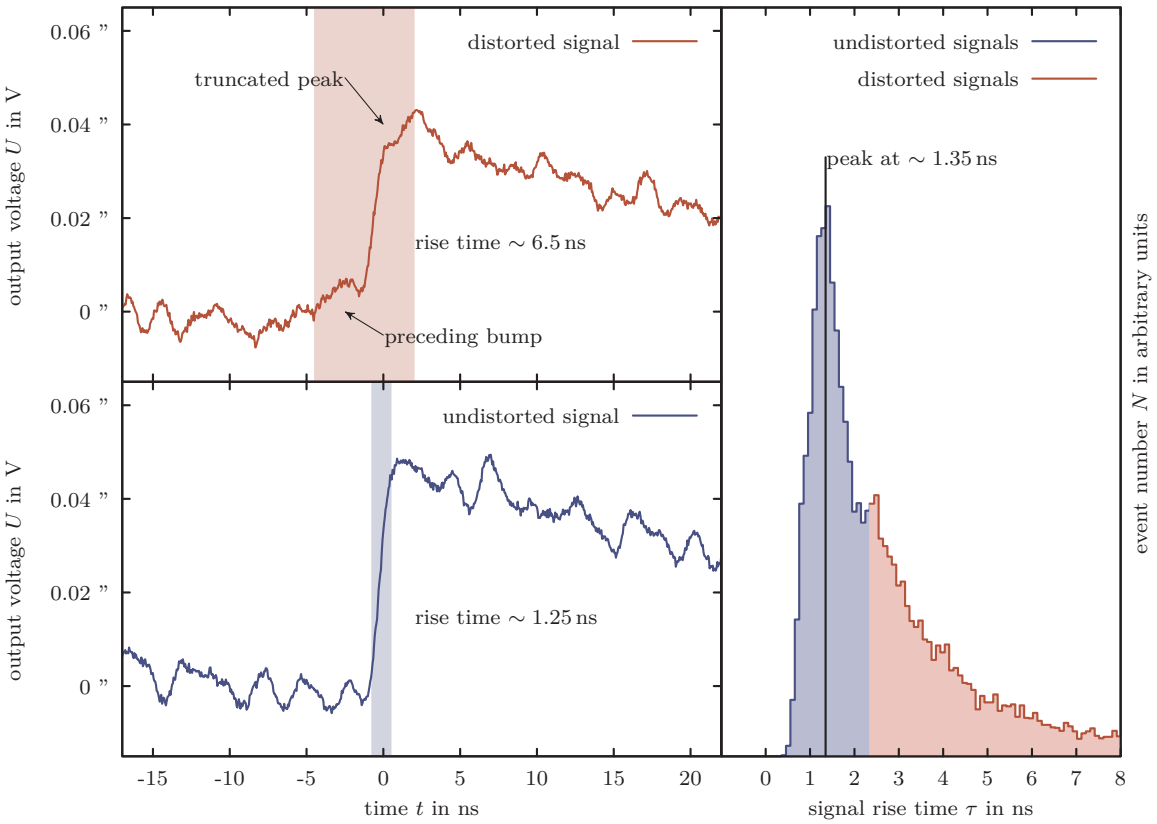

Figure 8.4.: Bottom left: The typical signal shape of the Hamamatsu S8664-1010 detector. The signal rise time determined by the oscilloscope in the blue shaded area is approximately 1.25 ns.
Top left: A distorted signal of the Hamamatsu S8664-1010. The preceding noise bump is interpreted by the oscilloscope as part of the signal as well as the truncated peak caused by noise interference. A longer rise time of approximately 6.5 ns is determined by the oscilloscope in the shaded red box.
Right: The rise time histogram created by the oscilloscope with a peak consisting of undistorted signals at approximately 1.35 ns and a tail towards slower rise times caused by distorted signals due to noise interference.
All measurements are made using the SAHAR module and an Agilent Technologies MSO 9254A 2.5 GHz oscilloscope with 20 $\mathrm{GSa\,s^{-1}}$ The former may constitute bandwidth limitations on the whole system. Thus, the determined signal rise time of 1.35 ns is an upper limit for the Hamamatsu S8664-1010 detector. For these measurements a ^{83}Rb source, enclosed in an Al foil that stops all CEs, is used. Thus the majority of the signals in this figure are created by a 9.4 keV γ or a 12.6 keV X-ray line.
The shape of a full signal of the S8664-1010 detector can be found in figure 8.6.

bump and the real signal. In the other case, a negative noise amplitude coincides with the real signal peak, thus truncating the real peak and increasing the determined rise time. These effects are likely to happen for signals with short rise time. Both cases may occur for one signal, leading to even longer rise times. An example for a typical and a distorted signal of the Hamamatsu S8664-1010 detector is given in figure 8.4 on the left side. Because the amplifier's bandwidth may limit the signal rise time, the value estimated from these measurements is the maximal signal rise time of this detector. Combining with the calculations a signal rise time from 0.45 ns to 1.35 ns can be derived for Hamamatsu's S8664-1010 detector.

A histogram of the signal rise times of Excelitas' C30703FH-200T can be found in figure 8.5 on the right side. The typical rise time for this detector is estimated to be 4.9 ns from the histogram, disregarding the tail towards faster rise times. This value is close to the value of 5 ns given in detector's datasheet [Exceli14a]. The tail towards shorter rise times is caused by a sharp maximum of underlying noise during the rise time of the signal. A step with a steep slope and a small dent with a local maximum is created in the rising signal and interpreted as its maximum by the oscilloscope leading to decreased rise times. This effect is more likely to occur for signals with longer rise times. An example for a typical and a signal with reduced rise time is given in figure 8.5 on the left side. The preamplifier bandwidth is not limiting the rise time in this case, much shorter rise times can be reached, see figure 8.4 and section 9.2.

8.2.3.2. Signal decay time

The signal decay time is limited by the terminal capacitance C_{term} of the detector chip and the amplifiers input resistance R_{in}. It can not decay faster than with the time constant $\tau = C_{\text{term}} R_{\text{in}}$ [BarKis06]. The decay time is relevant for experiments where high rates are expected, for PAC experiments it does not play a major role.

The input resistance of the preamplifier used in this work is $R_{\text{in}} = 50\,\Omega$ parallel to a $1\,\text{k}\Omega$ resistor connected to ground. the terminal capacitances are 100 pF, 60 pF and 270 pF for Excelitas' C30703FH-120T, C30703FH-200T and Hamamatsu's S8664-1010, respectively, limiting the decay times to 4.8 ns, 2.9 ns and 12.9 ns. For the two latter detectors the overall signal shape is shown in figure 8.6, the longer decay time for the S8664-1010 detector is obvious. The decay constant τ can be estimated using an exponential fit for the C30703FH-200T, for the Hamamatsu detector the shape of the signal during the first nano seconds after the maximum is better represented by a linear function. The $1/e$ decay times are approximately 8 ns and 35 ns, respectively.

8.3. Alternative low energy γ and CE detectors

Next to APDs, there are some other detector types that are considered to detect the 9.4 keV γ radiation and the 17.8 keV CEs. They are discussed in the following sections 8.3.1 to 8.3.3.

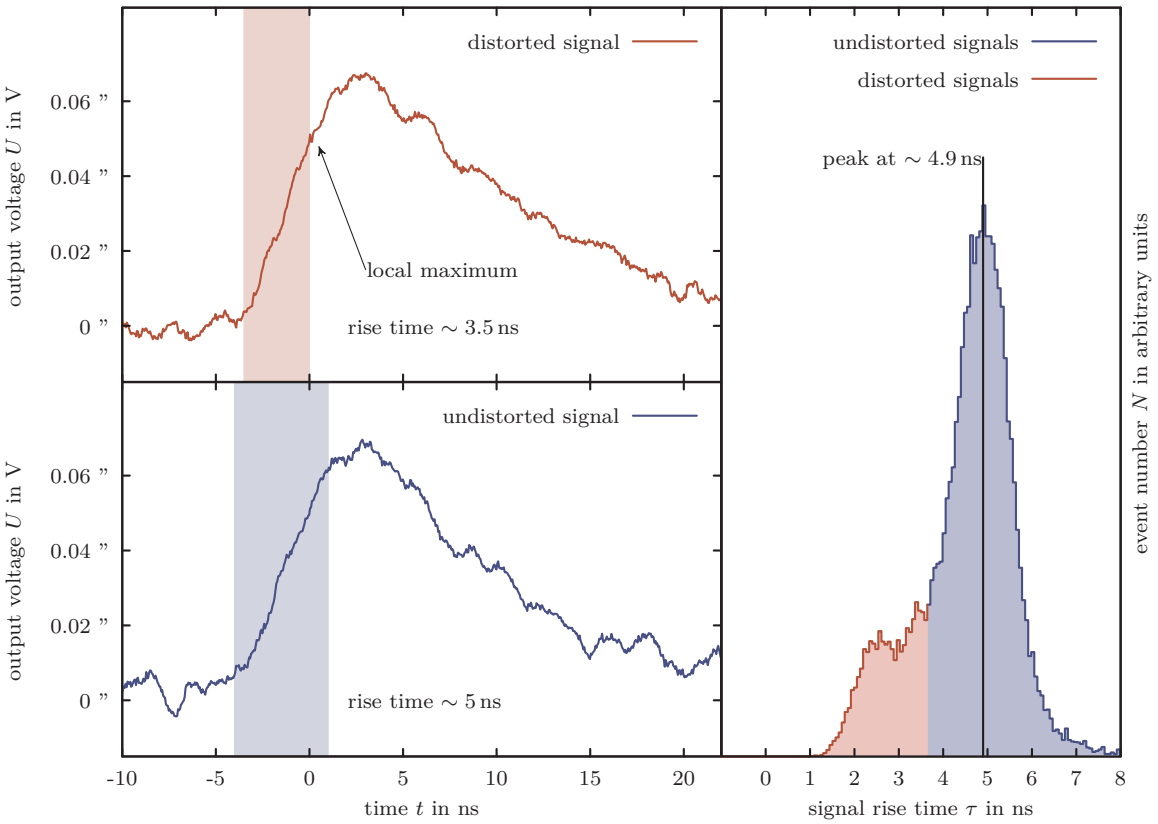

Figure 8.5.: Bottom left: The typical signal shape of the Excelitas C30703FH-200T detector. The rise time is determined by the oscilloscope in the shaded blue box and is approximately 5 ns.
Top left: A distorted signal with noise interference. In the rising slope a kink with a local maximum is created that is interpreted as the signal's maximum by the oscilloscope. The determined signal rise time is shortened to approximately 3.5 ns.
Right: The rise time histogram for the C30703FH-200T detector created by the oscilloscope with a peak at approximately 4.9 ns consisting of undistorted signal. The tail towards faster rise time is caused by signals with a dent in the rising signal due to noise interference.
All measurements are carried out using the SAHAR module and an Agilent Technologies MSO 9254A 2.5 GHz oscilloscope with 20 $\mathrm{GSa\,s^{-1}}$. For these measurements a ^{83}Rb source, enclosed in an Al foil that stops all CEs, is used. Thus the majority of the signals in this figure are created by a 9.4 keV γ or a 12.6 keV X-ray line.
The shape of a full signal of the C30703FH-200T detector can be found in figure 8.6.

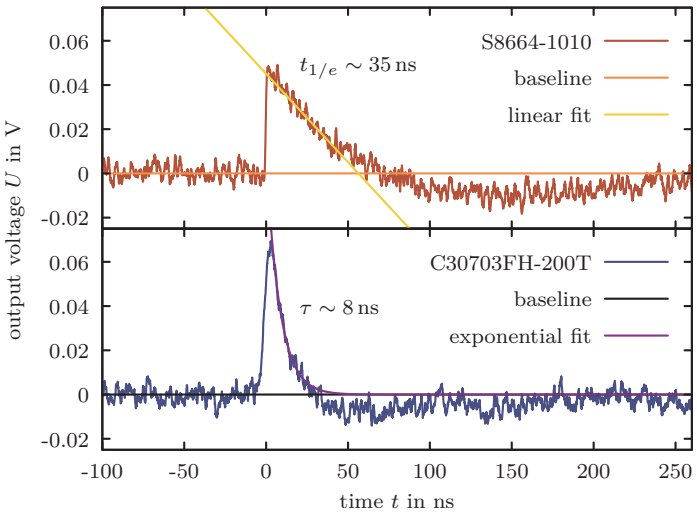

Figure 8.6.: A direct comparison of the typical output signals' shape of Hamamatsu's S8664-1010 (top) and Excelitas' C30703FH-200T (bottom). The $1/e$ decay time is estimated using a linear fit for the former and an exponential fit for the latter detector. The undershoot below the baseline is discussed in section 9.2.3, differences in signal rise behaviour are depicted in figures 8.4 and 8.5

8.3.1. PIN diodes

Windowless Positive Intrinsic Negative (PIN) diodes are suitable to detect the radiation in question as well. They are available as large area devices with sufficiently thick active region to provide a high quantum efficacy. Additionally, they are approximately a factor of ten cheaper than APDs. However, due to the lack of intrinsic amplification the output signal amplitude for both 9.4 keV γ radiation as well as 17.8 keV CEs is very small. Using a charge sensitive amplifier solves this problem at the expense of a short signal rise time, rendering this combination unsuitable for the use in this work.

8.3.2. Microchannel plates

MicroChannel Plates (MCPs) are available in different shapes and sizes. They feature a high gain in the range of e.g. 10^4 to 10^7 [Hamama16b], a high temporal resolution of approximately 1 ns [Shikha97] and they provide a spatial resolution as well. They can reach high quantum efficacies of $\sim 80\,\%$ if they are tailored to match a energy range and radiation type, otherwise the detection probability for 0.02 keV to 10 keV γ radiation is in the range of 5 % to 15 % [Shikha97]. However, the quantum efficacy varies with the incident angle of the radiation [LeePea97] making it difficult to calculate the detection probability if the source is close to the detector causing the radiation quanta to hit the MCP under varying angles. The detection probability for electrons in the relevant range $< 32\,\mathrm{keV}$ (including L,M and N CEs) is not better than 60 % for the models examined by Fraser [Fraser83] and the literature mentioned therein. Furthermore, MCPs are only to be operated in vacuum with pressures around 1×10^{-6} mbar making testing these detectors cumbersome. Due to these limitations and the rather high price, MCPs are not chosen as detector.

8.3.3. Scintillation crystals

Scintillation crystals can be coupled to APDs to detect a wide range of γ radiation [KatSai05]. Reverse reach-through APDs like Hamamatsu's S8664-1010 are especially suitable due to their special doping structure, see section 8.2 and figure 8.2. The quantum efficacy can be adjusted by choosing an appropriate scintillator material and thickness in which the absorption takes place. However, there are some drawbacks of using scintillator crystals.

For maximum light yield, the scintillation crystal should be covered with a reflective material to avoid light losses on the faces of the crystal that are not coupled to the APD. For the 17.8 keV CEs, it is not feasible to work with such a cover at all. Energy loss in this cover would lead to smeared out CE lines in the energy spectrum. This would cause an overlap of the CE lines with the ^{83}Kr X-rays with energies of approximately 12.6 keV or even the 9.4 keV γ stop line. If the cover is chosen too thick it will absorb the electron lines altogether. Measuring without such a cover leads to loss of scintillation light and will thus decrease the signal amplitude.

In order to detect low energy signals like the 9.4 keV γ stop line, the signal to noise ratio can pose a problem. The light emitted in the crystal after detection is not fully transmitted to the APD. In the reflective material surrounding the crystal and due to imperfect coupling between crystal and detector, losses may occur. Furthermore the spectral sensitivity of the APD will, in general, not match the emitted light of the scintillation crystal causing further losses. Low energy signals and noise may thus become undistinguishable.

For detecting high energies like the 553 keV γ start line with a probability of approximately 50 %, scintillation crystals have to be quite thick, e.g. ∼ 10 mm in case of Cerium doped Lutetium Yttrium OxyorthoSilicate (LYSO:Ce) [SaiGob04]. In the case of this more penetrating radiation, it is easier to mount a scintillation detector with photomultiplier outside the vacuum chamber without spatial constraints. Difficulties arising when electronics have to be operated in vacuum conditions, like thermal and outgassing problems are avoided.

Coupling a scintillator crystal to an APD may have an impact on timing properties of the detection system as well. The scintillator's afterglow and the finite length of the APD's signal may lead to rise time performance degradation. Furthermore, covering the scintillation crystal with reflective material increases the average number of reflections per photon before it is detected by the APD and can thus leads to light trapping [SeiSte12].

In this work, Hamamatsu's S8664-1010 detector is coupled to a $(10 \times 10 \times 1)\,\mathrm{mm}^3$ LYSO:Ce scintillator crystal. The APD is ordered at Hamamatsu with a polished surface, a bit of silicone oil is applied between crystal and APD package to avoid reflections and refractions. Polytetrafluoroethylene (PTFE) tape is used as reflective wrapping to reduce scintillation light losses and to fix the scintillation crystal on the detector.

The APD's photo sensitivity depending on the wavelength of the incident light and the emission spectrum of LYSO:Ce are shown in figure 8.7. Despite the quite good match

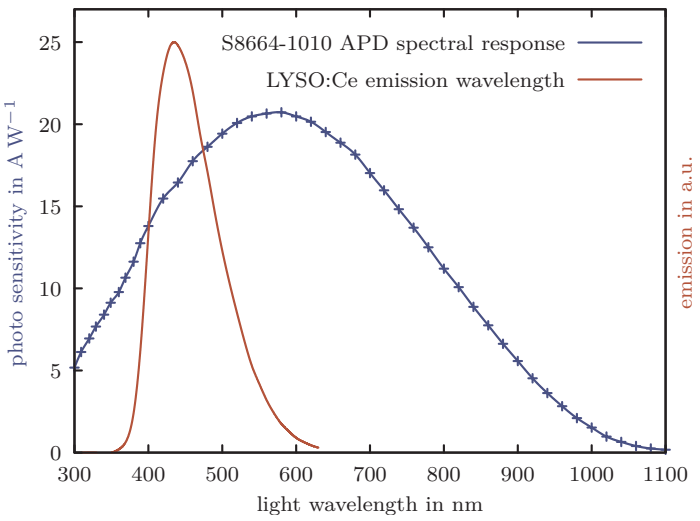

Figure 8.7.: The emission of LYSO:Ce [SaiGob04] (red) and the photo sensitivity of Hamamatsu's S8664-1010 APD (blue) [Hamama12] versus the wavelength. The points provided by Hamamatsu [Hamama12] are interpolated with a cubic spline. The scintillator crystal's emission matches the photo sensitivity curve of the APD, still the detector is not operated at its maximum sensitivity.

of both characteristic curves, losses are inevitable. For LYSO:Ce scintillation light, the quantum efficacy of Hamamatsu's S8664-55 detector, from the same series as the S8664-1010, is reported to be 75 % [Zhu11].

The LYSO:Ce scintillation crystal and Hamamatsu's S8664-1010 are tested with a preliminary preamplifier version. In this configuration, it is not possible to detect the ^{83}Rb 12.6 keV X-rays and 9.4 keV γ radiation due to an insufficient signal-to-noise ratio. The 59.5 keV ^{241}Am γ line is easily distinguished from the noise, indicating a lower detection threshold between 12.6 keV and 59.5 keV.

In comparison to the signal created by direct detection of radiation, the signal rise time increases by approximately a factor of 10 with the LYSO:Ce scintillation crystal. A direct comparison between a signal created by direct detection and through the scintillator coupled to Hamamatsu's S8664-1010 is shown in figure 8.8. Both signals were measured with a ^{241}Am source, the former signal is the response to a γ quantum or X-ray in the range of 13 keV to 26 keV, the latter to 59.5 keV γ radiation. The increased signal rise time is caused by the 41 ns $1/e$ decay time of the LYSO:Ce crystal [SaiGob04] and the rather long tail of the detectors response to radiation, see figure 8.8, that is caused by its high terminal capacitance of 270 pF [BarKis06; Hamama05].

8.4. Detector data summary and conclusions

In principal both Excelitas detectors, and Hamamatsu's S8664-1010 can be used for PAC measurements. A summary of those detectors' properties can be found in table 8.1. Hamamatsu's detector has excellent timing properties when used for direct detection but its low detection probability makes long measurement times necessary. Coupling a scintillation crystal to this detector is possible and increases the quantum efficacy drastically. However, the signal rise and decay time increase significantly and the noise threshold is too

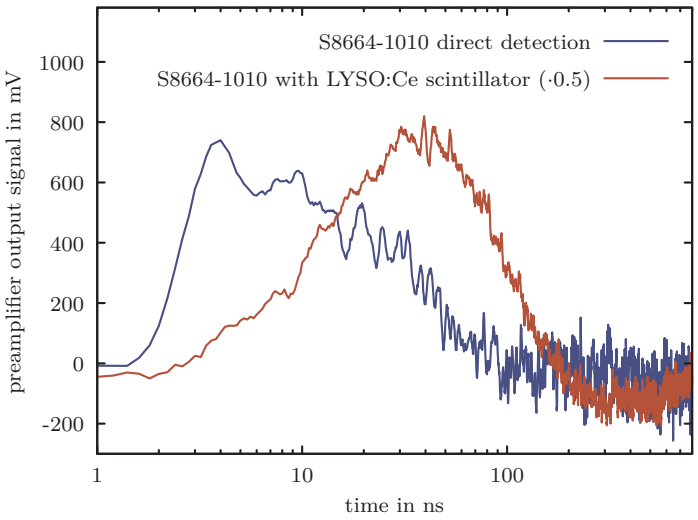

Figure 8.8.: Two signals produced by Hamamatsu's S8664-1010 APD. A directly detected γ in the range from 13 keV to 23 keV (blue) and a 59.5 keV γ detected with a $(10 \times 10 \times 1)\,\mathrm{mm}^3$ LYSO:Ce scintillator coupled to the APD (red, signal multiplied by 0.5). The signal rise time degrades from $\sim$ 3 ns to $\sim$ 30 ns.

high to measure the desired 9.4 keV γ line. The timing properties of Excelitas' C30703FH-200T detector are not as favourable. For the use in the PAC set-up, the signal rise time is sufficient. The signals produced by the APD and the preamplifier are processed by a Constant Fraction Discriminator (CFD) (see section 9.4) making a time resolution below the signal rise time of the detector itself possible. With the coincidence electronics used in this work, time resolutions of 1.6 ns are feasible, see section 10.2.3. The thick active layer is the main advantage of Excelitas' C30703FH-200T, resulting in a high quantum efficacy of 84 %. Additionally, the resulting small terminal capacitance makes the detector preamplifier system less susceptible to oscillations. Hence, Excelitas' C30703FH-200T detector is chosen for the measurements in this work.

Manufacturer	Excelitas	Hamamatsu
Type number	C30703FH-200T	S8664-1010
Doping type	reach-through	reverse reach-through
Active area	$(10 \times 10)\,\mathrm{mm}^2$	$(10 \times 10)\,\mathrm{mm}^2$
Active layer thickness	200 µm	5 µm
Direct detection probability @ 9.4 keV	84 %	4.7 %
Terminal capacitance	60 pF	270 pF
Signal rise time (10 % to 90 %)	5 ns	$0.45\,\mathrm{ns} < t_{\mathrm{rise}} < 1.35\,\mathrm{ns}$
Signal decay time ($1/e$)	∼8 ns	∼35 ns
Available windowless?	yes	yes
Passivation layer thickness	1.2 µm	∼1 µm

Table 8.1.: A summary of Excelitas' C30703FH-200T and Hamamatsu's S8664-1010 detector properties discussed in this chapter. The information on the former detector are taken from the data sheets [EG&G98; Exceli14a] and provided by Excelitas [Exceli16]. The data on the latter is taken from the data sheets [Hamama05], Kataoka et al. [KatSai05], Henke et al. [HenGul93] and provided by Hamamatsu [Hamama16a]. The C30703FH-200T APD by Excelitas is chosen to be used in this work, mainly due to its high quantum efficacy at 9.4 keV.

9. The PAC set-up

In this work Perturbed Angular Correlation (PAC) measurements with two different radiation cascades of the nuclei ^{83m}Kr(^{83}Kr) and ^{83}Rb(^{83}Kr) are carried out simultaneously. The start quantum of the first cascade is a 17.8 keV Conversion Electron (CE), the second cascade is started by a 553 keV γ quantum. Both cascades use the same 9.4 keV γ as stop quantum. ^{83m}Kr(^{83}Kr) and ^{83}Rb(^{83}Kr) as probe nuclei are discussed in detail in section 4.4. While the 553 keV γ radiation is detected using a standard Caesium Fluoride (CsF) scintillation detector (see section 8.1), a custom build preamplifier module is used in conjunction with an Avalanche Photo Diode (APD) (see section 8.2) to detect the remaining radiation. Because CEs are involved in these measurements, the semiconductor detectors are placed inside a vacuum chamber.

In this chapter, the components of the 3+1 detector PAC set-up consisting of three APDs and one CsF scintillation detector are discussed. The mechanical and vacuum aspects are covered in section 9.1, the custom build preamplifier circuit developed in this work, its properties and the signal shaping are described in sections 9.2 and 9.3. In section 9.4 the coincidence electronics and data acquisition are discussed. Finally, in section 9.5 the instrument-based changes of the effective anisotropy are calculated.

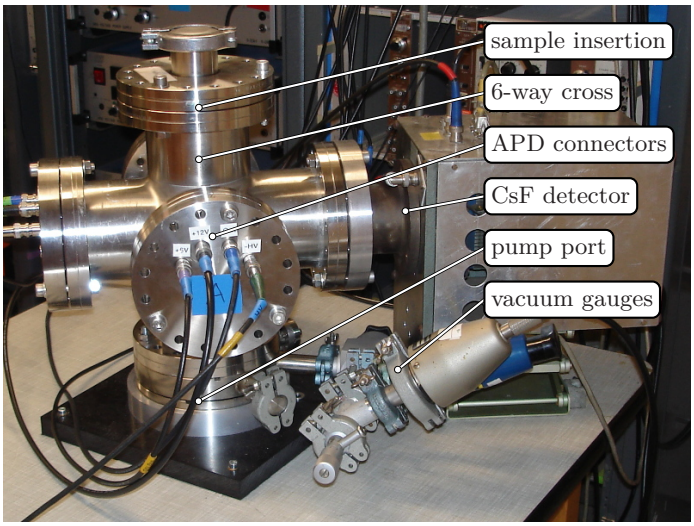

Figure 9.1.: A photograph of the full PAC set-up.

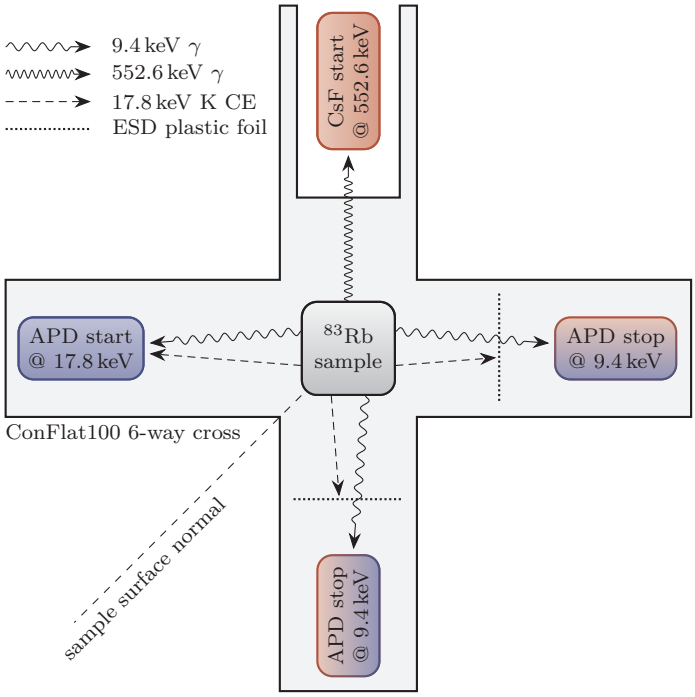

Figure 9.2.: A schematic view of the 3+1 detector set-up. The sample and the three APDs including the preamplifiers are placed in the vacuum, the CsF scintillation detector outside. ESD plastic absorber foils are used to select only electromagnetic radiation for the windowless APDs. Detectors measuring the ^{83}Rb(^{83}Kr) cascade consisting of a 553 keV and a 9.4 keV γ are marked in red, while detectors measuring the ^{83m}Kr(^{83}Kr) cascade consisting of a 17.8 keV CE and a 9.4 keV γ are shown in blue.

9.1. Mechanical set-up

The backbone of the set-up is a DN100 ConFlat six-way cross vacuum chamber. The sample is placed in its centre, one detector is mounted on each flange in a horizontal plane. A schematic of the set-up can be found in figure 9.2, a photograph of the full set-up in figure 9.1. The vacuum chamber's geometry fixes the detector and sample alignment and allows for measurements with fixed 90° angles between all detectors only.

To place the CsF detector used to detect the 553 keV γ quanta outside the vacuum but still close to the sample, a hollow Al cylinder is inserted into and flanged to one of the ports of the chamber. This way, the CsF detector can be placed as close as 29 mm to the sample. The amplifier cases also containing the APDs are inserted into the vacuum through the remaining three side ports in the six-way cross. To provide a good ground connection and thermal coupling to the housing, the amplifier cases are fixed on two Cu rails. These are hard-soldered to a Cu sheet that is pressed firmly on the flange surface using eleven M4 screws. This allows for a heat exchange as good as possible without installing a heat pipe or an active cooling. The flange provides three BNC and one SHV feed-through for bias and supply voltages as well as for the output signal. A photograph of a flange with mounted amplifier case is shown in figure 9.3.

To allow for different distances between sample and the APDs detectors, the amplifier cases are clamped on the Cu rails. The geometry of the case front limits the distance between the surface of the APDs and the sample to 15 mm. The dimensions of the six-way cross allow for a maximum distance of up to 50 mm. A photograph of the vacuum chamber with mounted amplifier cases and sample is shown in figure 9.4.

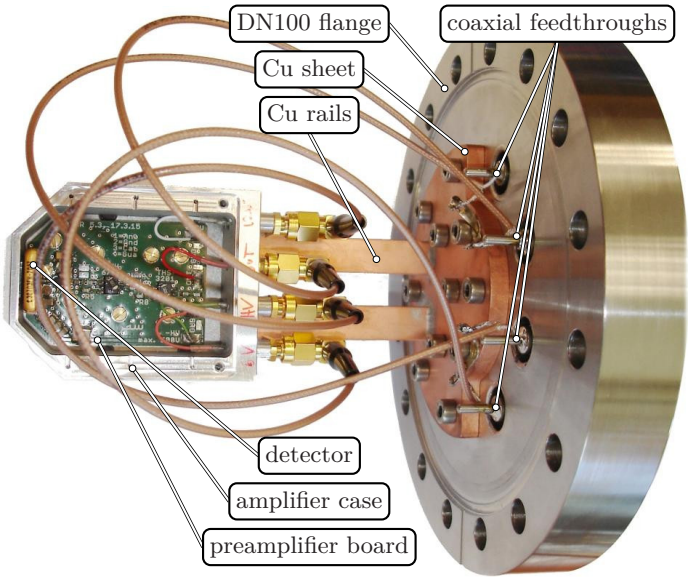

Figure 9.3.: The amplifier case mounted on a DN100 flange via a Cu holding and cooling structure. The case is on ground potential, the cable shields are connected to the Cu sheet next to the coaxial feedthroughs.

The amplifier cases have to be fixed on the Cu rails before being installed in the six-way cross. Once the flanges are fixed, the distance between case and the centre of the vacuum chamber can not be changed using the clamps any more. However, the O-ring tightened flanges make fine tuning of the detector cases' position possible. By applying more or less torque to the screws, the O-rings get more or less compressed. This leaves roughly 2 mm of fine tuning margin. Furthermore, applying more torque on one side, allows for a left-right or up-down adjustment of the amplifier cases' position.

A TurboMolecular Pump (TMP) with an associated roughing pump is connected from below. A fine copper mesh is soldered on the centring ring used to connect the six-way cross and the vacuum hose that leads to the vacuum pumps. It prevents objects from entering the pump port. The measurements take place in pressures ranging from 4×10^{-6} mbar to 8×10^{-6} mbar.

The sample is inserted from the top flange and is placed between the detectors on a platform mounted on one of the amplifier cases. Samples are fixed on an Al frame using conductive silver as described in section 9.1.1.

9.1.1. Sample holders and positioning

For the PAC measurements in this work, the samples have to be placed between the detectors with its surface normal in the detector plane, forming a 45° angle with the start and one semiconductor stop detector. For this a sample holder is necessary.

During the decay of ^{83m}Kr to the ground state, there is a high probability for the emission of CEs. The two prominent 32 keV and the 9.4 keV transitions are converted with conversion factors of 1950 (no uncertainty given) and 16.3(3), respectively [McCutc15]. In order to avoid an electrostatic charging of the samples, they are glued on an Al frame with conductive

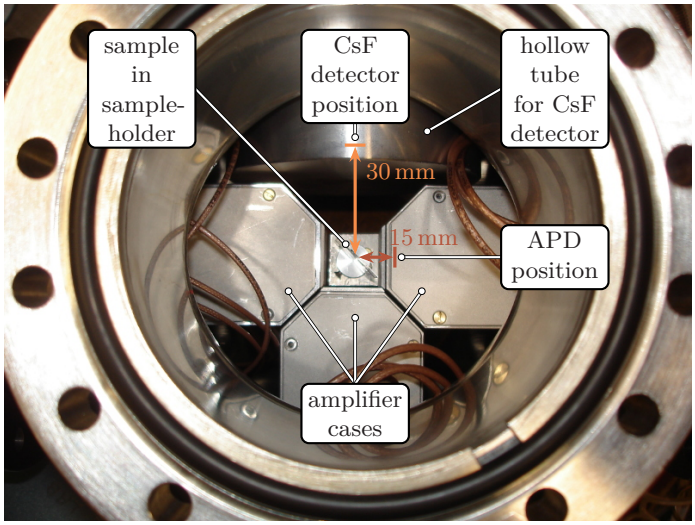

Figure 9.4.: The top view on the detectors and a sample. The sample is placed between the detectors in a sample holder (see section 9.1.1). The distances between the sample and the detectors for this particular situation are shown in the figure.

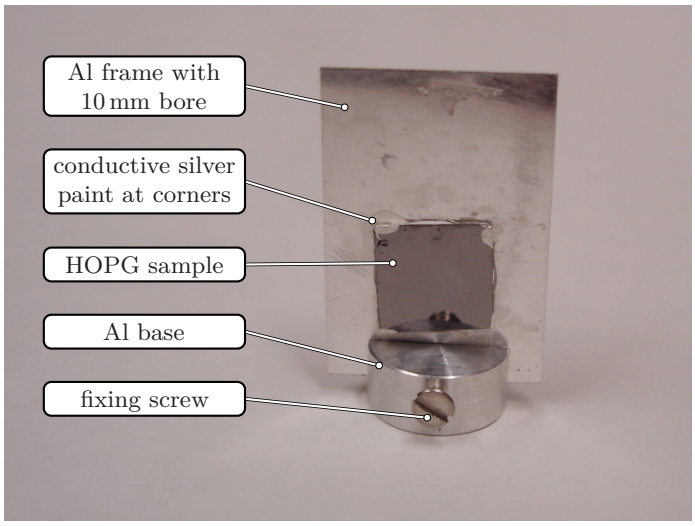

Figure 9.5.: A Highly Oriented Pyrolytic Graphite (HOPG) sample mounted on an Al frame with 10 mm bore behind the sample. The HOPG chip is fixed at its corners with conductive silver paint. The frame is mounted in the base using a fixing screw.

silver paint. The Al frame is fixed on an Al base used for all samples. A mounted sample is shown in figure 9.5.

The sample is placed between the detectors on a platform. The detectors' high voltage is ramped up still under ambient pressure. The height of the 12.6 keV X-ray peak is used to measure whether the sample is positioned central between the three APDs. Absorption for radiation passing through the samples is considered. A schematic of this set-up is shown in figure 9.2, a photograph in figure 9.4.

9.1.2. Amplifier cases

When working with high frequency amplifiers, a proper shielding is essential to reduce electromagnetic interference. The Sequentially Arranged High-gain AmplifieR (SAHAR)

module (see section 9.2) is mounted in an Al case. The detector window in the front can be covered by an aperture, a foil or both, if necessary. For the PAC experiments, circular apertures and ElectroStatic Discharge (ESD) plastic foils are used. The apertures restrict the active area of the windowless APDs hit by radiation to circles with 10 mm diameter. This facilitates the calculation of the anisotropy correction factors shown in section 9.5.1. The ESD foils are used to stop the electrons from entering the stop detectors (see figure 9.2), only 9.4 keV γ radiation is used as stop signal. Their conductive properties prevent the foils from getting charged by electron impact.
The shape of the front allows four of these cases to be mounted with 15 mm between the detectors and a central point. The width of the case is limited by the APD that needs to be installed as close to the front of the case as possible. Venting channels of 1 mm diameter connect the cavity of the case and the measuring chamber via two 90° bends allowing for an operation in vacuum without reducing the shielding properties of the case.

The supply and bias voltages as well as the output are connected via coaxial cables and SubMiniature version A (SMA) connectors providing a well shielded and reliable connection. Wide-band low-pass filters are screwed into the case for the supply and bias lines. The amplifier board is mounted on Al posts in the case and is fixed using nine screws to provide a good ground connection close to the ground pins of the amplifier chips.

The amplification of APDs depends on the bias voltage and the operating temperature. In vacuum, the heat produced by the amplifier can not be dissipated by convection, making thermal conduction the dominant heat dissipation process. The nine screws fixing the amplifier provide a good thermal coupling between the Printed Circuit Board (PCB) and the case.

9.2. The preamplifier module

The preamplifier module used with the C30703FH-200T detector is a voltage-sensitive amplifier consisting of different sequentially arranged amplifier chips with a total voltage gain of ~ 450 abbreviated SAHAR (Sequentially Arranged High-gain AmplifieR). In contrast to the more commonly used charge-sensitive amplifiers, this type allows for fast signal rise times that are necessary for a good time resolution at the expense of energy resolution. The latter is of less interest for PAC measurements as long as the relevant lines can be identified in an energy spectrum.
Developing a custom circuitry has some advantages. Firstly, a circuit and PCB design tailored to a specific detector allows for very short signal lines between detector output and the input terminal of the amplifier. This is crucial to reduce electromagnetic pick-up, minimise parasitic capacitance and the possibly resulting signal distortions. Furthermore, a custom circuit board allows to match the board's mechanical design with the measurement geometry. Lastly, the components used for the amplifier chip are cheaper than a commercial device.
The circuit design is influenced by Baron et al. [BarRüf97] and Flaxer [Flaxer06] but neither

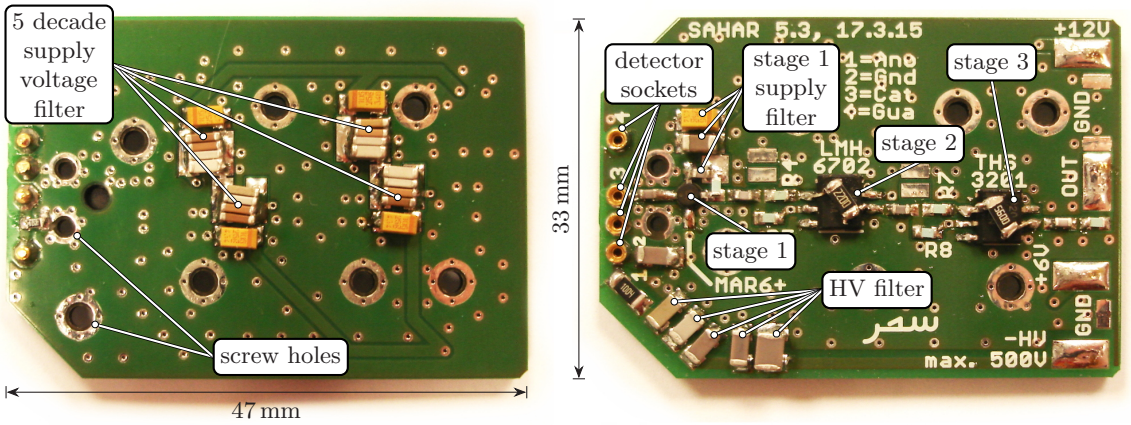

Figure 9.6.: The SAHAR circuit board from top and bottom. The most important components are labelled. For a simplified circuit diagram, see figure 9.7, for the full circuitry figure C.2.

of the circuit designs was chosen due to their individual drawbacks regarding the task at hand. The first design offers limited flexibility due to the fixed amplification of the suggested amplifier chips. Furthermore, it is difficult to find a board layout with a stable circuit not oscillating after excitations by vibrations or electromagnetic pick-up. The second design is not developed for the use with APDs but for MicroChannel Plates (MCPs) and thus lacks amplification. Moreover it is difficult to realise a short connection between detector and first amplifier stage using the suggested amplifier chips because two supply and one feedback line have to be connected.

9.2.1. The circuitry

In this section, the circuitry of the SAHAR preamplifier module is described. It is designed to be used in conjunction with the C30703FH-200T APD by Excelitas. To process the signals with a rise time of 5 ns [Exceli14a] generated by this detector, a bandwidth of $\gtrsim 100\,\mathrm{MHz}$ is necessary. A photo of the PCB is shown in figure 9.6, a simplified circuit diagram in figure 9.7. Additional technical details can be found in appendix C.1.

The negative bias voltage for the C30703FH-200T APD is applied via a $1\,\mathrm{M\Omega}$ resistor. The voltage drop across a $1\,\mathrm{k\Omega}$ resistor grounding the detector and the $50\,\Omega$ input impedance of the first amplifier stage is amplified. The input stage of the preamplifier is AC-coupled to the detector using a 10 nF capacitor.

The first stage of the SAHAR module is a MAR-6+ voltage amplifier [MinCir16a]. This wideband amplifier features a $-3\,\mathrm{dB}$ bandwidth of 2 GHz and a voltage gain of 21.8 dB with an acceptable noise figure of 2.3 dB.
Its VV105 footprint makes it especially well suited as input stage of this amplifier. The MAR-6+ has only four connectors: input, output and twice ground. There is no need for a feedback resistor and only one supply voltage needs to be connected. Furthermore,

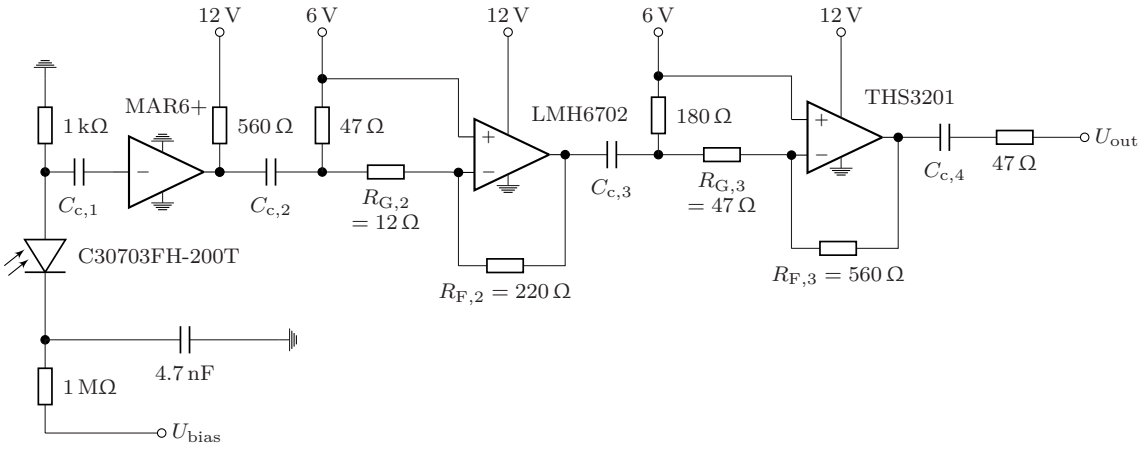

Figure 9.7.: A simplified circuit diagram of the SAHAR module. All coupling capacitors $C_{\text{c},i}$ are 10 nF. The full circuitry can be found in figure C.2, a full list of all components in table C.1.

its body is just 2.16 mm in diameter. These properties allow for a very short connection between detector and amplifier input stage, reducing electromagnetic pick-up and parasitic capacitances.

The second amplifier stage is a current feedback operational amplifier of the type LMH6702 with a SOIC-8 footprint [TexIns14] operated in inverting mode. It is chosen mostly due to its favourable noise characteristics. In the relevant frequency range of over 100 kHz, the noise voltage is in the range of $1\,\text{nV}/\sqrt{\text{Hz}}$, the noise current in the range of $20\,\text{pV}/\sqrt{\text{Hz}}$. Its slew rate of $3100\,\text{V}\,\mu\text{s}^{-1}$ is sufficient to avoid signal distortion. The −3 dB bandwidth of the LMH6702 is not better than 400 MHz for the chosen amplification and thus considerably lower than of the first stage. However, the signals generated by the C30703FH-200T APD can be processed without losses or distortion with this bandwidth.

The final stage of the SAHAR circuit is a THS3201 current feedback operational amplifier with a SOIC-8 footprint [TexIns09] and is operated in inverting mode. The −3 dB bandwidth is comparable to the second stage, the mediocre noise figure of 11 dB is of minor relevance here. The high slew rate of $6700\,\text{V}\,\mu\text{s}^{-1}$ is sufficient even for high signal amplitudes.

9.2.2. Bandwidth, amplification and noise properties

To verify a sufficient bandwidth of $\gtrsim 100$ MHz, the amplification of the SAHAR module's amplification is measured as a function of the input signal frequency. A sinusoidal test signal produced by a Rohde und Schwarz SML 02, 9 kHz … 2 GHz generator is coupled into the amplifier using the detector sockets. Input and output signals are monitored on a Tektronix TDF3054 500 MHz $5\,\text{GSa}\,\text{s}^{-1}$ oscilloscope.
Additionally, the input signal frequency dependent amplification is simulated using the

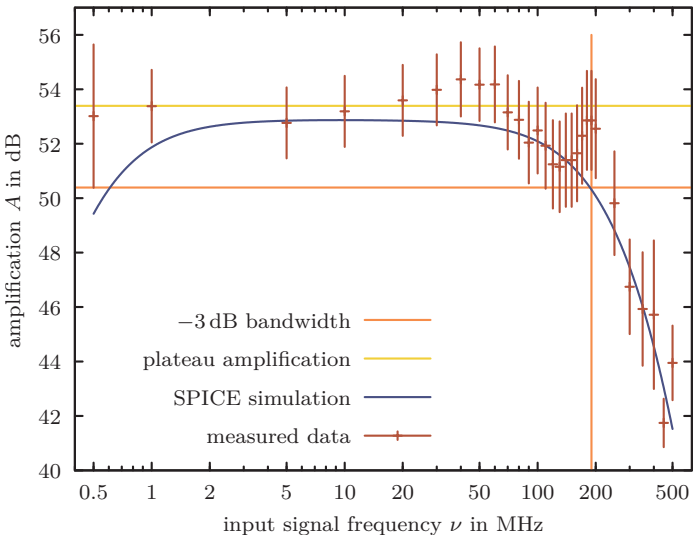

Figure 9.8.: The SPICE simulation and the measurement of the amplification as a function of the input signal frequency. The low frequency cut is caused by the 10 nF coupling capacitors.

SPICE (Simulation Program with Integrated Circuit Emphasis) simulation TINA-TI (version 9.3.150.4). No SPICE macro is available for the MAR-6+ amplifier chip. The SPICE simulation is thus limited to the second and third preamplifier stages. To compare the measurements with the simulation, the amplification in the range of 50 MHz to 1 GHz of the MAR-6+ chip is taken from the data sheet [MinCir16b], interpolated with a cubic polynomial and added to the simulation results.
Within the uncertainties of the measurement, a good agreement between measurement and simulation is achieved. The drop in amplification for frequencies close to 1 MHz is caused by the 10 nF coupling capacitors. The amplification plateau of 53.4 dB is determined using a least square fit of a constant function to the the measured values in the interval from 1 kHz to 100 MHz. The results of the measurement as well as the simulation can be found in figure 9.8.

The amplification of 53.4 dB corresponds to a total voltage amplification of 468. When planning the preamplifier module, two operational amplifiers were chosen as second and third amplifier stage. Both amplifiers were planned to be operated with a voltage amplification in the range of 4 to 18, leading to possible total voltage gains from 190 to 3900 for all three stages. The amplification can be changed for both operational amplifier stages to avoid ringing and oscillations and can be adapted to the experimental needs. However, after the assembly of the amplifier, it was discovered that the LMH6702 does not show the expected behaviour in this circuit. The amplification is limited to ~ 4, thus the total amplification remains in a range from 190 to 890.
Because the preamplifier is stable and an amplification of 53.4 dB is sufficient in conjunction with the C30703FH-200T APD, it was decided not to change the circuitry.

To determine the dynamic range of the SAHAR module, a sinusoidal input signal is applied to the input of the amplifier circuit. For different signal frequencies ν, the input signal's amplitude $U_{\text{out}}(\nu)$ is increased until either a distortion of the output signal is observed, or the amplitude of the output signal does not increase any more. Furthermore, the amplifier's

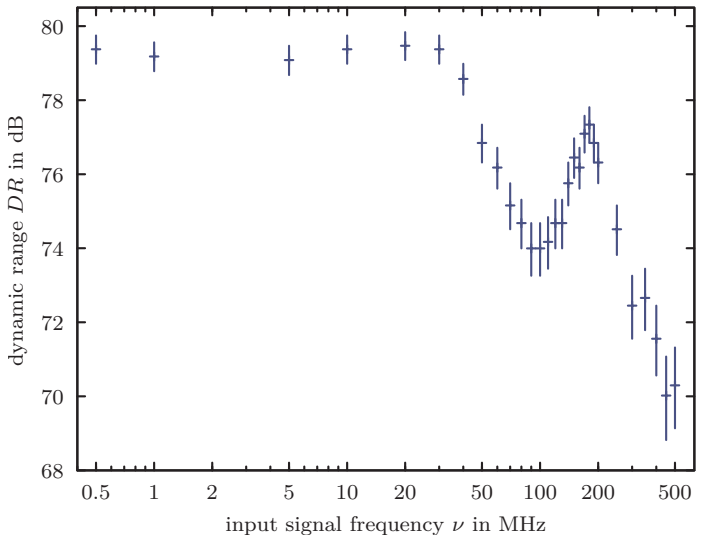

Figure 9.9.: The dynamic range of the SAHAR preamplifier as a function of the signal frequency.

property	frequency range	value
$-3\,\mathrm{dB}$ bandwidth	$\sim 190\,\mathrm{MHz}$	–
voltage gain	$1\,\mathrm{kHz} - 100\,\mathrm{MHz}$	$53.4\,\mathrm{dB}$
dynamic range	$1\,\mathrm{kHz} - 200\,\mathrm{MHz}$	$> 74\,\mathrm{dB}$
	$1\,\mathrm{kHz} - 30\,\mathrm{MHz}$	$> 79\,\mathrm{dB}$
noise RMS (open input)	–	$4.1\,\mathrm{mV}$
noise RMS (shorted input)	–	$2.4\,\mathrm{mV}$
noise RMS ($47\,\Omega$ terminated input)	–	$3.5\,\mathrm{mV}$
noise figure	–	$2.8\,\mathrm{dB}$

Table 9.1.: Some properties of the SAHAR module.

Root Mean Square (RMS) noise level with attached and biased detector is determined. From these values the dynamic range in dB is calculated

$$DR(\nu) = 20\log\left(\frac{U_{\mathrm{out}}^{\mathrm{max}}(\nu)}{U_{\mathrm{noise}}^{\mathrm{RMS}}}\right) \tag{9.1}$$

In figure 9.9, the dynamic range of the SAHAR module is plotted as a function of the input signal frequency.

The noise figure of the SAHAR module can be estimated using the RMS noise voltage obtained with shortened and $47\,\Omega$ terminated input given in table 9.1. Both input signal S_{in} and input noise power P_{in} are amplified by the power gain G. The amplifier's noise contribution P_{amp} is added to the output noise power.

$$S_{\mathrm{in}} \cdot G = S_{\mathrm{out}} \quad \text{and} \quad P_{\mathrm{in}} \cdot G = P_{\mathrm{out}} + P_{\mathrm{amp}} \tag{9.2}$$

The amplifier's noise power contribution corresponds to the output noise power of 115 nW of the amplifier with short-circuited input. If the amplifier is connected to ground via an

47 Ω resistor, a well-defined noise source is added. This leads to an increase in output noise power to 245 nW. The difference of 130 nW in noise power can be attributed to the resistor's thermal noise. This value is in good agreement with the directly calculated thermal noise power [Friis44] generated by a 47 Ω resistor R at temperature $T = 295\,\mathrm{K}$ with a bandwidth $B = 190\,\mathrm{MHz}$

$$P_\mathrm{R} = \frac{4k_B \cdot B \cdot R \cdot T}{R_\mathrm{term}} = 160\,\mathrm{nW} \tag{9.3}$$

The noise factor F is defined as the ratio of the input and the output signal to noise ratios [Friis44]. Using equation (9.2), it follows

$$F = \frac{G \cdot P_\mathrm{in} + P_\mathrm{amp}}{G \cdot P_\mathrm{in}} \quad \text{and} \quad F_\mathrm{dB} = 10 \cdot \log(F) \tag{9.4}$$

From this, a noise factor of $F = 1.9$ and a noise figure of $F_\mathrm{dB} = 2.8\,\mathrm{dB}$ is calculated.

9.2.3. Signal shape

The shape of the preamplifier's output depends on the characteristics of detector and amplifier. The signal rise time is limited to 5 ns by the C30703FH-200T APD [Exceli14a], the limiting factors are discussed in section 8.2.3.1. The signal decays with a $1/e$ decay time of roughly $\tau_\mathrm{sig} = 11\,\mathrm{ns}$ to an undershoot plateau. Its amplitude is roughly 10 % of the signal's height. After 20 ns to 30 ns the undershoot reaches its minimum and decays with $\tau_\mathrm{us} \approx 124\,\mathrm{ns}$ to the baseline. The example signal presented in figure 9.10 is most probably produced by a Compton scattering event of one of the γ quanta over 500 keV emitted by ^{83}Rb. It is chosen because of the better signal to noise ratio, compared to the lower energy signals while retaining the overall signal shape.
For signals arriving within the decay time of a previous signal's undershoot, the subsequent signal's height is decreased with respect to the baseline. If the signal is processed without correcting for this difference, the electronics registers this event with a reduced energy. For PAC measurements using the $^{83\mathrm{m}}$Kr(^{83}Kr) and ^{83}Rb(^{83}Kr) as probe nuclei with activities below 0.5 MBq this does not pose a problem. A rough overestimate for the average time interval between two events is 1.5 µs. For this estimation it is assumed that the X-rays produced by the Electron Capture (EC) decay of ^{83}Rb and the radiation emitted in the 32.2 keV and 9.4 keV transition are detected in one detector with a solid angle of 2π and 100 % detection efficacy.
The undershoot is caused by the RC coupling between detector and first amplifier stage as well as between the following amplifier stages. Strategies to alleviate this problem are discussed in section 9.6.

9.2.4. Temperature dependent amplification

The APDs as well as the preamplifier modules are mounted in vacuum for this experiment. This means that the waste heat produced by the amplifiers can not be dissipated by

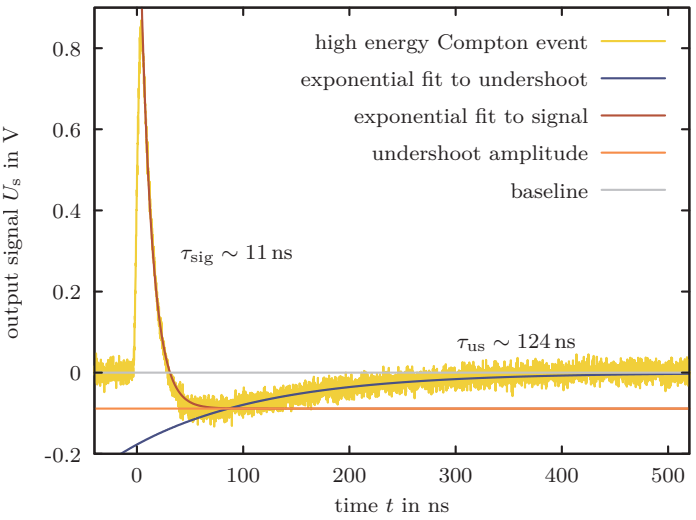

Figure 9.10.: The output signal's shape produced by the C30703FH-200T and the SAHAR module. Exponential fits to the signal's falling edge and the undershoot recovery and the $1/e$ decay times are shown. The undershoot amplitude amounts to roughly 10 % of the signal height.

convection any more. Despite the thermally well-conducting connection to the flange (see section 9.1), this leads to temperature changes of the detector and the amplifier board after evacuating the measurement vessel. Because the intrinsic amplification of APDs strongly depends on the operating temperature, the measurement can not be started before a thermal equilibrium is reached

The stabilizing time is determined with one detector-preamplifier combination at a fixed bias voltage. The position in channels of the most dominant line consisting of the Kr Kα_1 and Kα_2 X-rays is measured repeatedly after turning on the vacuum pumps. The measurement interval is kept as short as 30 s to reduce the drift during the data acquisition itself. For reference, one spectrum is recorded at ambient pressure and room temperature with closed vacuum vessel. All measurements are carried out with a plastic foil in front of the detector to shield the APD from electrons.
The drift in the peak position observed this way can be described by an exponential function. After 12 h the line position has stabilised sufficiently that a measurement can be started. The measurements as well as the exponential fit can be found in figure 9.11

The temperature change of the detector chip can be estimated using the change in amplification from the previous measurement. Although the temperature change can have an effect on the amplification of the SAHAR module as well, this effect is superimposed and dominated by the stronger drift of the APD. The change in amplification caused by the preamplifier is thus neglected. The drop in amplification determined from the measurement shown in figure 9.11 amounts to 19 %. From this and the APDs' individual voltage gain characteristic [Exceli14b] as well as the bias voltage temperature dependence coefficient of $2.4\,V\,K^{-1}$ [EG&G98], the APD's temperature change with respect to the laboratory temperature (22 °C) is estimated. The temperature difference between operation at ambient air and in vacuum is smaller than 15 K for all detectors. Hence, the higher operation temperature does not pose a problem for neither the APDs nor the preamplifier.

A drift of the bias voltage could not be observed with the same method and, consequently, has no effect on the measurements.

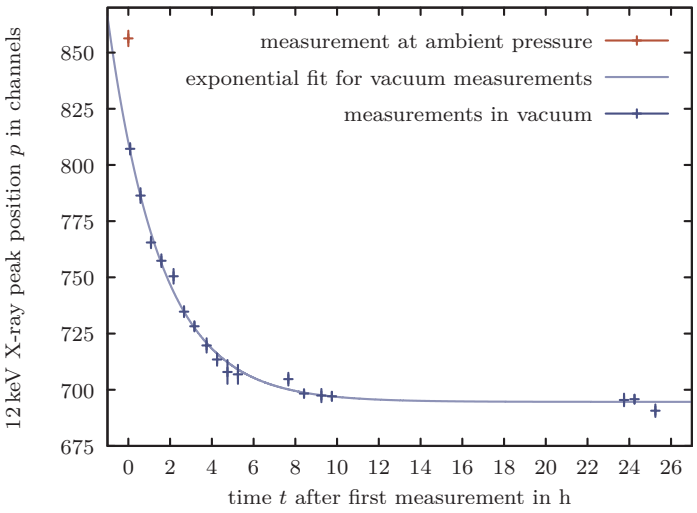

Figure 9.11.: The preamplifier's temperature stabilisation in vacuum. After 12 h the line position is stable enough to start a measurement.

9.3. The splitter module

The signals generated by the SAHAR module have a rise time of 5 ns and a $1/e$ decay time in the range of 11 ns. This is ideal for fast timing using Constant Fraction Discriminators (CFDs). However, the timing in this experiment is realised with a fast-slow coincidence circuit as described in section 9.4. Hence, two signals, are needed: A fast timing signal that is progressed by a CFD and a slow signal that allows for energy selection via a Double Delay Line (DDL) amplifier and Single Channel Analysers (SCAs). These two signals are generated by the splitter module.

9.3.1. The circuitry

To split the signal that is generated by the preamplifier, the so-called splitter module is used. Both outgoing branches of this simple voltage divider are connected to operational amplifiers to avoid load on these branches. The fast signal is directly passed on to the CFD. A full sketch of the splitter module can be found in figure C.3, the core components of the splitter's slow branch are shown in figure 9.12.
The DDL amplifier is not able to process signals with a decay time of 11 ns as they are generated by the SAHAR module. Its input signal should have a decay time in the range of µs. Hence, before the slow signal can be passed on to the DDL amplifier, it has to be shaped.

To generate a longer signal in the slow branch of the splitter module, a 1 nF capacitor is charged by the preamplifier signal. It is discharged via a 10 kΩ resistor generating a signal with a decay time of $\tau = R_\tau C_\tau = 10\,\mu s$. A forward biased BAT83 Schottky diode (D_1) that is positioned before prevents the capacitor from discharging into the input branch. The incoming signal has to pass this diode. For practical reasons, a Schottky diode was preferred over a backward diode. To avoid an amplitude loss of this signal due to the necessary forward bias that is required to make the diode conducting, the diode is forward biased

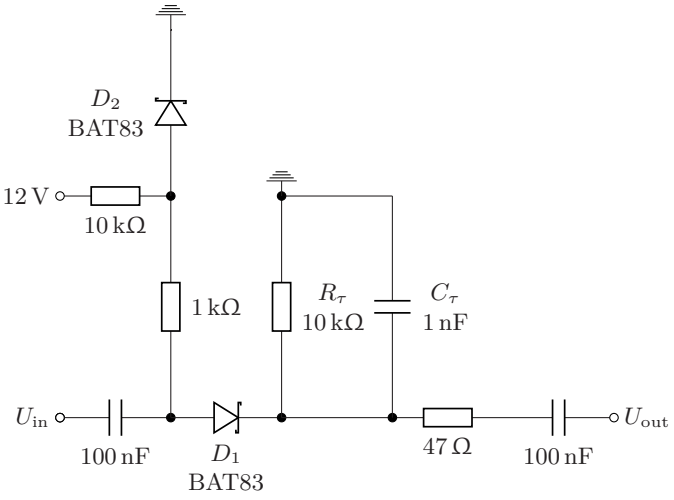

Figure 9.12.: The main components of the splitter module's slow branch. The diode D_2 defines the forward bias voltage for D_1, keeping it close to the conducting threshold. A signal passing D_1 charges C_τ which is discharged via R_τ subsequently, generating an elongated signal. U_{in} and U_{out} are connected to operational amplifiers. The full circuitry can be found in figure C.3.

permanently. The bias voltage is generated using a second Schottky diode (D_2) of the same type. This diode is grounded in forward direction, the voltage drop creates a voltage that is just on the conduction threshold of this diode, which is used to forward-bias D_1. A 10 kΩ resistor in the bias branch prevents the current from getting too high. The signal is amplified using an operational amplifier afterwards to adjust the output signal's amplitude to a desired value.

9.3.2. Signal shape

The shaping circuitry that is described in section 9.3.1 does not work without limitations regarding the linearity of the signal transmission. Due to the non-linearity of the Schottky diode, the amplitude ratio $U_{\text{in}}/U_{\text{out}}^{\text{slow}}$ is not constant. This is in contrast to the fast branch, $U_{\text{in}}/U_{\text{out}}^{\text{fast}}$ is constant over the range of interest.

To measure the relation between the input and the output amplitude of both splitter module branches, a signal generated by a Philips PM 5771 1 Hz – 100 MHz pulse generator, closely resembling the signal shape of the SAHAR module, is fed into the splitter's input. The output signals are monitored on a LeCroy Waverunner 204MXi-A 2 GHz, 10 GSa s^{-1} oscilloscope. Some examples of these measurements are shown in figure 9.13. While the fast signal is passed on with a similar amplitude, barely without distortion, there are some irregularities in the slow branch.
Because the signal has to overcome the rest of the threshold voltage of the Schottky diode, a part of the signal is lost. For signals below 30 mV, the output voltage amplitude is not proportional to the input voltage amplitude, signals below 20 mV are attenuated by at least a factor 2. Between 30 mV and 90 mV input signal amplitude, there is a linear relation to the output signal amplitude.
For input amplitudes over 110 mV, the slow output signal exhibits an overshoot that gets even more pronounced for higher input amplitudes. Even if the overshoot is ignored, the relation between the input's and output's signal amplitude is not linear any more.

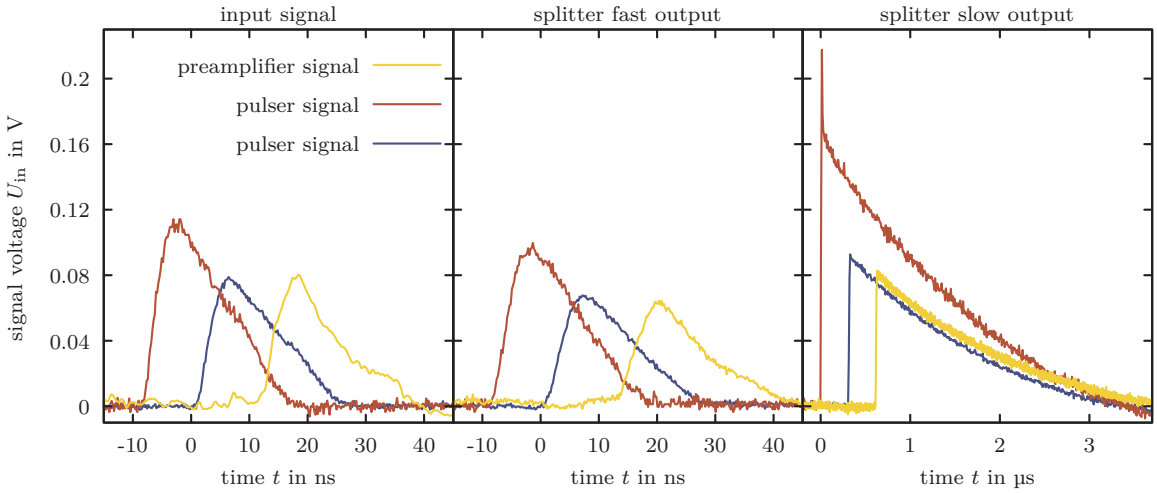

Figure 9.13.: The input signal, the fast and slow branch output signals. Red, blue and yellow output signals belong to the input signal of the same colour.
Left: The input signals generated with a pulse generator and an output signal generated by the SAHAR module, presumably from a 12 keV X-ray quantum. The detector was operated at −345 V during this measurement. The pulse generator signal resembles the preamplifier signal closely but with varying amplitudes.
Centre: The output signal of the fast branch. The signals passes the splitter module with just a slight distortion.
Right: The output signal of the slow branch looks as required for lower input signal amplitudes, an obvious overshoot is visible for higher input signals.

In figure 9.14 the output signal amplitudes of the fast as well as the slow channel are plotted versus the input signal amplitude.

9.3.3. Energy resolution and detection threshold

The signals produced by the slow branch of the splitter module are processed by a DDL amplifier and are used to select events based on the energy deposited in the detector. Although the energy resolution is not of major interest for PAC measurement, the start and stop lines have to be identifiable.

When detecting X-rays or low-energy γ rays, the energy resolution of an APD depends on the energy of the incident radiation. Radiation of sufficiently high energy can penetrate deep enough into the device to reach the charge carrier multiplication region. Charge carriers created there, do not undergo the full multiplication process and thus lead to a low energy tail of the recorded line. The structure of APDs and the different layers including their functions are shown in figure 8.2.

To measure the energy resolution of the C30703FH-200T APD in conjunction with the SAHAR module and the slow branch of the splitter, the X-ray fluorescence radiation of

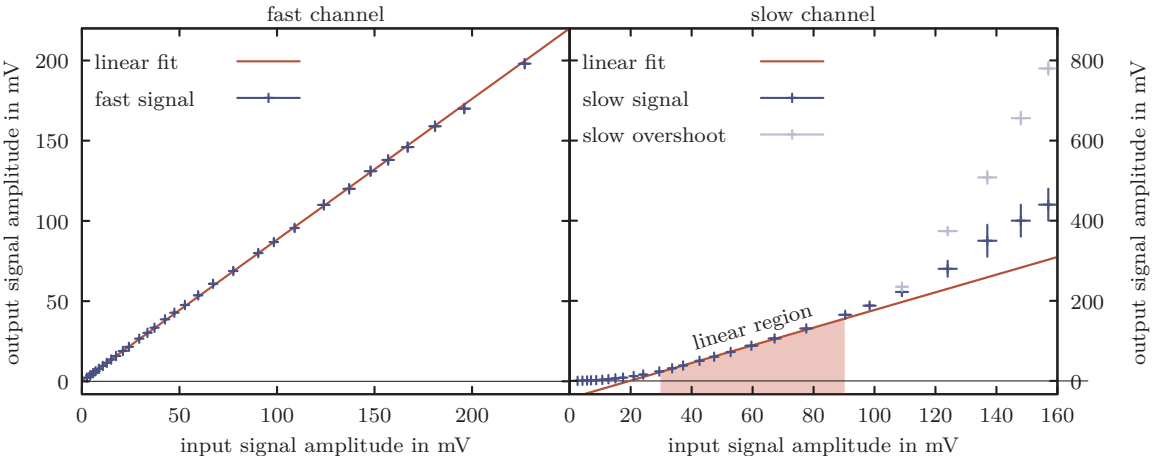

Figure 9.14.: Fast (left) and slow (right) splitter module output voltage amplitude versus input voltage amplitude. While the fast channel is linear over the whole measured range, the slow channel shows a region of linearity beween 30 mV and 90 mV.

material	condition	K$\bar{\alpha}$/keV	Kβ_1/keV	$\overline{\mathrm{K}}_{\alpha,\beta}$/keV	E-res. (left/right)/%
Ti	foil	4.5	4.9	4.5	17/21
Fe_3[C]	bulk	6.4	7.1	6.5	20/22
Cu	bulk	8.0	8.9	8.1	23/22
Br [in SiO]	liquid	11.9	13.3	12.0	36/27
Zr[O] [on Al]	powder	15.7	17.7	15.9	41/23
Mo	foil	17.4	19.6	17.6	48/25

Table 9.2.: The materials used for the X-ray fluorescence measurements. K$\bar{\alpha}$ are intensity weighted averages of the Kα lines used for the energy calibration of the XR-100CR Si detector, $\overline{\mathrm{K}}_{\alpha,\beta}$ for all K lines used for the calibration of the C30703FH-200T detector used in conjunction with the SAHAR module. Elements that are not visible in the spectra are in square brackets. All X-ray data are taken from the X-ray data booklet [ThoLin09].

different materials is used. These materials are irradiated with a collimated 30 keV X-ray beam, some of their properties are compiled in table 9.2. The radiation is detected with the device under test and an Amptek XR-100CR, a cooled Si detector tuned towards a good energy resolution for comparison. The spectra are recorded simultaneously using two different Multi Channel Analyzers (MCAs). The set-up is shown in figure 9.15.

Due to the change in line shape with increasing energy of the incident radiation, no analytical function can be fitted to determine the line position and width. Both, the position of the line and the left and right half maxima are determined using splines to model the form of the spectra. The calculations are carried out using a Python script that is described in appendix C.3.

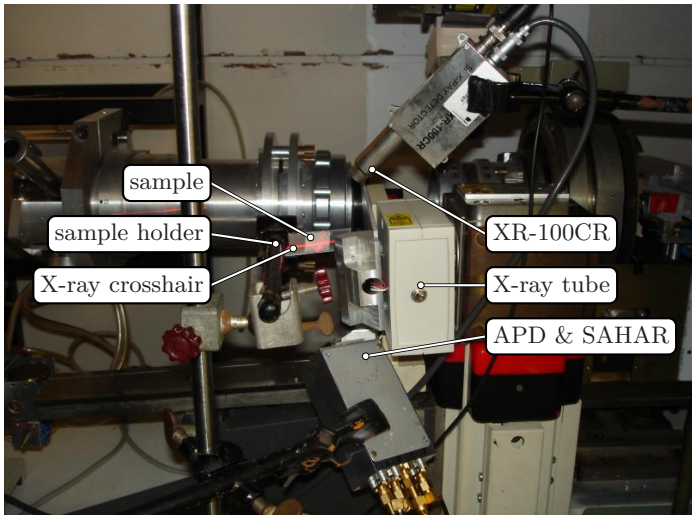

Figure 9.15.: The set-up used to measure X-ray fluorescence radiation with the C30703FH-200T APD in conjunction with the SAHAR module and with the XR-100CR Si detector. The X-ray tube's collimator points towards the point indicated by the crosshair. Fluorescence material available as powder is applied to a double sided scotch tape and an Al sheet.

For all elements compiled in table 9.2 the line position and the left and right half maxima are determined. An energy calibration is carried out using the intensity weighted averages of the K-X-ray lines of each element. The energy resolution for each side of the line is determined, once using the left and once the right half width at half maximum. The results for both sides can be found in table table 9.2. The energy resolution for the right side does not vary significantly. The obtained values have to be considered an upper limit because the emitted X-ray lines are averaged and thus treated as monoenergetic. Hence, the contribution of the $K\beta_1$ line widening the right edge leads to an underestimation of the energy resolution. The energy resolution of the left side deteriorates quickly for energies above 8 keV and improves for energies below this threshold. For higher energies, the previously described effect of incomplete charge carrier multiplication occurs. For lower energies, the splitter module's non-linearity shown in figure 9.14 distorts the shape of the line.

From the measurement shown in figure 9.16 it is obvious that electromagnetic radiation down to an energy of 4.5 keV can easily be measured using the C30703FH-200T APD together with the SAHAR module.

The problems described for electromagnetic radiation do not occur when detecting electrons in the energy range relevant for this work. The 32.2 keV transition's L,M and N-CE lines, although unresolvable with the presented detector preamplifier combination, do not show such a distortion, see figure 10.8. Because no monoenergetic electron source is available, the energy resolution of electron lines is not examined. Instead, the right sided half width at half maximum of X-ray measurements is assumed to be the energy resolution for electron lines.

9.4. The coincidence electronics

PAC experiments rely on the detection of two successive radiations emitted by the same nucleus. All other events do not carry information and have to be discarded. The co-

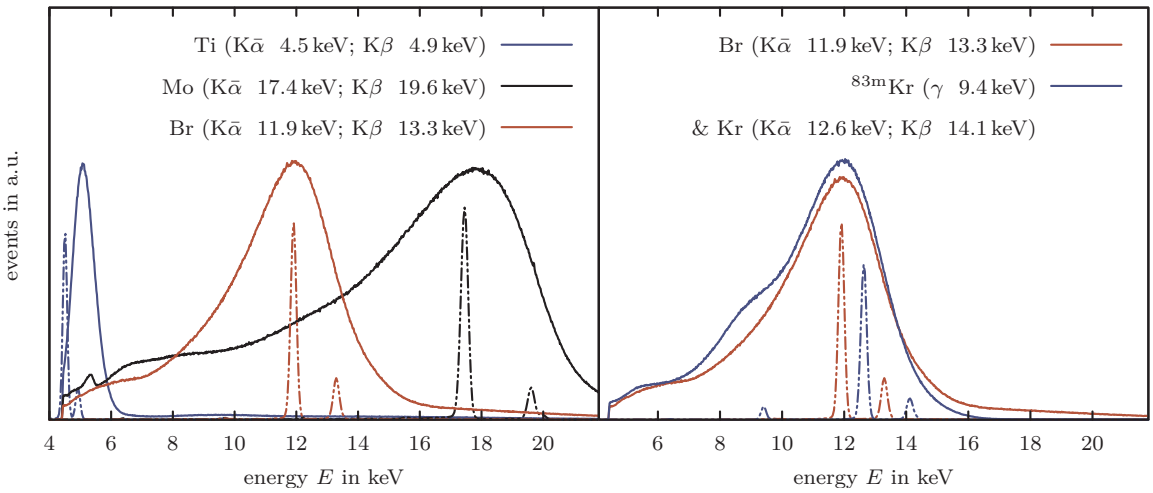

Figure 9.16.: Left: Examples for X-ray lines measured with the C30703FH-200T detector in conjunction with the SAHAR and an Amptek XR-100CR (dash-dotted lines). The asymmetry for lines of higher energy is clearly visible. The offset between the Ti lines measured with both detectors is caused by the non-linearity discussed in section 9.3.3 and shown in figure 9.14
Right: A direct comparison of Br X-ray fluorescence radiation and the radiation (γ and X-ray) emitted during the ^{83}Rb/^{83m}Kr decay. The shift to lower energies of the ^{83}Rb spectrum with respect to the X-ray fluorescence measurements is due to a much higher count rate for the ^{83}Rb measurement and an undershoot in the preamplifier's output, see section 9.2.3.
All spectra are scaled along the y axis for better comparability, thus, this axis is not labelled.

incidence electronics registers all events and records those obeying energy and time selection criteria only. In the following, the fast-slow coincidence electronics is described. The set-up available prior to this work is modified for PAC measurements with the nuclei ^{83}Rb(^{83}Kr) and ^{83m}Kr(^{83}Kr) as described. A block diagram can be found in figure 9.17.

All four branches of the fast-slow coincidence set-up require a separate fast and slow signal. The fast signal is usually generated at the last dynode of a PhotoMultiplier (PM), while the slow signal is taken from a preceding dynode. The CsF detector used to detect the 553 keV line is connected to the electronics in this way. The APDs, however, do not generate two signals and need the splitter module (see section 9.3) to generate a second signal. Here, APD, the preamplifier and the splitter module replace a scintillation crystal and a PM for the 17.8 keV CE and 9.4 keV γ detection.

In the energy branch, the slow signal is processed by a DDL amplifier and forwarded to two SCAs, the first of those handles the start, the second the stop signals. The energy range accepted for start and stop events is defined here, all other events are discarded. For every event within the SCAs' energy windows, a logical pulse is send to an AND gate. In the

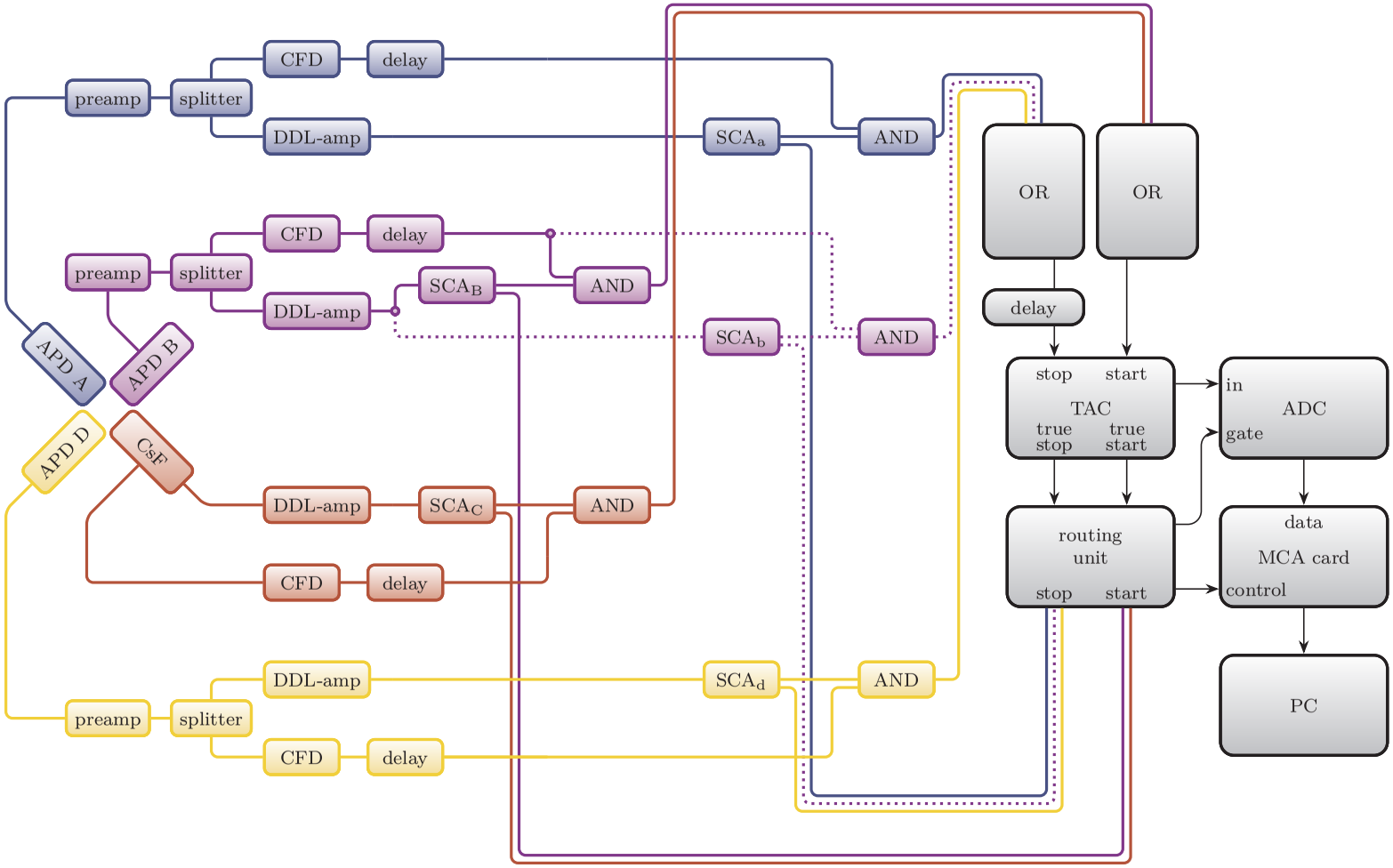

Figure 9.17.: The block diagram of the fast-slow coincidence set-up adapted from Koch [Koch92] and modified to represent the configuration used in this work. The dashed lines are connected but the resulting data can not be used for the data evaluation. See section 9.4 for details.

spectrum	1	2	3	4	5
start detector	APD(purple)	APD(purple)	CsF(red)	CsF(red)	CsF(red)
start quantum	17.8 keV CE	17.8 keV CE	553 keV γ	553 keV γ	553 keV γ
stop detector	APD(blue)	APD(yellow)	APD(yellow)	APD(blue)	APD(purple)
stop quantum	9.4 keV γ	9.4 keV γ	9.4 keV γ	9.4 keV γ	see caption
spectrum type	e-γ, 90°	e-γ, 180°	γ-γ, 90°	γ-γ, 180°	γ-γ, 90°

Table 9.3.: The routing in the fast-slow coincidence set-up. Five spectra are recorded simultaneously. The fifth is discarded because 9.4 keV γ and N and M-CEs from the same transition are detected as stop signal, leading to a mixture of different anisotropies in this spectrum.

timing branch, the fast output is connected to a CFD. There, a logical pulse is generated for all detected quanta. This signal is split, delayed and send to the start and stop AND gates in the energy branch. Hence, the AND gate only generates a signal if the energy branch registered an event within the predefined energy window. If a start signal arrives at the Time to Amplitude Converter (TAC), the measurement is started. The TAC signal is routed to the MCA via an Analog to Digital Converter (ADC) after a stop signal is registered. The results are recorded in one of twelve available spectra, for each combination of start and stop detectors, one spectrum is reserved. The routing unit [Marque96] is connected to all SCAs and controls the correct allocation of the data to one of the twelve spectra.

In measurements using isotopes like ^{111}In, all detectors can act as start and stop detector for one γ-γ cascade. In this work, two cascades are measured simultaneously. For each cascade, one detector acts as a dedicated start detector. A CsF scintillation detector is used as start detector of the 553 keV-9.4 keV γ-γ cascade while one of the APDs is used as start detector of the 17.8 keV-9.4 keV e-γ cascade. The two remaining detectors serve as stop detectors for both cascades. ESD foils prevent electrons from being detected. This results in four recorded spectra, a 90° and a 180° spectrum for each cascade. A schematic of this set-up can be found in figure 9.2. Unnecessary parts of the available fast-slow coincidence electronics remain unconnected, a block diagram can be found in figure 9.17.
The CE detector detects the 9.4 keV stop γ quantum as well. However, it is not possible to use it as additional stop detector. The line is superimposed by N and M-CE lines with different anisotropies due to the particle parameter. The resulting spectrum is still recorded but is not used in the data evaluation.

9.5. Anisotropy change

The anisotropy of the cascades calculated in section 4.5 is a property of the nucleus itself. It is not observed in the experiment because the set-up reduces the anisotropy. The effect of finite detector and sample size as well as intrasource scattering (sections 9.5.1 to 9.5.3) on

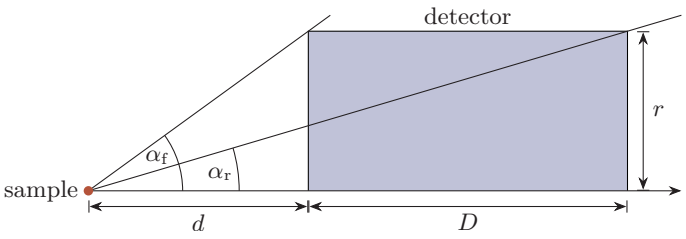

Figure 9.18.: The geometry used to parametrise the detection efficacy for the CsF detector, to scale.

the anisotropy is discussed in this section. The theoretical background for these calculations can be found in sections 4.1, 4.2.1 and 4.2.2.

9.5.1. Finite detector size

To obtain the factor $q_{k,j}(r_j, d_j, \varepsilon_j, E_j, \alpha_j)$ expressing the change of the anisotropy coefficient A_{kk} due to the finite detector size, the detection efficacy as a function of the incident angle and energy $\varepsilon_j(\alpha_j, E_j)$ is required. The efficacy depends on the effective detector thickness D_{eff}, the length of the radiation's trajectory in the detector material. For a fixed energy, it can be described by [BarLam71]

$$D_{\text{eff}}(\alpha \leq \alpha_r) = \frac{D}{\cos\alpha} \tag{9.5}$$

$$D_{\text{eff}}(\alpha_r < \alpha \leq \alpha_2) = \frac{r}{\sin(\alpha)} - \frac{d}{\cos(\alpha)} \tag{9.6}$$

$$D_{\text{eff}}(\alpha_f < \alpha) = 0, \tag{9.7}$$

with the detector's thickness D, the distance d between detector and sample, the detector's radius r and the incident angle α. The definitions of the angles $\alpha_{r/f}$ can be found in figure 9.18. Using equation (4.9) one can write

$$\varepsilon(\alpha) = 1 - \exp\left(-\frac{\mu}{\varrho} \cdot \varrho \cdot D_{\text{eff}}(\alpha)\right) \tag{9.8}$$

The detection efficacy's angular dependence is calculated for the detection of γ radiation using Si and CsF mass absorption coefficients and densities summarised table 9.4. The result is plotted in figure 9.19.

For the detection of the 17.8 keV CEs, the detector's efficacy is $\approx 100\,\%$ and the angular dependence vanishes. In this case, the correction factors are given by equations (4.10) and (4.11) are exact solutions.
When the 9.4 keV γ radiation is detected with the C30703FH-200T APD, the formulae used in the case above become approximations. However, only a small fraction of quanta entering the detector through the front face will pass through the side faces due to the small detector thickness $D = 200\,\mu\text{m}$. In figure 9.18, the angle difference between α_r and α_f gets negligibly small and thus: $\alpha_r \approx \alpha \approx \alpha_f$. Due to the thin active layer, the effective detector thickness and thus the detector efficacy varies only slightly for the relevant incident angles α.

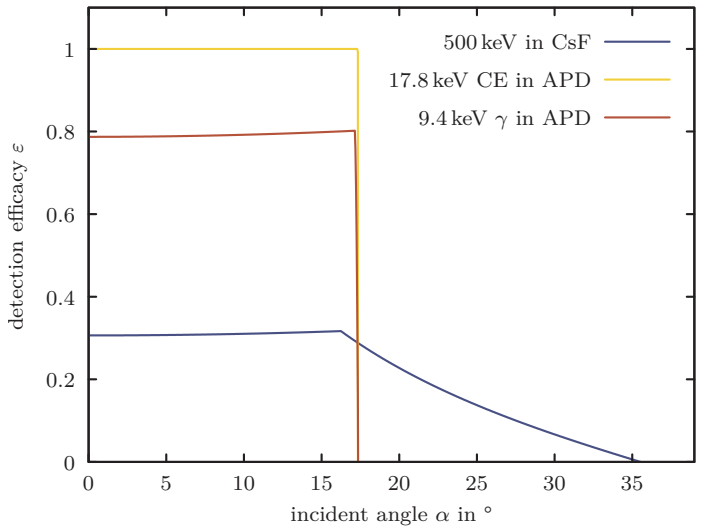

Figure 9.19.: The detection efficacy as a function of the radiation incident angle for all relevant detector radiation combinations.

For the CsF detector, these approximations are not valid any more. A significant fraction of radiation can escape the detector through the lateral surface of the cylindrical CsF crystal. It is necessary to solve the equation (4.7) numerically. The integration is carried out using a fixed-tolerance Gaussian quadrature method in a Python script. The results are compiled in table 9.4. Furthermore, for energies around 500 keV the photoelectric effect is not the dominant interaction process. Hence, it is not a possible to approximate the photo peak efficacy using the total mass absorption coefficient. Instead, the photoelectric mass absorption coefficient is used.

9.5.2. Finite sample size

The effect of the sample's finite size is typically smaller than of the finite detector size. The corresponding correction factors $a_k(A_{22}, A_{44}, r_s, d_j, \vartheta_j)$ can be obtained using equations (4.14) to (4.16). For the calculations, a source diameter of 4 mm is assumed. All measured PAC samples are implanted using the BONn Isotope Separator (BONIS) retarding lens (see section 7.5) leading to beam spot sizes in this range. The A_{22} and A_{44} are taken from section 4.5. All these values as well as the results are summarised in table 9.5.
In the derivation of formulae equations (4.14) to (4.16) an angle independent and constant detection efficacy is assumed. As demonstrated in section 9.5.1 and plotted in figure 9.19, the detection efficacy of the CsF detector at 500 keV differs from this assumption.
To estimate the correction for this case, it is calculated twice: For the first calculation the distance between the front scintillation crystal face and sample is used, for the second calculation the distance between sample and the rear face of the CsF crystal. For the former case, the detection probability is overestimated, while it is underestimated for the latter case. All distances in the derivation of the used formulae by Verheul et al. [VerBlo65] are expressed in units of the distance between sample and detector. The small ratio of the sample's radius and the distance between sample and the CsF crystal reduces the effect of the finite sample size for this detector in comparison to the APDs. This leads to small differences between

detector	APD		CsF	
	value	reference	value	reference
γ radiation energy	9.4 keV		500 keV†	
detector thickness	200 µm	[Exceli14a]	2 ”	section 8.1
detector radius	10 mm	section 9.1.2	1 ”	section 8.1
detector - sample distance	16 mm		35 mm	
detector material density	2.33 g cm^{-3}	[JacCan77]	3.6 g cm^{-3}	[Lavoie73]
mass absorption coefficient	40.42 cm^2 g^{-1}‡	[HenGul93]	0.02 cm^2 g^{-1}♣	[Lavoie73]
approximated $q_{2,j}$	0.933		0.732	
numerically calculated $q_{2,j}$	0.933		0.834	
approximated $q_{4,j}$	0.788		0.290	
numerically calculated $q_{4,j}$	0.789		0.525	

Table 9.4.: All values needed to calculate the corrections for finite detector size and the results of these calculations. The approximated values are obtained using equations (4.10) and (4.11).
†: A γ energy of 500 keV is used for these calculations, no mass absorption coefficient for 553 keV is found in literature.
‡: This value is obtained through linear interpolation using the two neighbouring total mass absorption coefficient values for $E = 9.88$ keV and $E = 8.05$ keV.
♣: The value given here is the photoelectric mass absorption coefficient. Lavoie states a value of 0.2 cm^2 g^{-1}. This is not possible because the total mass coefficient is 0.096 cm^2 g^{-1}, stated in the same paper. In this work, a photoelectric mass absorption coefficient of 0.02 cm^2 g^{-1} and a misplaced decimal point in the work of Lavoie is assumed.

spectrum	e-γ (90°)	e-γ (180°)	γ-γ (90°)	γ-γ (180°)
start quantum	17.8 keV CE		553 keV γ	
stop quantum	9.4 keV γ		9.4 keV γ	
start detector - sample distance	16 mm		35 mm	
stop detector - sample distance	16 mm		16 mm	
A_{22}	−0.14		0.056	
A_{44}	5×10^{-6}		0	
a_0 (underestimated/overestimated)	1.01	0.99	1.00/1.00	1.00/1.00
a_2 (underestimated/overestimated)	1.04	1.04	1.02/1.01	1.02/1.01
a_4 (underestimated/overestimated)	1.11	1.11	1.06/1.04	1.06/1.04
used a_0	1.00		1.00	
used a_2	1.04		1.01	
used a_4	1.11		1.05	

Table 9.5.: All correction factors for finite sample size and the values used to calculate these.

sample material	Pt		HOPG		Be	
density ϱ	$21.45\,\mathrm{g\,cm^{-3}}$		$2.27\,\mathrm{g\,cm^{-3}}$		$1.85\,\mathrm{g\,cm^{-3}}$	
atomic number Z	78		6		4	
molecular mass M	195		12		9	
implantation energy E	4 keV	8 keV	4 keV	8 keV	4 keV	8 keV
implantation depth $z \Rightarrow$ thickness δ	0.6 nm	1.2 nm	4 nm	6.5 nm	5.0 nm	8.5 nm
correction factor s_2	0.99	0.97	1.00	1.00	1.00	1.00
correction factor s_4	0.96	0.93	1.00	0.99	1.00	1.00

Table 9.6.: The anisotropy correction factors for intrasource scattering for all relevant substrates and all values used for the calculation.

the underestimated and overestimated correction factor, the average value for a_0 and a_2 is used. The slightly bigger difference for a_4 is irrelevant because $A_{44} = 0$.
For the measurement of the e-γ cascade, all assumptions that were made during the derivation of these formulae are fulfilled.
Because of the small differences for the correction factors for the 90° and the 180° spectra, the average is used henceforth. All results are summarised in table 9.5.

9.5.3. Intrasource scattering

The anisotropy parameter in PAC measurements involving electrons is altered by scattering processes in the sample itself, see section 4.1. This effect gets more pronounced for thicker and more dense samples with high atomic numbers and lower electron energies. The correction to the anisotropy parameter can be calculated using equation (4.3).
In this work, the emitted electrons are detected only on one side, the ion implanted side, of the sample. The thickness δ that enters in equation (4.3) is thus determined by the implantation depth of the probe nuclei determined by the implantation energy and the properties of the substrate itself. Implantation depth profiles can be simulated using the program Stopping and Range of Ions in Matter (SRIM) (see section 6.2). Results of these simulations for all substrates used in this work and various implantation energies can be found in the respective subsection of chapter 6. The maximum of these distributions is taken as sample thickness δ.
The influence of intra source scattering is minor for the substrates used in this work due to the low implantation energy. For implantation energies around 30 keV the intrasource scattering quickly gets relevant (i.e. $s_2(\mathrm{Pt}, E = 30\,\mathrm{keV} = 0.91)$). The scattering parameters s_k relevant for 17.8 keV CEs and all values used for the calculation are summarised in table 9.6.

9.6. Conclusions and outlook

The preamplifier developed in this work operates reliably without oscillations and is well suited for PAC experiments using the probe nuclei ^{83m}Kr(^{83}Kr) and ^{83}Rb(^{83}Kr). However, there is room for improvement depending on the application of the amplifier.

The most relevant constraint for experiments with high count rates is the undershoot exhibited by the output signal. It is mostly caused by the RC coupling between the three amplifier stages. Usually an undershoot can be cancelled out by a pole-zero cancellation. However, if this is not available the problem can be alleviated by choosing coupling capacitors with higher capacitance. While exchanging $C_{c,1}$ has no measurable effect, replacing $C_{c,k}$ with $k \in 2, 3, 4$ reduces the undershoot significantly. To examine the amplifier's behaviour with different coupling capacitors, the circuit design used for the PAC measurements and one altered design with $C_{c,i} = 1\,\mu F$ are compared in a measurement and in a SPICE simulation.

For the measurement, a Philips PM 5771 1 Hz – 100 MHz pulse generator is connected to the detector sockets of the device under test via a 10 kΩ resistor. The signal applied to the first amplifier stage is triangular with a rise time of ∼ 4 ns, a decay time of ∼ 12 ns and an amplitude of ∼ 6 mV. The same signal is applied to the circuit in a SPICE simulation. Because the MAR-6+ is not available as spice model, it is replaced by an ideal operational amplifier with the appropriate 50 Ω input and output resistors [MinCir16a].
The simulation and the real circuit show comparable behaviour for the original layout, although the undershoot's amplitude and decay time constants differ slighly, see figure 9.20. For the altered layout, the undershoot vanishes in both cases.

The rising edge of the signal produced by the SAHAR module is not limited by the 190 MHz bandwidth of the preamplifier, but by the properties of the used C30703FH-200T detector. The signal-to-noise characteristic and the stability can be improved by including e.g. a 100 MHz high-pass without disadvantages for the PAC measurements. Applying higher bias voltages to the APD and increasing the amplification of the preamplifier module allows to decrease the 4.5 keV detection threshold of the set-up. The limit can be explored in further experiments.

Finally, the supply voltages can be changed to 6 V/−6 V. The 12 V/6 V supply are a result of the evolution of the amplifier and do not serve a purpose any more. In this configuration, however, the coupling capacitors creating the undershoot are necessary. The problem with lacking amplification of the second amplifier stage can be addressed and solved.

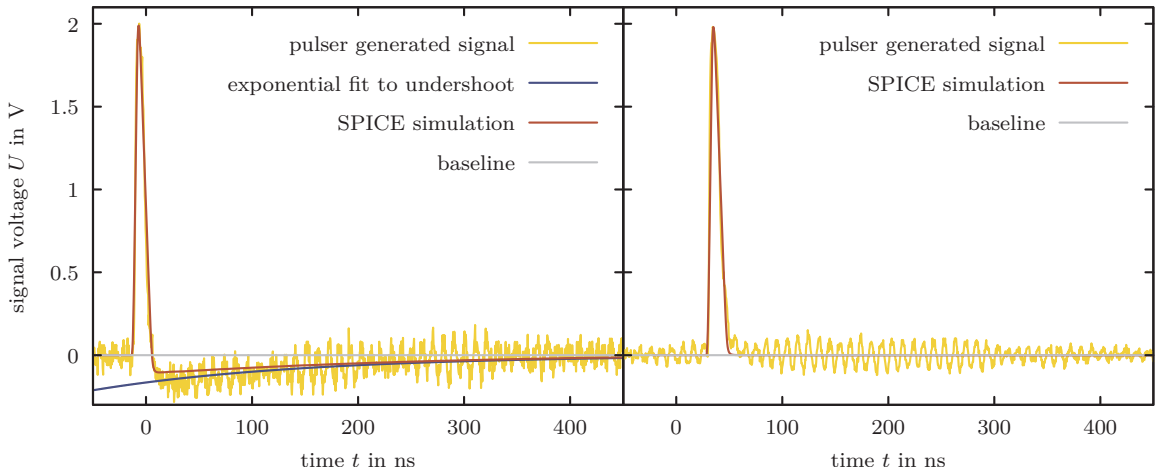

Figure 9.20.: A comparison of simulated and measured signals with the original ($C_{\mathrm{c},i} = 10\,\mathrm{nF}$) and an altered preamplifier circuit ($C_{\mathrm{c},i} = 1\,\mu\mathrm{F}$). The pulser generated signals are noisy because of high frequency electromagnetic pick-up by the connector between pulse generator and amplifier.
Left: The output signal of the original preamplifier design. An undershoot in both the simulated and the measured signal is visible.
Right: For both the simulated and the measured output signal, the undershoot is not visible anymore.

10. PAC measurements using ^{83m}Kr/^{83}Kr & ^{83}Rb/^{83}Kr as probe nuclei

In this chapter the Perturbed Angular Correlation (PAC) and all related measurements are presented. In section 10.1 all measurements verifying the correct operation of the detector systems are discussed. In section 10.2, some preparatory measurements with the full PAC set-up are shown. Finally the PAC measurements of ^{83m}Kr(^{83}Kr) and ^{83}Rb(^{83}Kr) in Be, Pt and Highly Oriented Pyrolytic Graphite (HOPG) can be found in section 10.3

10.1. Test measurements

In this section, the test measurements using ^{83}Rb samples with different combinations of the Caesium Fluoride (CsF) scintillation detector and the C30703FH-200T Avalanche Photo Diode (APD) in conjunction with the Sequentially Arranged High-gain AmplifieR (SAHAR) preamplifier module are described. The correct operation of both detector types and an accurate timing is demonstrated.

10.1.1. APD-APD test coincidence measurements

In the first step towards a working PAC set-up, the preamplifier module developed in this work and the C30703FH-200T detector are tested in a timing experiment. The half life of 155.1(12) ns [McCutc15] of the isomeric 9.4 keV spin $7/2^+$ level of ^{83m}Kr is measured as proof of principle. A simplified decay scheme of ^{83}Rb and ^{83m}Kr can be found

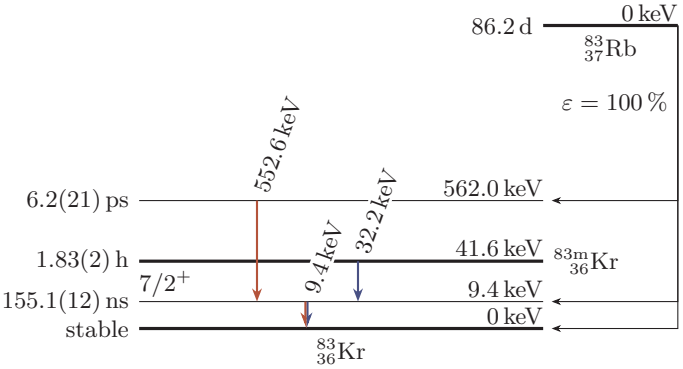

Figure 10.1.: A simplified decay scheme of ^{83}Rb/^{83m}Kr based on data by McCutchan [McCutc15]. A more detailed sketch can be found in figure 4.3. The γ-γ and e-γ cascades are highlighted in red and blue, respectively.

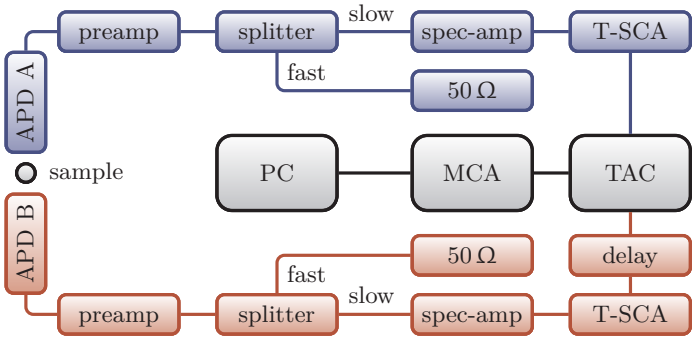

Figure 10.2.: A sketch of the coincidence test set-up. The Timing Single Channel Analysers (T-SCAs) replace the Single Channel Analysers (SCAs) and Constant Fraction Discriminators (CFDs) for the timing in this experiment.

in figure 10.1, a detailed version in figure 4.3. The $\sim 12.6\,\mathrm{keV}$ K$\alpha_{1/2}$ and the $14.1\,\mathrm{keV}$ Kβ_1 X-rays [ThoLin09] emitted after the emission of the $17.8\,\mathrm{keV}$ Conversion Electron (CE) are used as start signal. The $9.4\,\mathrm{keV}$ γ serves as stop signal in this and the PAC measurements. Avoiding the measurement of CEs greatly simplifies this experiment, the set-up does not need to be placed in vacuum. Because no angular correlation is measured, the Al foil implanted with $15\,\mathrm{kBq}$ ^{83}Rb is placed directly between two detectors that nearly cover a solid angle of 2π.

For this measurement, a preliminary version of the SAHAR module is used. It differs from the one described in section 9.2 mostly in mechanical dimensions and is equipped with a linear voltage generator on-board, discarded later for its excessive generation of heat. The SAHAR board and the C30703FH-200T detector mounted on it are enclosed in an Al case to protect both against electromagnetic interference. The detector windows are covered with a $13\,\mu\mathrm{m}$ Al foil to shield them from visible light. The preamplifier is connected to the splitter module (see section 9.3), whose slow output is connected to a spectroscopy amplifier, the fast output is terminated with $50\,\Omega$ to avoid oscillations. Timing Single Channel Analysers (T-SCAs) define the energy windows and generate the logical pulse starting and stopping the Time to Amplitude Converter (TAC). The spectrum is recorded using a Multi Channel Analyzer (MCA) card in a PC. A block diagram of the set-up is shown in figure 10.2.

For the first test, the energy windows of the T-SCAs are set to accept energies from $8\,\mathrm{keV}$ to $15\,\mathrm{keV}$ as start and stop. In this case where start and stop window fully overlap, the resulting time spectrum is symmetric with respect to $t = 0$. The apparatus is time calibrated using a time of flight generator, an uncertainty of $1\,\%$ is assumed.

After $92\,\mathrm{h}$ of measurement time, two exponential functions are fitted to the symmetric time spectrum to obtain the half life of the isomeric $9.4\,\mathrm{keV}$ ^{83m}Kr level, see figure 10.3. The half lifes determined from the left and right part of the spectrum are $153(4)\,\mathrm{ns}$ and $154(4)\,\mathrm{ns}$, respectively. Both are in good agreement with the literature value $155.1(12)\,\mathrm{ns}$ [McCutc15]. The fits converge with a reduced χ^2 of 1.16 and 1.19 and yield uncertainties of $3.4\,\mathrm{ns}$ and $3.3\,\mathrm{ns}$ for the half life including an uncertainty of $1\,\%$ for the time calibration. The prompt part of the spectrum is most probably due to a $12.6\,\mathrm{keV}$ Kα_i X-ray emitted after the Electron Capture (EC) decay of ^{83}Rb and a promptly following $530\,\mathrm{keV}$ γ quantum undergoing Compton scattering in the detector. The width of some ten ns of the prompt

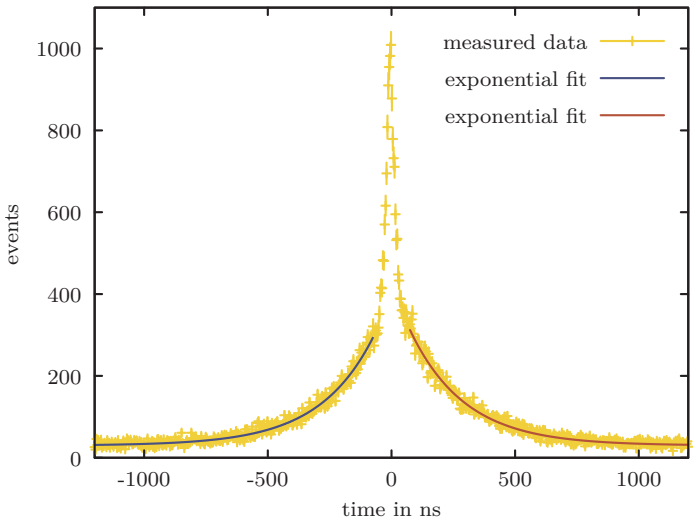

Figure 10.3.: The first timing measurements using the SAHAR module and the C30703FH-200T APD. The half life of the 9.4 keV isomeric level of ^{83m}Kr is determined using the exponential fits. The prompt part of the curve is most probably caused by a 12.6 keV Kα_i X-ray and a 553 keV Compton scattering event in the detector.

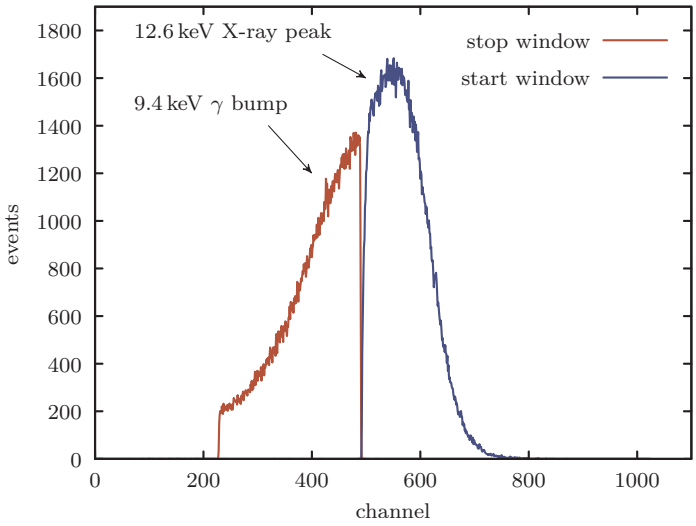

Figure 10.4.: The start and stop windows for the measurements of the isomeric 9.4 keV ^{83m}Kr level's half life. The strong 12.6 keV X-ray start and the 9.4 keV γ stop line overlap but can still be used for the timing measurement.

curve indicates the limited time resolution of this set-up caused by the T-SCAs not suited for fast timing experiments and the use of the slow signals from the splitter modules. Because the time resolution of this particular set-up is of no further interest, it is not discussed in detail.

The experiment is repeated with disjoint start and stop energy windows. The same quanta as before start and stop the measurement. The stop window selects the 9.4 keV bump that can be seen on the left flank of the 12.6 keV Kα_i X-ray peak. The rest of this peak towards higher energies is covered by the start window. The start and stop windows are depicted in figure 10.4.

The resulting time spectrum after 1168 h of measurement time is shown in figure 10.5. The asymmetrical shape of the spectrum shows that start and stop are correctly registered in the respective detector. The prompt part of the spectrum is still present with a width of some ten ns.

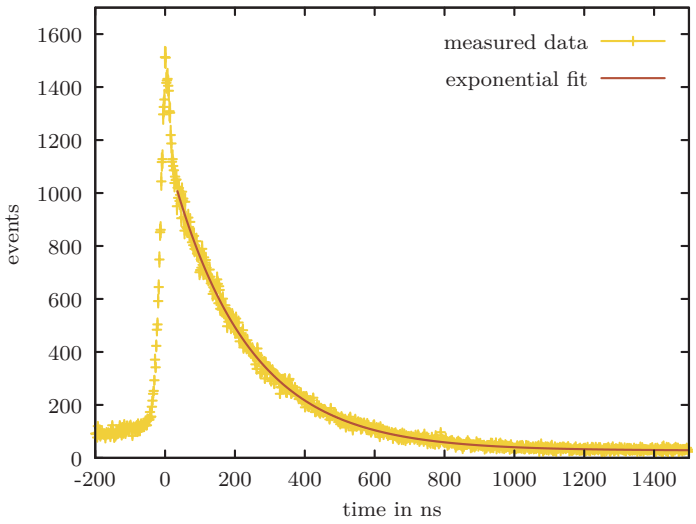

Figure 10.5.: The time spectrum measured with disjoint start and stop energy windows. The energy windows for this measurement are shown in figure 10.4. An exponential function is fitted to the data to determine the half life of the isomeric 9.4 keV ^{83m}Kr level.

Again, an exponential function is fitted to the spectrum to obtain the half life of the 9.4 keV isomeric ^{83m}Kr level. The result of 153.7(18) ns is in good agreement with the literature value of 155.1(12) ns [McCutc15]. The fit converged with a reduced χ^2 of 0.99. The uncertainty results from a combination of the fit's (0.75 ns) and the time calibration's uncertainty (1 %).

10.1.2. APD-scintillator test coincidence measurements

After the correct operation of the APD detectors with the custom preamplifier module is verified, a combination of APD and the CsF scintillation detector is set up. During this test, the 553 keV-9.4 keV γ-γ PAC cascade is measured.

The 553 keV γ is detected by the CsF scintillation detector described in section 8.1, it's fast output is connected to a CFD. The energy window is centred on the 553 keV start line. Contributions from the 520 keV and 530 keV lines are unavoidable due to CsF detector's limited energy resolution. The former two only contribute to accidental coincidences and thus to the background. The CFD is connected to the TAC.
The C30703FH-200T APD is used in conjunction with the SAHAR module again, its output is connected to the splitter module. The splitter's slow output is terminated with 50 Ω, the fast output is connected to a CFD. The energy window is set to include the 9.4 keV γ bump on the 12.6 keV X-ray peak as shown in figure 10.4. The CFD is connected to the TAC via a 100 ns delay cable. The data acquired by the TAC is plotted using an MCA card in a PC. A block diagram can be found in figure 10.6.

The time spectrum measured with this apparatus is shown in figure 10.7. The half life of the isomeric 9.4 keV ^{83m}Kr level is determined by fitting an exponential function to the time spectrum. The fit converges with a reduced χ^2 of 0.96 and results in a half life of 152.4(16) ns which is again in agreement with the literature value of 155.1(12) ns [McCutc15]. As before, the uncertainty is a result of the fit's (0.6 ns) and the time calibration's (1 %) uncertainty.

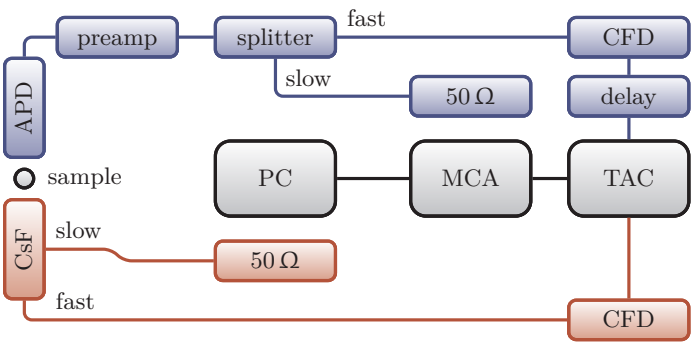

Figure 10.6.: A sketch of the set-up to measure the half life of the isomeric 9.4 keV ^{83m}Kr level using a CsF scintillation detector and an APD. The CFDs define the energy windows and are connected to the splitter's and the CsF scintillation detector's fast output.

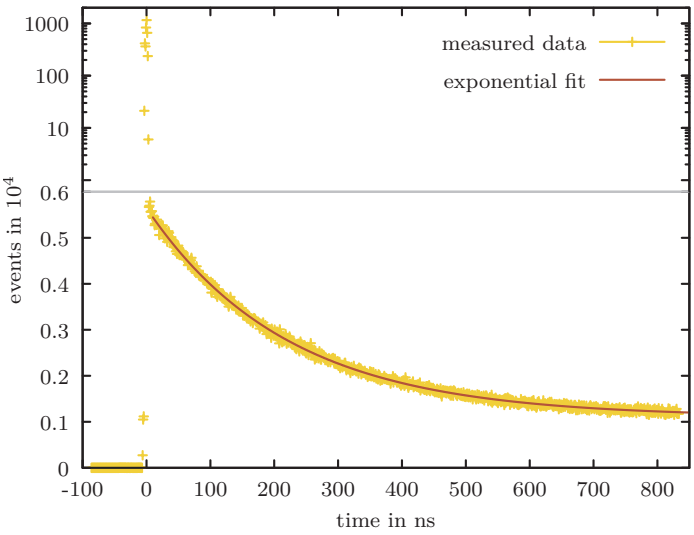

Figure 10.7.: A time spectrum recorded with a CsF scintillation detector and an APD coupled to a SAHAR module. The ordinate's scale changes from linear to logarithmic at $y = 0.6$. The 553 keV-9.4 keV γ-γ cascade is used to measure the half life of the isomeric 9.4 keV ^{83m}Kr level. The prompt part of the spectrum is caused by a 12.6 keV X-ray emitted during the EC decay of ^{83}Rb being detected as stop.

In the time spectrum, the prompt part is prominent. It is caused by 12.6 keV Kα_i X-rays emitted after the EC decay of ^{83}Rb and registered as stop quantum. The 553 keV γ start quantum is emitted after a half life of 6 ps (see figure 10.1) after this decay. Because this difference is not resolvable using the present set-up, they are registered as simultaneous event. The height of the prompt curve can be explained by the relative emission probability of the 9.4 keV γ and the X-rays. While the latter are emitted for every decay, the former is only emitted in 5.9 % of all decays. Due to the overlap of both lines in the energy spectrum (see figure 10.4), many Kα_i X-rays are registered by the stop detector. In contrast to the previous measurements, the prompt curve is less wide. Its width of some ns suggests a big improvement in time resolution when using the fast signals with CFDs. The value of the time resolution of this test set-up is not of relevance, it is not determined in more detail.

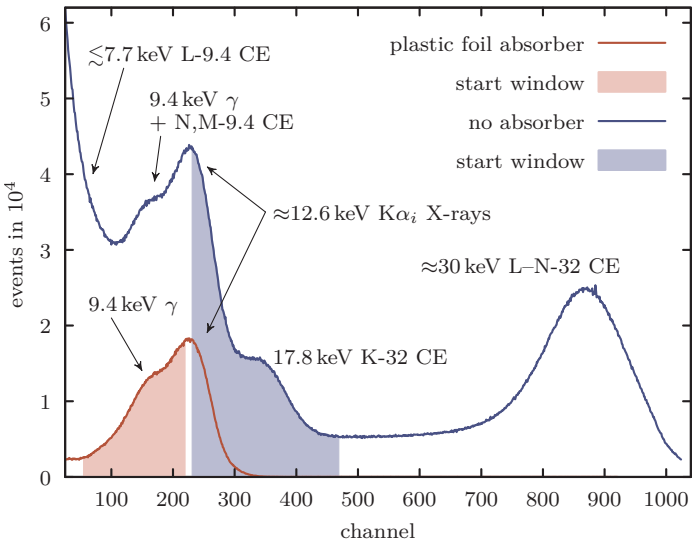

Figure 10.8.: Energy spectra recorded with APDs with and without ESD plastic foil absorber. The energy windows of start and stop window centred on the 17.8 keV CE and the 9.4 keV γ line, respectively, are shown in shaded colours. They do not overlap but include considerable fractions of the Kα_i X-ray lines around 12.6 keV.

10.2. Preparatory measurements

After the proof of principle measurements showing that the timing with both detectors works as anticipated, the full set-up as described in chapter 9 is assembled. A block diagram of the coincidence electronics can be found in figure 9.17, a description of the mechanical aspects in section 9.1.
Prior to the PAC measurements, the energy spectra of the detectors in vacuum are measured and the range of the energy windows is adjusted. Using a set of recorded spectra, the time resolution is determined.

10.2.1. Energy spectrum and energy windows

The full 3+1 detector set-up consists of one CsF scintillation detector and three C30703FH-200T APDs. The former detects the 553 keV start quantum of the γ-γ cascade, while one of the latter measures the 17.8 keV CE, the start signal of the e-γ cascade. The remaining two APDs detect the 9.4 keV γ stop quanta for both cascades. To prevent electrons from interfering with this measurement, ElectroStatic Discharge (ESD) plastic foils are mounted in front of the windowless APDs detecting the stop signals, as described in section 9.1.2. The energy spectra of the shielded and unshielded APDs are recorded and the energy windows are adjusted. The energy window centred on the 17.8 keV CE start line and the 9.4 keV stop line are 10 keV and 6.5 keV wide to ensure the registration of most quanta without an overlap of the energy windows. Corresponding spectra are shown in figure 10.8, the energy windows are highlighted. As a consequence, a big part of the 12.6 keV Kα_i X-ray peak is included in both windows. This does not pose a problem for the time spectrum but results in a big prompt contribution in each cascade and more accidental coincidences.

10.2.2. Half life measurements with the full setup

To ensure the 3+1 detector system's functionality including the peripheral electronics, timing measurements similar to those described in sections 10.1.1 and 10.1.2 are carried out with the PAC measurement electronics. A block diagram is shown in figure 9.17. The vacuum chamber is evacuated simulating the situation during PAC measurements. The 17.8 keV CE and the 553 keV γ are used as start quanta, the 9.4 keV γ as stop for both cascades (see figure 10.1), resulting in four time spectra shown in figure 10.9. All spectra are fitted with an exponential function to determine the half life of the intermediate state. All of these least square fits converge with a reduced $\chi^2 \approx 1$. The results of these fits and the corresponding χ^2 values can be found in figure 10.9. The uncertainties result from the uncertainty of the fit and of the time calibration (1 %), with the latter contribution being the dominant one. The uncertainty weighted average of the four half lifes from the fits is 155.8(2) ns. With the uncertainty of the time calibration the combined result for the half life of the spin $7/2^+$ 9.4 keV level is 155.8(16) All values measured with the full PAC set-up, single or combined, are in good agreement with the literature value 155.1(12) ns [McCutc15].

10.2.3. Time resolution

For PAC measurements, the time resolution plays an important role. The better the time resolution, the finer the details which can be resolved in the time spectra. To measure the time resolution, two simultaneous events are necessary. For both cascades, γ-γ and e-γ, a pair of simultaneous events is available.
After the EC decay of ^{83}Rb an X-ray is emitted. This can be detected in the energy window for the 9.4 keV stop quantum. The 562 keV $5/2^+$ level relevant for the γ-γ cascade is populated with a probability of 61(4) %. Due to the half life of just 6 ps, the emission of the 553 keV or the 520 keV γ line with emission probabilities of 16.0(11) % and 45(5) %, respectively, takes place on a ps time scale (see figure 10.1). Because the set-up can not resolve the time difference between the X-ray and the γ quanta, they are registered as simultaneous and contribute to a prompt part in the time spectrum measured using the ^{83}Rb(^{83}Kr) γ-γ cascade.
After the emission of the 17.8 keV CE, an X-ray is emitted. The latter can be assumed to be emitted simultaneously. While the CE is detected in the start detector, instead of a 9.4 keV γ, a 12.6 keV Kα_i X-ray may be detected in the 9.4 keV stop window at the same time. These events contribute to a prompt curve in the time spectrum measured with the ^{83m}Kr(^{83}Kr) e-γ cascade.

To measure the time resolution, a Be sample is ion implanted with ^{83}Rb at 4 keV. The time spectra are recorded with the four detector combinations used for the PAC measurements. The prompt part of the spectrum can be approximated by a Gaussian function. After the fit, the Full Width at Half Maximum (FWHM) is an estimate on the time resolution of the apparatus. The data of all four spectra, the fits and the results are shown in figure 10.10. For both detector combinations, APD-APD and APD-scintillator the time resolution is in

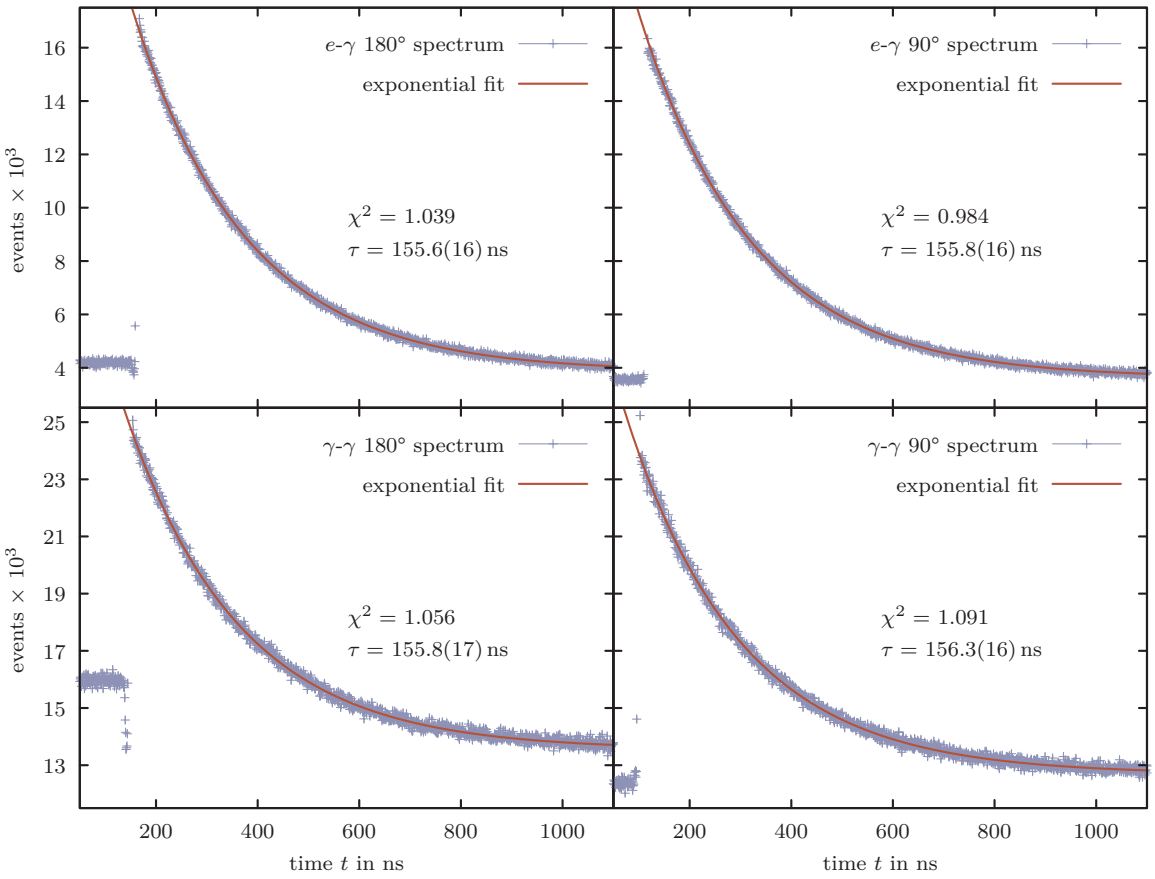

Figure 10.9.: Time spectra recorded with all detector combinations of the full PAC set-up. An exponential function is fitted to all spectra and the half life of the $7/2^+$, 9.4 keV level is determined. The value obtained is stated in the associated quarter of the figure including the reduced χ^2 of the fit. The half life's uncertainty is a combination of the fit and the time calibration uncertainties for each of the spectra. All measured values are in good agreement with the literature value of 155.1(12) ns [McCutc15]. The routing glitch in the lower left corner of the 180° γ-γ spectrum has no effect on the measurement.

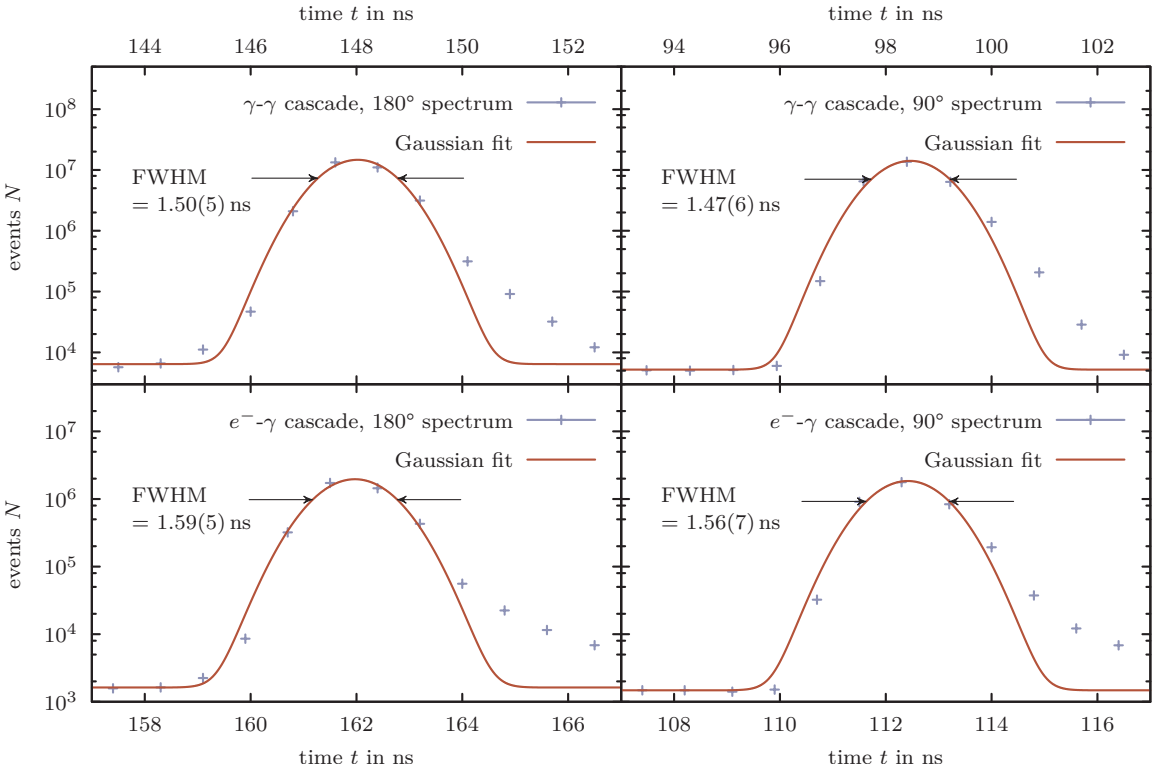

Figure 10.10.: Prompt curves and Gaussian fits to all four recorded spectra. The deviation of fit and data on the trailing edge is caused by the onset of the time spectrum. The uncertainties of the measured points are too small to be visible.

the range of 1.6 ns. It can be concluded that the time resolution of the full 3+1 detector set-up is 1.6 ns.

10.3. PAC measurements

In this section the first PAC measurements with the apparatus developed and described in this work are presented. All aspects of the set-up are discussed in chapter 9. The sample materials, Be, Pt and HOPG are presented in chapter 6 in detail.

The effective anisotropy coefficients are calculated from the anisotropy coefficients A_{22} and the particle parameter b_2 from section 4.5 and the limiting factors given by the set-up (see section 9.5). $q_{2,x}$ is the anisotropy reduction due to finite detector size (detector type x), a_2 results from finite sample size and s_2 from intrasource scattering.

$$A_{22}^{\gamma\text{-}\gamma} = q_{2,\mathrm{APD}} \cdot q_{2,\mathrm{CsF}} \cdot a_2 \cdot A_{22} \tag{10.1}$$

$$A_{22}^{\mathrm{e}\text{-}\gamma} = s_2 \cdot b_2 \cdot q_{2,\mathrm{APD}}^2 \cdot a_2 \cdot A_{22} \tag{10.2}$$

While $A_{22}^{\gamma\text{-}\gamma}$ is the same for all measurements, $A_{22}^{e\text{-}\gamma}$ depends on the substrate due to possible intrasource scattering. In practice, the e-γ cascade's anisotropy coefficient of Pt is slightly reduced, the others remain unchanged. The results of these calculations are listed in table 10.1.

For the fits shown in this section, the program Nightmare is used [Nédéle07], see section 5.3. In principal, the free fit parameters are the additive and multiplicative constants, the damping parameter δ and the interaction frequency ω_0. In some fits, the multiplicative constant assumes unphysical values of more than one. In these cases, the constant is fixed at one. Constant fit parameters and parameters common to all measurements are summarised in table 10.1.

In all fits, the first 5.74 ns are excluded from the fit. In this region an influence of the prompt curve occurring for all cascades can not be excluded. In the plots, this region is shaded in grey. The prompt curves in two different spectra are measured with different detector combinations. Thus, their shape may differ slightly. When calculating the $R(t)$-value, these differences may give rise to single outlying points. An example can be seen in the lower spectrum shown in figure 10.11. There, in the shaded area, one point lies far above all others. A further problem can arise from the time zero calibration. The data is sampled in time intervals of 0.82 ns channel^{-1}. In practice the time zero may lie between two such data points for a given spectrum. In this case it is not possible to match this to another spectrum exactly. In general, the two spectra may be offset by up to 0.42 ns. In three detector configurations this can give rise to spurious, sharply rising signals in the first ns [AreHoh80].

In the following sections, the quadrupole frequency ω_Q, the quadrupole coupling constant ν_Q and the Electric Field Gradient's (EFG) largest component V_{zz} are calculated. The uncertainties given for all values of ω_Q and ν_Q result from the uncertainty of the time calibration amounting to 1 % and from the fit's uncertainties. The Electric Field Gradient (EFG)'s largest component's uncertainty is determined from the aforementioned and the Nuclear Quadrupole Moment's (NQM) uncertainty, $Q = 491(10)$ mb.

Parameter	
Nuclear spin I of intermediate level	$7/2^+$
Time calibration	0.82 ns channel^{-1}
Azimuthal angle Φ	45°
Polar angle Θ	90°
Damping	Gaussian
Fit points	600
Effective $A_{22}^{\gamma\text{-}\gamma}$	0.044
Effective $A_{22}^{e\text{-}\gamma}$ (Be, HOPG)	−0.1698
Effective $A_{22}^{e\text{-}\gamma}$ (Pt)	−0.1664

Table 10.1.: General parameters used for fitting all PAC spectra in sections 10.3.1 to 10.3.4. For a definition of the angles Θ and Φ, see section 3.3.1, details on damping can be found in section 3.3.2. The $A_{22}^{e\text{-}\gamma}$ value of Pt is reduced due to intrasource scattering.

10.3.1. ^{83m}Kr/^{83}Kr and ^{83}Rb/^{83}Kr in Be

For the first PAC measurement, a Be sample implanted with ^{83}Rb at 4 keV is chosen. Rb and Kr have ion radii comparable to the elements Cs and Xe known to occupy the octahedral sites in the hexagonal close-packed (hcp) structured Be where an EFG is present. Thus, a similar behaviour and a visible signal in the time spectra can be expected. For more details see section 6.5.3.

In this section, the results of the measurements of ^{83}Rb and ^{83m}Kr in Be are discussed. These measurements are carried out as-implanted without prior thermal annealing in order to characterise the behaviour of ^{83}Rb in Be which was not studied before. Hence, no information on appropriate annealing temperatures can be found in the literature. The implanted activity is chosen low for this first measurement to keep a ratio of true to accidental coincidences much better than 1. For an activity of 180 kBq, this ratio is expected to be 5.5 for $\tau = 1\,\mu s$, see equation (4.22). However, this formula does not take into account that a significant amount of 12.6 keV X-rays are detected in the energy window of the 9.4 keV γ stop line. Furthermore, events of the 520 keV and 530 keV γ lines are registered in the energy window of the 553 keV start line. This gives rise to an increase in accidental coincidences.

The $R(t)$-value of the γ-γ cascade can be fitted with a single interaction frequency $\omega_0^{\gamma\text{-}\gamma}$ of $345(6)\,\mathrm{Mrad\,s^{-1}}$ resulting in $\nu_Q^{\gamma\text{-}\gamma} = 122.2(23)\,\mathrm{MHz}$. The data and the fit can be found in the upper plot in figure 10.11. The multiplicative constant of 0.77(13) shows that a big fraction of probe nuclei occupies a unique lattice site with a low damping $\delta^{\gamma\text{-}\gamma} = 3.9(13)\,\%$. This is remarkable because this sample was not annealed prior to the measurement.

In contrast to that, the $R(t)$-value of the e-γ cascade is dominated by the strong damping of $\delta^{\text{e-}\gamma} = 450(50)\,\%$ indicating inhomogeneous EFGs at the probes' sites. This is characteristic for samples with implantation damage measured as-implanted. Due to the strong damping, the signal quickly decays to a constant value, the so-called hard core, see the bottom plot in figure 10.11 for the measured data and the fit. However, the measured points after the prompt curve's region of influence, clearly suggest a quadrupole interaction. The fit gives $\nu_Q^{\text{e-}\gamma} = 13.1(18)\,\mathrm{MHz}$ which corresponds to $V_{zz}^{\text{e-}\gamma} = 11.0(16) \times 10^{20}\,\mathrm{V\,m^{-2}}$. All fit parameters are listed in table 10.2. Density Functional Theory (DFT) simulations of Kr in Be carried out by Cottenier [Cotten16] in a $5 \times 5 \times 3$ supercell give $V_{zz}^{\text{e-}\gamma} = -8 \times 10^{20}\,\mathrm{V\,m^{-2}}$ for the octahedral lattice site. Given that frequencies with a high damping are caused by broadly distributed EFGs, they can be inaccurate. Hence, the $V_{zz}^{\text{e-}\gamma}$ from the fit and from the simulation are in fair agreement. Because the EFG's sign can not be determined using γ-γ and e-γ PAC measurements, the negative sign of the simulated EFG can be disregarded. This suggests the ^{83}Kr being incorporated on the octahedral lattice site in a lattice with plenty of implantation damage.

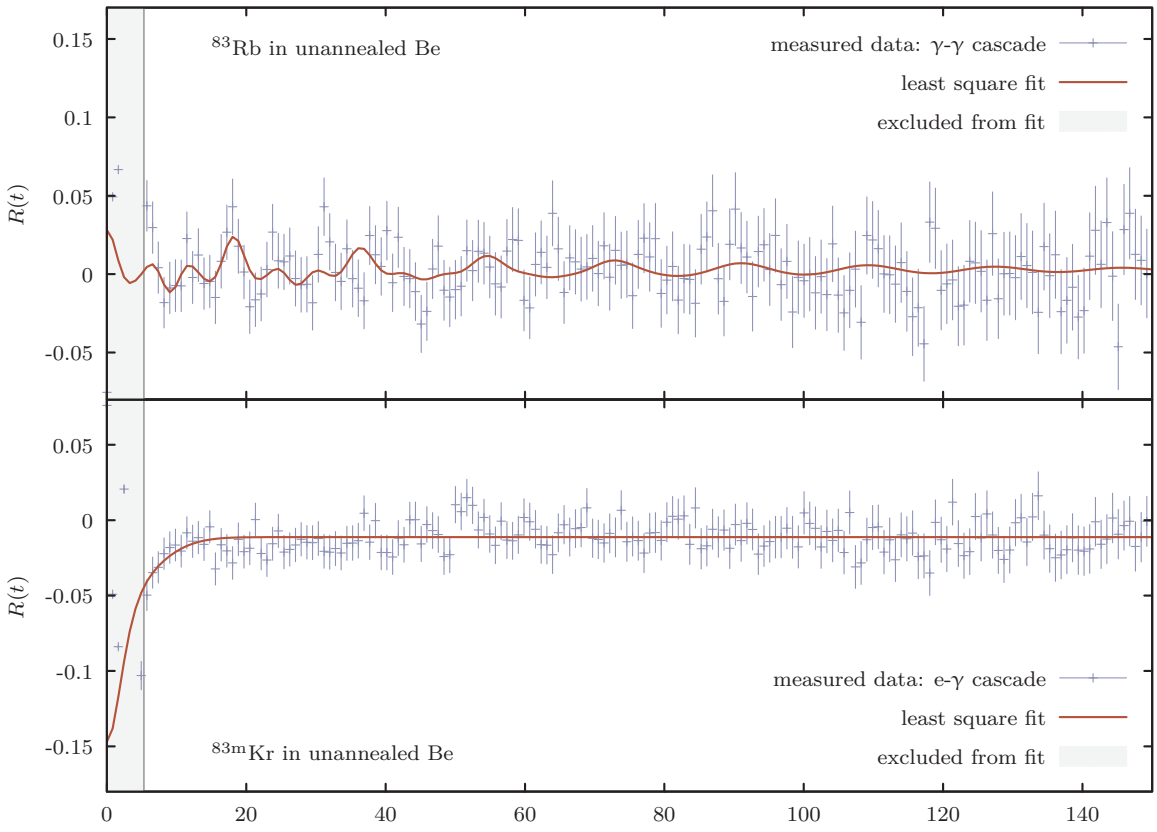

Figure 10.11.: The $R(t)$-spectra of the measurements of ^{83}Rb in unannealed Be (γ-γ cascade, top) and ^{83m}Kr in unannealed Be (e-γ cascade, bottom) including the least square fits. The resulting fit parameters can be found in table 10.2.

Parameter	^{83}Rb(^{83}Kr)	^{83m}Kr(^{83}Kr)
Cascade	γ-γ	e-γ
Activity	180 kBq	
Structure	hcp, polycrystalline	
Implant. energy	4 keV	
Meas. time	57 d	
Fit start at	5.74 ns	
Fit red. χ^2	0.50	0.57
Multipl. const.	0.77(13)	fixed: 1
Additive const.	0†	0.02†
Damping	3.9(13) %	450(50) %
ω_0/Mrad s^{-1}	345(6)	37(5)
ω_Q	9.14(18) MHz	980(130) kHz
ν_Q	122.2(23) MHz	13.1(18) MHz
$V_{zz}/10^{20}$	103(3) V m^{-2}	11.0(16) V m^{-2}

Table 10.2.: A summary of data related to the measurement of ^{83}Rb and ^{83m}Kr in unannealed Be. The upper block contains general information about measurement, implantation and fit. The second block shows the resultant fit parameters. The third block summarises values deduced from the fit parameters. The uncertainties of values with † were rounded down to 0 by Nightmare.

The EFGs for the lattice sites occupied by ^{83}Rb and ^{83m}Kr differ roughly by a factor of 10 and the damping differs nearly by a factor of 100. This may be caused by ^{83}Rb and ^{83m}Kr decaying on different lattice sites. ^{83}Rb decays to the noble gas ^{83}Kr or ^{83m}Kr. After the decay to the metastable ^{83m}Kr with a half life of 1.83 h the noble gas Kr might undergo diffusion processes and might get incorporated on a different, non-equivalent lattice site. In contrast to this, the γ-γ cascade's initial level's half life is 6 ps making diffusion of the probe nucleus before its decay to ^{83}Kr improbable. The big difference in damping could be explained if the ^{83}Rb decays in a homogeneous environment, while the ^{83m}Kr decays in a considerably less homogeneous surrounding.
A possible scenario is the ^{83}Rb being incorporated on an octahedral lattice site prior to the decay while the ^{83m}Kr changes to a non-equivalent lattice site before its decay. This change in lattice site is in contradiction to the channeling measurements carried out by Kaufmann et al. [KauVia79]. The authors show that the noble gas Xe as well as the alkali metal Cs are incorporated on octahedral lattice sites. Thus, Kr and Rb were expected to behave similarly. However, the damage to the lattice due to the ion implantation may cause the Kr atoms to combine with vacancies, provided the ^{83m}Kr was more mobile in Be than ^{83}Rb. In this scenario Kr is not incorporated on an octahedral site, as suggested by the DFT simulations.

If one assumes that the pattern in the data suggesting the interaction frequency are of statistical nature, the fit yields a pattern similar to the e-γ case: the fit is dominated by a strong damping but with a small and positive anisotropy. In this case, both probes, ^{83}Rb and ^{83m}Kr are incorporated in an inhomogeneous environment. This could be the octahedral site described by Kaufmann et al. [KauVia79] with the inhomogeneity caused by implantation damage. This is in agreement with the DFT simulations as well.

10.3.2. ^{83m}Kr/^{83}Kr and ^{83}Rb/^{83}Kr in Pt

The polycrystalline Pt foils ion implanted for this measurement (see section 6.5.1 for details on the sample) have an face-centered cubic (fcc) lattice structure. Due to the high symmetry, no EFG is present in materials of this structure.

The Pt samples used for the calibration of the high voltage system of the KArlsruhe TRItium Neutrino (KATRIN) experiment are not annealed after the ion implantation. In the PAC measurements, the situation present in the solid state calibration samples is to be investigated. Hence, in the PAC measurements, the Pt sample is measured without an annealing after the implantation. The sample is implanted twice with implantation energies of 8 keV and 4 keV, the activities and more details on the sample can be found in table 10.3. During the implantation, less than the desired activity is deposited.

The results of both cascades' fits are characterised by large damping values and low frequencies, see figure 10.12. If there is a signal with high interaction frequency, its damping is large enough to suppress it within the first 5.74 ns that are excluded from the fit. These results are in agreement with the expectation that no EFG is present. In the case of the γ-γ

cascade the interaction frequency is so low that it might as well originate from statistical fluctuations. For the e-γ measurement, the fraction of atoms contributing to the interaction is just 11(1) % and the damping is very high. The origin of this is most likely implantation damage.
The curvature of both spectra limits the fits to anisotropies with the correct sign showing a correct operation of the apparatus. No further information is extracted from the measurements or fits.

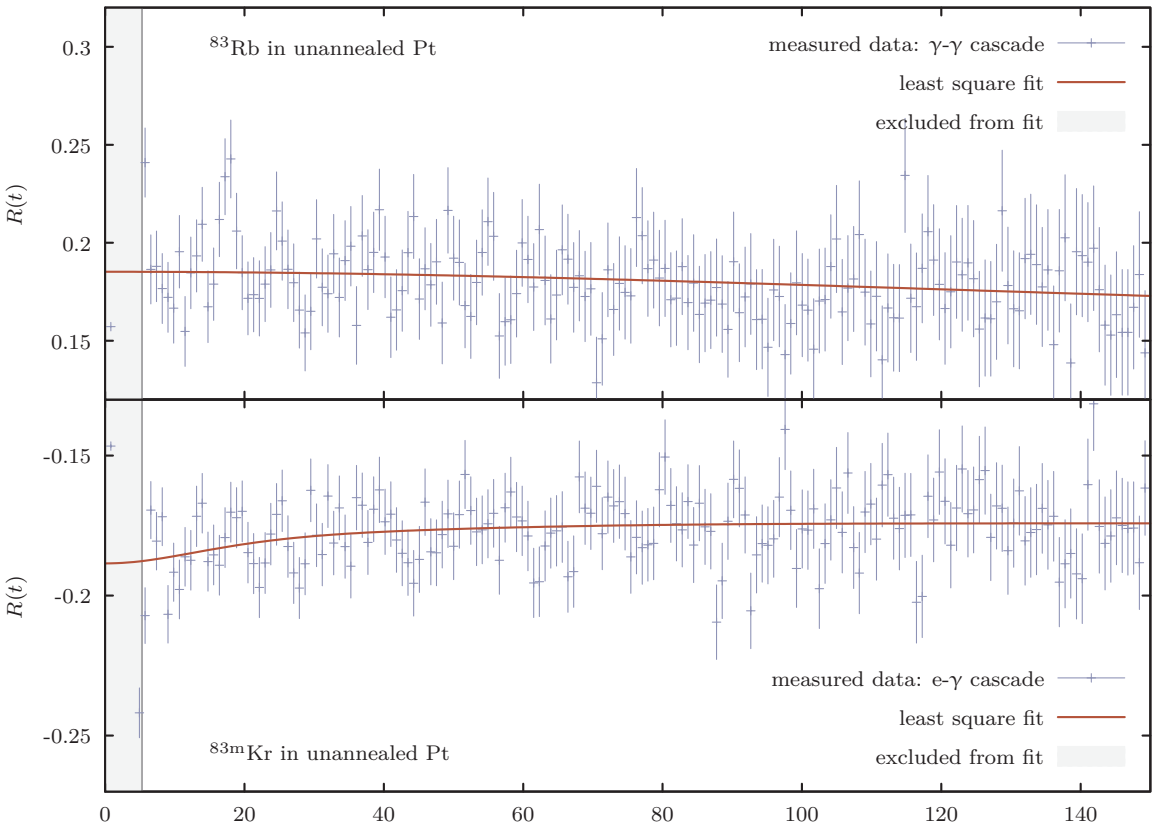

Figure 10.12.: The $R(t)$-spectra of the measurements of ^{83}Rb in unannealed Pt (γ-γ cascade, top) and ^{83m}Kr in unannealed Pt (e-γ cascade, bottom) including the least square fits. The resulting fit parameters can be found in table 10.3.

Table 10.3.: A summary of data related to the measurement of ^{83}Rb and ^{83m}Kr in Pt. The first block lists information about measurement, implantation and fit. This sample is implanted twice, the total activity is thus the sum of two activities. The second block lists the resulting fit parameters. The last block summarises values deduced from the fit parameters. The uncertainties of values with † were rounded down to 0 by Nightmare.

Parameter	^{83}Rb(^{83}Kr)	^{83m}Kr(^{83}Kr)
Cascade	γ-γ	e-γ
Activity	80 kBq + 220 kBq	
Structure	fcc, polycrystalline	
Implant. energy	8 keV and 4 keV	
Meas. time	48 d	
Fit start at	5.74 ns	
Fit red. χ^2	0.53	0.66
Multipl. const.	fixed: 1	0.11(1)
Additive const.	0.14†	−0.17†
Damping	410(60) %	600(160) %
ω_0/Mrad s^{-1}	0.61(9)	4.1(11)
ω_Q	16.2(23) kHz	110(30) kHz
ν_Q	0.22(4) MHz	1.5(4) MHz
$V_{zz}/10^{20}$	0.18(3) V m^{-2}	1.2(4) V m^{-2}

10.3.3. ^{83m}Kr/^{83}Kr and ^{83}Rb/^{83}Kr in unannealed HOPG

This HOPG sample is produced alongside the Be sample described in section 10.3.1 and is implanted with a comparable activity. Being measured after the Be, the initial activity at the start of the measurement is lower than the Be sample's. During the measurement, a sample with higher activity became available. Thus this sample is measured for 11 d only. Ion implanted HOPG chips are used as solid state electron source for calibration purposes at the KATRIN experiment. These samples are not annealed after the ion implantation. In order to study a comparable situation, this HOPG sample is not annealed either. An annealed HOPG sample is investigated in section 10.3.4.

The spectrum resulting from the measurement of the γ-γ cascade is dominated by a strong damping $\delta^{\gamma\text{-}\gamma} = 120(50)\,\%$ indicating inhomogeneous environments of the probes most probably caused by implantation damage. It can be fitted using a fixed multiplicative constant and $\omega_0^{\gamma\text{-}\gamma} = 49(12)\,\mathrm{Mrad\,s^{-1}}$ corresponding to $\nu_Q^{\gamma\text{-}\gamma} = 17(5)\,\mathrm{MHz}$. Because of the pseudo monocrystalline structure of the substrate, a monocrystalline probe environment is assumed for the probes, although a reasonable fit assuming a polycrystalline environment is possible too. Both, the spectrum and the fit can be found in figure 10.13. However, the insufficient statistics and the small anisotropy make this fit unreliable. All fit parameters can be found in table 10.4.

The measurement of the e-γ cascade produces a spectrum that can be fitted using $\omega_0^{\mathrm{e}\text{-}\gamma} = 52.4(24)\,\mathrm{Mrad\,s^{-1}}$ leading to $\nu_Q^{\mathrm{e}\text{-}\gamma} = 18.6(9)\,\mathrm{MHz}$. The multiplicative constant indicates $60(4)\,\%$ of the probes occupying this lattice site. In this spectrum the damping of $\delta^{\mathrm{e}\text{-}\gamma} = 54(4)\,\%$ is moderate. In comparison to the γ-γ spectrum, only a monocrystalline environment yields a good match between data and fit. The $R(t)$-spectrum and the least square fit are shown in figure 10.13, the fit parameters are summarised in table 10.4.

The similar interaction frequencies for the γ-γ and the e-γ cascade suggest the ^{83}Rb and ^{83m}Kr being incorporated on similar lattice site. However, the large difference of the damping values in both spectra shows a significant difference in homogeneity in the vicinity of the probes. Rb is known to intercalate in HOPG [KamDre80]. It can thus be assumed to remain stationary and in the volume of implantation damage after the implantation. This is supported by the high damping which typically occurs in unannealed samples with implantation damage.
^{83m}Kr, however, is likely to diffuse and will most probably be trapped in a vacancy cluster, see sections 6.5.2.1 and 6.5.2.2. In this case the similar EFGs are a coincidence.

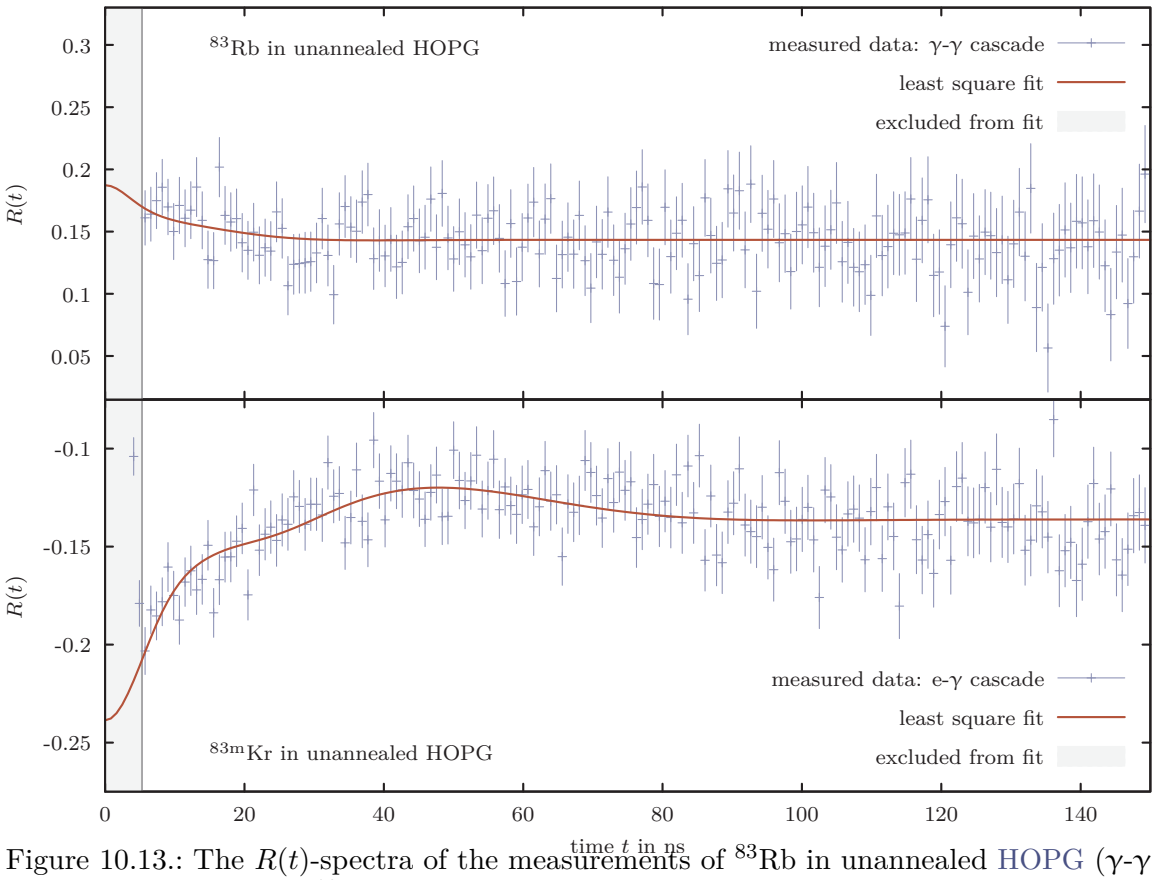

Figure 10.13.: The $R(t)$-spectra of the measurements of ^{83}Rb in unannealed HOPG (γ-γ cascade, top) and ^{83m}Kr in unannealed HOPG (e-γ cascade, bottom) including the least square fits. The resulting fit parameters can be found in table 10.4.

Table 10.4.: A summary of data associated with the measurement of ^{83}Rb and ^{83m}Kr in unannealed HOPG. The upper block summarises general information about the sample and the fit. The middle block shows the resulting fit parameters. The lower block contains values derived from ω_0. The uncertainties of values with † were rounded down to 0 by Nightmare.

Parameter	^{83}Rb(^{83}Kr)	^{83m}Kr(^{83}Kr)
Cascade	γ-γ	e-γ
Activity	130 kBq	
Structure	α-graphite, pseudo monocryst.	
Implant. energy	4 keV	
Meas. time	11 d	
Fit start at	5.74 ns	
Fit red. χ^2	0.57	0.79
Multipl. const.	fixed: 1	0.60(4)
Additive const.	0.14†	−0.14†
Damping	120(50) %	54(4) %
ω_0/Mrad s^{-1}	49(12)	52.4(24)
ω_Q	1.3(3) MHz	1.39(7) MHz
ν_Q	17(5) MHz	18.6(9) MHz
$V_{zz}/10^{20}$	15(4) V m^{-2}	15.7(8) V m^{-2}

10.3.4. ^{83m}Kr/^{83}Kr and ^{83}Rb/^{83}Kr in annealed HOPG

Additionally to the unannealed HOPG sample, an annealed sample is measured. Due to the low activity of the previously measured HOPG sample (see section 10.3.3) it was decided to produce a new sample rather than annealing and remeasuring the previous sample. It is heated up to 873 K in vacuum for 15 min as described in section 6.3, higher temperatures lead to ^{83}Rb losses during the annealing process. This sample's activity of 350 kBq is the highest of all samples measured in this work.
During this measurement, several problems occurred: The high voltage supply of the CsF scintillation detector broke down. This malfunction occurred after the first third of the measurement and most probably caused no start signals of the γ-γ cascade to be detected during this time reducing the acquired data for this spectrum. Furthermore, the MCA crashed. Only data acquired prior to the crash are presented, data taken after the crash are lost. Lastly, in the e-γ spectrum at approximately $t = 12$ ns a structure looking like an electronic glitch appears. This area is excluded in the fit, the first point used is at 14.76 ns.

The $R(t)$-spectrum associated with the γ-γ cascade results in $\omega_0^{\gamma\text{-}\gamma} = 28.3(21)$ MHz corresponding to $\nu_Q^{\gamma\text{-}\gamma} = 10.0(8)$, a multiplicative constant of 0.50(11) and a damping of $\delta^{\gamma\text{-}\gamma} = 16(7)$ %. This means that approximately half of the probes occupy a unique lattice site. Again, the fit can be carried out assuming a polycrystalline or monocrystalline environment of the probes. The $R(t)$-value and the fit can be found in figure 10.14, the fit parameters in table 10.5. Due to the failure of the start detector measuring this cascade, the statistics are not sufficient to draw further conclusions from this spectrum.

Despite the problem around 12 ns a fit of the remaining data is possible. Obviously, the limitation of the fit range decreases the reliability of the fit. It yields a damping of 77(4) % and $\omega_0^{\text{e-}\gamma} = 43.2(12)$ MHz which corresponds to $\nu_Q^{\text{e-}\gamma} = 15.3(5)$ MHz. The fit yields reasonable results assuming a monocrystalline environment only.

The strong difference in the damping values for the γ-γ and e-γ cascades suggests a lattice site change between the ^{83}Rb and the ^{83m}Kr decay again. The arguments from section 10.3.3 are valid in this case as well. However, in comparison to the unannealed case, the differing interaction frequencies suggest ^{83}Rb and ^{83m}Kr occupying non-equivalent lattice sites.

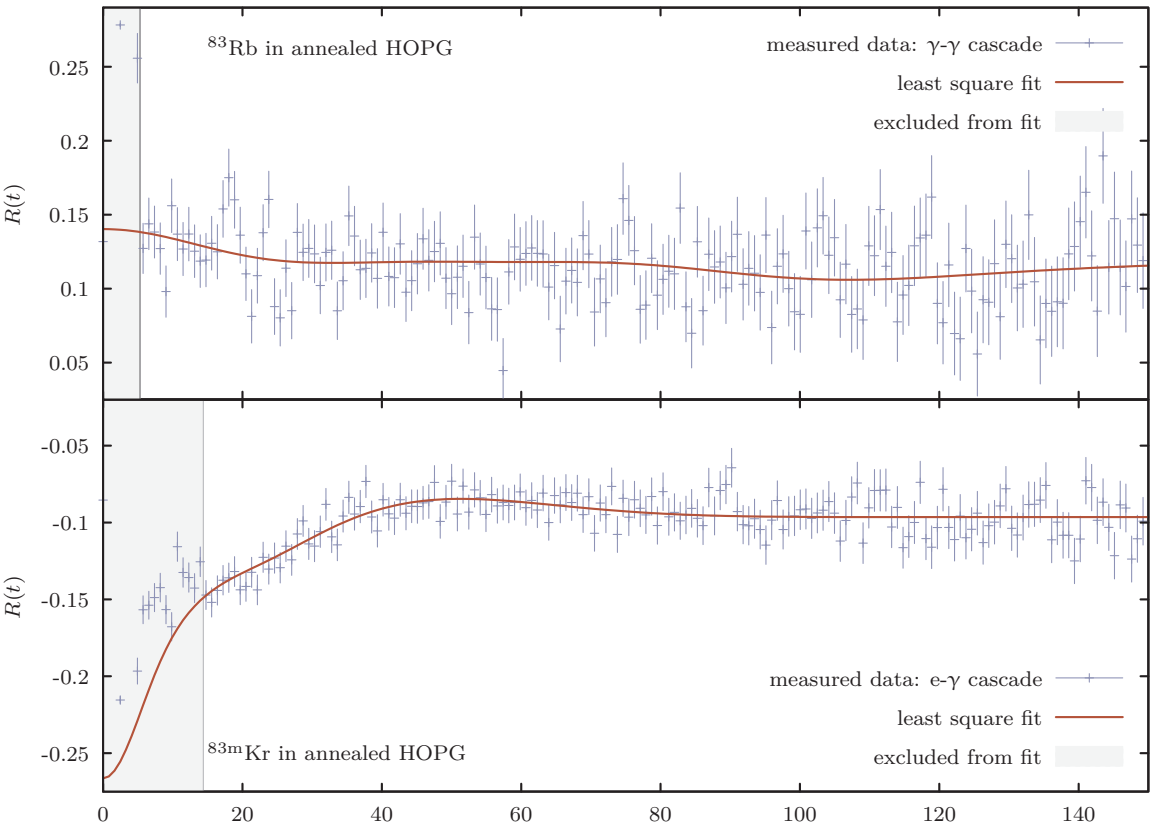

Figure 10.14.: The $R(t)$-spectra of the measurements of ^{83}Rb in annealed HOPG (γ-γ cascade, top) and ^{83m}Kr in annealed HOPG (e-γ cascade, bottom) including the least square fits. The resulting fit parameters can be found in table 10.5.

Table 10.5.: A compilation of data associated with the measurement of ^{83}Rb and ^{83m}Kr in annealed HOPG. In the upper block, general parameters of the sample and the fits are summarised. In the central block, the resulting fit parameters are listed. In the lower block, values deduced from the fit parameters are shown. The uncertainties of values with † were rounded down to 0 by Nightmare.

Parameter	^{83}Rb(^{83}Kr)	^{83m}Kr(^{83}Kr)
Cascade	γ-γ	e-γ
Activity	350 kBq	
Structure	α-graphite, pseudo monocryst.	
Implant. energy	4 keV	
Meas. time	51 d	
Fit start at	5.74 ns	14.76 ns
Fit red. χ^2	0.81	0.71
Multipl. const.	0.50(11)	1.0(6)
Additive const.	0.12†	−0.10†
Damping	16(7) %	77(4) %
ω_0/Mrad s^{-1}	28.3(21)	43.2(12)
ω_Q	0.75(6) MHz	1.15(4) MHz
ν_Q	10.0(8) MHz	15.3(5) MHz
$V_{zz}/10^{20}$	8.5(7) V m^{-2}	12.9(4) V m^{-2}

10.3.5. Comparison of annealed and unannealed HOPG samples

The results of the γ-γ cascade of the annealed and unannealed sample show a significant reduction in damping. This is an expected behaviour as the thermal treatment reduces the lattice damage caused by the ion implantation and with this the inhomogeneity of the probes' vicinity. At the same time the interaction frequency is reduced by a factor of roughly 1.6. This can be caused by a lattice site change during the annealing process. Alternatively, a significant reduction in lattice damage can cause this effect.

Comparing the e-γ results of the unannealed sample with the results of the annealed one, shows that the interaction frequency $\omega_Q^{e\text{-}\gamma}$ shifts from 1.39(7) MHz to 1.15(4) MHz. This can be caused by the limitation of the fit range for the annealed sample, both values are similar. The damping increases from 54(4) % to 77(4) %. Usually, annealing recovers the sample material and leads to more homogeneous EFGs. This means that the annealing programme did not fully recover the host lattice and higher annealing temperatures or longer periods are necessary. ^{83m}Kr seems to accumulate in these not recovered regions.

The behaviour of the HOPG samples before and after the annealing process can be explained quantitatively with help of the considerations in sections 6.5.2.1 and 6.5.2.2:
After the implantation process the ^{83}Rb probes are incorporated and remain in a region with a lot of implantation damage. This is shown by the high damping values of the γ-γ measurements in the unannealed sample. After the decay, the ^{83m}Kr will not remain on the lattice site previously occupied by the ^{83}Rb atom. Because it can not combine with a single vacancy, it will most probably be trapped by a vacancy cluster. In comparison to the ^{83}Rb lattice site, its environment is less inhomogeneous, shown by a reduction in damping.
During the annealing process, the ^{83}Rb atoms do not recombine with vacancies. C atoms, however, do recombine with these interstitials leading to a more homogeneous environment of the ^{83}Rb atoms. The damping decreases significantly. The EFG is lower, most probably due to less inhomogeneities changing the field gradient generated by the lattice. After the radioactive decay to ^{83m}Kr, these atoms can diffuse. Again, they are trapped by vacancy clusters because they can not combine with single vacancies. In comparison to the unannealed sample, a slight reduction of the EFG and an small increase in damping is observed. These minor changes can be caused by the limitation of the fit range of the e-γ $R(t)$-spectrum. This discussion is visualized in figure 10.15.

10.3.6. Consequences for the KATRIN experiment

The conclusions from the previous section give a hint to the origin of the energy drift of the CEs emitted by the solid state calibration sources (see section 6.6) produced in Bonn and measured in the Monitor Spectrometer (MoS) at the KATRIN experiment. PAC measurements show [SchVia87] the formation of Kr filled cavities in Cu after the ion implantation with the noble gas. A similar behaviour is found for He ion implanted in pyrolytic graphite [CheKes96]. Such a process could cause more and more of the continuously produced ^{83m}Kr atoms to be trapped in such cavities in HOPG over time. ^{83m}Kr atoms decaying in such a cavity will find slightly different environments depending on the number

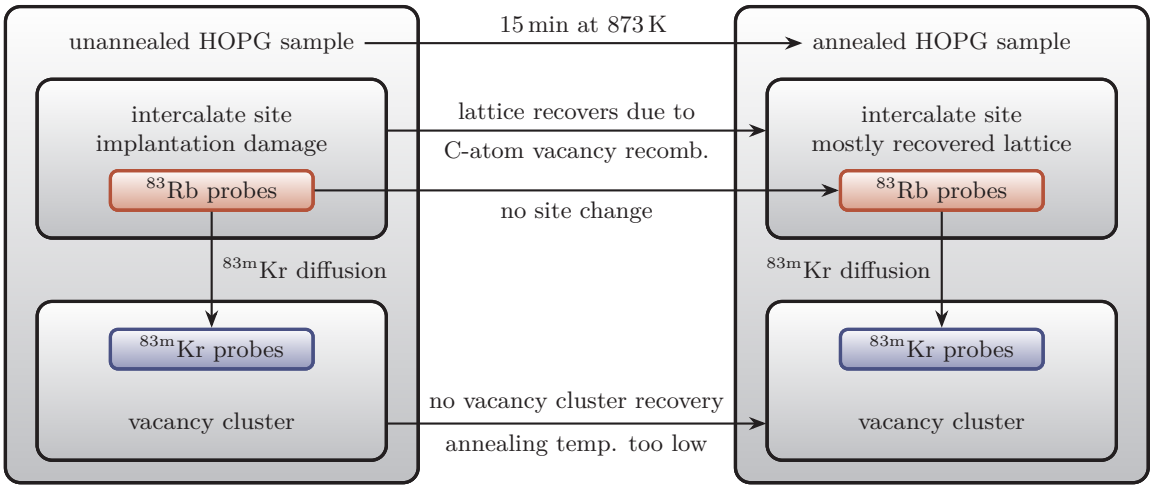

Figure 10.15.: A schematic showing the occupied ^{83}Rb and ^{83m}Kr lattice sites before and after the annealing of a HOPG sample. For a more detailed discussion, see section 10.3.5.

of Kr atoms trapped there. The process leading to a change in the emitted CE's energy can, however, not be analysed using the PAC method.

It is not possible to recover the HOPG lattice to a point where these trapping processes do not occur any more because annealing temperatures of over 900 K will lead to a loss of ^{83}Rb (see section 6.5.2.2). In fact it might be counterproductive to remove the vacancy clusters as they might be responsible for the Kr retention. Samples implanted with low implantation energies like 4 keV exhibit a high Kr retention but show a significant energy drift. This could mean that the cavities storing the Kr atoms are either close and can influence each other or grow faster and bigger. This is in contrast to samples implanted with higher energies or larger beam spots where the implanted nuclei and the implantation damage is spread out. In this case the cavities would either grow slower or have less influence on each others. If the formation and growth of these cavities causes the drift, spreading the ^{83}Rb and with this the implantation damage over the sample during the implantation will reduce the drift. This would be in agreement with the observations in section 6.6.1.
This hypothesis could be tested by measuring samples pre-implanted with stable Kr. This would lead to the pre-formation of Kr filled cavities. The relative change for an additional Kr being trapped in such a cavity is small. Hence, the drift should decrease for such a sample, even for small beam spot sizes and low implantation energies.

It can be concluded that implanting samples with large beam spots is a good way to alleviate the energy drift while reducing the implantation energy to gain more no-loss-electrons. Tempering the samples after the implantation is not necessary and increases the risk of damage to the implanted surface due to handling glitches.

10.4. Conclusions and outlook

The measurements presented in this chapter show the functionality of the 3+1 detector set-up developed in this work.
Firstly, this work demonstrates the feasibility to carry out PAC measurement utilizing APDs to detect low energy γ radiation as well as CEs. The time resolution in both APD-APD and APD-scintillator branches of 1.6 ns is sufficient for PAC measurements. Secondly, PAC measurements with both probes ^{83}Rb(^{83}Kr) and ^{83m}Kr(^{83}Kr) are carried out in three different substrates. The probe environments are studied simultaneously by observing both cascades in one set-up.

The results from the measurement of unannealed and annealed HOPG samples give hints towards a better understanding of the energy drift of the emitted CEs, as described in section 6.6. The formation of Kr filled cavities might cause the energy drift and the high Kr retention in HOPG. The approach to increase the beam spot size using the Isotope mass Separator On-Line DEvice (ISOLDE) retarding lens is supported by the results. It would lead to smaller and slower growing cavities and might thus cause a reduction of the energy drift. Additionally, the measurements suggest that an annealing of solid state calibration sources for the KATRIN experiment is not necessary.

The ability to measure both cascades parallel implies some drawbacks for both measurements. By replacing one APD by a further CsF scintillation detector the apparatus can easily be focussed on measuring the ^{83}Rb(^{83}Kr) cascade only. Exchanging the CsF scintillation detector for another APD gives the possibility to measure the ^{83m}Kr(^{83}Kr) cascade with four detectors. Next to the increased count rate, sample displacement and sample self-absorption drops out in first order when calculating the $R(t)$-value for such a configuration [AreHoh80]. Both specialisations are feasible without major changes in the set-up.

For further measurements, if possible, thinner samples are recommended. Thinner samples reduce the self absorption, especially of the 9.4 keV line and thus reduce the offset compensated by the additive constant in the fit. At the cost of a higher background, samples with a higher activity are advisable to improve the statistics of the measurements. A smaller time window τ (see equation (4.22)) would partially compensate for the increase in background.

11. Summary

The KArlsruhe TRItium Neutrino (KATRIN) experiment is the next-generation experiment to determine the neutrino mass with a 5σ discovery potential for a mass of $m_{\bar{\nu}_e} = 0.35\,\mathrm{eV}\,c^{-2}$. This aim will be accomplished by scanning the endpoint of the β-decay spectrum of tritium. The Windowless Gaseous Tritium Source (WGTS) is a high luminosity source providing the experiment with approximately 10^{11} β-electrons per second. In the main spectrometer, a high luminosity Magnetic Adiabatic Collimation combined with an Electrostatic (MAC-E) filter spectrometer with an energy resolution of $\Delta E = 0.93\,\mathrm{eV}$, the electron energy is analysed. The retarding voltage selecting the threshold of this high-energy pass filter has to be controlled to a precision of 3 ppm and is monitored in the separate Monitor Spectrometer (MoS) using a well-known nuclear standard. For this, the K-Conversion Electron (CE) emitted during the 32.2 keV transition of $^{83\mathrm{m}}$Kr was chosen. These electrons are provided by ion implanted solid state sources produced at the BONn Isotope Separator (BONIS) facility.

The first part of this work reports on the activities undertaken to reliably provide these ion implanted solid state calibration sources every half year and the necessary changes to the BONIS set-up. Supported by simulations of the ion source's temperature behaviour, its mechanical design was optimized to improve the ^{83}Rb ion yield from approximately 2 % to peak efficacies of 31 %. Due to the short half life of $^{83\mathrm{m}}$Kr of 1.83 h, its generator ^{83}Rb is implanted, continuously replenishing the $^{83\mathrm{m}}$Kr. Reducing the implantation energy leads to sources emitting more CEs utilisable for the monitoring process. For this kind of sources, drifts of up to 2.5 ppm per month of the emitted CE's energy, depending on the implanted ^{83}Rb concentration are reported.

With the standard implantation parameters at BONIS, implantation energies down to 20 keV are feasible. To extend this range to lower implantation energies, two retarding lenses were implemented in the BONIS set-up to provide implantation energies from 4 keV to 12.5 keV. The first lens is optimized towards the production of samples with small beam spots of approximately 8 mm^2. The second lens is used in conjunction with deflection capacitors to provide large beam spots more than 50 mm^2 in size. To monitor the implanted activities in real-time during the ion implantations with these lenses, a detector system was developed. It can be mounted on either of the retarding lens' mounting plates.

Using the new additions to the BONIS facility, ion implanted ^{83}Rb solid state calibration samples with a wide variety of characteristics can be produced routinely during the KATRIN experiment's measurement period. The retarding lenses allow for an implantation with low implantation energies, while keeping the ^{83}Rb concentration low by increasing the beam spot size. This will result in solid state calibration sources with a high electron

yield and a low energy drift.

The ion implanted ^{83}Rb and its daughter nucleus ^{83m}Kr implanted for the KATRIN experiment can not only be used for calibration purposes. The nuclei decay via a γ-γ and an e-γ cascade, respectively, making them candidates for Perturbed Angular Correlation (PAC) probe nuclei. This well-established nuclear solid state physics method can extract information from the immediate environment of the probe nuclei in the substrate. It makes use of the interaction between the probe nucleus' Nuclear Quadrupole Moment (NQM) and Electric Field Gradients (EFGs) present at the probe nuclei's lattice site. In the second part of this work, an apparatus to carry out PAC measurements with the probe nuclei ^{83}Rb(^{83}Kr) and ^{83m}Kr(^{83}Kr) was designed and set up. Avalanche Photo Diodes (APDs) were used to detect the e-γ cascade's 17.8 keV CE start and the 9.4 keV γ stop signal of both cascades. A suitable detector with active layer thickness of 200 µm and a resulting high quantum efficacy of more than 84 % for the relevant radiation was chosen for this experiment. A custom voltage sensitive preamplifier was developed to suit the experimental needs of the PAC experiment. Its −3 dB bandwidth of 190 MHz is not limiting the set-up's time resolution. In conjunction with the APD, its voltage gain of 53.4 dB in combination with the noise figure of 2.8 dB allows for the detection of radiation down to 4.5 keV. A Caesium Fluoride (CsF) scintillation detector was used to detect the 553 keV γ start signal of the γ-γ cascade.

The performance of the PAC set-up was demonstrated for the APD-APD as well as the APD-CsF detector combinations. To verify the accuracy of the timing, the half life of the 9.4 keV of ^{83m}Kr was measured with both detector combination. All measurements were found to be in excellent agreement with the literature. Making use of simultaneous events, the fast-slow coincidence circuit's time resolution for both detector combinations was measured to be 1.6 ns.

Finally, PAC measurements of the substrate materials Be, Pt and Highly Oriented Pyrolytic Graphite (HOPG) were carried out. While the two former substrates were used as proof of principle measurement, the latter substrate was investigated in more detail. Both probe environments were measured for an as-implanted and an annealed HOPG sample.

The measurements suggest ^{83}Rb to be incorporated in a lattice volume with a lot of implantation damage, while ^{83m}Kr does not seem to remain stationary after it is created by a ^{83}Rb decay. After an annealing at 873 K a recovery of the HOPG in the vicinity of ^{83}Rb is observed. The environment of the probe ^{83m}Kr does not seem to be affected by the annealing. The measurements suggest that after the generation of ^{83m}Kr it decays in a similar environment as before the annealing. While Rb intercalates in HOPG, Kr seems to be mobile and to get trapped in cavities created during the production or the implantation process of HOPG. These cavities might grow over time causing the energy drift observed for the samples used for the high voltage monitoring at the KATRIN experiment.

A. Appendix: efficacy calibration of the HPGe detector

In this section, the efficacy calibration of the High Purity Ge (HPGe) detector is described. After discussing the detector efficacy for an individual γ line, the procedure to fit a model function that includes correlations between parameters is presented. Finally, it is shown how the fit parameter uncertainties are estimated.

A.1. Efficacy for individual lines

In order to determine the activity of radioactive samples, the efficacy of the detector in use is required. It is a function of the energy of the impinging γ radiation and the distance between detector and sample. The efficacy for a single line can be calculated if the activity A, the branching ratio b_1 (and those of possibly overlapping weaker lines b_2, b_3), the measurement time t and the events in the corresponding peak N are known.

$$\varepsilon = \frac{N}{(b_1 + b_2 + b_3) \cdot t \cdot A \cdot \frac{\mathrm{d}\Omega}{4\pi}} \tag{A.1}$$

In this case, for a cylindrical detector, the solid angle $\mathrm{d}\Omega$ is given by

$$\mathrm{d}\Omega = \int_0^{2\pi} \int_0^{\alpha} d\varphi \; d\vartheta \; \sin(\vartheta) = 2\pi(1 - \cos(\alpha)) \tag{A.2}$$

The angle α between the detector's surface normal through the sample and the connection between outer diameter of the detector crystal and the sample is

$$\alpha = \arctan\left(\frac{D}{2r}\right) \tag{A.3}$$

with the distance r between detector and sample and the detector's diameter D. For the efficacy of a cylindrical detector for positive parameters can be expressed as

$$\varepsilon = \frac{2N}{A \cdot (b_1 + b_2 + b_3) \cdot t \cdot \left(1 - \frac{2r}{\sqrt{D^2 + 4r^2}}\right)} \tag{A.4}$$

The individual uncertainty of the efficacy for one measured line is given by

$$\begin{aligned} \Delta\varepsilon^2 = &\left(\frac{\partial\varepsilon}{\partial N} \cdot \Delta N\right)^2 + \sum_{i=1,2,3} \left(\frac{\partial\varepsilon}{\partial b_i} \cdot \Delta b\right)^2 + \left(\frac{\partial\varepsilon}{\partial t} \cdot \Delta t\right)^2 \\ &+ \left(\frac{\partial\varepsilon}{\partial A} \cdot \Delta A\right)^2 + \left(\frac{\partial\varepsilon}{\partial D} \cdot \Delta D\right)^2 + \left(\frac{\partial\varepsilon}{\partial r} \cdot \Delta r\right)^2 \end{aligned} \tag{A.5}$$

A.2. Fitting a model function

To obtain efficacy values over a wide range of energies that can be interpolated by a continuous function, measurements with calibrated sources are carried out. A ^{152}Eu, a ^{137}Cs and a ^{133}Ba source are used, all γ lines with sufficient intensity ($\gtrsim 0.5\,\%$ according to the NuDat database [NuDat16]) are evaluated as described in section 6.7 and appendix B.2. The branching ratios and their uncertainties are taken from the NuDat database [NuDat16] as well. The detector's properties are specified in [Ortec95b; Ortec95a], the distance between sample and detector is kept constant.
After the measurements, the efficacies calculated with equation (A.4) are plotted versus the energy of the detected radiation and a model function to represent the relation is chosen. This function is not supported by physical models, it only represents the observed data and is used as interpolation. An extrapolation is not possible this way. For the detector used in this work, the following function was chosen:

$$\psi(p_1, p_2, p_3, p_4, E) = p_1 \cdot p_2^E + p_3 \cdot E + p_4 \tag{A.6}$$

To fit the function to the efficacy data obtained, the correlation of values measured with the same radioactive preparation has to be considered. The activity uncertainty of one sample affects all points measured with this source in the same way. A similar argument holds for the distance between detector and this source and the duration of this measurement. Additionally, all results for efficacies are correlated because the detector diameter's uncertainty affects all measurements in the same way.
These correlations are represented by the off-diagonal elements of the covariance matrix that enters when the χ^2 function is set up [Barlow89]:

$$\chi^2(p_1, p_2, p_3, p_4, E) = (\varepsilon - \psi(p_1, p_2, p_3, p_4, E))^T \cdot \sigma^{-1} \cdot (\varepsilon - \psi(p_1, p_2, p_3, p_4, E)) \tag{A.7}$$

How the covariance matrix σ can be obtained for this particular problem is discussed in appendix A.2.1. Once the χ^2 function is fully set up, it is minimised using the Nelder-Mead method to obtain the fit parameters p_i. The uncertainties of the fit parameters and the model function are obtained as described in appendix A.3.

A.2.1. The covariance matrix

The matrix elements of the covariance matrix σ for different functions f_k and f_l and several variables are given by [Barlow89]

$$\sigma^{n,k} = \mathrm{cov}(f_n, f_k) = \sum_\alpha \sum_\beta \left(\frac{f_n}{\partial x_\alpha}\right)\left(\frac{f_k}{\partial x_\beta}\right)\mathrm{cov}(x_\alpha, x_\beta) \tag{A.8}$$

In the case of the efficacy calibration of the HPGe detector this is written as

$$\sigma^{n,k} = \mathrm{cov}(\psi_n, \psi_k) = \sum_{\alpha=(A,t,D,r,N,b_i)} \sum_{\beta=(A,t,D,r,N,b_i)} \left(\frac{\partial \psi_n}{\partial x_\alpha}\right)\left(\frac{\partial \psi_k}{\partial x_\beta}\right)\mathrm{cov}(x_\alpha, x_\beta) \tag{A.9}$$

Focusing on the term with $x_\alpha = A_n$ and writing down equation (A.9) for $x_\beta = (A_k, t_k, D_k, r_k, N_k, b_{i,k})$ yields

$$\begin{aligned}\operatorname{cov}(\psi_n, \psi_k) = &\left(\frac{\partial\psi_n}{\partial A_n}\right)\left(\frac{\partial\psi_k}{\partial A_k}\right)\operatorname{cov}(A_n, A_k) \\ &+ \left(\frac{\partial\psi_n}{\partial A_n}\right)\left(\frac{\partial\psi_k}{\partial t_k}\right)\operatorname{cov}(A_n, t_k) + \left(\frac{\partial\psi_n}{\partial A_n}\right)\left(\frac{\partial\psi_k}{\partial D_k}\right)\operatorname{cov}(A_n, D_k) \\ &+ \left(\frac{\partial\psi_n}{\partial A_n}\right)\left(\frac{\partial\psi_k}{\partial r_k}\right)\operatorname{cov}(A_n, r_k) + \left(\frac{\partial\psi_n}{\partial A_n}\right)\left(\frac{\partial\psi_k}{\partial N_k}\right)\operatorname{cov}(A_n, N_k) \\ &+ \sum_{i=1,2,3}\left(\frac{\partial\psi_n}{\partial A_n}\right)\left(\frac{\partial\psi_k}{\partial b_{i,k}}\right)\operatorname{cov}(A_n, b_{i,k}) \end{aligned} \tag{A.10}$$

A parameter of the nth efficacy measurement can only be correlated to the same parameter in the kth efficacy measurement in the present case, hence, all covariances besides $\operatorname{cov}(A_n, A_k)$ vanish. The same argument holds for all other values for x_j. The matrix elements of σ can thus be simplified:

$$\begin{aligned}\operatorname{cov}(\psi_n, \psi_k) = &\left(\frac{\partial\psi_n}{\partial A_n}\right)\left(\frac{\partial\psi_k}{\partial A_k}\right)\operatorname{cov}(A_n, A_k) \\ &+ \left(\frac{\partial\psi_n}{\partial t_n}\right)\left(\frac{\partial\psi_k}{\partial t_k}\right)\operatorname{cov}(t_n, t_k) + \left(\frac{\partial\psi_n}{\partial D_n}\right)\left(\frac{\partial\psi_k}{\partial D_k}\right)\operatorname{cov}(D_n, D_k) \\ &+ \left(\frac{\partial\psi_n}{\partial r_n}\right)\left(\frac{\partial\psi_k}{\partial r_k}\right)\operatorname{cov}(r_n, r_k) + \left(\frac{\partial\psi_n}{\partial N_n}\right)\left(\frac{\partial\psi_k}{\partial N_k}\right)\operatorname{cov}(N_n, N_k) \\ &+ \sum_{i=1,2,3}\left(\frac{\partial\psi_n}{\partial b_{i,n}}\right)\left(\frac{\partial\psi_k}{\partial b_{i,k}}\right)\operatorname{cov}(b_{i,n}, b_{i,k}) \end{aligned} \tag{A.11}$$

A.2.1.1. Correlation via detector size

For spectra measured with different radioactive preparations, the only parameter that introduces a correlation is the detector diameter. All measurements are influenced in the same way by an uncertainty in the detector diameter. In this case the covariances of all other parameters vanish. Because $D_n = D_k = D$ the covariance equals the variance of the detector diameter:

$$\operatorname{cov}(D_n, D_k) = \operatorname{cov}(D, D) = \operatorname{var}(D) = (\Delta D)^2 \tag{A.12}$$

Using this, the covariance matrix element contribution caused by using the same detector for all measurements follows from equation (A.11):

$$\operatorname{cov}_{\mathrm{D}}(\psi_n, \psi_k) = \left(\frac{\partial\psi_n}{\partial D_n}\right)\left(\frac{\partial\psi_k}{\partial D_k}\right)(\Delta D)^2 \tag{A.13}$$

The derivation of equation (A.4) of D can be written as

$$\frac{\partial\psi}{\partial D} = \psi \cdot \frac{2Dr}{\tau^2 \cdot \eta} \tag{A.14}$$

for ψ_n and ψ_k because D, r as well as $\tau = \sqrt{D^2 + 4r^2}$ and $\eta = \tau - 2r$ are the same for both measurements n and k. With this, the entries of the covariance matrix contribution become

$$\Sigma_D^{n,k} = \mathrm{cov_D}(\psi_n, \psi_k) = \psi_n \psi_k \left(\frac{2Dr}{\tau^2 \cdot \eta} \right)^2 \tag{A.15}$$

A.2.1.2. Correlation via sample activity, measurement time and distance

If multiple detector efficacy values for different γ energies are determined from a spectrum recorded with one calibrated source, a correlation between these values is introduced. The uncertainty in the activity calibration affects all efficacies in the same way. Furthermore, if the sample positioning was not changed and all lines were acquired in one measurement run, a correlation through the measurement time and the distance between detector and samples is created as well. Due to a similar argument as in appendix A.2.1.1, the covariances of the mentioned parameters equal their variances:

$$\mathrm{cov}(A_n, A_k) = \mathrm{cov}(A, A) = \mathrm{var}(A) = (\Delta A)^2 \tag{A.16}$$

$$\mathrm{cov}(r_n, r_k) = \mathrm{cov}(r, r) = \mathrm{var}(r) = (\Delta r)^2 \tag{A.17}$$

$$\mathrm{cov}(t_n, t_k) = \mathrm{cov}(t, t) = \mathrm{var}(t) = (\Delta t)^2 \tag{A.18}$$

The correlation from appendix A.2.1.1 is still present, equation (A.12) still holds. All other covariances vanish. Using the derivations of equation (A.4)

$$\frac{\partial \psi}{\partial A} = -\frac{\psi}{A} \tag{A.19}$$

$$\frac{\partial \psi}{\partial t} = -\frac{\psi}{t} \tag{A.20}$$

$$\frac{\partial \psi}{\partial r} = \psi \frac{1}{\eta} \left(\frac{4r\eta}{\tau^2} + 2 - \frac{4r}{\tau} \right) \tag{A.21}$$

Based on equation (A.11) the contribution to the covariance matrix elements from measurements with one calibrated activity, at the same distance to the detector and within the same measurement time interval can now be written

$$\begin{aligned} \mathrm{cov_A}(\psi_n, \psi_k) &= \mathrm{cov_D}(\psi_n, \psi_k) + \left(\frac{\partial \psi_n}{\partial A_n} \right) \left(\frac{\partial \psi_k}{\partial A_k} \right) (\Delta A)^2 \\ &\quad + \left(\frac{\partial \psi_n}{\partial t_n} \right) \left(\frac{\partial \psi_k}{\partial t_k} \right) (\Delta t)^2 + \left(\frac{\partial \psi_n}{\partial r_n} \right) \left(\frac{\partial \psi_k}{\partial r_k} \right) (\Delta r)^2 \qquad \text{(A.22)} \\ &= \mathrm{cov_D}(\psi_n, \psi_k) + \psi_n \psi_k \left(\frac{(\Delta A)^2}{A^2} + \frac{(\Delta t)^2}{t^2} + \frac{1}{\eta} \left(\frac{4r\eta}{\tau^2} + 2 - \frac{4r}{\tau} \right) \right) \qquad \text{(A.23)} \\ &= \Sigma_{\mathrm{D}}^{n,k} + \Sigma_{\mathrm{A}}^{n,k} \qquad \text{(A.24)} \end{aligned}$$

This is possible because τ, η, A, t and r are the same for the nth and the kth measurement.

A.2.1.3. Uncorrelated contributions

Parameters that do not cause correlations between two efficacy measurements are the branching ratio and the events in the measured γ lines. Because correlation terms are off-diagonal elements of the covariance matrix, these parameters contribute only to the diagonal elements of the covariance matrix, restricting the following discussion to $n = k$. The covariances from the previous sections, equation (A.12) and equations (A.19) to (A.21) are still valid, additionally because $n = k$:

$$\mathrm{cov}(N_n, N_n) = \mathrm{cov}(N_n, N_n) = \mathrm{var}(N_n) = (\Delta N)^2 \tag{A.25}$$

$$\mathrm{cov}(b_{i,n}, b_{i,n}) = \mathrm{cov}(b_{i,n}, b_{i,n}) = \mathrm{var}(b_{i,n}) = (\Delta b_i)^2 \tag{A.26}$$

With the derivations of equation (A.4)

$$\frac{\partial \psi}{\partial N} = \frac{\psi}{N} \tag{A.27}$$

$$\frac{\partial \psi}{\partial b_i} = -\frac{\psi}{b_1 + b_2 + b_3} \tag{A.28}$$

equation (A.11) can be written for the diagonal elements

$$\begin{aligned}
\mathrm{cov}(\psi_n, \psi_n) &= \mathrm{cov_D}(\psi_n, \psi_n) + \mathrm{cov_A}(\psi_n, \psi_n) + \left(\frac{\partial \psi_n}{\partial N_n}\right)\left(\frac{\partial \psi_n}{\partial N_n}\right)\mathrm{cov}(N_n, N_n) \\
&\quad + \sum_{i=1,2,3}\left(\frac{\partial \psi_n}{\partial b_{i,n}}\right)\left(\frac{\partial \psi_n}{\partial b_{i,n}}\right)\mathrm{cov}(b_{i,n}, b_{i,n}) && \text{(A.29)} \\
&= \mathrm{cov_D}(\psi_n, \psi_n) + \mathrm{cov_A}(\psi_n, \psi_n) \\
&\quad + \sum_{i=1,2,3} \psi_n^2 \left(\frac{(\Delta N)^2}{N^2} + \frac{(\Delta b_i)^2}{(b_1 + b_2 + b_3)^2}\right) && \text{(A.30)} \\
&= \Sigma_{\mathrm{D}}^{n,n} + \Sigma_{\mathrm{A}}^{n,n} + \Sigma_{\mathrm{U}}^{n,n} && \text{(A.31)}
\end{aligned}$$

A.2.2. Constructing the covariance matrix

From the results of the discussions in appendices A.2.1.1 to A.2.1.3 the covariance matrix is constructed. Assuming that efficacy values from m ^{152}Eu γ lines, p ^{137}Cs γ lines and q ^{133}Ba γ lines are determined, the covariance matrix can be written as the sum of the following matrices:

$$\sigma = \begin{pmatrix} \Sigma_{\mathrm{U}}^{\mathrm{Eu}} + \Sigma_{\mathrm{A}}^{\mathrm{Eu}} & & 0 \\ & \Sigma_{\mathrm{U}}^{\mathrm{Cs}} + \Sigma_{\mathrm{A}}^{\mathrm{Cs}} & \\ 0 & & \Sigma_{\mathrm{U}}^{\mathrm{Ba}} + \Sigma_{\mathrm{A}}^{\mathrm{Ba}} \end{pmatrix} + \Sigma_{\mathrm{D}} \tag{A.32}$$

with the submatrices

$$\Sigma_{\mathrm{A}}^{\mathrm{Eu}} = \begin{pmatrix} \Sigma_{\mathrm{A}}^{1,1} & \cdots & \Sigma_{\mathrm{A}}^{m,1} \\ \vdots & \ddots & \vdots \\ \Sigma_{\mathrm{A}}^{1,m} & \cdots & \Sigma_{\mathrm{A}}^{m,m} \end{pmatrix} \quad \text{and} \quad \Sigma_{\mathrm{U}}^{\mathrm{Eu}} = \begin{pmatrix} \Sigma_{\mathrm{U}}^{1,1} & & 0 \\ & \ddots & \\ 0 & & \Sigma_{\mathrm{U}}^{m,m} \end{pmatrix} \tag{A.33}$$

which are both $m \times m$ matrices. For the other radioactive preparations, the matrices look similar. For the ^{137}Cs source the submatrices are $p \times p$, for ^{133}Ba $q \times q$. Let $u = m + p + q$, then

$$\Sigma_{\mathrm{D}} = \begin{pmatrix} \Sigma_{\mathrm{D}}^{1,1} & \dots & \Sigma_{\mathrm{D}}^{u,1} \\ \vdots & \ddots & \vdots \\ \Sigma_{\mathrm{D}}^{1,u} & \dots & \Sigma_{\mathrm{D}}^{u,u} \end{pmatrix} \tag{A.34}$$

which is a $(m + p + q) \times (m + p + q)$ matrix, just like the resulting covariance matrix σ.

A.3. The fit parameter and model function uncertainties

To determine the uncertainties of the fit parameters as well as their correlation, the fit parameter covariance matrix S is calculated. It is given by

$$S_{i,j} = 2\left(H^{-1}\right)_{i,j} = \mathrm{cov}(p_i, p_j) \tag{A.35}$$

with the Hessian matrix H and its matrix elements

$$H_{i,j} = \frac{\partial^2 \chi^2}{\partial p_i \partial p_j} \tag{A.36}$$

The diagonal elements $S_{i,i}$ equal the variances of the fit parameters $\mathrm{var}(p_i)$, while the off-diagonal elements $S_{i,j}$ are the covariances $\mathrm{cov}(p_i, p_j)$ between two fit parameters. Using these results, the uncertainty of the efficacy function follows

$$\Delta\psi(p_1, p_2, p_3, p_4, E) = \left[\sum_{\substack{i=1,2,3,4 \\ j=1,2,3,4}} \frac{\partial \psi}{\partial p_i} \frac{\partial \psi}{\partial p_j} \mathrm{cov}(p_i, p_j) \right]^{\frac{1}{2}} \tag{A.37}$$

B. Appendix: the BONIS facility

B.1. Beam spot size determination by counting pixels

The definition of the beam spot size is the same in this work and in the work by Slezák [Slezák15a]. All pixels with count rates more than half of the maximal count rate contribute. These pixels are colour coded red, the half maximum count rate is coded white, all others blue. By counting the pixels coded red, knowing the total pixel size and the detector chip area, the beam spot size can be calculated.

To count the pixels, the Timepix image is opened with the program GIMP (version 2.8.14). An example for the following process is shown in figure B.1. The colour components for each pixel in RGB mode are represented by a triplet

$$\begin{pmatrix} x_\mathrm{R} \\ x_\mathrm{G} \\ x_\mathrm{B} \end{pmatrix} \quad \text{with} \quad x_i \in [0, 255] \tag{B.1}$$

with each x_i defining the amount of the respective colour. The original picture is decomposed into three layers, one for each RGB colour. These are grey level image layers, the brightness $y_i = x_i/255 \cdot 100$ of each pixel indicates the content of the respective colour in the original picture. The green layer is irrelevant and thus discarded. Dividing the blue layer by the red layer yields

$$\mathscr{D} : z = \frac{y_\mathrm{B}}{y_\mathrm{R}} \cdot 100 \begin{cases} \in [0, 100[& \text{for } y_\mathrm{B} < y_\mathrm{R} & \text{pixel appears red} \\ > 100 & \text{for } y_\mathrm{B} > y_\mathrm{R} & \text{pixel appears blue} \\ = 100 & \text{for } y_\mathrm{B} = y_\mathrm{R} \neq 0 & \text{pixel is grey or white} \\ = 0 & \text{for } y_\mathrm{B} = y_\mathrm{R} = 0 & \text{pixel is black} \end{cases} \tag{B.2}$$

The resulting layer is a grey level image again with brightness $z \in [0, 100]$ per pixel. Because the brightness is clipped at 100, pixels with $y_\mathrm{B} > y_\mathrm{R}$ are shown in white ($z = 100$). White and grey pixels are mapped to white as well, black pixels remain black ($z = 0$). The red pixels are mapped to shades of grey ($z \in [0, 100[$).
The layer obtained by the division $\mathscr{D}$ is now inverted in colour space:

$$\mathscr{D}^{-1} : z' = |z - 100| \tag{B.3}$$

All pixels that are blue or white in the original picture are now black ($z' = 0$). Multiplication of this layer with the original picture eliminates all blue and white pixels, consequently. Pixels that are black in the original picture do not change their colour. The remaining red pixels are counted using the histogram function, excluding all black pixels.

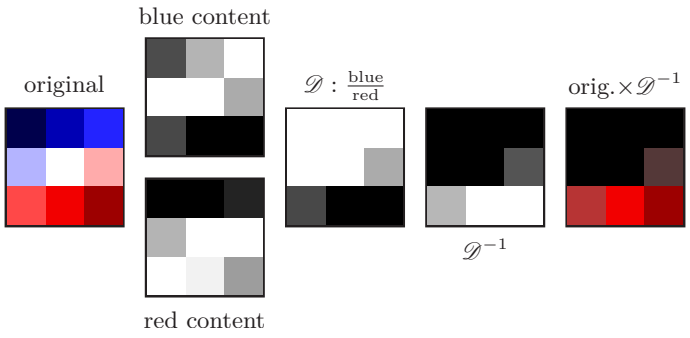

Figure B.1.: An example for the colour processing used to determine beam spot sizes from Timepix measurements. All colours are taken from Timepix measurements.

B.2. Peak evaluation of HPGe detector γ lines

All activities in this work are determined using a HPGe detector. For this, it is necessary to evaluate the number of events in a γ line. It is, however, not possible to use a Gaussian fit to the lines measured with this detector. Due to effects like incomplete charge carrier collection the lines exhibit an energy dependent skewness towards lower energies [PhiMar76]. Despite the availability of complicated fit procedures [PhiMar76; VarTri69; HelLee80] and dedicated programs, a simpler yet sufficient approach is used.
The total events are determined by summing over all events within an symmetric interval around the centroid of the γ line and then subtracting the background. All steps described in the following are performed by a Gnuplot (version 4.6, patchlevel 5) script and are checked for errors and corrected if necessary afterwards. Sometimes slight changes to the script are necessary, e.g. if two lines overlap.

A Gaussian with constant background is fitted to the measured data to obtain a first guess of the mean μ' and the standard deviation σ' of the line. A linear background is assumed between the limits of the interval $[\mu' - 4\sigma', \mu' + 4\sigma']$, an initial estimate of the corresponding y values are obtained by averaging over 6 points around $\mu' \pm \sigma'$. The fit of the Gaussian function is repeated, this time including the linear background, in the interval $[\mu' - \sigma'/2, \mu' + 4\sigma']$ to minimise the influence of the skewness on the fit. From the fit the values μ and σ are obtained. All events in the interval $[\mu - 4\sigma, \mu + 4\sigma]$ are added up, the uncertainty is the square root of the event number. The background that is subtracted consists of two constituents, the constant and the linear background. The linear background corresponds to the area between a horizontal line through the lower intersection of the Gaussian and the interval limits and the higher intersection of the Gaussian and the other interval limit. Because little is known about the precise shape of the background, the uncertainty is assumed to be half of this area. The constant background is the rectangular area between both interval limits and the horizontal line through the lower intersection of the Gaussian and the interval limits. The width of this rectangle is assumed to be without uncertainty , the height's uncertainty is the square root of the height. This procedure is illustrated in figures 6.13 and B.2.

The method discussed gives consistent results for the activity for ^{83}Rb from the 520 keV,

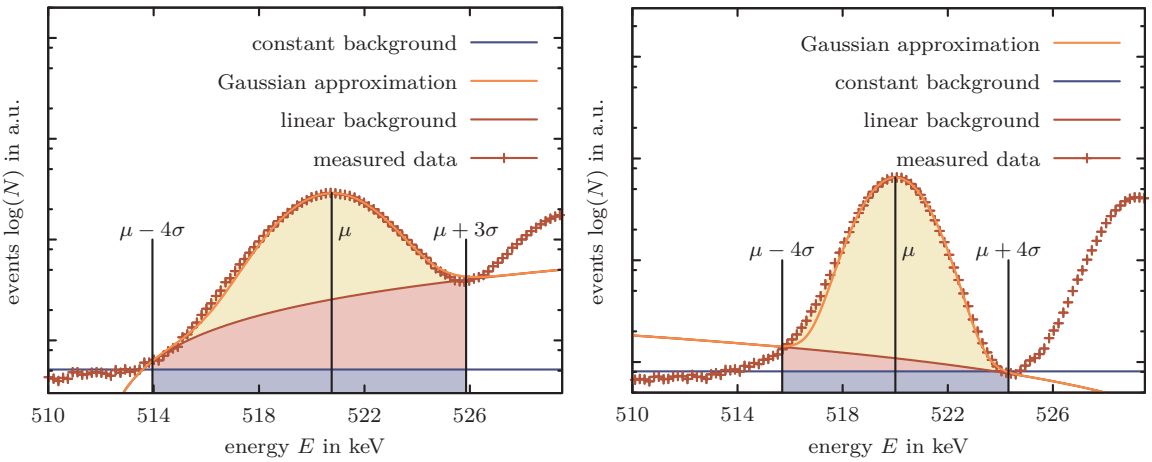

Figure B.2.: A direct comparison between a fit of the 520 keV ^{83}Rb line with reduced and good energy resolution. The right summation interval limit is shifted to $\mu + 3\sigma$ in the case of the reduced energy resolution, a background with positive slope is created by the adjacent peak. For the case of the good energy resolution the summation limits are not altered by the neighbouring line. The background has a negative slope caused by the peak skewness due to incomplete charge carrier collection.

the 529 keV and the 553 keV line if the energy resolution of the detector is not impaired by an insufficient insulation vacuum. In these situations, the shortcomings of this method become obvious. The limit of the summation interval adjacent to the overlapping line needs to be adjusted manually to be in the minimum between both lines. Through this deviation the events in the line are underestimated, the background consisting of parts of the neighbouring line and the real background is overestimated. A direct comparison between lines with reduced and normal energy resolution can be found in figure B.2.
An other drawback of this method is, that the higher the energy of the line is, the more events in the low energy tail are cut away. This however, does not pose a problem, as long as the measurement method is not changed and the calibration is done using the same method.

B.3. ISOLDE lens test implantation beam spots

In this section all test beam spots implanted with ^{83}Rb are listed with the corresponding implantation parameters.

B.4. Estimation of the ^{85}Rb admixture

Based on the assumptions presented in section 7.6.3.1 the derivation of equation (7.3) is shown here in detail.

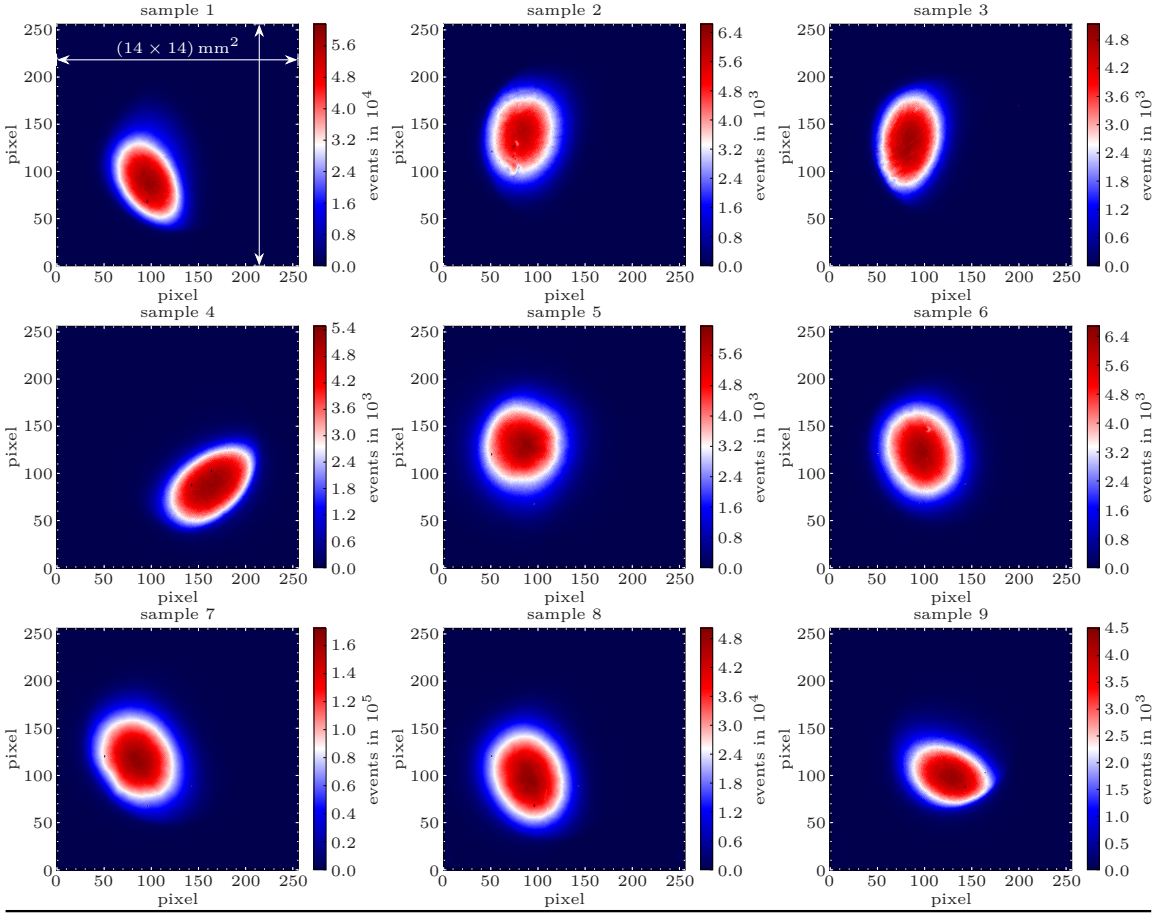

#	implantation energy / keV	x/y deflection / scale div.	implantation angle / °	beam spot area A / mm^2	implanted activity / kBq
1	8	0/0	0	10	270
2	8	20/20	0	11	220
3	4	0/0	0	12	200
4	8	0/0	10	13	280
5	4	40/40	10	13	100
6	4	20/20	0	14	220
7	8	20/20	10	14	220
8	4	20/20	10	14	210
9	4	0/0	10	10	190

Figure B.3.: All samples implanted during the first test of the ISOLDE retarding lens including all important implantation parameters. Timepix measurements carried out by Slezák [Slezák16b].

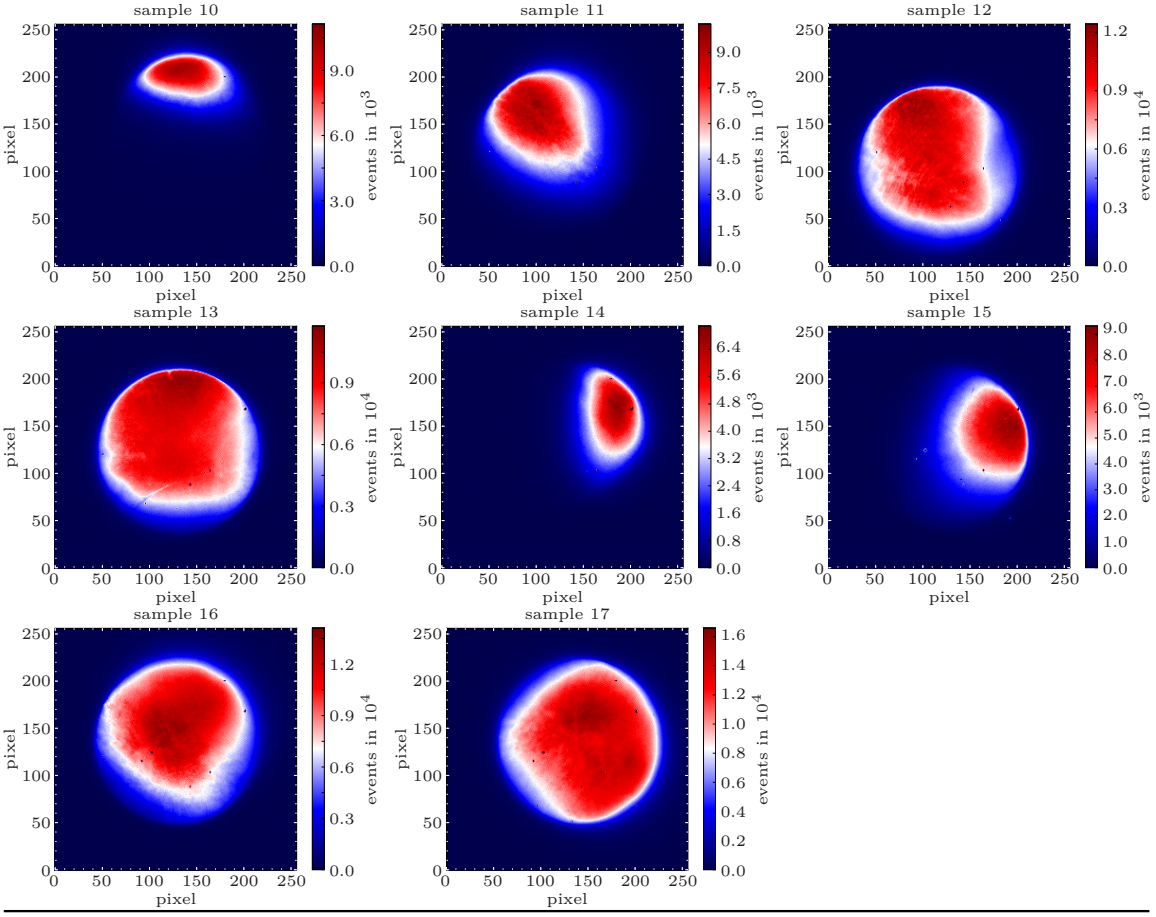

#	implantation energy / keV	x/y deflection / scale div.	implantation angle / °	beam spot area A / mm^2	implanted activity / kBq
10	4	0/0	0	8	170
11	4	80/80	0	21	170
12	4	120/120	0	45	180
13	4	140/140	0	51	160
14	4	0/0	0	10	180
15	4	80/80	0	15	140
16	4	120/120	0	45	150
17	4	140/140	0	56	140

Figure B.4.: All samples implanted during the second and third test of the ISOLDE retarding lens including all important implantation parameters. Timepix measurements of sample 10 to 13 carried out by Sentkerestiová and Vénos [SenVén16], 11 to 17 by Sentkerestiová [Sentke16b].

Due to the assumed circular symmetry, it is sufficient to solve this problem in one dimension. The overlap of the ^{84}Rb Gaussian peak $\mathcal{G}_{84}$ with the sample interval $[-a\sigma, a\sigma]$ is used to calculate the spatial separation distance d of both peaks as multiple of the beam's standard deviation σ. The ^{84}Rb admixture can be expressed by the integral

$$\bar{S}_{84} = \int_{-a\sigma}^{a\sigma} \mathcal{G}_{84}\, dx = \int_{-\infty}^{\mu_{84}} \mathcal{G}_{84}\, dx - \int_{-\infty}^{-a\sigma} \mathcal{G}_{84}\, dx - \int_{a\sigma}^{\mu_{84}} \mathcal{G}_{84}\, dx \tag{B.4}$$

Because the mass separator magnet deflects lighter ions more to the left (see figure 7.1), most of the ^{84}Rb ions are implanted on the right side of the sample. Assuming much more ^{84}Rb ions being implanted into the sample, than into the paper backing on the *left* side

$$\int_{-\infty}^{-a\sigma} \mathcal{G}_{84}\, dx \ll \int_{a\sigma}^{\mu_{84}} \mathcal{G}_{84}\, dx \tag{B.5}$$

allows to simplify the integral. It can thus be rewritten as

$$\bar{S}_{84} = \frac{1}{2} - \int_{a\sigma}^{\mu_{84}} \mathcal{G}_{84}\, dx \tag{B.6}$$

Substituting $t = (x - \mu_{84})/(\sqrt{2}\sigma)$ in the Gaussian and using

$$\int_0^a e^{-t^2} dt = \frac{1}{2}\sqrt{\pi}\mathrm{erf}(a) \tag{B.7}$$

[BroSem99], the integral can be solved yielding

$$\mu_{84} = d = \sigma\left(a - \sqrt{2}\mathrm{erf}^{-1}\left(2\bar{S}_{84} - 1\right)\right) \tag{B.8}$$

If there is a sufficient amount of ^{84}Rb in the ion source, resulting in a measurable ^{84}Rb contamination on the implanted sample, $\bar{S}_{84}(E, m = 83)$ is directly assessable via an activity measurement. Now the average admixture $\bar{S}_{85}(E, A = 83)$ of ^{85}Rb can be calculated using the assumption $\mu_{85} = 2d = 2\sigma(a - \sqrt{2}\mathrm{erf}^{-1}(2\bar{S}_{84} - 1))$. The same integral as before has to be solved, yielding

$$\bar{S}_{85} = \frac{1}{2} + \frac{1}{2}\mathrm{erf}\left(-\frac{a}{\sqrt{2}} + 2\mathrm{erf}^{-1}\left(2\bar{S}_{84} - 1\right)\right) \tag{B.9}$$

The only remaining unknown quantity in this equation is the width of the sample in multiples of the standard deviation σ. It can be estimated comparing the ^{83}Rb activity A_s implanted into the sample and into the paper backing A_b covering the target holder to prevent it from being ion implanted. Again, assuming circular symmetry the ratio can be written as

$$\frac{A_\mathrm{b}}{A_\mathrm{s}} = \frac{\frac{1}{2} - \int_{\mu_{83}}^{a\sigma} \mathcal{G}_{83}\, dx}{\int_{\mu_{83}}^{a\sigma} \mathcal{G}_{83}\, dx} = \frac{1}{2\int_{\mu_{83}}^{a\sigma} \mathcal{G}_{83}\, dx} - 1 \tag{B.10}$$

using $\mu_{83} = 0$ and equation (B.7) one obtains

$$a = \mathrm{erf}^{-1}\left(\frac{A_\mathrm{s}}{A_\mathrm{s} + A_\mathrm{b}}\right) \cdot \sqrt{2} \tag{B.11}$$

The average admixture of ^{85}Rb in the ^{83}Rb beam can thus be expressed using equations (B.9) and (B.11):

$$\bar{S}_{85} = \frac{1}{2} + \frac{1}{2}\mathrm{erf}\left(-\mathrm{erf}\left(\frac{A_\mathrm{s}}{A_\mathrm{s} + A_\mathrm{b}}\right) + 2\mathrm{erf}^{-1}\left(2\bar{S}_{84} - 1\right)\right) \tag{B.12}$$

C. Appendix: the Perturbed Angular Correlation (PAC) set-up

C.1. The preamplifier

The Sequentially Arranged High-gain AmplifieR (SAHAR) is inverting and has a total amplification of ~ 450 and a bandwidth of $\sim 190\,\mathrm{MHz}$.

All operational amplifier supply voltages are equipped with filter capacitor cascades from 0.1 nF to 1 µF, the MAR-6+ from 10 nF to 1 µF. The bias voltage is filtered using a 0.1 nF, a 1 nF, a 4.7 nF, a 8.2 nF and a 33 nF capacitor. The feedback resistors of the operational amplifiers are mounted directly on top of the amplifier chip to reduce additional inductances to a minimum.
All resistors used in the SAHAR circuit are thin film resistors. The only exception is the bias voltage resistor , which is a metal film resistor. All non-polarised capacitors are ceramic, the polarised are Ta electrolyte capacitors. SMD (Surface Mount Device) components with 0603 footprint (JEDEC standardised) components are used to keep the signal trace as short as possible, most other components have a 1206 footprint.
The two operational amplifiers are operated on 6 V potential making DC decoupling capacitors between them necessary. A previous version of the SAHAR module was operated with only a 12 V voltage supply, a 6 V supply was generated using a linear voltage regulator on-board. This feature was dropped later on, but it was decided not to alter the rest of the working circuit.

A circuit diagram of the amplifier can be found in figure C.2, a full list of all used parts in table C.1. The Gerber files used to produce the Printed Circuit Board (PCB) are shown in figure C.1.

C.2. The splitter module

The splitter module board is equipped with a linear voltage regulator generating a 6 V supply voltage from the 12 V supply voltage. 10 kΩ resistors are metal film, all others are thin film. All polar capacitors are Ta capacitors, the rest are ceramic. The operational amplifiers that are used in the splitter's circuity are of type THS3201, they are chosen for the same reasons that are described in section 9.2.

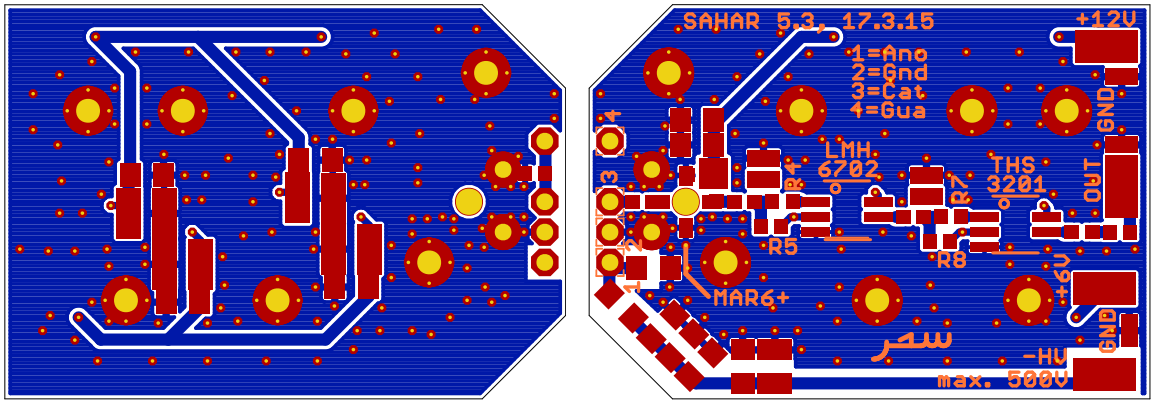

Figure C.1.: Visualization of the Gerber files of the SAHAR module. The different layers are colour coded: blue = copper, red = (negative) solder mask, yellow = drill and orange = silk screen.

name	type	value	footprint
R_1	thin film resistor	560 Ω	0603
R_2	thin film resistor	47 Ω	0603
R_3	thin film resistor	180 Ω	0603
R_4	thin film resistor	47 Ω	0603
R_s	thin film resistor	1 kΩ	0603
R_{g2}	thin film resistor	12 Ω	0603
R_{g3}	thin film resistor	47 Ω	0603
R_{f2}	thin film resistor	220 Ω	1206
R_{f3}	thin film resistor	560 Ω	1206
R_{hv}	metal film resistor	1 MΩ	1206
$C_{c,i}^{\dagger}$	C0G capacitor	10 nF	0603
C_1	C0G capacitor	0.1 nF	1206
C_2	C0G capacitor	1 nF	1206
C_3	X7R capacitor	10 nF	1206
C_4	X7R capacitor	100 nF	1206
C_5	Ta capacitor	1 µF	1206
C_6	C0G capacitor	10 nF	0603
C_{hv1}	C0G capacitor	0.1 nF	1206
C_{hv2}	C0G capacitor	1 nF	1206
C_{hv3}	C0G capacitor	4.7 nF	1206
C_{hv4}	C0G capacitor	8.2 nF	1206
C_{hv5}	C0G capacitor	33 nF	1210
THS3201	operational amplifier	–	SOIC-8
LMH6702	operational amplifier	–	SOIC-8
MAR-6+	amplifier	–	VV105

Table C.1.: The list of components used for the SAHAR circuit. †: The RC coupling with 10 nF capacitors cause the undershoot in the output signal of the SAHAR module. Choosing bigger capacitors can alleviate this problem, see section 9.6

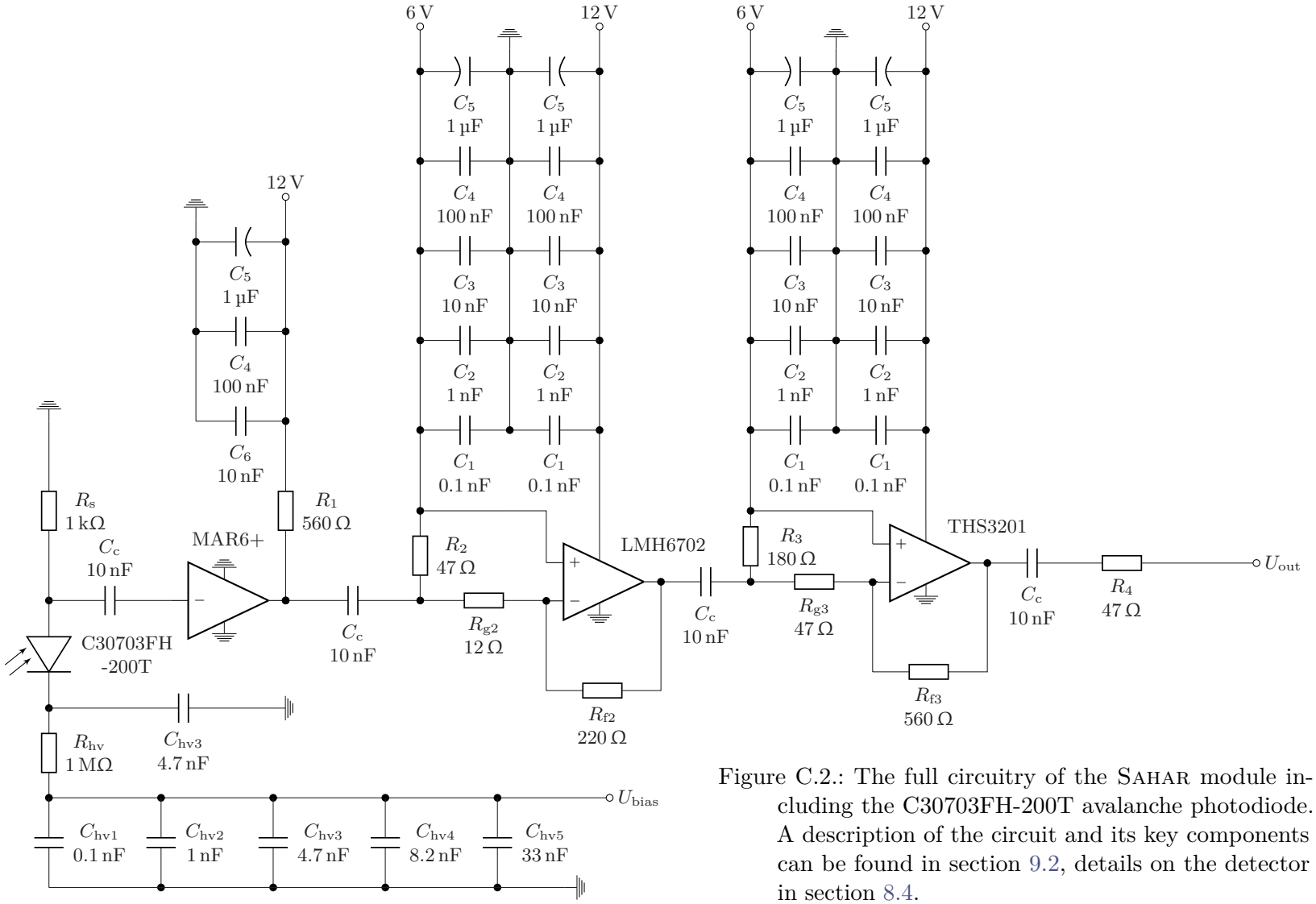

Figure C.2.: The full circuitry of the SAHAR module including the C30703FH-200T avalanche photodiode. A description of the circuit and its key components can be found in section 9.2, details on the detector in section 8.4.

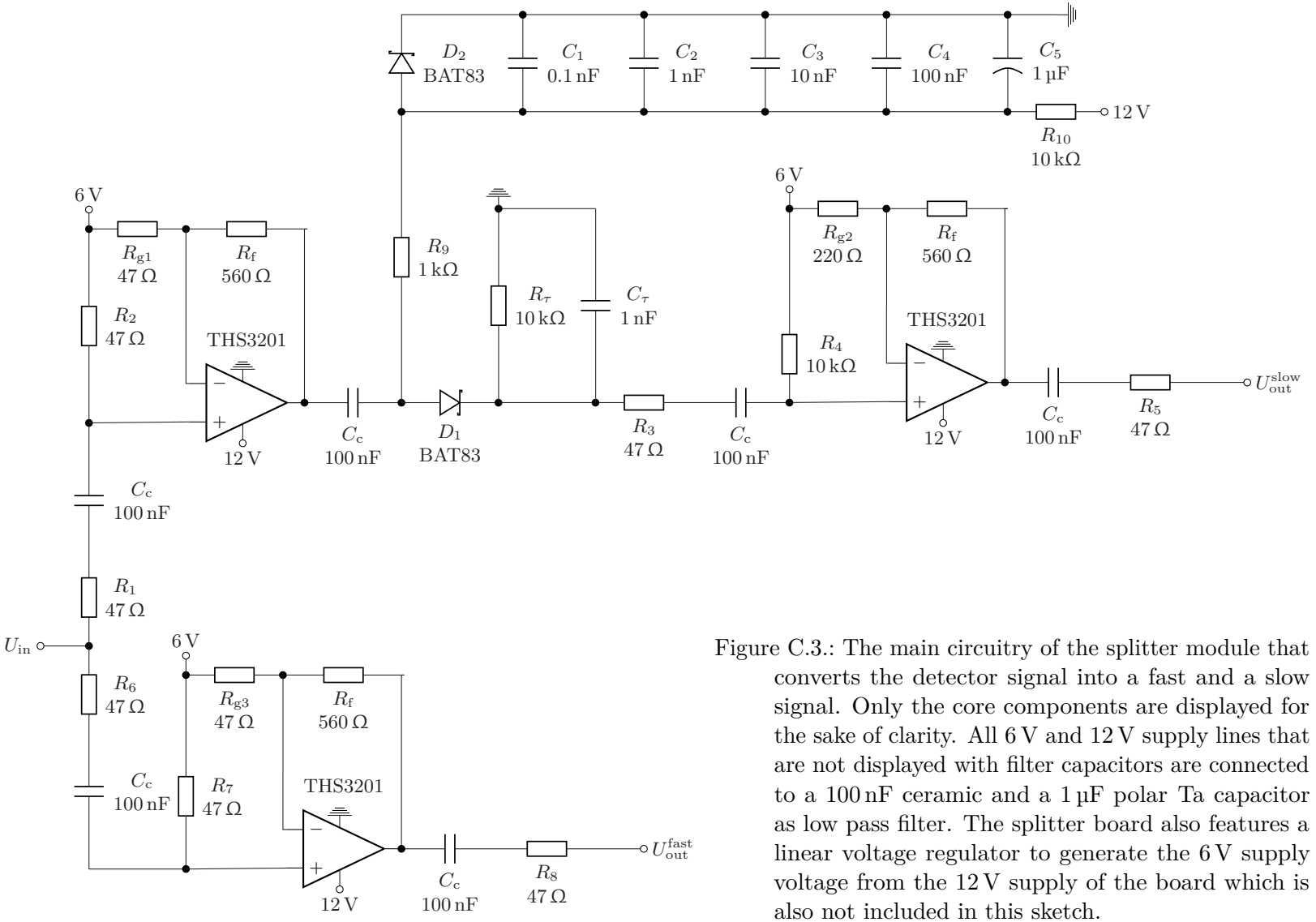

Figure C.3.: The main circuitry of the splitter module that converts the detector signal into a fast and a slow signal. Only the core components are displayed for the sake of clarity. All 6 V and 12 V supply lines that are not displayed with filter capacitors are connected to a 100 nF ceramic and a 1 µF polar Ta capacitor as low pass filter. The splitter board also features a linear voltage regulator to generate the 6 V supply voltage from the 12 V supply of the board which is also not included in this sketch.

name	type	value	footprint
R_1 – R_3	thin film resistor	47 Ω	1206
R_4	metal film resistor	10 kΩ	1206
R_5 – R_8	thin film resistor	47 Ω	1206
R_9	metal film resistor	1 kΩ	1206
R_10	metal film resistor	10 kΩ	1206
R_f	thin film resistor	560 Ω	1206
R_{g1}	thin film resistor	47 Ω	1206
R_{g2}	thin film resistor	220 Ω	1206
R_{g3}	thin film resistor	47 Ω	1206
C_c	C0G capacitor	100 nF	1206
C_1	C0G capacitor	0.1 nF	1206
C_2	C0G capacitor	1 nF	1206
C_3	X7R capacitor	10 nF	1206
C_4	X7R capacitor	100 nF	1206
C_5	Ta capacitor	1 µF	1206
D_1, D_2	BAT83 Schottky diode	–	DO-34
THS3201	operational amplifier	–	SOIC-8

Table C.2.: A list of components used for the splitter module. The linear voltage generator is not included.

A circuit diagram of the splitter module can be found in figure C.3, a list of parts in table C.2 (both excluding the linear voltage regulator).

C.3. Line position and width determination

To determine the line positions and widths of γ and X-ray lines measured with the C30703FH-200T Avalanche Photo Diode (APD) and the SAHAR module, a spline is fitted to the measured data using a Python script. The steps carried out are sketched in the following.

Firstly, a rough guess for the position of the maximum $x_{\mathrm{max?}}$ is needed. A Gaussian kernel with a smoothing parameter of 20 is used to reduce the fluctuations, especially for spectra with low statistics, in the measured data. For $x_{\mathrm{max?}}$, the channel with most events is chosen. The true maximum x_{max} of the fitted line is expected within an interval I_{max} of $\pm 30\,\%$ around this value.

In the second step, the original data are smoothed using a Gaussian kernel with a smoothing parameter of one. A spline of fourth degree is fitted to the smoothed data, the derivative and second derivative are calculated to obtain all extrema and inflection points. The maxima in the interval I_{max} and the inflection points in the interval I_{inf} of $\pm 15\,\%$ around $x_{\mathrm{max?}}$ are counted. If more than one maximum or more than two inflection points are found in I_{max} and I_{inf}, respectively, the smoothing parameter is increased by one and the above steps are repeated. Once the smoothing parameter is found this way, it is kept fixed.

In order to assess the maximum's uncertainty and the left and right half maxima including the uncertainties in the third step, a Monte Carlo method is used. The event numbers in every channel from the original data are randomised with a Poissonian distribution. The data are smoothed using the smoothing parameter that was obtained in the second step. Using the first derivative, the maximum x^i_{max} of the ith Monte Carlo run is determined. With this known maximum, the left and right half maxima $x^i_{\mathrm{hmax,l/r}}$ of the ith Monte Carlo run are calculated. This process is repeated N times, all x^i_{max} and $x^i_{\mathrm{hmax,l/r}}$ are recorded.

In the last step, the position of the maximum and the half maxima can be determined including the corresponding uncertainties by calculating the average and the standard deviation of all x^i_{max} and $x^i_{\mathrm{hmax,l/r}}$, respectively.

List of acronyms

ADC Analog to Digital Converter

APD Avalanche Photo Diode

BNC Bayonet Neill-Concelman

BONIS BONn Isotope Separator

CE Conversion Electron

CERN Conseil Européen pour la Recherche Nucléaire

CFD Constant Fraction Discriminator

CNC Computer Numeric Control

CPS Cryogenic Pumping Section

CsF Caesium Fluoride

DDL Double Delay Line

DFT Density Functional Theory

DPS Differential Pumping Section

EC Electron Capture

EDM Electrical Discharge Machining

EFG Electric Field Gradient

ESD ElectroStatic Discharge

FBM Forward Beam Monitor

FPD Focal Plane Detector

fcc face-centered cubic

FWHM Full Width at Half Maximum

hcp hexagonal close-packed

HISKP Helmholtz-Institut für Strahlen- und Kernphysik

HOPG Highly Oriented Pyrolytic Graphite

HPGe High Purity Ge

ISOLDE Isotope mass Separator On-Line DEvice

KATRIN KArlsruhe TRItium Neutrino

KIT Karlsruhe Institute of Technology

LYSO Lutetium Yttrium OxyorthoSilicate

LYSO:Ce Cerium doped Lutetium Yttrium OxyorthoSilicate

MAC-E Magnetic Adiabatic Collimation combined with an Electrostatic

MCA Multi Channel Analyzer

MCP MicroChannel Plate

MoS Monitor Spectrometer

NPI Nuclear Physics Institute

NQM Nuclear Quadrupole Moment

PAC Perturbed Angular Correlation

PCB Printed Circuit Board

PIN Positive Intrinsic Negative

PM PhotoMultiplier

PTFE Polytetrafluoroethylene

RMS Root Mean Square

SAHAR Sequentially Arranged High-gain AmplifieR

SCA Single Channel Analyser

SHV Safe High Voltage

SMA SubMiniature version A

SPICE Simulation Program with Integrated Circuit Emphasis

SRIM Stopping and Range of Ions in Matter

T-SCA Timing Single Channel Analyser

TAC Time to Amplitude Converter

TMP TurboMolecular Pump

TRIM TRansport of Ions in Matter

WGTS Windowless Gaseous Tritium Source

List of figures

List of tables

Bibliography

[AbrBos09] D. Abriola, M. Bostan, et al. "Nuclear Data Sheets for A = 84". *Nuclear Data Sheets* 110.11 (2009), pp. 2815–2944. DOI: 10.1016/j.nds.2009.10.002 (cit. on p. 40).

[AldAlb53] K. Alder, H. Albers-Schönberg, et al. "The measurement of nuclear moments of excited states by angular correlation methods. I". *Helvetica Physica Acta* 26 (1953), pp. 761–784. DOI: 10.5169/seals-112438 (cit. on pp. 21, 22).

[AreHoh80] A. R. Arends, C. Hohenemser, et al. "Data reduction methodology for perturbed angular correlation experiments". *Hyperfine Interactions* 8.1 (1980), pp. 191–213. DOI: 10.1007/BF01026869 (cit. on pp. 43, 44, 152, 164).

[BahBah68] J. N. Bahcall, N. A. Bahcall, and G. Shaviv. "Present Status of the Theoretical Predictions for the ^{37}Cl Solar-Neutrino Experiment". *Physical Review Letters* 20 (21 1968), pp. 1209–1212. DOI: 10.1103/PhysRevLett.20.1209 (cit. on p. 4).

[BarKis06] A. Q. R. Baron, S. Kishimoto, et al. "Silicon avalanche photodiodes for direct detection of X-rays". *Journal of Synchrotron Radiation* 13 (2006), pp. 131–142. DOI: 10.1107/S090904950503431X (cit. on pp. 103, 105–107, 110, 114).

[BarLam71] J. Barrette, G. Lamoureux, and S. Monaro. "Geometrical correction factors for angular correlation measurements with Ge(Li) detectors". *Nuclear Instruments and Methods* 93.1 (1971), pp. 1–11. DOI: 10.1016/0029-554X(71)90131-5 (cit. on pp. 31, 136).

[Barlow89] R. Barlow. *Statistics*. John Wiley & Sons Ltd., 1989 (cit. on p. 168).

[Baron06] A. Q. R. Baron. *Avalanche Diodes (APD) Detectors: Introduction and Recent Advances (Focus on Fast X-Ray Detection)*. International Symposium on the Development of Detectors for Particle, Astro-Particle, and Synchrotron Radiation Experiments (SNIC). Apr. 2006 (cit. on p. 106).

[Barrad92] Nuno Pessoa Barradas. *NNFIT the PAC MANual*. 1992 (cit. on p. 44).

[BarRüf97] A. Q. R. Baron, R. Rüffer, and J. Metge. "A fast, convenient, X-Ray detector". *Nuclear Instruments and Methods in Physics Research Section A: Accelerators, Spectrometers, Detectors and Associated Equipment* 400 (1997), pp. 124–132. DOI: 10.1016/S0168-9002(97)00936-4 (cit. on p. 121).

[BeaPor80] G. Beamson, H. Q. Porter, and D. W. Turner. "The collimating and magnifying properties of a superconducting field photoelectron spectrometer". *Journal of Physics E: Scientific Instruments* 13.1 (1980), p. 64. URL: http://stacks.iop.org/0022-3735/13/i=1/a=018 (cit. on p. 6).

[BieHag80] J. P. Biersack and L. G. Haggmark. "A Monte Carlo computer program for the transport of energetic ions in amorphous targets". *Nuclear Instruments and Methods* 174.1 (1980), pp. 257–269. DOI: 10.1016/0029-554X(80)90440-1 (cit. on p. 48).

[BieRos53] L. C. Biedenharn and M. E. Rose. "Theory of Angular Correlation of Nuclear Radiations". *Reviews of Modern Physics* 25 (1953), pp. 729–777. DOI: 10.1103/RevModPhys.25.729 (cit. on pp. 13, 18, 19, 25, 26, 38).

[Binder99] H. H. Binder. *Lexikon der chemischen Elemente*. Hirzel Verlag, 1999 (cit. on pp. 53, 54, 57).

[BroSem99] I. N. Bronstein, K. A. Semendjajev, et al. *Taschenbuch der Mathematik*. 4th ed. Verlag Harri Deutsch, 1999 (cit. on p. 178).

[Butz89] T. Butz. "Analytic Perturbation Functions for Static Interactions in Perturbed Angular Correlations of γ-rays". *Hyperfine Interactions* 52 (1989), pp. 189–228. DOI: 10.1007/BF02651311 (cit. on pp. 13, 20).

[CheKes96] V.N. Chernikov, W. Kesternich, and H. Ullmaier. "Radiation effects and gas cavities in pyrolytic graphite implanted with helium ions". *Journal of Nuclear Materials* 227.3 (1996), pp. 157–169. DOI: 10.1016/0022-3115(95)00157-3 (cit. on p. 162).

[Cotten16] S. Cottenier. *Personal message*. July 2016 (cit. on p. 153).

[DatTay56] S. Datz and E. H. Taylor. "Ionization on Platinum and Tungsten Surfaces. I. The Alkali Metals". *Journal of Chemical Physics* 25.3 (1956), pp. 389–394. DOI: 10.1063/1.1742931 (cit. on p. 70).

[DavHar68] R. Davis, Don S. Harmer, and K. C. Hoffman. "Search for Neutrinos from the Sun". *Physical Review Letters* 20 (21 1968), pp. 1205–1209. DOI: 10.1103/PhysRevLett.20.1205 (cit. on p. 4).

[DreDre81] M.S. Dresselhaus and G. Dresselhaus. "Intercalation compounds of graphite". *Advances in Physics* 30.2 (1981). 10.1080/00018738100101367, pp. 139–326. DOI: 10/c2rnxw (cit. on p. 53).

[DueSch69] G. Duesing and W. Schilling. "Stage III recovery in electron-irradiated platinum". *Radiation Effects* 1.1 (1969). 10.1080/00337576908234461, pp. 65–67. DOI: 10/cthx7k (cit. on p. 51).

[EG&G98] EG&G Optoelectronics Canada. *C30703E/F Series 10 x 10 mm Silicon Avalanche Photodiodes*. Personal message. Oct. 1998 (cit. on pp. 116, 127).

[Elling16] E. Ellinger. *Acceptance test for the Forward Beam Monitor*. Presentation at the 31st KATRIN collaboration meeting. 2016 (cit. on p. 56).

[Eversh16] P.-D. Eversheim. *Personal message*. Nov. 2016 (cit. on pp. 63, 95, 96).

[Exceli14a] Excelitas Technologies. *C30703FH Avalanche Photodiode Interim Datasheet*. Feb. 2014 (cit. on pp. 107, 108, 110, 116, 122, 126, 138).

[Exceli14b] Excelitas Technologies. *Personal message*. Aug. 2014 (cit. on p. 127).

[Exceli16] Excelitas Technologies. *Personal message*. May 2016 (cit. on pp. 107, 116).

[FeiFra55] A. M. Feingold and S. Frankel. "Geometrical Corrections in Angular Correlation Measurements". *Physical Review* 97.4 (1955), pp. 1025–1030. DOI: 10.1103/PhysRev.97.1025 (cit. on pp. 31, 32).

[FerRos68] M. Ferentz and N. Rosenzweig. "Table Of Angular Correlation Coefficients". *Alpha-, Beta- and Gamma-Ray Spectroscopy*. Ed. by E. Karlsson. 3rd ed. Vol. 2. North-Holland Publishing Company Amsterdam, 1968. App. 8, pp. 1687–1690 (cit. on p. 19).

[Flaxer06] E. Flaxer. "A low-cost, ultra-fast and low-noise preamplifier for micro channel plates". *Measurement Science and Technology* 17.8 (2006), p. 37. DOI: 10.1088/0957-0233/17/8/N02 (cit. on p. 121).

[FraKar76] S. Fraga, J. Karwowski, and K. M. S. Saxena. *Handbook of atomic data*. Elsevier Scientific Publishing Company, 1976 (cit. on p. 55).

[Franke51] S. Frankel. "The Effect of Scattering on Angular Correlation Measurements". *Physical Review* 83.3 (1951), p. 673. DOI: 10.1103/PhysRev.83.673 (cit. on p. 29).

[Fraser83] G.W. Fraser. "The electron detection efficiency of microchannel plates". *Nuclear Instruments and Methods in Physics Research* 206.3 (1983), pp. 445–449. ISSN: 0167-5087. DOI: 10.1016/0167-5087(83)90381-2 (cit. on p. 112).

[FraSte68] H. Frauenfelder, R. M. Steffen, et al. "Angular Distribution of Nuclear Radiation". *Alpha-, Beta- and Gamma-Ray Spectroscopy*. Ed. by Kai Siegbahn. 3rd ed. Vol. 2. North-Holland Publishing Company Amsterdam, 1968. Chap. 19, pp. 997–1198 (cit. on pp. 13, 14, 18–20, 22, 26, 31, 32, 39, 207).

[FreHei70] K. Freitag, C. Heising, et al. "Isotopen-Separator". *Jahresbericht ISKP*. Institut für Strahlen- und Kernphysik, Rheinische Friedrich-Wilhelms-Universität Bonn, 1969 – 1970, p. 62 (cit. on pp. 65, 95, 96).

[FreHei76] K. Freitag, C. Heising, et al. "The preparation of ^{166}Er targets for in-beam experiments". *Nuclear Instruments and Methods* 139 (1976). 10.1016/0029-554X(76)90659-5, pp. 83–85. DOI: 10/d97tdv (cit. on pp. 63, 78, 100).

[Freita77] K. Freitag. "Bestimmung des "Penetration"-Parameters λ der anomalen M1-Konversion des 482 keV-Übergangs in ^{181}Ta mit Hilfe der zeitlich differentiellen Beobachtung gestörter e^--γ-Winkelkorrelationen in Beryllium". PhD thesis. Rheinische Friedrich-Wilhelms-Universität Bonn, 1977 (cit. on pp. 88, 96).

[Freita79] K. Freitag. "A facility for ion implantation in samples colder than 0.5 K". *Radiation Effects* 44.1-4 (1979). 10.1080/00337577908245993, pp. 185–190. DOI: 10/ffqx6r (cit. on pp. 63, 64).

[Friis44] H. T. Friis. "Noise Figures of Radio Receivers". *Proceedings of the IRE* 32.7 (1944), pp. 419–422. DOI: 10.1109/JRPROC.1944.232049 (cit. on p. 126).

[GimHee56] F. Gimmi, E. Heer, and P. Scherrer. "Beiträge zur Konversionselektronenkorrelation". *Helvetica Physica Acta* 29 (1956), pp. 147–186. DOI: 10.5169/seals-112702 (cit. on pp. 30, 32).

[GolFra56] R. K. Golden and S. Frankel. "Electron Scattering in the K-Electron – Gamma Angular Correlation in Sn^{117}". *Physical Review* 102.4 (1956), pp. 1053–1057. DOI: 10.1103/PhysRev.102.1053 (cit. on p. 30).

[Goodfe17] Goodfellow GmbH. *Standardpreisliste für Platin*. 13.5.2017. URL: http://www.goodfellow.com/ (cit. on pp. 50, 51).

[GouSau40a] S. Goudsmit and J. L. Saunderson. "Multiple Scattering of Electrons". *Physical Review* 57.1 (1940), pp. 24–29. DOI: 10.1103/PhysRev.57.24 (cit. on pp. 29, 30).

[GouSau40b] S. Goudsmit and J. L. Saunderson. "Multiple Scattering of Electrons II". *Physical Review* 58.1 (1940), pp. 36–42. DOI: 10.1103/PhysRev.58.36 (cit. on p. 29).

[GriPon69] V. Gribov and B. Pontecorvo. "Neutrino astronomy and lepton charge". *Physics Letters B* 28.7 (1969), pp. 493–496. DOI: 10.1016/0370-2693(69)90525-5 (cit. on p. 4).

[Haas77] H. Haas. "Quadrupolmomente isomerer Zustände in ^{79}Kr und ^{77}Br". *Wissenschaftlicher Ergebnisbericht 1977*. Hahn-Meitner-Institut für Kernforschung Berlin GmbH, 1977, p. 50 (cit. on p. 38).

[Hamama05] Hamamatsu Photonics K.K., Solid State Division. *Si APD S8664 series*. 1126-1 Ichino-cho, Hamamatsu City, 435-8558 Japan. Oct. 2005. URL: www.hamamatsu.com (cit. on pp. 114, 116).

[Hamama12] Hamamatsu Photonics K.K., Solid State Division. *Product information: S8664vsS11625 Spectral response (M=50)*. Personal message. Feb. 2012 (cit. on p. 114).

[Hamama16a] Hamamatsu Photonics K.K. *Personal message*. May 2016 (cit. on pp. 107, 116).

[Hamama16b] Hamamatsu Photonics K.K., Electron Tube Division. *MCP (microchannel plate) and MCP assembly*. 314-5, Shimokanzo, Iwata City, Shizuoka Pref., 438-0193, Japan. Jan. 2016. URL: www.hamamatsu.com (cit. on p. 112).

[HelLee80] R.G. Helmer and M.A. Lee. "Analytical functions for fitting peaks from Ge semiconductor detectors". *Nuclear Instruments and Methods* 178.2–3 (1980), pp. 499–512. DOI: 10.1016/0029-554X(80)90830-7 (cit. on pp. 61, 174).

[HenGul93] B.L. Henke, E.M. Gullikson, and J.C. Davis. "X-Ray Interactions: Photoabsorption, Scattering, Transmission, and Reflection at E = 50-30,000 eV, Z = 1-92". *Atomic Data and Nuclear Data Tables* 54.2 (1993), pp. 181–342. DOI: 10.1006/adnd.1993.1013 (cit. on pp. 51, 52, 55, 107, 116, 138).

[Hillec68] D. Hillecke. "Absolutmessung der Ionisierungsausbeute von Alkaliatomen an Metalloberflächen". *Zeitschrift für Physik* 215.4 (1968), pp. 343–349. DOI: 10.1007/BF01380014 (cit. on p. 70).

[HolSch77] J. H. Holloway, G. J. Schrobilgen, et al. "Mössbauer spectroscopy of KrF_2 and $KrF_2 \cdot MF_5$ (M=As, Sb)". *Journal of Chemical Physics* 66 (1977), p. 2627 (cit. on p. 36).

[Honisc15] C. Honisch. "Design, Aufbau und Test einer neuen Ausleseelektronik für das Crystal-Barrel-Kalorimeter". PhD thesis. Rheinische Friedrich-Wilhelms-Universität Bonn, 2015. URL: http://hss.ulb.uni-bonn.de/2015/4111/4111.pdf (cit. on p. 83).

[HuhLiu00] C.A. Huh and L.G. Liu. "Precision Measurements of the Half-Lives of Some Electron-Capture Decay Nuclides: ^{7}Be, ^{54}Mn, ^{83}Rb, and ^{84}Rb". *Journal of Radioanalytical and Nuclear Chemistry* 246.1 (2000), pp. 229–231. DOI: 10.1023/A:1006788022029 (cit. on pp. 88, 90).

[IAEA17] IAEA Nuclear Data Section. *Live Chart of Nuclides*. 19.05.2017. URL: https://www-nds.iaea.org/relnsd/vcharthtml/VChartHTML.html (cit. on pp. 39, 40, 88, 96).

[JacCan77] C. Jacoboni, C. Canali, et al. "A review of some charge transport properties of silicon". *Solid-State Electronics* 20.2 (1977), pp. 77–89. DOI: 10.1016/0038-1101(77)90054-5 (cit. on pp. 108, 138).

[Jackso99] J. D. Jackson. *Classical Electrodynamics*. 3rd ed. John Wiley & Sons, Inc., 1999 (cit. on pp. 13, 14).

[JohBol73] P. G. Johnson, A. Bolson, and C. M. Henderson. "A high temperature ion source for isotope separators". *Nuclear Instruments and Methods* 106.1 (1973), pp. 83–87. DOI: 10.1016/0029-554X(73)90049-9 (cit. on pp. 68, 70).

[KamDre80] N. Kambe, G. Dresselhaus, and M. S. Dresselhaus. "Electron diffraction from superlattices in graphite-rubidium intercalation compounds". *Physical Review B* 21 (8 1980), pp. 3491–3501. DOI: 10.1103/PhysRevB.21.3491 (cit. on pp. 53, 54, 158).

[KATRIN04] The KATRIN collaboration. *KATRIN Design Report 2004*. 2004 (cit. on pp. 3, 4, 8, 58).

[KATRIN16] The KATRIN collaboration. "Commissioning of the vacuum system of the KATRIN Main Spectrometer". *Journal of Instrumentation* 11.04 (2016), P04011. URL: http://stacks.iop.org/1748-0221/11/i=04/a=P04011 (cit. on p. 10).

[KatSai05] J. Kataoka, T. Saito, et al. "Recent progress of avalanche photodiodes in high-resolution X-rays and γ-rays detection". *Nuclear Instruments and Methods in Physics Research Section A: Accelerators, Spectrometers, Detectors and Associated Equipment* 541 (2005), pp. 398–404. DOI: 10.1016/j.nima.2005.01.081 (cit. on pp. 104–106, 113, 116).

[KauVia79] E. Kaufman and R. Vianden. "The electric field gradient in noncubic metals". *Reviews of Modern Physics* 51 (1 1979), pp. 161–214. DOI: 10.1103/RevModPhys.51.161 (cit. on pp. 17, 155).

[KelPyy01] V. Kellö, P. Pyykkö, and A. J. Sadlej. "Nuclear quadrupole moments of Kr and Xe from molecular data". *Chemical Physics Letters* 346 (2001), pp. 155–159. DOI: 10.1016/S0009-2614(01)00940-X (cit. on p. 38).

[Keßler08] P. Keßler. "Implantationsschäden in polaren und unpolaren ZnO Einkristallen". Diploma Thesis. Helmholtz-Institut für Strahlen- und Kernphysik, University of Bonn, 2008 (cit. on p. 56).

[Koch92] H. Koch. "Defekt-Fremdatom Wechselwirkungen in den hexagonalen Metallen Rhenium und Lutetium". PhD thesis. Rheinische Friedrich-Wilhelms-Universität Bonn, 1992 (cit. on p. 134).

[KopHer07] K. Kopitzki and P. Herzog. *Einführung in die Festkörperphysik*. Vieweg + Teubner, 2007 (cit. on pp. 51, 55).

[Kotz12] C. Kotz. *Personal message*. May 2012 (cit. on p. 69).

[KovTár91] Z. Kovács, F. Tárkányi, et al. "Excitation functions for the formation of some radioisotopes of rubidium in proton induced nuclear reactions on $^{nat.}$Kr, ^{82}Kr and ^{83}Kr with special reference to the production of ^{81}Rb(^{81m}Kr) generator radionuclide". *International Journal of Radiation Applications and Instrumentation. Part A. Applied Radiation and Isotopes* 42.4 (1991), pp. 329–335 (cit. on p. 40).

[Kuiper61] H. Kuiper. "Messung der Hyperfeinstruktur-Aufspaltung des metastabilen3 P 2-Zustandes des Kr83 nach der Atomstrahl-Resonanzmethode". *Zeitschrift für Physik* 165.4 (1961), pp. 402–418. DOI: 10.1007/BF01381898 (cit. on p. 36).

[Kürten13] S. Kürten. "Untersuchung über die Zurückhaltung von ^{83}Rb beim thermischen Ausheilen von Platin, Zinkoxid und Graphit". Bachelor Thesis. Helmholtz-Institut für Strahlen- und Kernphysik, University of Bonn, 2013 (cit. on pp. 49, 56).

[LatRai75] A. Latuszyński and V.I. Raiko. "Studies of the ion source with surface-volume ionization". *Nuclear Instruments and Methods* 125.1 (1975), pp. 61–66. DOI: 10.1016/0029-554X(75)90553-4 (cit. on pp. 70, 71, 101).

[LatZub74] A. Latuszyński, K. Zuber, et al. "Method of electromagnetic separation of radioactive isotopes of rare-earth elements directly from targets". *Nuclear Instruments and Methods* 120.2 (1974), pp. 321–328. DOI: 10.1016/0029-554X(74)90053-6 (cit. on p. 71).

[Lavoie73] I. Lavoie. "Comparison of radiation detector materials for imaging applications in nuclear medicine". *Physics in Medicine and Biology* 18.1 (1973), p. 120 (cit. on pp. 103, 138).

[Lebeda15] O. Lebeda. *Personal message*. July 2015 (cit. on p. 92).

[Lebeda16] O. Lebeda. *Personal message*. Aug. 2016 (cit. on p. 41).

[Lebeda17] O. Lebeda. *Personal message*. Jan. 2017 (cit. on p. 40).

[LeePea97] J.E. Lees and J.F. Pearson. "A large area MCP detector for X-ray imaging". *Nuclear Instruments and Methods in Physics Research Section A: Accelerators, Spectrometers, Detectors and Associated Equipment* 384.2 – 3 (1997), pp. 410–424. ISSN: 0168-9002. DOI: 10.1016/S0168-9002(97)81164-3 (cit. on p. 112).

[LloBal07] X. Llopart, R. Ballabriga, et al. "Timepix, a 65k programmable pixel readout chip for arrival time, energy and/or photon counting measurements". *Nuclear Instruments and Methods in Physics Research Section A: Accelerators, Spectrometers, Detectors and Associated Equipment* 581.1 –2 (2007), pp. 485–494. DOI: 10.1016/j.nima.2007.08.079 (cit. on p. 47).

[LobAse99] V.M Lobashev, V.N Aseev, et al. "Direct search for mass of neutrino and anomaly in the tritium beta-spectrum". *Physics Letters B* 460.1 – 2 (1999), pp. 227–235 (cit. on p. 6).

[MagPfe06] J. Magill, G. Pfennig, et al. *Karlsruhe Nuclide Chart*. 2006 (cit. on p. 39).

[MalLan39] L. Malter and D. B. Langmuir. "Resistance, Emissivities and Melting Point of Tantalum". *Physical Review* 55 (8 1939), pp. 743–747 (cit. on p. 74).

[Marque96] José J. G. Marques. "Interacções hiperfinas em monocristais de cobalto e niobato de lítio usando ^{111}Cd, ^{181}Ta, ^{197}Hg e ^{199}Hg: desenvolvimento experimental e deerminação precisa de constantes de interacção". PhD thesis. Faculdade de Ciências da Universidade de Lisboa, 1996 (cit. on p. 135).

[McCutc15] E.A. McCutchan. "Nuclear Data Sheets for A = 83". *Nuclear Data Sheets* 125 (2015), pp. 201–394. DOI: 10.1016/j.nds.2015.02.002 (cit. on pp. 11, 19, 36–38, 119, 143, 144, 146, 149, 150).

[MinCir16a] Mini-Circuits. *MAR-6+: Drop-In Monolithic Amplifier*. P.O. Box 350166, Brooklyn, NY 11235-0003. 10.5.2016. URL: www.minicircuits.com (cit. on pp. 122, 140).

[MinCir16b] Mini-Circuits. *MAR-6+: MMIC Amplifier, Typical Perfomance Data*. P.O. Box 350166, Brooklyn, NY 11235-0003. Downloaded on 10.5.2016. URL: www.minicircuits.com (cit. on p. 124).

[MiyGot81] H. Miyahara, T. Gotoh, and T. Watanabe. "Half-lives and γ-ray intensities per decay of ^{86}Rb and ^{103}Ru". *The International Journal of Applied Radiation and Isotopes* 32.8 (1981), pp. 573–579. DOI: 10.1016/0020-708X(81)90036-3 (cit. on pp. 88, 98).

[MosAll83] M. Moszyński, R. Allemand, et al. "Recent progress in fast timing with CsF scintillators in application to time-of-flight positron tomography in medicine". *Nuclear Instruments and Methods in Physics Research* 205.1 – 2 (1983), pp. 239–249. DOI: 10.1016/0167-5087(83)90194-1 (cit. on p. 103).

[Nédéle07] R. Nédélec. "Seltene Erden in GaN und ZnO untersucht mit der PAC-Methode". PhD thesis. Helmholtz-Institut für Strahlen- und Kernphysik, University of Bonn, 2007. URL: https://tdpac.hiskp.uni-bonn.de/ (cit. on pp. 44, 152).

[NegSin15] A. Negret and B. Singh. "Nuclear Data Sheets for A = 86". *Nuclear Data Sheets* 124 (2015), pp. 1–156. DOI: 10.1016/j.nds.2014.12.045 (cit. on p. 40).

[NuDat16] National Nuclear Data Center. *Nudat 2.6*. 21/09/2016. URL: http://www.nndc.bnl.gov/nudat2/ (cit. on pp. 61, 168).

[Ortec95a] Ortec. *Germanium Detector Diagram, Serial Number 35-N11136A*. 801 S. Illinois Ave., Oak Ridge TN 37831, 1995 (cit. on p. 168).

[Ortec95b] Ortec. *Quality Assurance Data Sheet, GMX Series HPGe GAMMA-X HPGE*. 801 S. Illinois Ave., Oak Ridge TN 37831, 1995 (cit. on p. 168).

[Ostric09] B. Ostrick. "Eine kondensierte 83mKr-Kalibrationsquelle für das KATRIN-Experiment". PhD thesis. Westfälische Wilhelms-Universität Münster, 2009. URL: http://nbn-resolving.de/urn:nbn:de:hbz:6-91519454708 (cit. on p. 11).

[Pauli30] Wolfgang Pauli. *Offener Brief an die Gruppe der Radioaktiven bei der Gauvereins/Tagung zu Tübingen*. online. 1930. URL: http://microboone-docdb.fnal.gov/cgi-bin/RetrieveFile?docid=953;filename=pauli%20letter1930.pdf (cit. on p. 3).

[PhiMar76] Gary W. Phillips and Keith W. Marlow. "Automatic analysis of gamma-ray spectra from germanium detectors". *Nuclear Instruments and Methods* 137.3 (1976), pp. 525–536. DOI: 10.1016/0029-554X(76)90472-9 (cit. on pp. 61, 174).

[PlaTro75] P. A. Platonov, E. I. Trofimchuk, et al. "Annealing of radiation damage in graphite". *Radiation Effects* 25.2 (1975), pp. 105–110. DOI: 10.1080/00337577508234735 (cit. on p. 54).

[RasMai08] M. Rasulbaev, K. Maier, et al. "Production of 83Rb for the KATRIN experiment". *Applied Radiation and Isotopes* 66.12 (2008), pp. 1838–1843. DOI: 10.1016/j.apradiso.2008.04.020 (cit. on pp. 39, 40).

[Rasulb10] M. Rasulbaev. "Isotopes for fundamental research". PhD thesis. Rheinische Friedrich-Wilhelms-Universität Bonn, 2010. URL: http://hss.ulb.uni-bonn.de/2011/2461/2461.pdf (cit. on pp. 39, 40).

[ReiCow56] F. Reines and C. L. Cowan. "The Neutrino". *Nature* 178 (1956), pp. 446–449. DOI: 10.1038/178446a0 (cit. on p. 3).

[ReiZwe55] J. Reiprich and W. v. Zwehl, eds. *Aluminiumtaschenbuch*. 11th ed. Aluminium-Verlag, 1955 (cit. on p. 57).

[RogVas75] J.D. Rogers and A. Vasquez. "Data reduction in perturbed angular correlation experiments". *Nuclear Instruments and Methods* 130.2 (1975), pp. 539–541. DOI: 10.1016/0029-554X(75)90054-3 (cit. on p. 24).

[RosBie52] M. E. Rose, L. C. Biedenharn, and G. B. Arfken. "Internal Conversion Angular Correlations". *Physical Review* 85 (1 1952), pp. 5–16. DOI: 10.1103/PhysRev.85.5 (cit. on pp. 13, 25–27, 39).

[Rose53] M. E. Rose. "The Analysis of Angular Correlation and Angular Distribution Data". *Physical Review* 91 (1953), pp. 610–615. DOI: 10.1103/PhysRev.91.610 (cit. on p. 31).

[Ruske01] F. Ruske. "Indiumimplantation in Galliumnitrid untersucht mit der γ-γ-Winkelkorrelationsmethode". Diploma Thesis. Helmholtz-Institut für Strahlen- und Kernphysik, University of Bonn, 2001 (cit. on pp. 43, 44).

[SaiGob04] Saint-Gobain Crystals. *PreLude 420*. 104 Route de Larchant, BP 52177794, Nemours Cedex, France. Apr. 2004. URL: www.crystals.saint-gobain.com (cit. on pp. 113, 114).

[Schäbe12] A. Schäbe. "Simulation und Messung der Temperaturverteilung einer Wolframionenquelle". Bachelor Thesis. Helmholtz-Institut für Strahlen- und Kernphysik, University of Bonn, 2012 (cit. on pp. 72, 75).

[Schäbe16] A. Schäbe. *Personal message*. Sept. 2016 (cit. on p. 75).

[SchVia87] R. Schumacher and R. Vianden. "Influence of rare gases on cavity formation at indium impurities in copper". *Physical Review B* 36 (16 1987), pp. 8258–8262. DOI: 10.1103/PhysRevB.36.8258 (cit. on p. 162).

[SchWei92] G. Schatz and A. Weidinger. *Nukleare Festkörperphysik*. 2nd ed. B.G. Teubner Stuttgart 1992, 1992 (cit. on pp. 13, 14, 19, 35, 36, 43, 45).

[SeiSte12] S. Seifert, J. H. L. Steenbergen, et al. "Accurate measurement of the rise and decay times of fast scintillators with solid state photon counters". *Journal of Instrumentation* 7.09 (2012), P09004. DOI: 10.1088/1748-0221/7/09/P09004 (cit. on p. 113).

[Sentke16a] J. Sentkerestiová. *Personal message*. Sept. 2016 (cit. on pp. 47, 50).

[Sentke16b] J. Sentkerestiová. *Personal message*. Oct. 2016 (cit. on pp. 47, 48, 50, 57, 177).

[SenVén16] J. Sentkerestiová and D. Vénos. *Personal message*. Sept. 2016 (cit. on pp. 47, 50, 85, 177).

[SevBel09] N. Severijns, A. A. Belyaev, et al. "Hyperfine field of einsteinium in iron and nuclear magnetic moment of ^{254}Es". *Physical Review C* 79 (2009), p. 064322. DOI: 10.1103/PhysRevC.79.064322 (cit. on pp. 63, 88).

[Shikha97] P. M. Shikhaliev. "Generalized hard x-ray detection model for microchannel plate detectors". *Review of Scientific Instruments* 68.10 (1997), pp. 3676–3684. DOI: 10.1063/1.1148011 (cit. on p. 112).

[Slezák15a] M. Slezák. "Monitoring of the energy scale in the KATRIN neutrino experiment". PhD thesis. Nuclear Physics Institute, Czech Academy of Sciences, 2015. URL: https://www.katrin.kit.edu/publikationen/phd-Martin_Slezak.pdf (cit. on pp. 12, 47–53, 58–60, 79, 85, 100, 173).

[Slezák15b] M. Slezák. *Personal message*. June 2015 (cit. on pp. 47, 50, 81, 85, 93).

[Slezák15c] M. Slezák. *Personal message*. Mar. 2015 (cit. on p. 57).

[Slezák16a] M. Slezák. *Measurements with the monitor spectrometer and possible implications*. Presentation at the 30th KATRIN collaboration meeting. 2016 (cit. on pp. 58, 60).

[Slezák16b] M. Slezák. *Personal message*. June 2016 (cit. on pp. 47, 176).

[SNO02] SNO Collaboration. "Direct Evidence for Neutrino Flavor Transformation from Neutral-Current Interactions in the Sudbury Neutrino Observatory". *Physical Review Letters* 89 (1 2002), p. 011301. DOI: 10.1103/PhysRevLett.89.011301 (cit. on p. 4).

[SopDup12] N. Soppera, E. Dupont, and M. Bossant. *JANIS Book of alpha-induced cross-sections*. OECD NEA Data Bank, 2012. URL: http://www.oecd-nea.org/janis/book/ (cit. on p. 40).

[SPISup15] SPI Supplies. *Technical Note, SPI Supplies HOPG*. 206 Garfield Ave., West Chester, PA 19380. Aug. 2015. URL: www.2spi.com (cit. on pp. 52–54).

[SPISup17] SPI Supplies. *SPI HOPG Grade 1*. 5.1.2017. URL: http://www.2spi.com/category/hopg-grade-1/hopg-spi-supplies/ (cit. on p. 52).

[Stull47] D. R. Stull. "Vapor Pressure of Pure Substances. Organic and Inorganic Compounds". *Industrial & Engineering Chemistry* 39.4 (1947), pp. 540–550. DOI: 10.1021/ie50448a023 (cit. on p. 71).

[TexIns09] Texas Instruments. *THS3201: 1.8-GHz, low distortion, current-feedback amplifier*. P.O. Box 655303, Dallas, Texas 75265. 2009. URL: www.ti.com (cit. on p. 123).

[TexIns14] Texas Instruments. *LMH6702: 1.7-GHz Ultra-Low Distortion Wideband Op Amp*. P.O. Box 655303, Dallas, Texas 75265. 2014. URL: www.ti.com (cit. on p. 123).

[ThoLin09] A. Thompson, I. Lindau, et al. *X-ray data booklet*. Lawrence Berkeley National Laboratory, University of California, Berkeley, CA 94720, 2009 (cit. on pp. 36, 57, 131, 144).

[ThüMar09] T. Thümmler, R. Marx, and C. Weinheimer. "Precision high voltage divider for the KATRIN experiment". *New Journal of Physics* 11.10 (2009), p. 103007. URL: http://stacks.iop.org/1367-2630/11/i=10/a=103007 (cit. on p. 10).

[ThyKru13a] ThyssenKrupp (UK) Ltd. *Aluminium Alloy 6060 Material Data Sheet*. Sept. 2013 (cit. on pp. 56, 57).

[ThyKru13b] ThyssenKrupp (UK) Ltd. *Aluminium Alloy 6082 Material Data Sheet*. Sept. 2013 (cit. on pp. 56, 57).

[Todd91] J. F. J. Todd. "Recommendations for nomenclature and symbolism for mass spectroscopy (including an appendix of terms used in vacuum technology)." *Pure and Applied Chemistry* 63 (10 1991), pp. 1541–1566. DOI: 10.1351/pac199163101541 (cit. on p. 94).

[ValVia10] R. Valentini and R. Vianden. "PAC studies with LSO scintillation crystals". *Nuclear Instruments and Methods in Physics Research Section A* 623.3 (2010), pp. 1002–1008. DOI: 10.1016/j.nima.2010.07.084 (cit. on p. 83).

[VarTri69] L. Varnell and J. Trischuk. "A peak-fitting and calibration program for Ge(Li) detectors". *Nuclear Instruments and Methods* 76.1 (1969), pp. 109–114. DOI: 10.1016/0029-554X(69)90298-5 (cit. on pp. 61, 174).

[VénKaš09] D. Vénos, J. Kašpar, et al. *Long term stability of the energy of conversion electrons emitted from solid* ^{83}Rb/^{83m}Kr *source*. 2009 (cit. on p. 36).

[Vénos13] D. Vénos. *Personal message*. June 2013 (cit. on p. 50).

[VénSle14] D. Vénos, M. Slezák, et al. "Gaseous source of ^{83m}Kr conversion electrons for the neutrino experiment KATRIN". *Journal of Instrumentation* 9.12 (2014), P12010. DOI: 10.1088/1748-0221/9/12/P12010 (cit. on pp. 39, 40).

[VénŠpa05] D. Vénos, A. Špalek, et al. "Kr radioactive source based on Rb trapped in cation-exchange paper or in zeolite". *Applied Radiation and Isotopes* 63.3 (2005), pp. 323–327. DOI: 10.1016/j.apradiso.2005.04.011 (cit. on pp. 39, 40).

[VerBlo65] H. Verheul, J. Blok, et al. "Geometrical corrections for angular correlation measurements with a large source and small detectors". *Physica* 31 (1965), pp. 565–572. DOI: 10.1016/0031-8914(65)90078-9 (cit. on pp. 32–34, 137).

[VerRam78] D. P. Verret and K. G. Ramanathan. "Total hemispherical emissivity of tungsten". *Journal of the Optical Society of America* 68 (9 1978), pp. 1167–1172. DOI: 10.1364/JOSA.68.001167 (cit. on pp. 73–75).

[ViaKau80] R. Vianden, E. N. Kaufmann, and J. W. Rodgers. "Impurity lattice location in ion-implanted beryllium: Measurements and systematics". *Physical Review B* 22.1 (1980), pp. 63–79. DOI: 10.1103/PhysRevB.22.63 (cit. on p. 55).

[WalHub50] M. Walter, O. Huber, and W. Zünti. "Experimente zur Richtungskorrelation sukzessiver Kernstrahlungen". *Helvetica Physica Acta* 23.VI – VII (1950), pp. 697–730. DOI: 10.5169/seals-112129 (cit. on p. 32).

[WeiDeg99] Ch. Weinheimer, B. Degenddag, et al. "High precision measurement of the tritium β spectrum near its endpoint and upper limit on the neutrino mass". *Physics Letters B* 460.1 – 2 (1999), pp. 219–226 (cit. on p. 6).

[ZakPei10] K. Zakeri, T. R. F. Peixoto, et al. "On the preparation of clean tungsten single crystals". *Surface Science*. 2nd ser. 604 (2010), pp. L1–L3. DOI: 10.1016/j.susc.2009.10.020 (cit. on p. 101).

[Zbořil11] M. Zbořil. "Feste Elektronenquellen für die Energieskalaüberwachung im KATRIN Experiment". PhD thesis. Westfälische Wilhelms-Universität Münster, 2011. URL: http://repositorium.uni-muenster.de/document/miami/79b74253-2dcd-493b-a08d-4eeb5a10b8c1/diss_zboril.pdf (cit. on pp. 11, 12, 50, 79).

[Zhu11] Ren-Yuan Zhu. *Crystal Scintillators & Time Resolution*. Talk given in Time Resolution Workshop, Chicago, USA. Apr. 2011 (cit. on p. 114).

[ZieZie10] J. F. Ziegler, M. D. Ziegler, and J. P. Biersack. "{SRIM} - The stopping and range of ions in matter (2010)". *Nuclear Instruments and Methods in Physics Research Section B: Beam Interactions with Materials and Atoms* 268.11 – 12 (2010), pp. 1818–1823. DOI: 10.1016/j.nimb.2010.02.091 (cit. on p. 48).

Acknowledgement

An dieser Stelle möchte ich mich herzlich bei meinen Betreuern, Mitarbeitern, Kollegen, Studenten und Freunden bedanken, die mich während der Zeit meiner Promotion unterstützt haben. Ohne diese Menschen wäre diese Arbeit nicht möglich gewesen.
Mein Dank gilt...

- insbesondere meinem Doktorvater und Arbeitsgruppenleiter Reiner Vianden, unter dessen Fittichen ich mich immer wohl gefühlt habe. Ich möchte mich für die hervorragende Arbeitsathmosphäre, die langjährige Betreuung, die interessanten Diskussionen, den gewährten Freiraum und die permanente Unterstützung bedanken. Auch die Fahrten zum KArlsruhe TRItium Neutrino (KATRIN) Meeting und zu den HFI/NQI Konferenzen waren immer eine willkommene Abwechslung. Trotz einiger (wissenschaftlicher) Härten werde ich mich an diese sechseinhalb Jahre immer gerne erinnern.
- meinem Stiefgruppenleiter Karl Maier für die Übernahme des Zweitgutachtens und für das stets offene Ohr bei technischen, physikalischen oder anderen Problemen.
- den fachangrenzenden und fachfernen Mitgliedern meiner Promotionskommission für die entstandenen Mühen und die unproblematische Terminfindung.
- Albrecht D'Hein für die unermüdliche Hilfe bei der Entwicklung des Verstärkers. Als eine Art Zweitbetreuer für Elektronikprobleme (und davon gab es zahlreiche) war er immer meine erste Anlaufstelle, wenn wieder etwas oszillierte oder gar nicht funktionierte. Bei ihm habe ich viel mehr gelernt, als ich jemals hätte behalten können, über Elektronik, Würfelnattern, Boote, Motoren, Rotationsschweißen, Kabelqualität und vieles mehr.
- Stefan Stahl für die Hilfe in vielen Telephonaten und Mails bei den ersten Schritten auf dem Gebiet des Platinendesigns und der HF-Technik.
- the 1×1 matrix Martin Slezák who became a good ~~colleague~~ friend over the years. For the time we spend together working, walking through Prague, slacking off and most notably: discussing. I dare to say that our cooperation was fruitful and one of the best I've ever had. The development of the MoS sources was a major project which would not have been possible without his measurements (Timepix, MoS, ^{83m}Kr retention), help, feedback and - did I already mention? - discussions. The help with my first Python programs and with the error propagation for the calibration of the HPGe detector is greatly appreciated as well. By the way: I will do 10^5 tosses as long as dogs lick their balls. We had a lot of good discussions too. The behaviour seems to be hard-coded on both sides.

- der BONn Isotope Separator (BONIS) Crew für die gute Zusammenarbeit und die schöne gemeinsame Zeit. Ich möchte mich bei Albert Dahl für die Zusammenarbeit beim Umsetzen von Neuerungen bei der Messelektronik am Massenseparator und für die zügigen Reparaturen wenn es nötig war bedanken. Auch bei Siggi Hinderlich bedanke ich mich für die regelmäßige und ordentliche Wartung der Ionenquelle und die Herstellung der vielen Wolframöfen. Vor allem, weil es manchmal auch wirklich schnell gehen musste. Besonderer Dank gilt hier natürlich Conny "Jonny" Noll für all die vielen Stunden und Tage, die Sie bei den zahllosen Testimplantationen und regulären Implantationen am Kontrollpult des Massenseparators verbracht hat. Vielen Dank auch für die vielen guten und auch amüsanten (Dierscher) Gespräche in dieser Zeit.

- my colleagues from Řež for the smooth cooperation. I'd like the thank Drahoslav Vénos for all the discussions, the quick responses whenever necessary. For organising last-minute irradiations, for always being rock-solid and incredibly reliable. And of course I want to express my gratitude to Ondrej Lebeda for the countless ^{83}Rb depositions, for the smooth and quick communication, the reliability. For all the answers on my questions regarding the irradiations and the chemistry of ^{83}Rb in the furnaces. And for all the double-strand breaks suffered from ^{83}Rb radiation for our purposes. I also want to thank Jana Sentkerestiová for picking it up quickly and doing all the retention and Timepix measurements when Martin left for Munich.

- Paul-Dieter Eversheim für die große Mühe des Probelesens, und für das stets offene Ohr bei Problemen mit Elektronik und meinem Vertrag.

- Bert Kann für die Hilfe bei diesen unzähligen Kleinigkeiten wie dem Abpumpen des HPGe Detektors, dem bedampfen/vorbereiten von Targets sowie für die ständige Hilfsbereitschaft.

- der Crew der feinmechanischen Werkstatt des HISKP für die Fertigung aller Bauteile und die umfassende und schnelle Hilfe bei allen Problemen mechanischer Natur. Auch bedanke ich mich für die vielen interessanten Diskussionen, ich habe viel gelernt.

- der Mannschaft der Elektronikwerkstatt des Helmholtz-Institut für Strahlen- und Kernphysik (HISKP) für die immer schnelle und freundliche Hilfe bei meinen Elektronikproblemen.

- der Crew vom Zyklotron für all' die langen Strahlzeit-Nächte. Für die Transporte meiner Radioaktivität danke ich Achim Henny und für den guten Support in Sachen Vakuumteile Stefan Birkenbach.

- Klaus Schlösser und der MoS-Mannschaft für das Messen der Proben, die produktiven Diskussionen und das zur Verfügung stellen der ISOLDE Linse.

- meinen beiden Arbeitsgruppen, der Gruppe Vianden und der (Adoptiv-)Gruppe Maier für die schöne Zeit und die angenehme Arbeitsathmosphäre. Es war immer ein angenehmes Arbeiten (und auch schon mal Nicht-Arbeiten).

- Michael Steffens für das Probelesen meiner Arbeit mit $v = c$ und die Diskussionen über die PAC-Ergebnisse. Dabei hat er eine ganze Arbeitsgruppe ersetzt.
- Sebastian Theilenberg für die Hilfe bei vielen TEX-nischen Kleinigkeiten und das Durchexerzieren der Fehlerrechnung mit Korrelationen bei der Kalibrierung des HPGe Detektors. Außerdem bedanke ich mich für die Einführungen in Python bei meinem Ti*k*z-Erklärbär.
- Patrick Keßler, Niels Räth und Pascal Newmaster für das regelmäßige Auffüllen des HPGe Detektors wenn ich mal wieder nicht da war.
- Ronan Nédélec für die Hilfe beim Verständnis der Winkelabhängigkeit der Wichtungsfaktoren bei Nightmare.
- Deniz Ulucay und Ben Slawski für die hilfreichen Diskussionen rund um GNUplot und Ti*k*z und das Drumherum (Kaffeemaschinen et al.)
- Alexander "Stumpf" Schäbe für die Hilfe bei einigen Problemen bei der PAC-Theorie und die Aktualisierung der Ofensimulation. Make it so!
- Henning Dickten für die Zeit beim Bioblockpraktikum. Jetzt können wir auch Reinigungskräfte werden. Mit Lappen können wir ja jetzt umgehen.
- Christoph Wendel für das Probelesen und die gute Zeit beim Praktikum.
- Christian Honisch für das zur Verfügung stellen von zwei Verstärkern und zwei APDs sowie die Hilfe beim Platinendesign und bei den SPICE-Simulationen.
- Johannes Müllers und der Gruppe Thoma für die Hilfe bei der Anfertigung meiner Platinen und das Fräsen der Splitterplatinen.
- dem DiWa für die Einführung in Inventor, die mein Arbeiten geprägt hat.
- Siegfried Schmid von Hamamatsu für die unkomplizierte und unbürokratische Hilfe.
- der Schnecke, die meine "Siegbahn"-Kopie [FraSte68] angefressen und mir gezeigt hat, dass eine intensive Beschäftigung mit der Theorie der gestörten Winkelkorrelation auch anders ausgehen kann als in meinem Fall. Ruhe in Frieden.
- allen, die mir irgendwie geholfen haben, mit Kleinigkeiten meine Arbeit im HISKP erleichtert, verbessert oder verschönert haben.
- meinem Vater für die Unterstützung bei den unzähligen LATEX-Problemen, deren Lösung diese Arbeit schöner gemacht haben. Ansonsten bedanke ich mich für die Unterstützung in allen Lebenslagen (egal ob's um die Diss, Konzerte, Kartfahren oder Einkaufen ging), und die immerwährende "kein Problem"-Haltung.
- meiner Freundin Sahar Hamidi für die fortwährende Unterstützung während dieser manchmal schwierigen Zeit. In diesen Phasen wo nichts geklappt hat und es einfach nicht vorwärts ging warst Du immer mein Joon. Dastet dard nakoneh, Azizam.